TITLE PAGE

Report Title: **SOFC Systems with Improved Reliability and Endurance**

Type of Report: Final Technical Report

Reporting Period Start Date: October 1, 2013

Reporting Period End Date: December 31, 2015

Principal Author: Hossein Ghezel-Ayagh

Date Report Issued October 2016

DOE Award No.: DE-FE0011691

Name & Address of Submitter: FuelCell Energy, Inc.
3 Great Pasture Road
Danbury, CT 06813

Subcontractors: Versa Power System, Inc.
10720 Bradford Road, Suite 110
Littleton, CO 80127-4298 USA

Versa Power Systems, Ltd.
4852 – 52nd Street SE
Calgary, Alberta, Canada T2B 3R2

DISCLAIMER

ABSTRACT

The overall goal of this U.S. Department of Energy (DOE) sponsored project was the development of Solid Oxide Fuel Cell (SOFC) technology suitable for ultra-efficient central power generation systems utilizing coal and natural gas fuels and featuring greater than 90% carbon dioxide capture. The specific technical objective of this project was to demonstrate, via analyses and testing, progress towards adequate stack life (≥ 4 years) and stack performance stability (degradation rate ≤ 0.2% per 1000 hours) in a low-cost SOFC stack design.

This final technical report summarizes the progress made during the project period of 27 months. Significant progress was made in the areas of cell and stack technology development, stack module development, sub-scale module tests, and Proof-of-Concept Module unit design, fabrication and testing. The work focused on cell and stack materials and designs, balance-of-plant improvements, and performance evaluation covering operating conditions and fuel compositions anticipated for commercially-deployed systems. In support of performance evaluation under commercial conditions, this work included the design, fabrication, siting, commissioning, and operation of a ≥ 50 kWe proof-of-concept module (PCM) power plant, based upon SOFC cell and stack technology developed to date by FuelCell Energy, Inc. (FCE) under the Office of Fossil Energy's Solid Oxide Fuel Cells program. The PCM system was operated for at least 1000 hours on natural gas fuel at FCE's facility. The factory cost of the SOFC stack was estimated to be at or below the DOE's high-volume production cost target (2011 $).

TABLE OF CONTENTS

ABSTRACT III

LIST OF FIGURES V

LIST OF TABLES 1

EXECUTIVE SUMMARY 2

INTRODUCTION AND OBJECTIVES 1

EXPERIMENTAL METHODS 2

RESULTS AND DISCUSSIONS 2

TASK 1. PROJECT MANAGEMENT AND PLANNING 2

TASK 2. CELL & STACK DEVELOPMENT 3

- 2.1. CELL TECHNOLOGY DEVELOPMENT 3
  - *2.1.1. Cell Material Development* *3*
  - *2.1.2. Cell Manufacturing Process Development and Fabrication* *29*
- 2.2. STACK TECHNOLOGY DEVELOPMENT 60
  - *2.2.1. Stack Design & Modeling* *60*
  - *2.2.2. Stack Component Development* *71*
  - *2.2.3. Stack Fabrication and Testing* *98*

TASK 3. STACK MODULE DEVELOPMENT 151

- 3.1. PROOF-OF-CONCEPT MODULE FABRICATION 151
- 3.2. DEVELOPMENT OF MW-CLASS MODULE 161

TASK 4. MW-CLASS PROCESS DESIGN AND STACK COSTING 164

TASK 5. PROOF-OF-CONCEPT MODULE (PCM) SYSTEM TEST 165

- 5.1. BALANCE-OF-PLANT (BOP) COMPONENT FABRICATION 165
- 5.2 PCM SYSTEM ASSEMBLY 179
- 5.3 PCM SYSTEM FACTORY TESTING 183

CONCLUSION 194

REFERENCES 196

LIST OF ACRONYMS 197

LIST OF FIGURES

Figure 2-1. Single-Cell Test (0.5A/cm^2, 750ºC) Featuring Design 2 Cr-getter in Cell, Co-Coated Cathode Hardware and Al-Coated Cathode Pipe (Cell GT101884) 4
Figure 2-2. Power Curves of Cell with PBSCF Cathode (in Temperature Range of 650 – 800°C) 5
Figure 2-3. Performance Stability of Cell GLOB 101899 Containing PBSCF Cathode............... 6
Figure 2-4. Performance Characteristics of Cell GLOB 101922 Containing LSCF Cathode (in Temperature Range of 650 – 800°C) 7
Figure 2-5. Performance Stability of Cell GLOB 101922 Containing LSCF 6428 Cathode 8
Figure 2-6. Power Curves for Cell GLOB 101927 Containing SSCF 5528 Cathode Material (at temperatures in 650 – 800°C range) 9
Figure 2-7. Performance Stability of Cell GLOB 101927 Containing SSCF 5528 Cathode 10
Figure 2-8. Performance Stability of Cell GLOB 101919 Containing Cr-getter Configuration C2 11
Figure 2-9. Performance Stability of Cell GLOB 101916 Containing Cr-getter Configuration C3 12
Figure 2-10. Thermal Cycling of Cell GLOB 101916 Containing Cr-getter Configuration 3........12
Figure 2-11. Performance Stability of Cell GLOB 101918 Containing Cr-getter Configuration C4 13
Figure 2-12. Performance Stability of Cells with Cr-getters Compared to Standard TSC-3 Cells in Six-Cell Stack GT055296-0140 (Cells 1, 3 and 5 contain Cr getter materials) 14
Figure 2-13. Single-Cell Tests with Coated Jigs (Hardware) 15
Figure 2-14. Stack Test GT0596000-0002 Evaluating MCO-coated and Cobalt-coated Interconnects..16
Figure 2-15. Nextech MCO Coating 17
Figure 2-16. PNNL MCO Coating...17
Figure 2-17. Sanergy Co Coating...17
Figure 2-18. Stack Test GT0596000-0003 Evaluating MCO-coated (by Nextech) ZMG232G10 Cathode Flow Fields...18
Figure 2-19. Cross Section of MCO Coated Cathode Flow Field in Channel (left) and in Contact Area (right) 19
Figure 2-20. Stack Test GT0596000-0004 Evaluating CoCe-coated 441 Alloy and Co-coated Sanergy Flow Fields (with Dry Cathode Air) 19
Figure 2-21. Stack Test GT059600-0004 Evaluating CoCe-coated 441 Alloy and Co-coated Sanergy Flow Fields (with Cathode Gas Humidity)..20
Figure 2-22. Cell Surface Analysis 21
Figure 2-23. Elements Analysis in Cell Layers; Ba in Ceria and Cr in Cathode 21
Figure 2-24. Oxide at Contact Area for Co-Ce Coated 441 Alloy Flow Fields............................22
Figure 2-25. Oxide at Contact Area for Co-coated Sanergy Flow fields....................................22
Figure 2-26. Oxide Thickness of Cathode Flow-Fields 23
Figure 2-27. Post-test Micrographs of Cross Sections of Coated Coupons Prepared with Additives A, B, and C 24
Figure 2-28. Single-Cell Test 101895 Evaluating MCO Coating with Additive C (Applied to Cathode Jig)...25
Figure 2-29. Single-Cell Test 101906 Evaluating Two-layer (Co and MCO) Coating with Additive B (Applied to Cathode Jig)...26
Figure 2-30. Cross Section of Coupon Coated (Two-layer) First Using Additive B-MC1.5 then Using Additive D-MC1.5 27
Figure 2-31. Single-Cell Test 101921 Evaluating Two-layer MCO Coating with Additives B-MC1.5 and D-MC1.5 (Applied to Cathode Jig)..28

Figure 2-32. Micrograph of a Cross Section of Tested Cell GLOB 101921 (Chemical Analysis by EDX of two boxed areas showed no Cr in either area) 29
Figure 2-33. High Level Mapping of Quality Improvement Plan 30
Figure 2-34. Pressure Equipment Platen Gaps before (left) and after (right) Re-Grinding 33
Figure 2-35. Flow Field Cut to Width 33
Figure 2-36. New Design of Go No-Go Gauge for Anode Flow Field..34
Figure 2-37. Go/No-Go Gauges for Cathode Flow Field Length and Width 34
Figure 2-38. General Seal Shape after Cutting...35
Figure 2-39. Seal Thickness Measurement Device (shows lower platen) 36
Figure 2-40. New Design Measurement Device for Seal Thickness 37
Figure 2-41. Seal Thickness Measurement Device View Looking Down 38
Figure 2-42. Seal Thickness Measurement Device View Looking Up.......................................38
Figure 2-43. Platen Displacement under Load (FEA results)...39
Figure 2-44. Consistency of Seal Corner Thickness Measurements in New Device (thickness shown in inch) 40
Figure 2-45. Cell Holder Thickness Measurement Using Micrometer Caliper...........................42
Figure 2-46. Pressure Drop Testing Jig...44
Figure 2-47. Flow Field Mounted in the Test Jig and Locations of Flow and Pressure Ports 45
Figure 2-48. Pressure Drop Characterization of Anode Flow Fields to be Used in Stack GT057235-0103 46
Figure 2-49. Deviations from Average Pressure Drop for Anode Flow Fields Selected for Use in Stack GT057235-0103 (Flow rate in slpm) 47
Figure 2-50. DP Measurement Consistency at 50 slpm Flow Rate (DP in psid) 48
Figure 2-51. Cell Edge Lip Measurement 49
Figure 2-52. Cell Leak Test and Edge Lip Checker 50
Figure 2-53. Cell Leak, Thickness, and Flatness Checker...51
Figure 2-54. Summary of Initial Gage R&R for Cell Thickness Performed Using New Measurement Tool 52
Figure 2-55. Theoretical Porosity (oxidized and reduced) and Ni and YSZ Volume % vs. Measured Cell Density 53
Figure 2-56. Performance Characteristics and Power Curves of GLOB 101896 0.3 mm RSOFC-7 Cell in Temperature Range of 650-800°C...54
Figure 2-57. Comparison of Performance Characteristics at 750°C for 0.6 mm TSC-3 Cells at Three Densities and a 0.3 mm RSOFC-7 Cell at Average Density of 5.45 g/cm^3..............55
Figure 2-58. Performance Characteristics of a 0.3 mm TSC-3 cell (in Temperature Range of 600 – 800ºC)..57
Figure 2-59. Theoretical Ni and YSZ Volume Percent, and porosity (oxidized and reduced) vs. Measured Cell Density for 50% w/w NiO Anode Substrate..58
Figure 2-60. Theoretical Ni and YSZ Volume Percent, and Porosity (oxidized and reduced) vs. Measured Cell Density for 60% w/w NiO Anode Substrate..59
Figure 2-61. Theoretical Ni and YSZ Volume Percent, and Porosity (oxidized and reduced) vs. Measured Cell Density for 65% w/w NiO Anode Substrate..60
Figure 2-62. 96-Cell Baseline Stack Block 61
Figure 2-63. In-Cell Manifold Stack 62
Figure 2-64. Conceptual Design of Non-Uniform Anode Flow Field Media Length for 80-Cell ICM Stack...63
Figure 2-65. Large Area Stack Unit Cell Temperature Profile..64
Figure 2-66. Large Area Stack Unit Cell Pressure Drop Profile 64
Figure 2-67. H_2 Profile on the Anode Layer...65
Figure 2-68. Nernst and Current Density Profiles...66

Figure 2-69. Pressure Drop Testing Jig for Cathode Flow Media G2 with a Split Slot in the Middle 66
Figure 2-70. Pressure Drop vs. Split Slot 67
Figure 2-71. 3-D modeling of a repeat layer with split cathode G2. 67
Figure 2-72. Split Cathode G2 (3 mm slot) has 6.8% Less Pressure Drop (right side)....68
Figure 2-73. Split Cathode G2 (3 mm slot) has 3.5°C Temperature Increase in Hotspot (right side) 68
Figure 2-74. Nickel Mesh Interconnection Layers in a 120-Cell Stack 69
Figure 2-75. Modeled vs Measured Pressure Drop Profiles of Nickel Mesh 70
Figure 2-76. Gas Bypass Due to Nickel Mesh Interconnection Layers 71
Figure 2-77. Performance Stability of Cell GLOB 101881 Containing NYG-353 Glass-ceramic Seals 72
Figure 2-78. SEM Image of Sample Taken from AO Region of Cell GLOB 101881....73
Figure 2-79. SEM Image of Anode to Glass Seal Interface at FO Region of Cell GLOB 101881 73
Figure 2-80. Leak Rate at 750°C and 0.5 psi Air of Thermicullite 866 LS (blue) and Standard Seals (red)....74
Figure 2-81. Post-Test Leak Test Plates with Thermicullite Seal Bonded to Both Sides by the Glass Coating....74
Figure 2-82. Effect of Seal Thickness on Leak Rate for Flexitallic Thermicullite 866 LS Seals ..75
Figure 2-83. SEM Cross-Section of Thermicullite Seal Broken Away from the Jigs....76
Figure 2-84. Power Curve Comparison of Cell with Thermicullite 866LS Seal on Anode....77
Figure 2-85. NYG-353 | Thermicullite 866 | NYG-353 Seals after Leak Testing 78
Figure 2-86. Dispensing Trials with Different Dispense Rates and Nozzle Sizes for Hybrid Seal Fabrication 79
Figure 2-87. Dispensing Trials on Cardboard Blanks to Define the Automated Program....79
Figure 2-88. Dispensing Trials on Thermicullite Seal to Verify the Process....80
Figure 2-89. Compression Plate after Thermiculite Seal Removed Showing Good Interfacial Bonding of the Glass Seal to the Inconnel 600 Compression Plate 81
Figure 2-90. Thermiculite Seal on Current Collector Showing Significant Cracking (especially at corners) of the Thermiculite Seal....81
Figure 2-91. Conceptual Design of Cr-filter Box for Stack Testing....83
Figure 2-92. Proof of Concept Cr-Getter Filter Test Apparatus....83
Figure 2-93. Proof of Concept Cr-Getter Filter Test #2 – Post-Test....84
Figure 2-94. Cr Getter Materials Tested for 1000 Hours at 800°C in Dry Air over Cr Pieces 85
Figure 2-95. CaO Cr Getter Supported on Various Materials Tested for 1000 Hours at 750°C in Air with 10% Humidity 85
Figure 2-96. SEM Images of Samples taken from Materials shown in Figure 2-6....86
Figure 2-97. SEM/EDX Analysis of 10% CaO on Alpha Alumina....87
Figure 2-98. SEM/EDX Analysis of 21% CaO on Gamma Alumina 88
Figure 2-99. Samples Before and After Thermal Cycling with Humidified Nitrogen 89
Figure 2-100. CaO Cr-Getter Supported on Various Materials and Tested for 5000 Hours at 750°C in 10% Humid Air Over Cr-pieces 90
Figure 2-101. Micrograph of Alumina-supported CaO Samples After 5000-Hour Test: Showing Discoloration Due to Cr-Species Interaction 91
Figure 2-102. SEM/EDX Analysis of Alpha Alumina-supported CaO After 5000-Hour Test Showing Cr Associated with Ca....92
Figure 2-103. SEM/EDX Analysis of Gamma Alumina-supported CaO After 5000-Hour Test Showing Cr Associated with Ca....93
Figure 2-104. Experimental setup for Cr evaporation rate evaluation 94
Figure 2-105. Schematic of Integrated Fuel Radiator and Pre-Reformer Unit....96

Figure 2-106. CFD Analysis Results for 50 kW Reformer - Radiator 97
Figure 2-107. Average Cell Voltage of 16-Cell Stack GT057235-0097....................................98
Figure 2-108. Individual Cell Voltages of 16-Cell Stack GT057235-0097 99
Figure 2-109. Distribution of Performance Degradation Rates for Stack GT057235-0097 at Phase II System Operating Conditions 100
Figure 2-110. Stack GT057235-0099 – Random Drooping of Cells after One Thermal Cycle .101
Figure 2-111. Stack GT057235-0101 – Cell 11 Voltage Drooped During Performance Characterization and Recovered During Steady-State Hold after One Thermal Cycle.....102
Figure 2-112. VPS Gas Replacement (GR) and FCE GR Test Conditions 102
Figure 2-113. Stack GT057235-0101 – Testing at VPS GR Conditions (after Two Thermal Cycles)..103
Figure 2-114. Stack GT057235-0101 – Testing at FCE GR Conditions (after Two Thermal Cycles)..104
Figure 2-115. Stack GT057235-0101 – Testing in Test Stand 26 (after relocating from Test Stand 24) 105
Figure 2-116. Stack GT057832-0005 Fuel Utilization Test After First Thermal Cycle 107
Figure 2-117. Stack GT057832-0005 Performance at Phase II System Operating Conditions (with increased N_2 flow) 108
Figure 2-118. Stack GT057832-0005 – Thermal Maps Before (top) and After (bottom) N_2 Flow Increase at Anode 109
Figure 2-119. Individual Cell Performance Trends of Stack GT057832-0005 at Phase 2 System Operating Conditions (with increased N_2 flow) 110
Figure 2-120. Stack GT057832-0005 Performance Stability at Phase 2 System Operating Conditions (with increased N_2 flow)..111
Figure 2-121. Stack GT057235-0108 Fuel Utilization Testing After First Thermal Cycle 112
Figure 2-122. Individual Cell Performance Trends for Stack GT057235-0108 at Phase 2 System Operating Conditions..113
Figure 2-123. Individual Cell Performance and Degradation Rates in Stack GT057235-0108 at Phase 2 System Conditions 114
Figure 2-124. Stack GT057235-0109 Performance at VPS GR Conditions 115
Figure 2-125. Individual Cell Performance Degradation Rate Distribution for Stack GT057235-0109 at VPS GR Conditions..116
Figure 2-126. Performance Stability of Stack GT058139-0002 at VPS Gas Replacement Conditions 117
Figure 2-127. Distribution of Individual Cell Performance Degradation Rates for Stack GT058139-0002 at VPS Gas Replacement Conditions 118
Figure 2-128. Performance Stability of Stack GT057235-0111 at Phase 2 System Conditions (with dry cathode air and with 10% cathode gas humidity) 119
Figure 2-129. Performance Stability of Stack GT057235-0112 at Phase 2 System Conditions120
Figure 2-130. Degradation Rate Distribution in Stack GT057235-0112.................................121
Figure 2-131. Test Stand Cathode Gas Humidifier Upgrade (left) with In-Stand Dew-Point Humidifier Vessel (right) 122
Figure 2-132. Newly Installed Cathode and Anode Preheaters after Insulation Work in Test Stand #28...124
Figure 2-133. 3 kW Thermally Self-sustaining SOFC Stack Module Installed in FCE Danbury Test Facility TF-30kW-5 125
Figure 2-134. Average Cell Voltage and Stack Current During 16-Cell Stack Test GT057235-0100...126
Figure 2-135. Individual Cell Voltages and End-Losses During 16-Cell Stack Test 127
Figure 2-136. Manifold and Heater Temperatures and Reactant Utilizations During 16-Cell Stack Test...128

Figure 2-137. Manifold Pressures and Cell Pressure Drops During 16-Cell Stack Test..........129
Figure 2-138. Cell Voltages and Stack Current During Load Cycle and N_2 Purge Testing 130
Figure 2-139. Cell Voltages after Load Cycles (of varying durations) during 16-Cell Stack Testing 131
Figure 2-140. 120-cell Stack Block Deliverable 132
Figure 2-141. 120-Cell Stack GT059636-0001 TC0 and TC2 Performance Test Results 135
Figure 2-142. Stack GT059636-0001 Performance at VPS GR Conditions 136
Figure 2-143. Stack GT059636-0001 Cell Voltage Distribution at VPS GR Conditions............137
Figure 2-144. Stack GT059636-0001 In-Stack Temperatures During TC2 Testing.................138
Figure 2-145. Stack GT059636-0002 TC0 & TC1 Performance Test Results.........................140
Figure 2-146. Stack GT059636-0002 In-Stack Temperatures During TC1 Testing.................141
Figure 2-147. Stack GT059636-0003 TC0 & TC1 Performance Test Results.........................142
Figure 2-148. Stack GT059636-0003 Full TC1 Performance Test Results.............................143
Figure 2-149. Stack GT059636-0003 TC1 In-Stack Temperatures..144
Figure 2-150. Stack GT059636-0004 TC0 & TC1 Performance Test Results.........................145
Figure 2-151. Stack GT059636-0004 Full TC1 Performance Test Results.............................146
Figure 2-152. Stack GT059636-0004 TC1 In-Stack Temperatures..147
Figure 2-153. Stack GT059636-0005 TC0 & TC1 Performance Test Results.........................148
Figure 2-154. Stack GT059636-0005 Full TC1 Performance Test Results.............................149
Figure 2-155. Stack GT059636-0005 TC1 In-Stack Temperatures..150
Figure 2-156. Performance During Factory Acceptance Tests of 120-Cell Stacks #2 - #5.......151
Figure 3-1. Cathode Secondary Air Inlet Design and CFD Analysis of Effects on Manifold Wall 153
Figure 3-2. Aluminized Non-Repeat Module Components. Left- Al Coated Ducts (Prior to Heat treatment). Right- Cast Compression Plate (After Heat Treatment). 154
Figure 3-3. Quad Base Refurbished...155
Figure 3-4. Quad Base Assembly with Radiator 156
Figure 3-5. (left) Piping Components Aluminized (right) Piping Components Masked and Aluminized...156
Figure 3-6. Module Awaiting Enclosure Installation 157
Figure 3-7. Module with Enclosure after Integration with BoP 158
Figure 3-8. Installing Stack Module in 50 kW PCM Plant...160
Figure 3-9. Illustration of Components and Materials Used in Internal Manifolding Design......162
Figure 3-10. Illustration of External Manifold Concept and Flow Configuration........................162
Figure 3-11 Securing External Manifold to Interconnect..163
Figure 3-12 Repeatable Cell Package...163
Figure 4-1 Block Cost Breakdown by Percent 165
Figure 5-1. Picture of the CPOx reactor system (left) and the catalytic heat exchanger (right) installed in the 400 kW Power Plant Facility at FCE 166
Figure 5-2 Schematic of Radiative Fuel Reformer...168
Figure 5-3. Reforming Catalyst Test Results: Measured Exit Gas Composition on Right, Compared with Expected Equilibrium Concentrations from ChemCAD Simulations on Left 168
Figure 5-4. Solid Models and CFD Boundary Assumptions for RFR Analysis 169
Figure 5-5. Comparison of CFD Analysis Results for Two Reforming Fin Insert Geometries (temperature scale shown in °F)..170
Figure 5-6. Solid Model of the Reforming Fin Insert (Left), and Actual Fin Insert (Right) 170
Figure 5-7. Photograph of Anode Recycle Blower at Vendor's Shop, Prior to Painting of the Base...171
Figure 5-8. Anode Recycle Blower Performance Characteristics Observed During The Factory Acceptance Test 172

Figure 5-9. CFD Analysis of Pipe Spool Design for Exit Connection from Anode Recycle Blower 173
Figure 5-10. Thermal Analysis of the Heater Including Heater Support (top) and 174
Figure 5-11. Isometric Model of the Anode Heater, Including Instrumentation 174
Figure 5-12. Anode Fuel Injector Model with Detailed View showing the Insulated Fuel Nozzle and Mixing of Fuel with the Anode Gas Stream 175
Figure 5-13. Detailed View of Fuel Injector with Triple Fluted Spiral Nozzle Tip 176
Figure 5-14. CFD Analysis showing Mixing Attributes of the Spiral Fuel Injector Design (Temperature scale shown in °F) 176
Figure 5-15. Anode Pipe Spool Assembly with Anode Water Injection 177
Figure 5-16. Anode Water Injector Details 177
Figure 5-17. EBOP Enclosure Showing DC-AC Inverter Section and DC-DC Converter Section. 178
Figure 5-18. EBOP Enclosure Showing Central Control System Section. 179
Figure 5-19 Fabrication Photos – Structural Skid w/ Desiccant and Desulfurizer 180
Figure 5-20 Fabrication Photos – Fresh Air, Recycle Blower, & Exhaust 180
Figure 5-21 Fabrication Photos – Inverter & Control Sides of EBOP Cabinet 181
Figure 5-22 Layout of the 50 kW PCM Plant on Pad 10 at FCE, Danbury, CT 181
Figure 5-23 50 kW BOP Installation & Frame for Protective Tent 182
Figure 5-24 Fabrication Photos – Module and BoP (left), Instrumentation Rack & Electrical Panel (right) 183
Figure 5-25 Façade Constructed around 50 kW PCM Plant 183
Figure 5-26 Stack Voltages During Hot Standby 185
Figure 5-27 Stack Temperatures During Hot Standby 185
Figure 5-28 Fuel Flow Rate and Utilization During 50 kW PCM System Factory Testing 188
Figure 5-29. Air Flow Rate and Utilization During 50 kW PCM System Factory Testing 189
Figure 5-30. Stack Currents During 50 kW PCM System Factory Testing (PC indicates testing using power conversion system) 190
Figure 5-31. Electrical Configuration Showing Stack-Load Bank Connections 190
Figure 5-32. SOFC Module Power Output During 50 kW PCM System Factory Testing 191
Figure 5-33. Radiative Reformer Temperatures 193

LIST OF TABLES

Table 2-1. Gage R&R Summary for Cell / Stack Quality Control 32
Table 2-2. Effect of Cell Thickness and Density on Performance at 750°C, 0.5 A/cm^2, 25% Uo and 50-90% Uf (before thermal cycle) 55
Table 2-3. Effect of Cell Thickness and Density on Uf Performance at 750°C, 0.5 A/cm^2, 25% Uo and 50-90% Uf(after one thermal cycle)....................................56
Table 2-4. Modeled Gas Compositions 70
Table 2-5. Cr evaporation rates for the alloys studied 95
Table 2-6. Stack GT057235-0101 Temperature Comparison During Performance Characterization in TS24 and TS26....................................106
Table 2-7. Acceptance Test Gas Compositions....................................133
Table 2-8. Stack Acceptance Criteria – Design and Height 133
Table 2-9. Stack Acceptance Criteria – Hot Test Results 134
Table 2-10. Stack Acceptance Criteria – Cold Test Results 134
Table 5-1.Evaluation of CPOx reactor performance at two different Air to Fuel inlet flow ratios (GC measurements compared with equilibrium concentrations estimated by ChemCAD process simulations)....................................166

EXECUTIVE SUMMARY

Significant progress was made in the areas of cell and stack technology development, stack module development, sub-scale module tests, and Proof-of-Concept Module (PCM) unit design, fabrication and testing. A brief summary for each follows.

Cell and Stack Technology Development:

Development of Chromium-tolerant cell technology was continued from the DOE SECA (Solid-state Energy Conversion Alliance) program (DE-FC26-04NT41837). A single-cell (81 cm^2 active area) test featuring a combination of Cr-tolerant technologies was conducted. The technologies included were Design 2 Cr-getter (30%-70% blend of Cr-getter materials Gb and Gc) in cell, Co-coated cathode hardware (jig) and Al-coated cathode feed pipe. The test was conducted at 500 mA/cm^2 and 750ºC, with 10% water vapor (moisture) added to the cathode stream. The test accumulated close to 2000 hours. No performance degradation (only cell voltage improvement) was observed during the 1774-hour period with humidified cathode air. The test met the Milestone: *Demonstrate Chromium Resistant Cell Technology with <0.5%/1000 hr Degradation Rate in >3% Humid Air.*

Scale-up (of cell area) and stack implementation of the Cr-tolerant cell technology and longer-term performance stability evaluation for further verification were pursued. Long-term testing of a six-cell (121 cm^2 cell active area) stack containing three cells with Cr-getter material (30% Gb-70% Gc blend) and three standard TSC-3 (third generation Tape casting, Screen printing and Co-firing cell manufacturing process) cells was conducted. The test accumulated over 8000 h of operation. The Cr-getter cell group exhibited a lower performance degradation rate of 0.39%/1000 h than the standard cell group (0.57%/1000 h) over a 7489-h period (at 388 mA/cm^2 and 750°C). The Cr-getter configuration 1 (Design 2) evaluation was conducted in 16-cell and 64-cell stacks (550 cm^2 cell active area) at PCM system representative conditions of 68% fuel utilization, 36.4% in-stack reforming, 15% oxidant utilization, and 291 mA/cm^2. The tests showed very low performance degradation rates of 0.26%/1000 h over 6500-h period in a 16-cell stack and 0.32%/1000 h over 10000-h period in a 64-cell stack. Cr-getter Configuration 1 was selected for 120-cell stacks fabricated for the Proof-of-Concept Module system test.

To further optimize TSC-3 (thin) cell anode substrate, a parametric study was conducted using single cell (81 cm^2 active area) tests. Effect of cell build (manufacturing) variables such as cell (anode substrate) thickness and cell density (via sintering temperature) on cell performance was studied in the operating temperature range of 650 to 800°C. The four cells used in the study covered a thickness range of 0.3 to 0.6 mm and density range of 5.25 to 5.75 g/cc. Though open circuit voltages for the cells were practically the same, there was quite a variation (53 mV) in cell voltage at 740 mA/cm^2 (highest current density tested). Cell performance (at 750°C and 500 mA/cm^2) was also characterized in the fuel utilization range of 50 to 90%. The results indicated that for improved cell performance at high current density and/or fuel utilization, thin anode substrate and cell density of less than 5.5 g/cc are desired. Power densities approaching 700 mW/cm^2 were exhibited by a cell featuring 0.3 mm thickness and 5.45 g/cc density. The power density envelope was further explored. Due to test equipment limitation, a smaller 25 cm^2 active area cell was used (to enable testing at current densities higher than the usual 740 mA/cm^2). The cell demonstrated the maximum power density of 2000 mW/cm^2 at 800°C and 800 mW/cm^2 even at a lower temperature of 650°C.

Progress was made to improve the quality and reliability of the stack technology. Anode side and cathode side flow fields are fin materials formed from stainless steel sheetmetal. Quality control of the procured fin components at VPS includes dimensional checks and visual observations. Limited cold flow testing of assembled stacks is also implemented. Focus on the flow field components revealed a need for development of a device for flow field pressure drop characterization (cold test) with the component constrained in a manner similar to that in a stack. Design of the test device (setup) was completed and the manufactured device was procured. Preliminary testing (characterization of flow fields using the device) showed that the device had the resolution necessary to differentiate between flow fields. Initial testing of anode flow fields to be used in a 16-cell (large area) stack was carried out using the device.

Advanced seal development activities included leak test evaluation of Thermicullite seal. The seal includes a commercial low viscosity glass coating on both sides. The seal functioned as expected (no interfacial leakage). The seal was also tested successfully in a single cell (81 cm^2 active area). The cell performance was very good (above 850 mV at 740 mA/cm^2, 750°C) and showed no significant change over three thermal cycles. Fuel utilizations up to 90% were tested without incident, indicating reasonable sealing. Testing of a glass seal material (from a Japanese company) was also conducted in a single cell. The test accumulated over 12,700 h and included 10 thermal cycles, exhibiting a low performance degradation rate of 0.5%/1000 h (at 500 mA/cm^2 and 750°C) over the test period. Post-test analysis of the cell was carried out. There was no evidence of any significant reaction or diffusion of glass components into the cell materials which was consistent with the low degradation rate observed over the 12,700-hour test period. This seal material can serve as a more stable substitute for the commercially available glass coating used in Thermicullite seal.

Stack Module Development, Sub-scale Module Tests and PCM (Module) Fabrication:

Sub-scale module tests were conducted to guide the development of SOFC stack module. Test of a 16-cell stack (550 cm^2 cell active area) in a module (thermally self-sustaining environment) at system operating conditions (representing 50 kW PCM system) was conducted at FCE, Danbury facility. The testing included three steady state test periods at system relevant conditions (273 mA/cm^2). The average cell performance degradation rates observed during the periods and durations were 0.85%/1000 h over 1135 h, 0.51%/1000 h over 930 h and 0.78%/1000 h over 1526 h. Overall, the stack operated at simulated system relevant conditions for more than 4,500 h with an average degradation rate below 1%/1000 h.

The fabrication of the PCM (SOFC module) was carried out. To facilitate Balance-of-Plant (BOP) system operational checkout (during initial phase of PCM system test), four 96-cell stacks previously used in 60 kW quad-based SOFC module test (conducted under DOE Project DE-FC26-04NT41837) were installed in the (PCM) module. Major equipment (installed) included Catalytic Cathode Air preheater (heat exchanger) and Radiative Fuel Reformer. Installation also included process piping components (aluminized), hot valves and electrical bus bars. Final assembly of the module included instrumentation, thermal insulation and wiring connections. Module enclosure was installed and the module was leak tested successfully. The module was integrated with the balance of plant for PCM system test.

Fabrication of 120-cell stacks (550 cm^2 cell active area) for PCM system test was completed. The stacks were built, conditioned and factory tested at VPS. The factory acceptance testing included fuel utilization testing (up to 75% fuel utilization) before and after thermal cycle, and steady state performance characterizations at Phase I system and PCM system operating conditions. Four (factory) accepted stacks were received at FCE, Danbury, for module integration (to replace used 96-cell stacks) and subsequent PCM system test.

Proof-of-Concept Module (PCM) Unit Design, Fabrication and Testing:

The PCM system (unit) included Mechanical BOP and Electrical BOP, in addition to the SOFC module (PCM). BOP component development was carried out. The integrated fuel preheater (radiative) and fuel pre-reformer, termed Radiative Fuel Reformer, was developed combining input from reforming catalyst vendors, CFD (computational fluid dynamics) analysis and sub-scale testing to ensure that the radiative fuel reformer heat duty, pressure drop, and methane conversion targets can be achieved. Coated monolith catalysts, to provide the desired reforming capability with reduced pressure drop, were evaluated. Testing at FCE validated the effectiveness of the catalyst coating by producing near-equilibrium outlet concentrations in a wide range of catalyst operating temperatures and space velocities. ChemCAD-based process simulations were performed in conjunction with CFD analyses to determine potential anode inlet gas temperatures and compositions based on catalyst loading and expected radiative heat duty. A corrugated fin design was selected for catalyst support in collaboration with the catalyst coating vendor. The full-scale radiative fuel reformer was fabricated for use in the PCM power plant.

PCM system drawings were developed. Specification, fabrication/ procurement, and testing of PCM system balance-of-plant components were carried out. Factory test of the Anode Recycle Blower was completed successfully. Fuel Injector (into anode recycle loop) and Water Injector designs were developed based on CFD analysis. The Power Conditioning System (part of Electrical BOP) design and layout of components were carried out. The components were procured and bench tested. A quotation was received from a fabrication vendor for assembly of the PCM System. Fabrication and assembly of the mechanical and electrical balance of plant, and the site preparations at FCE, Danbury were completed. PCM system component verification, final end-to-end checkout and leak testing were carried out. Process and control tests for the 50 kW PCM system were performed. The issues identified were resolved.

First stage of the 50 kW PCM system checkout and commissioning using pre-tested SOFC stacks was carried out. Control system verification was performed and the issues identified with the control logic were resolved. Preliminary testing of the 50 kW PCM plant included successful start-up and operation in hot standby mode. Grid connected testing to verify the power control system function and load step transitioning was then carried out. The system was tested up to the 30% load level. The plant was shutdown to replace the old stacks with new (unused) factory tested 120-cell stacks. A post-test examination of the module and stacks was conducted prior to the stack replacement. Lessons learned from commissioning and post-test examination were implemented in the module rebuild for success of the PCM system demonstration test. No issues were observed related to Radiative Fuel Reformer and Catalytic Heat Exchanger (cathode air preheater), imparting confidence in the BOP component design.

The reassembled stack module was integrated with the PCM plant and testing was resumed. Some power conversion subsystem (PCS) related issues were resolved. The system operation at full load (100% load level) was accomplished. The PCM system factory testing was completed, meeting the test requirement of >1000 hours of hot operation. Due to reliability issue with the power conditioning system, factory testing was conducted using a DC (direct current) load bank. The full load testing was performed generating a gross DC stack power of 55.8 kW. The system was run at a target (overall) fuel utilization of 85%. The power plant efficiency was estimated using a DC/AC conversion efficiency of 97%. The overall power plant efficiency taking into account the fuel utilization was 61% which met the target efficiency of >50%. Overall, the 50 kW SOFC power plant test was successful. The testing performed during this project verified the performance of the cell stacks under field conditions. Several issues were overcome during the commissioning and testing phase. Knowledge gained will be used for developing the 200 kW SOFC system. The 50 kW test served as an important step in the development of robust process control algorithms and control strategies. In addition, valuable system design experience was gained and will result in smaller, more compact anode recycle blowers, improved fresh air desiccant system controls and improved plant heat-up strategies.

MW-class Module Development:

Toward MW-class module development, concepts using external stack manifolds (based on the carbonate fuel cell success) were generated. The design considered facilitated elimination of cathode and anode shim seals, significantly reducing the quantity of stack components required. To facilitate scale-up to a larger cell package (more suited for MW-class stack module), the concept employed U-flow configuration for cell cathode side. This flow configuration with the cathode gas turn manifold is expected to provide better thermal management of the MW-class SOFC stack that is required to accommodate significant in-stack reforming of natural gas fuel on anode side.

INTRODUCTION AND OBJECTIVES

FuelCell Energy, Inc. (FCE), along with its wholly owned subsidiary Versa Power Systems is developing solid oxide fuel cell (SOFC) technology and SOFC systems with improved reliability and endurance. The goal of this U.S. Department of Energy (DOE) sponsored project is the development of SOFC technology suitable for ultra-efficient central power generation systems (utilizing coal and natural gas fuels) featuring greater than 90% carbon dioxide capture. The development of this technology will significantly advance the nation's energy security and independence interests while simultaneously addressing environmental concerns, including greenhouse gas emissions and water usage.

The specific technical objective of this project is to demonstrate, via analyses and testing, progress towards adequate stack life (≥ 4 years) and performance stability (≤ 0.2% per 1000 hours degradation) in a low-cost SOFC stack design. The work will focus on cell and stack materials and designs, balance-of-plant improvements to extend stack life and limit degradation, and performance evaluation covering operating conditions and fuel compositions anticipated for commercially-deployed systems. In support of performance evaluation under commercial conditions, this work includes the design, fabrication, siting, commissioning, and operation of a ≥ 50 kWe proof-of-concept (fuel cell) module (PCM) power plant, based upon SOFC cell and stack technology developed to date by FCE within the Office of Fossil Energy's Solid Oxide Fuel Cells program. The PCM system will be operated for at least 1000 hours on natural gas fuel at FCE's facility. The cost of the SOFC stack will be at or below the DOE's high-volume production cost targets (2011 $).

In support of the aforementioned goal and project objective, activities to be conducted during this project will include:

- SOFC cell and stack technology research and development (R&D) focusing on performance, reliability, cost and manufacturing enhancements through cell and stack designs and material development.
- Fabricate and test fuel cells and stacks. This activity includes endurance testing (≥1000 hours) under system-relevant operating conditions.
- Design and fabricate a ≥50 kWe PCM system, including the SOFC stacks, mechanical balance-of-plant (MBOP) and electrical balance-of-plant (EBOP).
- Commission and operate the PCM system for at least 1000 hours using natural gas fuel at FCE's CT facility.
- Estimate SOFC stack costs, based on operating conditions expected in a commercial SOFC product and high-volume manufacturing levels.
- Develop conceptual process design and module concept for MW-class power plant systems.

The work will focus on SOFC stack reliability and endurance, especially in a system configuration. As shown in the following table, a number of key issues associated with stack failure have been identified and prioritized.

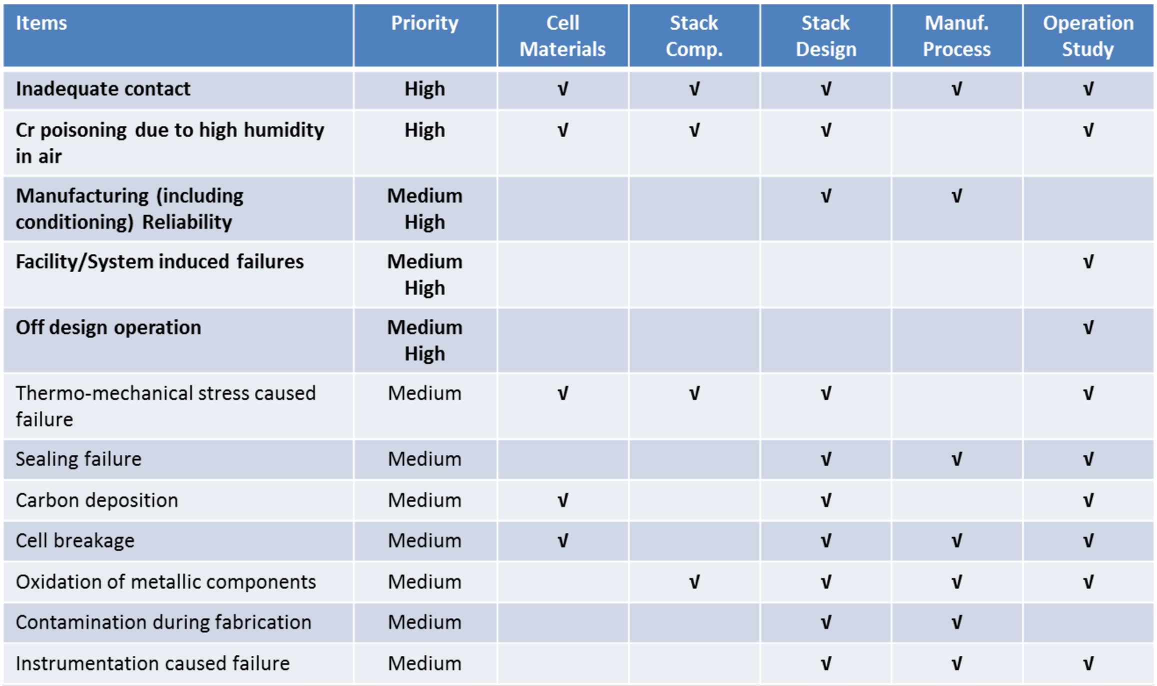

Items	Priority	Cell Materials	Stack Comp.	Stack Design	Manuf. Process	Operation Study
Inadequate contact	**High**	**√**	**√**	**√**	**√**	**√**
Cr poisoning due to high humidity in air	**High**	**√**	**√**	**√**		**√**
Manufacturing (including conditioning) Reliability	**Medium High**			**√**	**√**	
Facility/System induced failures	**Medium High**					**√**
Off design operation	**Medium High**					**√**
Thermo-mechanical stress caused failure	Medium	√	√	√		√
Sealing failure	Medium			√	√	√
Carbon deposition	Medium	√		√		√
Cell breakage	Medium	√		√	√	√
Oxidation of metallic components	Medium		√	√	√	√
Contamination during fabrication	Medium			√	√	
Instrumentation caused failure	Medium			√	√	√

Through R&D in the five key areas – (1) cell materials, (2) stack materials, (3) stack design, (4) manufacturing process, and (5) stack operation study – technical solutions will be developed, analyzed, down-selected, and implemented. Validation testing of proposed solutions will be conducted leading to selection of an optimum-scale design configuration, material set and manufacturing processes for cells to be implemented in the stack building block unit. Stack blocks will be fabricated, validated, and delivered for testing of the PCM system.

The detailed design and fabrication of the PCM will be completed and the module will undergo factory inspection and acceptance tests. Detailed design and fabrication of the MBOP and EBOP skids will be completed and the skids will be acceptance tested prior to integration. The module, MBOP, and EBOP will be integrated into a PCM power plant and tested at FCE's site. PCM test duration will be at least 1000 hours. The test plan, delineating the details of system operation, will be submitted to DOE for concurrence.

EXPERIMENTAL METHODS

The project involved cell component development and scale-up; manufacturing process improvements and scale-up; stack block, stack tower and multi-stack module design and testing; and balance-of-plant (BOP) system design and component testing. Various tests such as single cell, short stack, stack block, stack tower, four-stack module, and out-of-cell characterization tests were used to support these developments and activities. FCE and VPS, both, have test stands and test facilities including analytical equipment. These test tools were used routinely throughout the reporting period. Additional experimental details and photographs are provided along with relevant test results under 'Results and Discussion' section of the report.

RESULTS and DISCUSSIONS

TASK 1. Project Management and Planning

FCE's Project Manager (PM) will manage and direct the project in accordance with the Project Management Plan (PMP) to meet all technical, schedule and budget objectives and requirements. The Recipient will coordinate activities among the various task and subtask leaders assigned by Team Members and with DOE/NETL in order to effectively accomplish the work. The Recipient will ensure that project plans, results, decisions, etc. are appropriately documented and project reporting and briefing requirements are satisfied. The PMP will be updated in coordination with the NETL Project Officer such that it accurately reflects the current status of the project. Management of project risks will occur in accordance with the risk management methodology delineated in the PMP in order to identify, assess, monitor and mitigate technical uncertainties as well as schedule, budgetary, resource, and environmental risks associated with all aspects of the project. The results and status of the risk management process will be presented during project reviews and in Progress Reports with emphasis placed on the medium- and high-risk items. The Recipient will invite the DOE Project Officer to participate in the program risk review meetings for this project.

The following project management activities will be performed:

- Conduct review meetings to ensure adequate communication among team leaders.
- Conduct technical area reviews to identify, discuss, and resolve technical issues.
- Prepare and/or oversee the preparation of the required deliverables.
- Hold periodic project review meetings with the US-DOE NETL.

Subcontract related discussions and development of the scope of work (SOW) for Versa Power Systems (VPS) portion of work were carried out. The Subcontract document was signed on January 21, 2014. Project management and planning activities were performed throughout the project period. Toward the end, no-cost extensions were requested to allow time required to complete 1000-h PCM system factory testing (under Task 5). The project end date was extended to December 31, 2015 by DOE.

TASK 2. CELL & STACK DEVELOPMENT

The cell and stack development work concentrated on key issues to reduce performance degradation and enhance endurance. The objectives of this task are to identify and prioritize degradation and failure mechanisms in state-of-the-art SOFC cells and stacks, to serve as the basis for R&D to achieve commercially-viable reliability and endurance. Opportunities for efficiency improvement and cost reduction are addressed as appropriate. The main technical work focused on the following subtasks:

2.1. Cell Technology Development

Development work in Task 2.1 concentrated on key cell issues related to material stability, cell robustness and performance degradation especially at system operating conditions. Solutions to these areas are being developed, analyzed, down-selected and implemented at the large area (up to 550 cm^2 nominal cell active area), full height stack level. Validation testing of proposed solutions is being conducted, leading to selection of a design configuration, material set and manufacturing processes for implementation in the stack building block unit.

2.1.1. Cell Material Development

The emphasis for this task is being placed on enhancing cell endurance in full size stack blocks at system operating conditions. Chromium (Cr) poisoning of the cathode due to humidity in air at system operating conditions has been identified as a key degradation mechanism. Research is being focused on two key activities: Cr-tolerant cell component development and development of coating technology for reduction of Cr species. Other material solutions are being evaluated with the considerations for reliability, cost and operational flexibility of the cell, stack and system.

Development of Cr-Tolerant Cell Technology

A long-term single-cell test was conducted featuring a combination of validated Cr tolerant technologies. The technologies included in this test were Design 2 Cr-getter in cell, Co-coated cathode hardware (jig) and Al-coated cathode pipe. The test started initially using dry cathode air. After about 200 hours, 10% water vapor (moisture) was added to the cathode stream. Steady state testing of the cell was conducted at 0.5A/cm^2 and 750ºC. The test accumulated close to 2000 hours. As shown in Figure 2-1, there was no performance degradation (only cell voltage improvement) during the 1774 hour-period with humidified cathode air. This test met the SECA FY14 Q1 (Dec 27, 2013) GPRA Milestone: *Demonstrate Chromium Resistant Cell Technology with <0.5%/1000 hr. Degradation Rate in >3% Humid Air.*

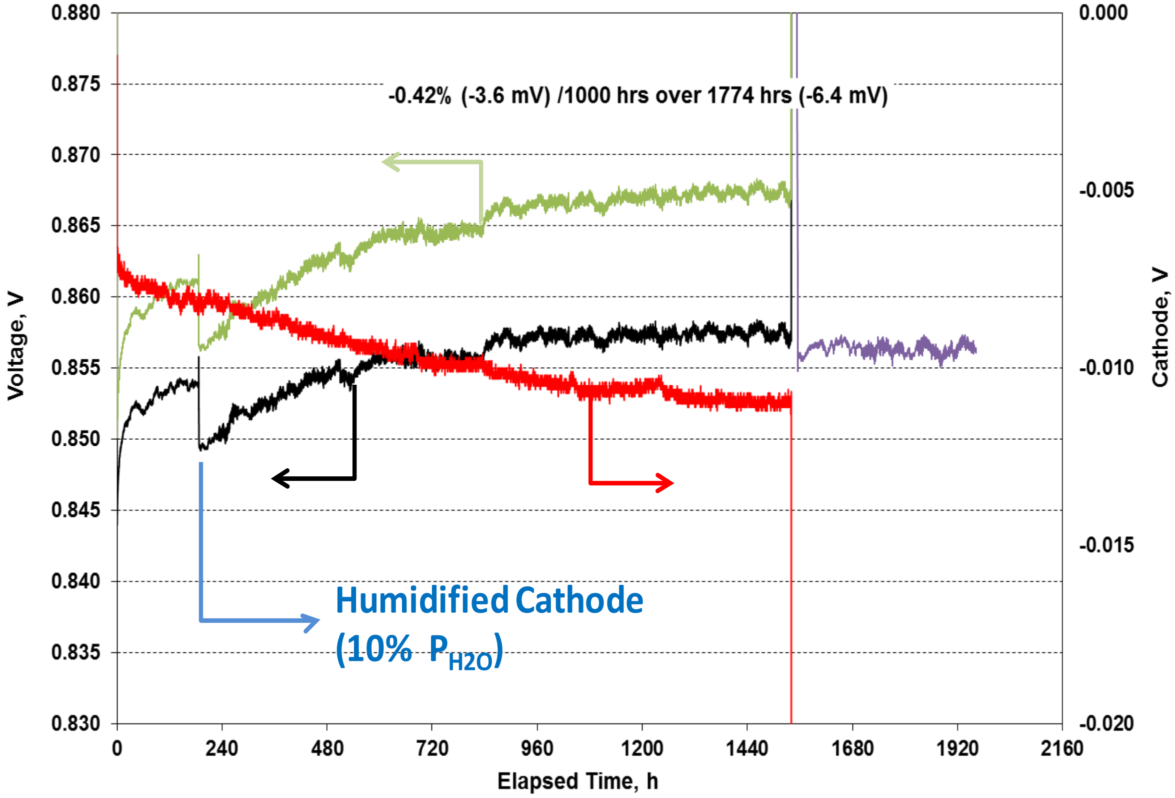

Figure 2-1. Single-Cell Test (0.5A/cm^2, 750ºC) Featuring Design 2 Cr-getter in Cell, Co-Coated Cathode Hardware and Al-Coated Cathode Pipe (Cell GT101884)

Cr-Tolerant Cathodes: A literature survey for Cr tolerant cathode materials was performed. Based on previous reporting (by Forschungszentrum Juelich) of cathodes tolerant to humidified air and recent reports of a new high performance cathode ($PrBa_{0.5}Sr_{0.5}Co_{1.5}Fe_{0.5}O_3$, PBSCF, double perovskite) in the literature [1], it was decided to prepare this cathode material and test it in a single cell to see if it exhibits Cr tolerance. Power curves at low utilization were characterized from 800 to 650°C up to 0.74 A/cm^2 (Figure 2-2). Cell voltage was acceptable but lower at low temperature than a standard TSC-3 cell.

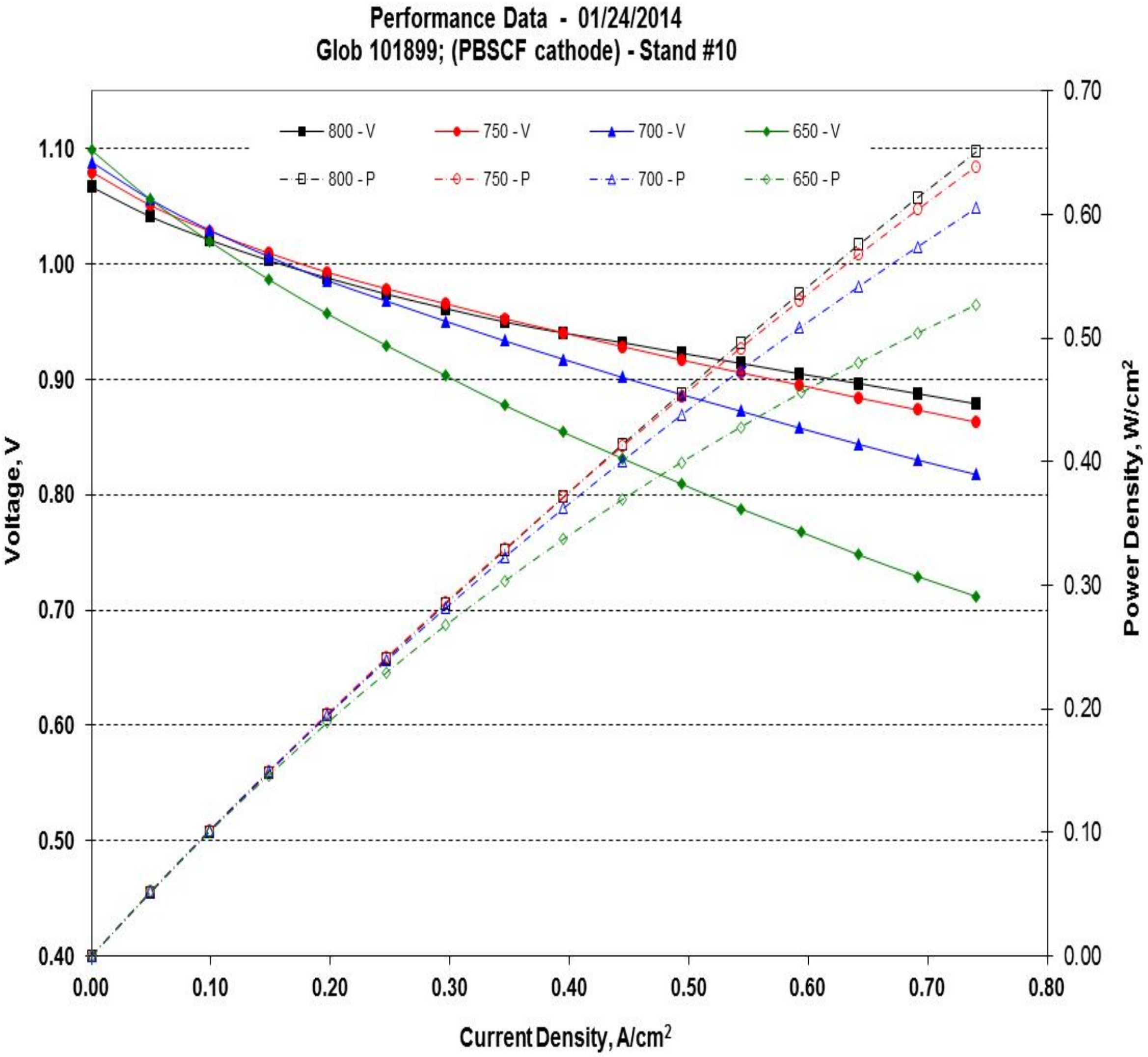

Figure 2-2. Power Curves of Cell with PBSCF Cathode (in Temperature Range of 650 – 800°C)

The cell was then set to run for 1000 hours in dry cathode air at 0.5 A/cm^2, 750°C furnace temperature, 50% Uf (hydrogen + 3% water) and 25% Uo. Figure 2-3 shows the cell voltage and temperature vs. time trends during this period. The cell performance degradation rate during 1003 hours with dry cathode air was 0.39% (3.4 mV) per 1000 hours. After completing the testing in dry cathode air, the cell was tested with 10% cathode gas humidity condition for 572 hours. During the 572-h period with 10% cathode gas humidity, the degradation rate was 1.75% (15 mV) per 1000 hours. It was decided to terminate the test to facilitate post-test analysis.

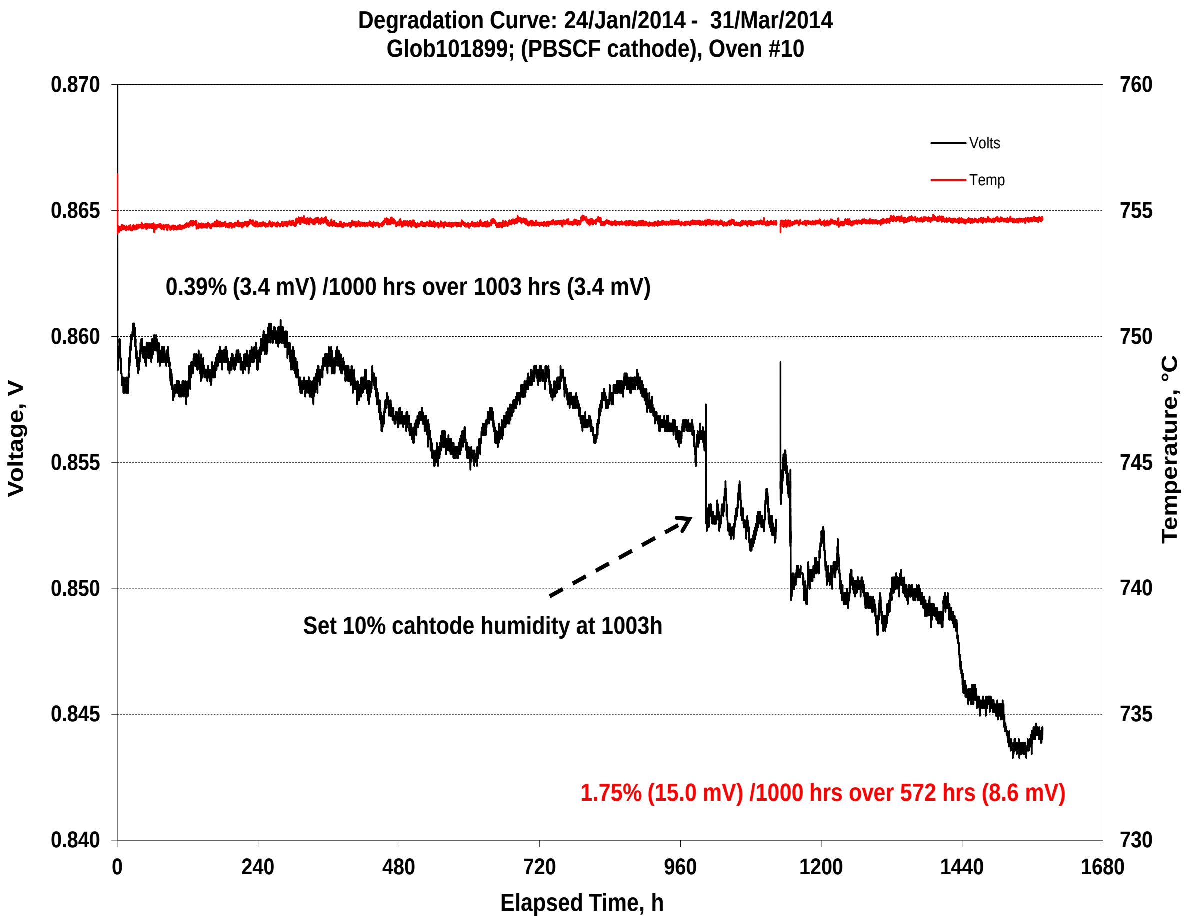

Figure 2-3. Performance Stability of Cell GLOB 101899 Containing PBSCF Cathode

Testing of LSCF (La substituting for PrBa) 6428 cathode in a single cell was also conducted to provide comparison. Power curves at low utilization were measured from 800 to 650°C up to 0.74 A/cm^2 and can be seen in Figure 2-4. Again, cell voltage was acceptable, but even lower at low temperature than the PBSCF cell. The cell was then tested for 250 hours with dry cathode air at 0.5 A/cm^2, 750°C furnace temperature, 50% Uf (hydrogen + 3% water) and 25% Uo. Figure 2-5 shows the cell voltage and temperature vs. time trends. The performance degradation over this short test period was negligible. After the 250-hour hold with dry air, 10% cathode humidity condition was introduced.

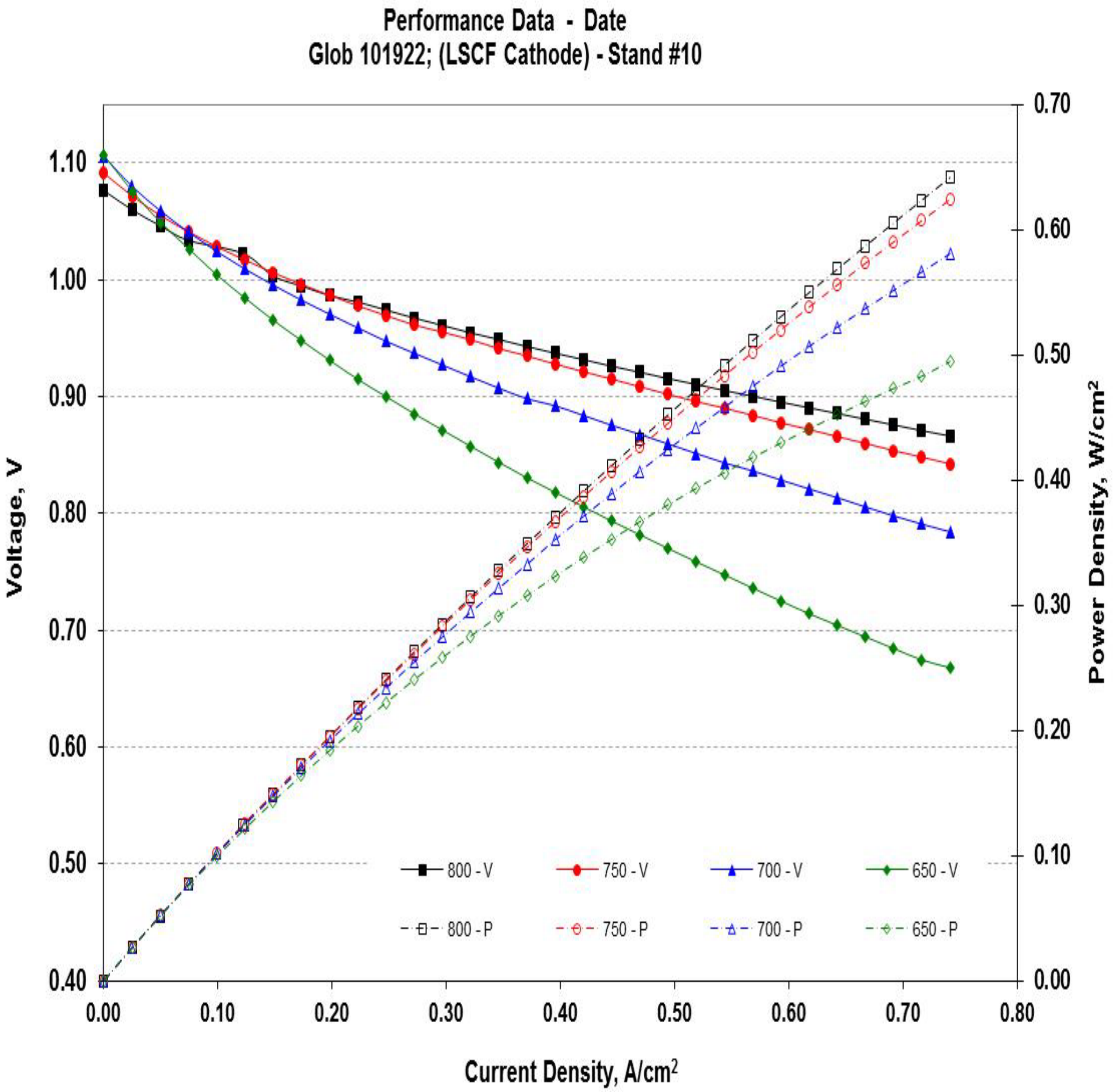

Figure 2-4. Performance Characteristics of Cell GLOB 101922 Containing LSCF Cathode (in Temperature Range of 650 – 800°C)

During testing with 10% cathode gas humidity (introduced to the air) the performance degradation rate increased with a final value of 2.4% (20 mV) per 1000 hours over 1100 hours before the test was terminated.

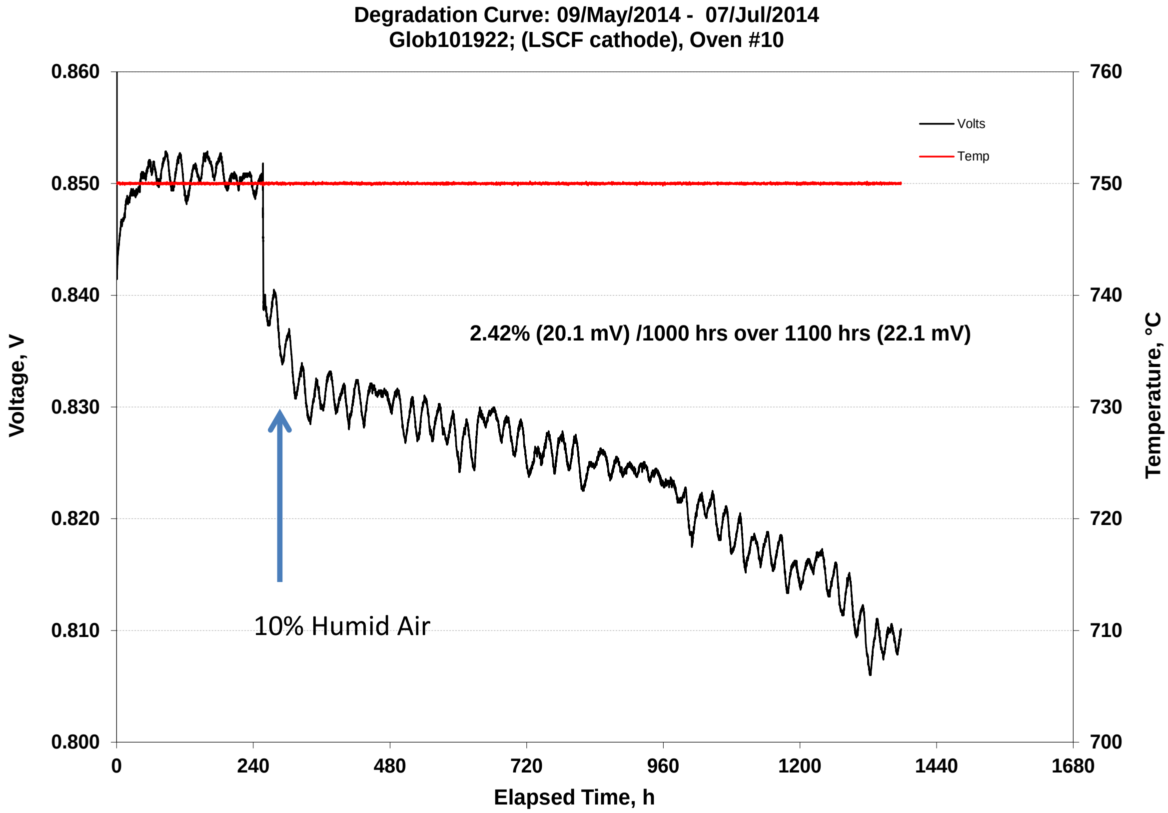

Figure 2-5. Performance Stability of Cell GLOB 101922 Containing LSCF 6428 Cathode

In addition to materials such as PBSCF ($PrBa_{0.5}Sr_{0.5}Co_{1.5}Fe_{0.5}O_3$ double perovskite [1]) and LSCF (identified in the literature survey), two other materials were identified for investigation. Yang described negligible change in surface oxygen exchange kinetics for Nd_2NiO_4 compared with LSC in the presence of Cr species [2]. Huang described no change in polarization resistance when using GDC-20 infiltrated into an LNF cathode at solids loading around 22% compared with LNF directly on scandia-zirconia [3]. This may simply have the same effect as using a ceria barrier layer on the zirconia, but could be interesting to investigate in addition to the ceria barrier layer.

Following the cell test with LSCF cathode, it was decided to investigate different A-site cation effects. Cell test GLOB 101927 was conducted to evaluate SSCF 5528 (Sm instead of La or Ba on A-site) cathode. Power curves at low utilization were characterized in the operating temperature range of 800 to 650°C up to current density of 0.74 A/cm^2 and can be seen in Figure 2-6. Cell voltage was acceptable—better than LSCF—but not as good as the standard VPS cathode. The cell was tested for 665 hours using dry cathode air at 0.5 A/cm^2, 750°C furnace temperature, 50% Uf (hydrogen + 3% water), and 25% Uo. The testing with 10% cathode gas humidity was then initiated. Figure 2-7 shows the cell voltage and temperature vs. time trends. The test was terminated after over 2900 h of operation at these conditions (cathode air with 10% humidity). The degradation rate was 2.29% (19.8 mV) per 1000 hours over the 2900-h period. The completed test showed SSCF to be the most stable cathode that had acceptable cell performance from 650-800°C. However, the degradation rate was still too high in humidified air, with the only meaningful difference being that it takes longer for performance to reach an unacceptably high degradation rate.

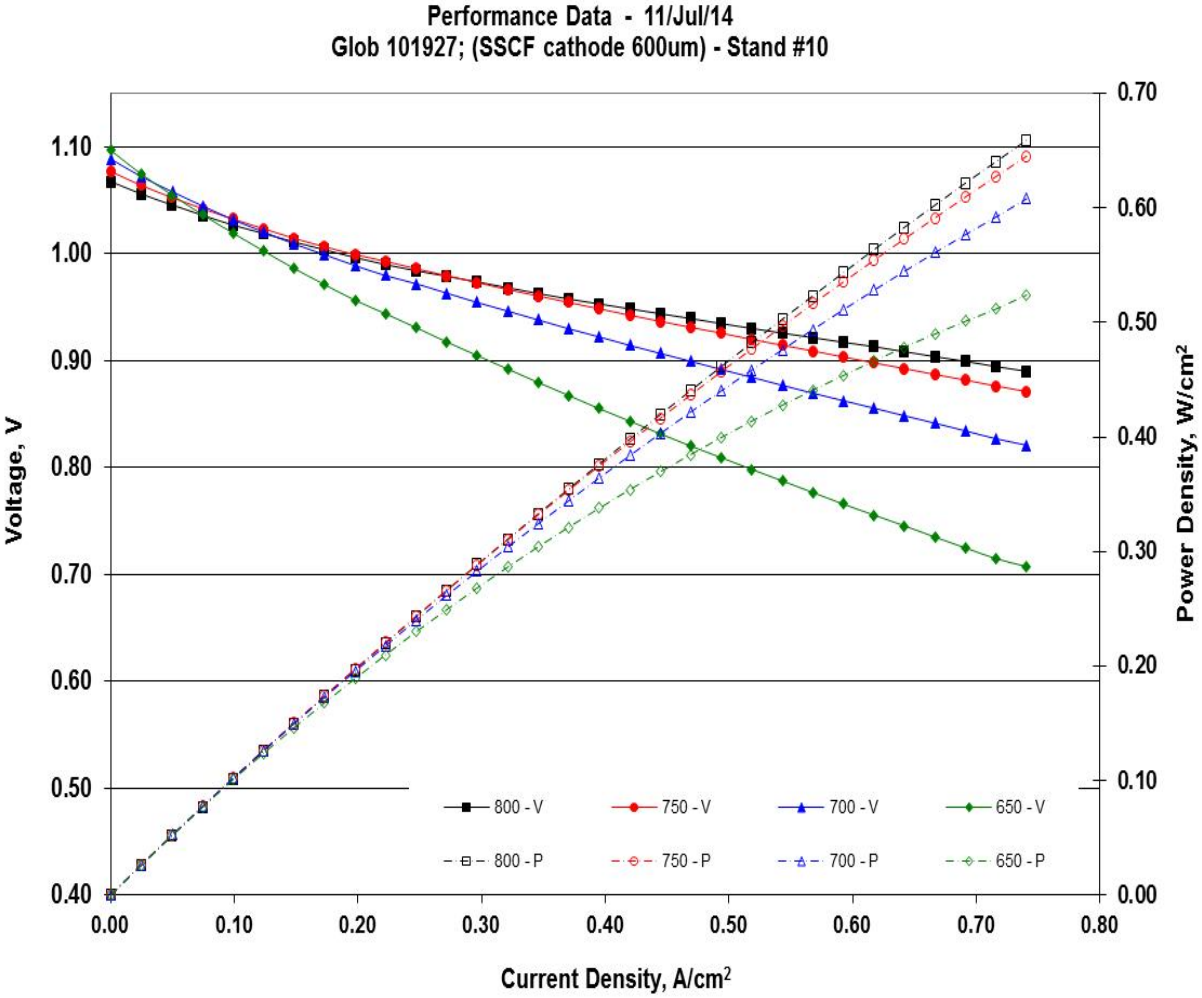

Figure 2-6. Power Curves for Cell GLOB 101927 Containing SSCF 5528 Cathode Material (at temperatures in 650 – 800°C range)

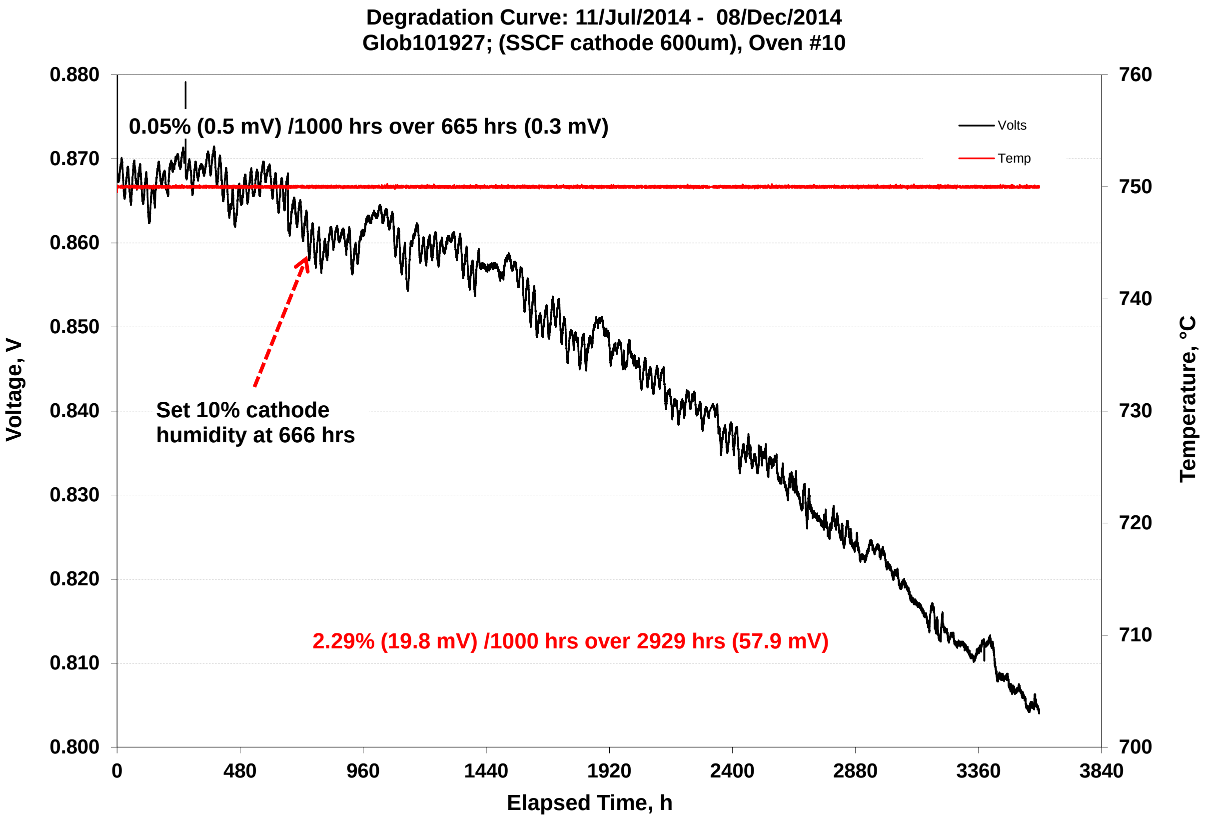

Figure 2-7. Performance Stability of Cell GLOB 101927 Containing SSCF 5528 Cathode

Cr-getter Configurations: Long-term single-cell test of a TSC-3 cell with Cr tolerant technology (GLOB 101859) was completed after more than 11,500 hours of operation at 750°C, 0.5 A/cm^2, 50% Uf (hydrogen) and 25% Uo (air with 10% water) including 10 full thermal cycles at the end of the test. Post-test examination of the cell was conducted. The main findings were that one of the Cr-getter materials, Gc, was transporting (substituting) into the perovskite cathode on the A-site to replace A-site cation that was migrating towards the electrolyte and reacting with the ceria barrier layer, chromium vapor species, and even the YSZ layer (over a small region at fuel inlet). It was decided to investigate alternative Cr-getter configurations in the stack. Three alternative configurations, C2, C3 and C4, were proposed. These configurations were first evaluated in single cell tests to determine the optimum design for Cr-getters in the stack.

Figure 2-8 presents cell voltage vs. time trend for cell with configuration C2 showing a low degradation rate of 0.32% per 1000 hours over 14496 hours of testing with dry cathode air at 0.5 A/cm^2, 25% Uo and 50% Uf (hydrogen + 3% water). Figure 2-9 includes the results for configuration C3 showing no measurable degradation over ten thermal cycles and 300 hours of testing with dry cathode air. An initial low degradation rate of 0.68% per 1000 hours was observed over 2391 hours of testing at accelerated degradation test conditions of 10% humidity in the cathode air stream. This cell contained only half the amount of Cr-getters on the cell. The onset of more rapid degradation from the accelerated testing conditions started sooner than for Cell GLOB101859 (which had full amount of Cr-getters, also considered Cr-getter Configuration 1 or C1). Over the total 5160 hours of testing with 10% humidified cathode air, the degradation rate was 1.04%/1000 hours. At this point, ten additional thermal cycles were performed. Degradation rate on average was 0.9 mV/cycle. After the thermal cycles, it was decided to investigate the effect of moisture at low temperature on the stability of the Cr-getter. Accelerated degradation thermal cycle tests were performed whereby the cell was cooled to 50°C and held for one week with cathode air containing more than 3% humidity flowing to ensure the maximum moisture was absorbed. The test article was then heated back up and set to the same test conditions to observe any performance degradation. The test was repeated (total two cycles) and then steady-state testing was conducted with dry cathode air for 400 hours. Figure 2-10 shows the test results in detail. The combined effect of ten thermal cycles and two accelerated degradation thermal cycles was degradation rate of 6 mV (or ~0.69%) per 1000 hours. The final 400-hour hold in dry air (before terminating the test) showed a degradation rate of 0.7 mV (or ~0.1%) per 1000 hours. Figure 2-11 presents cell voltage vs. time trend for cell with configuration C4, showing a low degradation rate of 0.36% per 1000 hours over 5500 hours of testing with dry cathode air. The test was terminated after 5513 hours of testing.

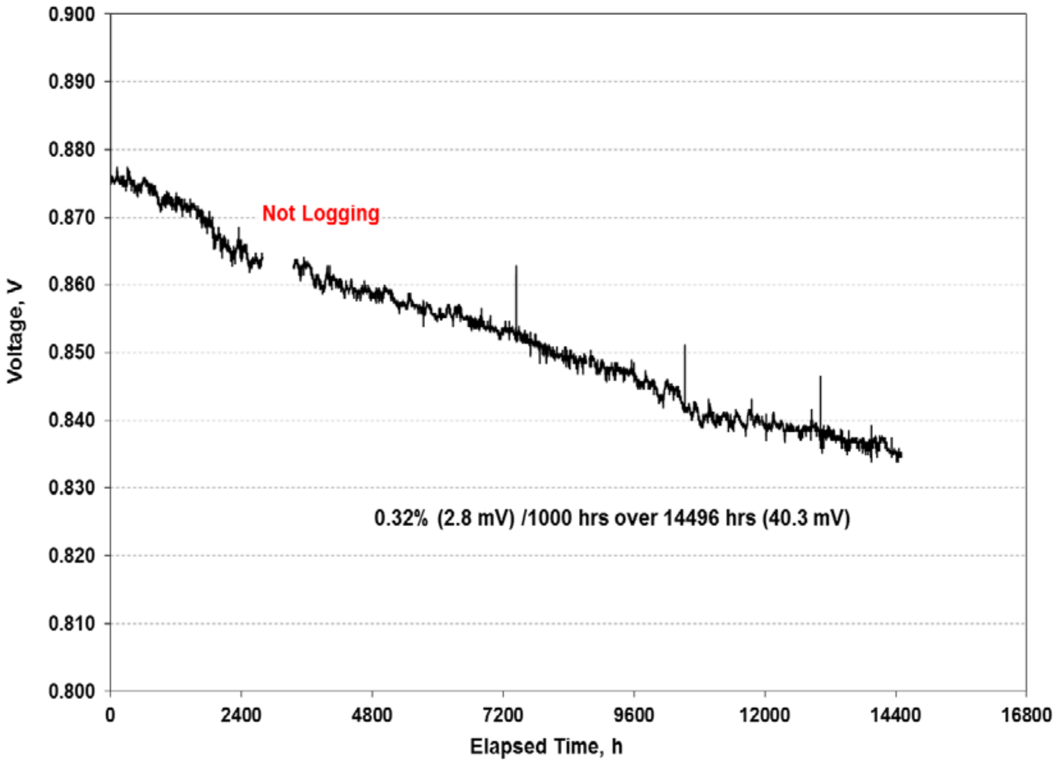

Figure 2-8. Performance Stability of Cell GLOB 101919 Containing Cr-getter Configuration C2

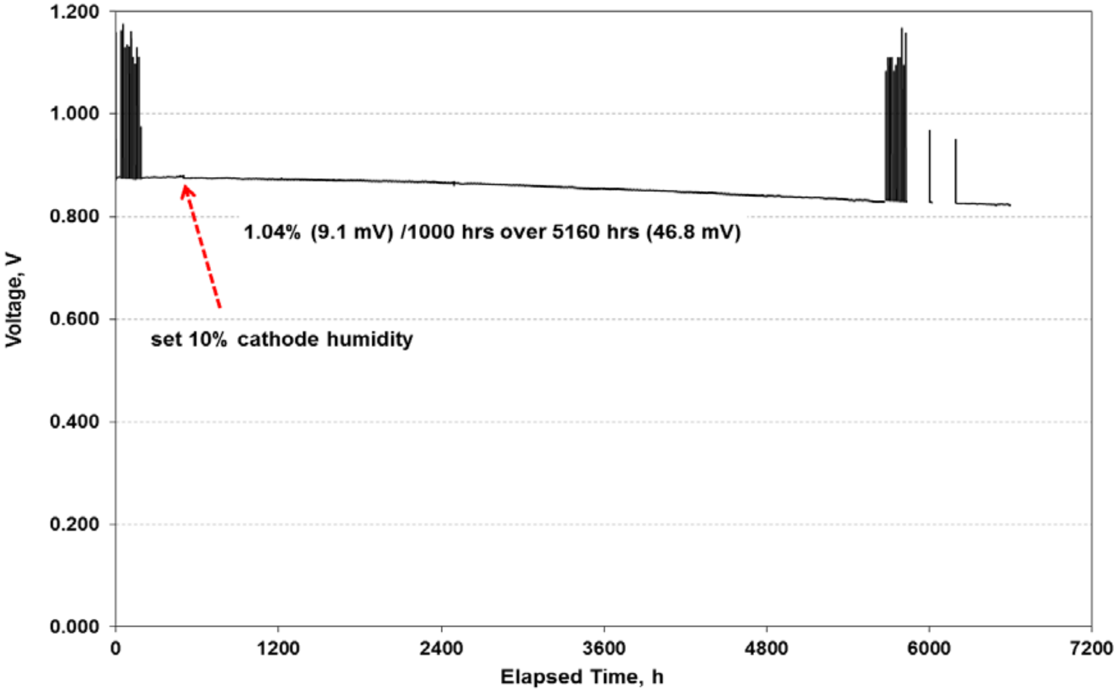

Figure 2-9. Performance Stability of Cell GLOB 101916 Containing Cr-getter Configuration C3

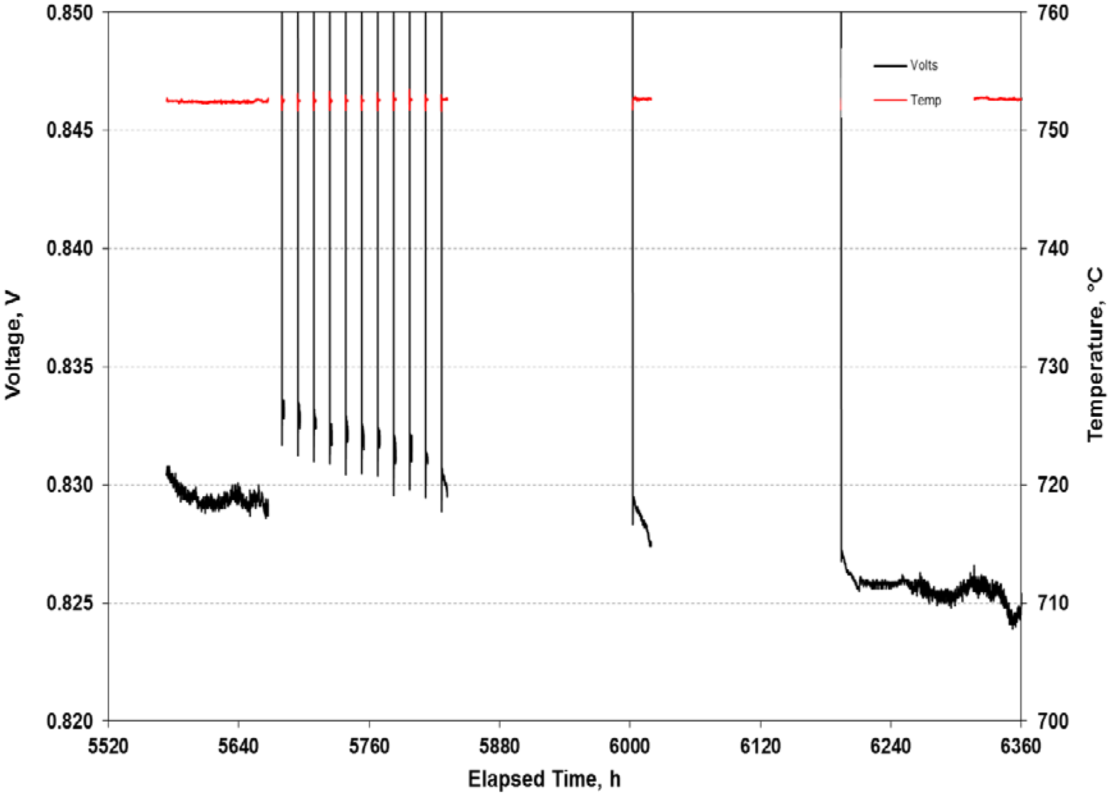

Figure 2-10. Thermal Cycling of Cell GLOB 101916 Containing Cr-getter Configuration 3

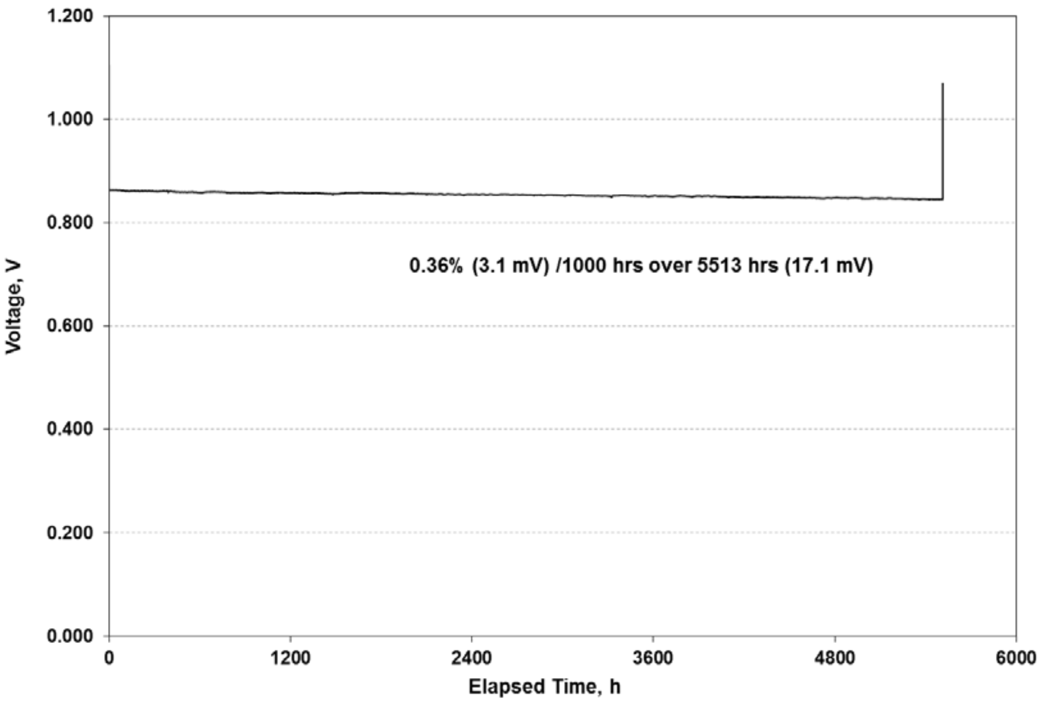

Figure 2-11. Performance Stability of Cell GLOB 101918 Containing Cr-getter Configuration C4

Configuration C2 was further tested in 16-cell stacks. Test results are discussed in Section 2.2.3 of this report.

A six-cell stack, GT055296-0140, was built with three standard TSC-3 cells (Cells 2, 4, and 6) and three cells incorporating the same Cr getters as GLOB 101859 (Cells1, 3, and 5). Figure 2-12 presents the cell voltage vs. time trends for the individual cells, showing that over more than 17200 hours (~2 years) of operation the cells with Cr-getters had lower degradation rates than regular TSC-3 cells (in dry cathode air).

It was decided to test large area stacks incorporating Cr getters and the results are reported in detail in the stack testing section. This was a key activity to lead to the stack design freeze for the stack module.

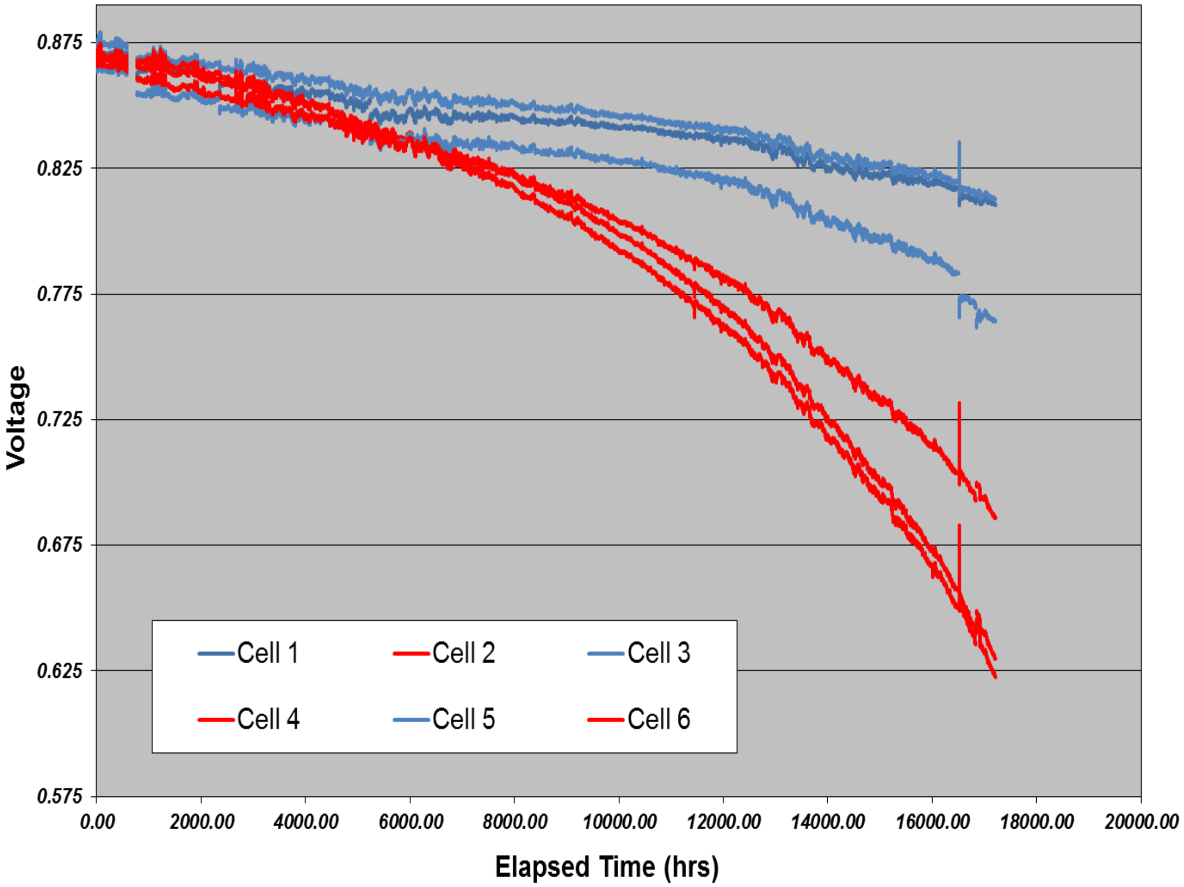

Figure 2-12. Performance Stability of Cells with Cr-getters Compared to Standard TSC-3 Cells in Six-Cell Stack GT055296-0140 (Cells 1, 3 and 5 contain Cr getter materials)

Development of Coating Technologies for Cr Reduction

Cobalt and MCO coatings had been tested in single cells using both dry and humidified cathode air with significant improvement to cell life. Figure 2-13 summarizes the long term single-cell accelerated tests with cathode gas humidity of 10%. Single-cell test GLOB 101863 (81 cm^2 active area) with PNNL-coated MCO on cathode jigs (hardware) performed the best. The second single-cell test with MCO coated jigs from PNNL (GLOB 101898) was conducted. The performance degradation rate was about 0.51%/1000h during testing in dry cathode air (at 500 mA/cm^2, 750°C) over 3564 hours. Cathode gas humidity was then introduced. The cell degradation rate was 1.37% per 1000 hours over 2365 hours of operation with 10% water in cathode air. It was also found that the first test GLOB 101863 with PNNL-coated jig had a testing fault and humidity addition stopped during the test thereby explaining its low degradation rate.

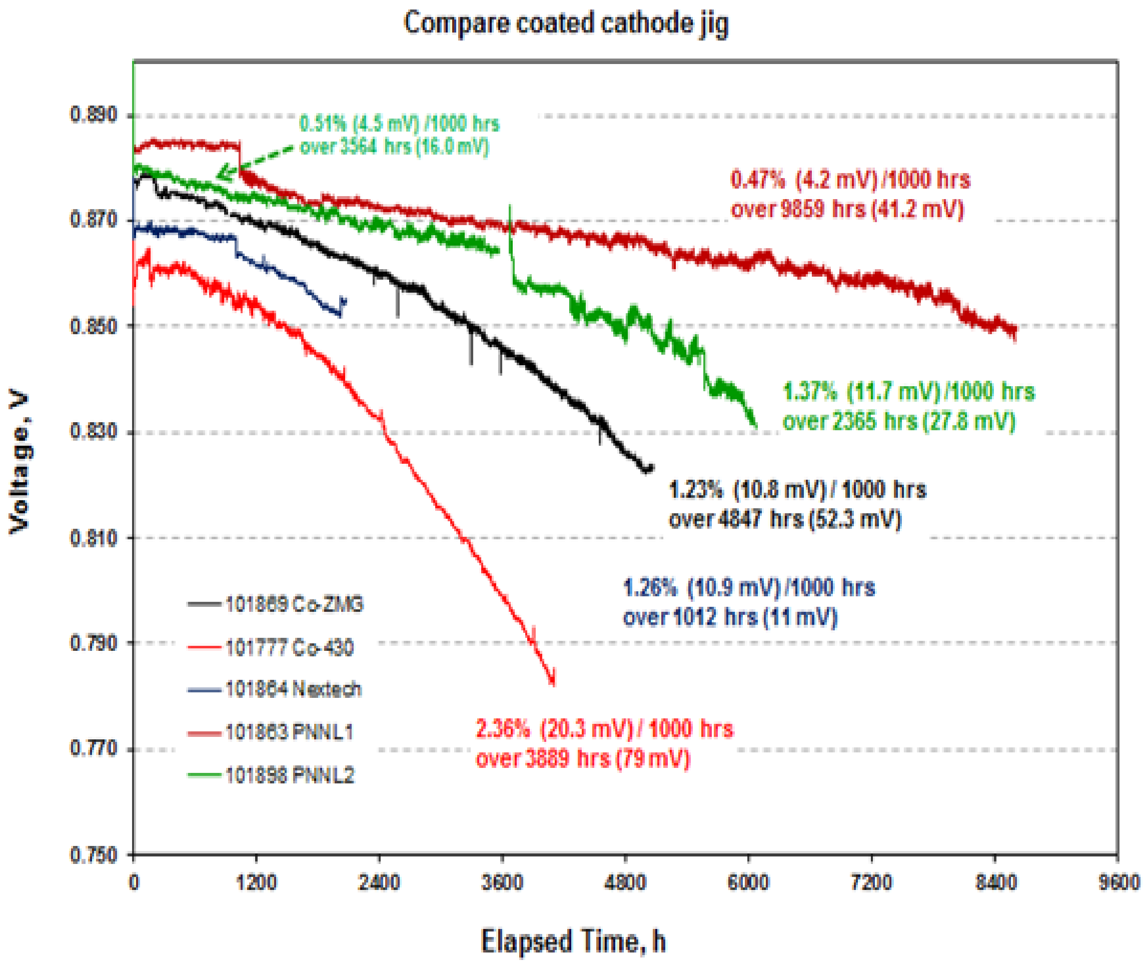

Figure 2-13. Single-Cell Tests with Coated Jigs (Hardware)

The introduction of the coating to the stack required some process development. Coated flow fields are difficult to spot weld to the flowplate. One option for assembly was to pre-weld the flow field before coating it. This option was tried, and the pre-welded assemblies were sent to PNNL and Nextech for MCO coating. A 28-cell PCI stack was built with three different groups of parts: Nextech MCO, PNNL MCO, and Sanergy Co-coated flowfields.

The first attempt was unsuccessful due to oxide build up on anode interconnect after coating heat treatment. The MCO coating process includes heat treatment at high temperature in reducing atmosphere as well as in air. That exposure at high temperature led to oxide build up on the anode surface. The oxide increased the resistance of that layer and led to low stack performance.

A 14-cell stack was built after cleaning the anode side oxide of the MCO coated ICs (interconnects). This was a multi-metal stack with three different cathode flow fields (G2):

- Sanergy Cobalt coated
- ZMG232G10 MCO coated by Nextech
- ZMG232G10 MCO coated by PNNL

The stack had good performance as shown in Figure 2-14. It was tested in dry air for ~600 hours. Cathode air humidity was introduced to further evaluate the coatings. With 3.5% cathode gas humidity, cells with MCO coated layers had lower performance degradation rate than the cells with Sanergy coated layers, over an 1123-h test period. The degradation rate increased significantly after increasing the cathode gas humidity level to 10%. The stack test was terminated to facilitate the post-test examination.

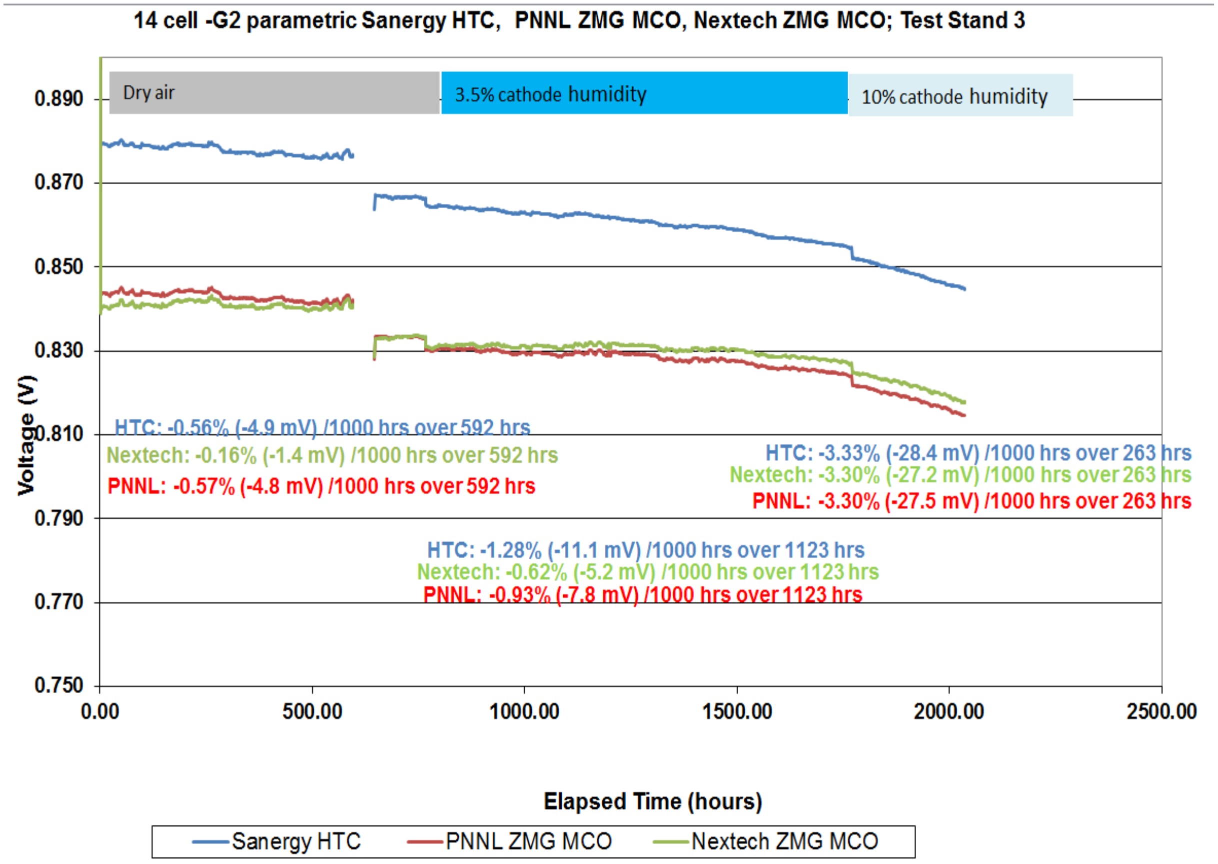

Figure 2-14. Stack Test GT0596000-0002 Evaluating MCO-coated and Cobalt-coated Interconnects

The stack was taken apart and fully analyzed. As shown in Figure 2-15, for cathode flow field coated by Nextech, the MCO coating was dense with no Cr present in the cell. The MCO coating from PNNL was less dense with some Cr present in the cell as shown in Figure 2-16. The oxide was a thin double layer on cathode flow field with Sanergy Co-coating in the contact area as shown in Figure 2-17. However, there was some oxide buildup at the edges of the flow-field where the Co-coating was disrupted during flow field forming process. The difference between the three groups was that coating quality with MCO coating from Nextech had the best surface coverage. This finding aligned well with the stack testing results.

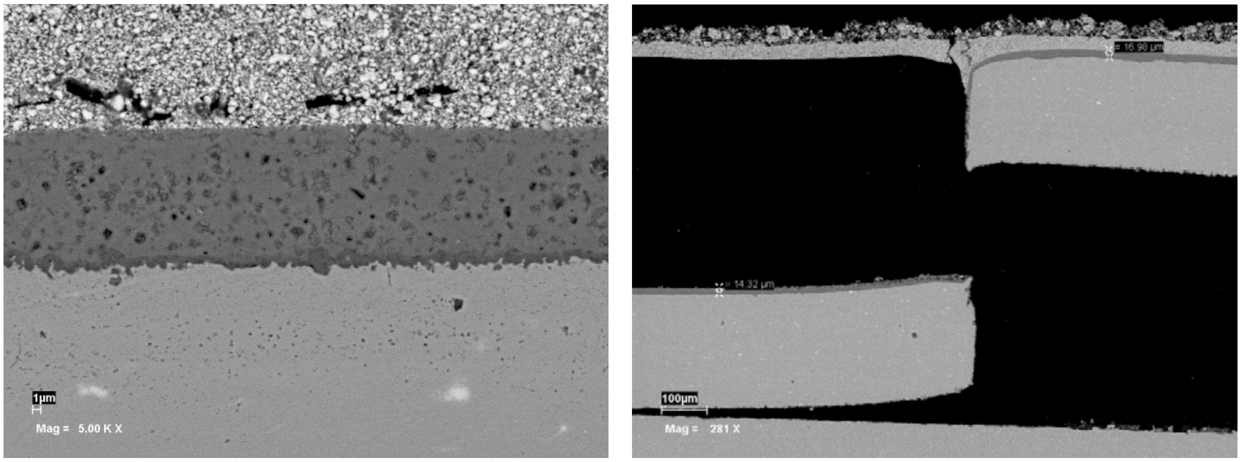

Figure 2-15. Nextech MCO Coating

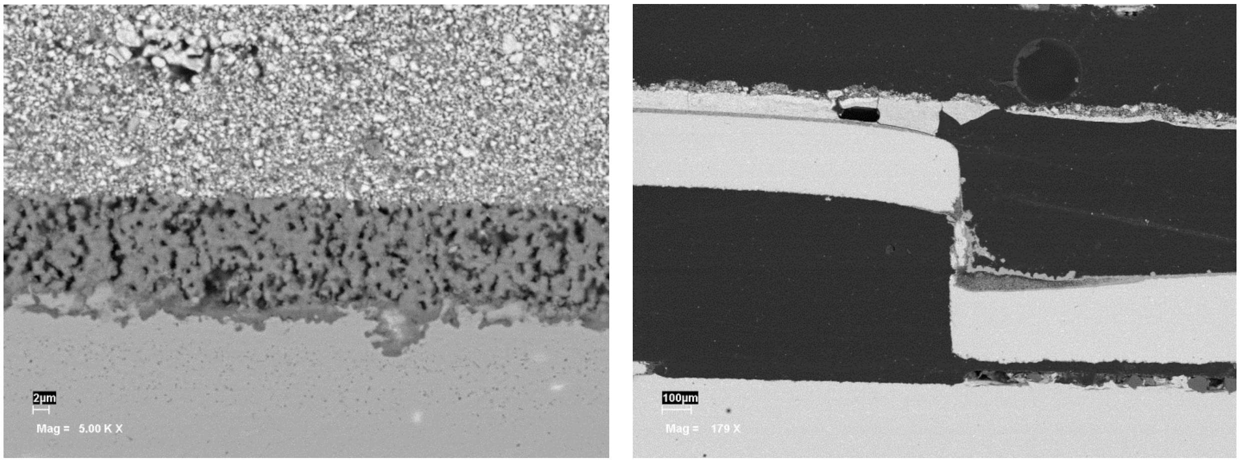

Figure 2-16. PNNL MCO Coating

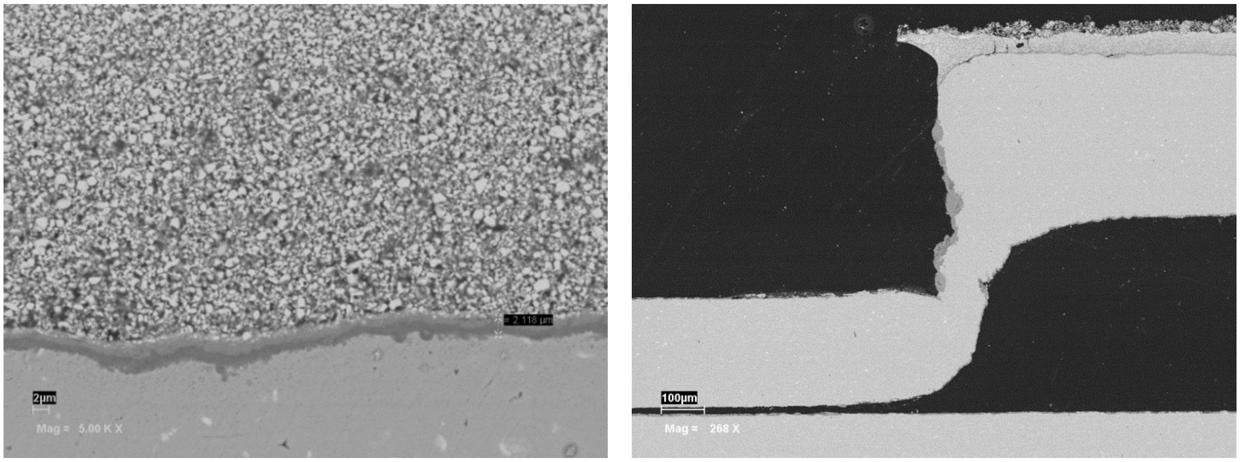

Figure 2-17. Sanergy Co Coating

Another 14-cell stack was built and tested. It had MCO-coated ZMG232G10 alloy cathode flow fields from Nextech. One group of cells contained flow fields welded before coating (pre-welded) and the other group contained flow fields welded after coating (post-welded). The stack completed 1000 hours of testing with dry cathode air.The cells with pre-welded layers had higher performance and slightly lower degradation rate than the cells with post-welded layers.

After completing 1000 hours of testing in dry cathode air, the stack was moved to another test stand capable of testing with cathode gas humidity. Cathode gas humidity was introduced for further testing with 3.5% and 10% humidity as shown in Figure 2-18. The performance degradation rates increased significantly after increasing cathode gas humidity to 10%. The test was terminated after more than 1600 hours of testing with cathode gas humidity.

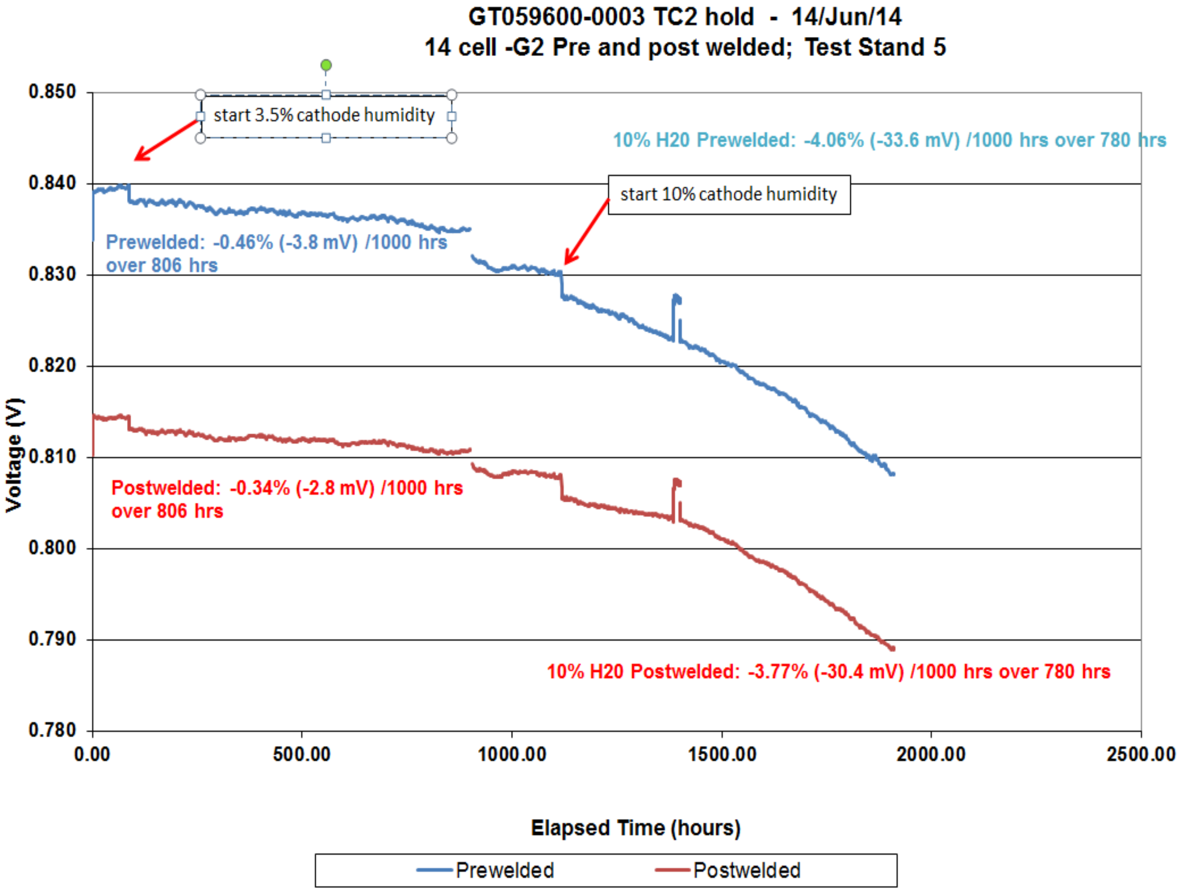

Figure 2-18. Stack Test GT0596000-0003 Evaluating MCO-coated (by Nextech) ZMG232G10 Cathode Flow Fields

A detailed stack post-test analysis was conducted. As shown in Figure 2-19, the coating in the channel of the flow fields was porous with a thick oxide on top. The oxide was from a reaction of chrome with Co and Mn in the coating. In comparison, the coating in the contact area was denser with no presence of chrome.

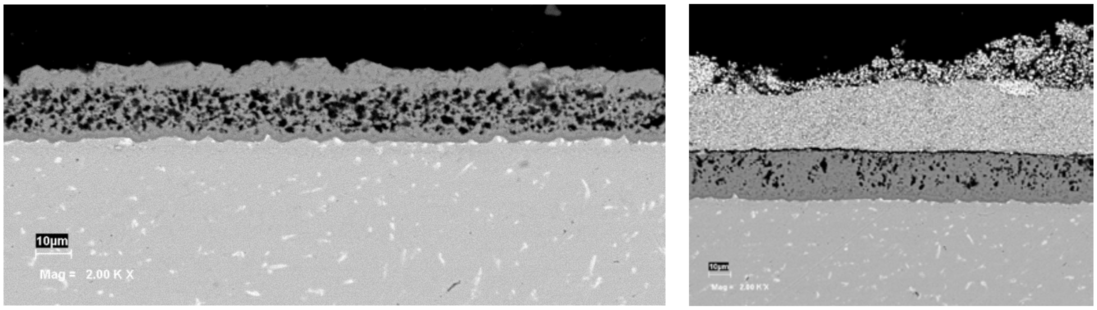

Figure 2-19. Cross Section of MCO Coated Cathode Flow Field in Channel (left) and in Contact Area (right)

A new 14-cell stack was built with Co-coated Sanergy and Co-Ce coated 441 alloy flow fields. This stack was to test the low-cost option of coated 441 alloy. As shown in Figure 2-20, cells with Co-Ce coated 441 layers initially (over a 661-h period) had lower degradation rate while the performance was similar to cells with Co-coated Sanergy layers. The performance degradation rate for both cell groups was then comparable over a 1681-h period. The stack was tested in dry cathode air conditions for more than 2000 hours before introducing humidity.

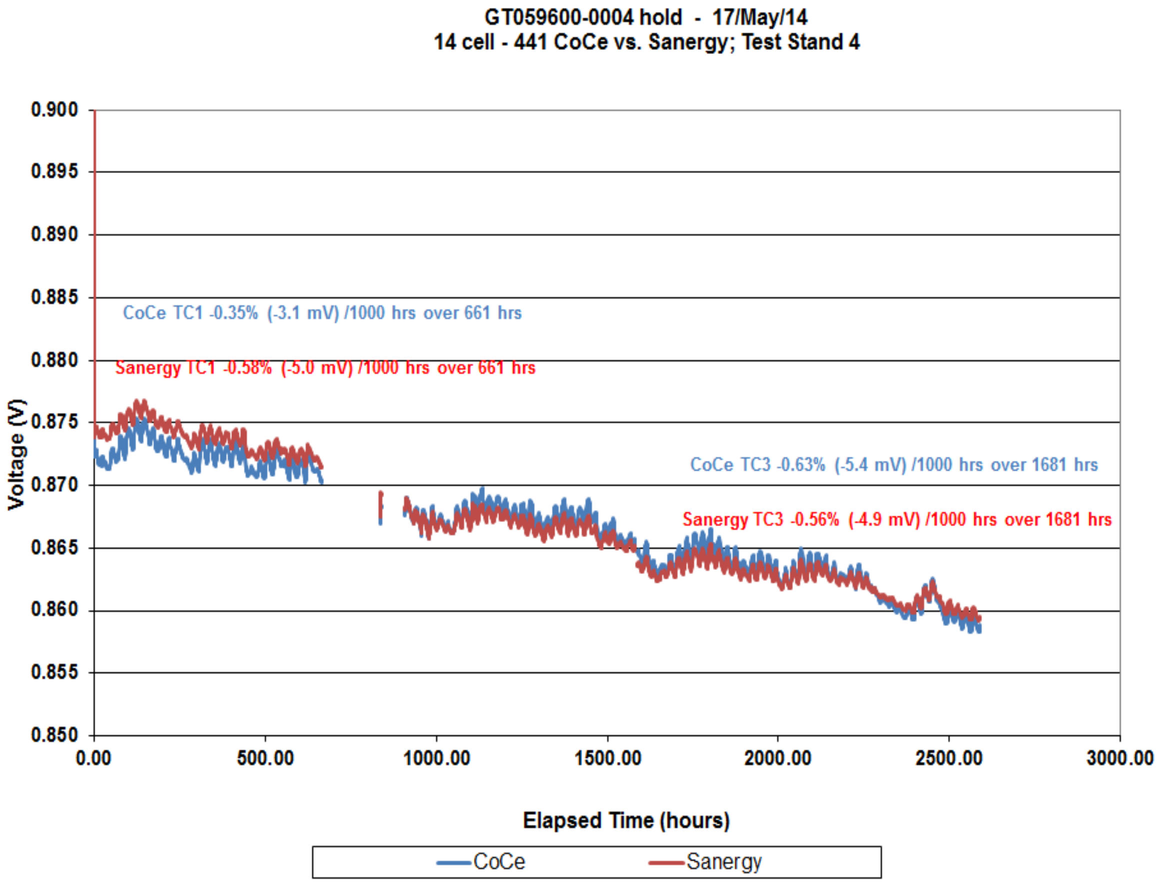

Figure 2-20. Stack Test GT0596000-0004 Evaluating CoCe-coated 441 Alloy and Co-coated Sanergy Flow Fields (with Dry Cathode Air)

Figure 2-21 shows the results from testing with cathode gas humidity. With 3.5% humidity for 980 hours, the cell group containing Co-Ce coated 441 layers showed higher performance degradation rate compared to Co-coated Sanergy cell group. The humidity was then increased to 10% for a 640-hour period. Degradation rates increased for both steels.

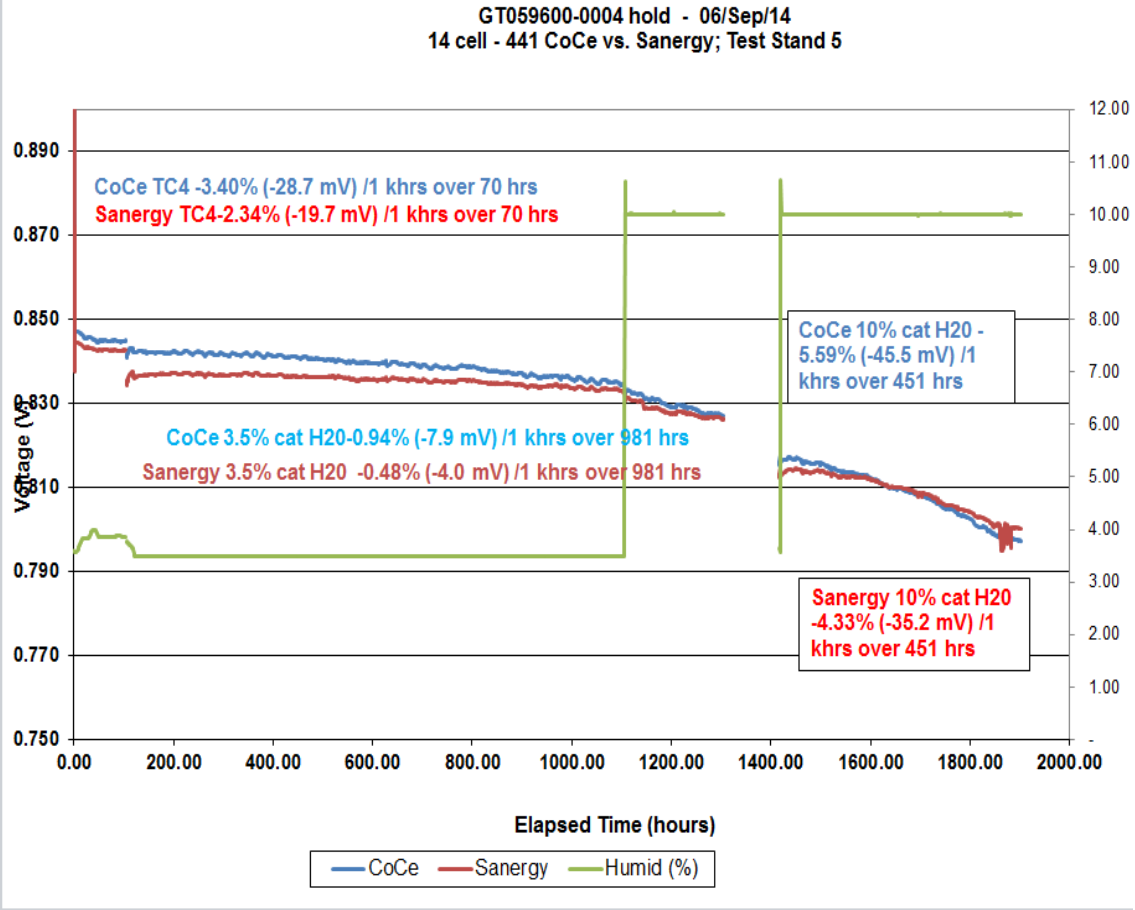

Figure 2-21. Stack Test GT059600-0004 Evaluating CoCe-coated 441 Alloy and Co-coated Sanergy Flow Fields (with Cathode Gas Humidity)

The stack test was terminated to facilitate post-test examination. Six layers (three for each steel) were selected for a detailed post-test analysis. There was some chrome presence in the cathode. As shown in Figure 2-22, chrome was present on the cell surface only above the flow field channels (area of Spectrum 1). No chrome was found above the contact areas (area of Spectrum 2).

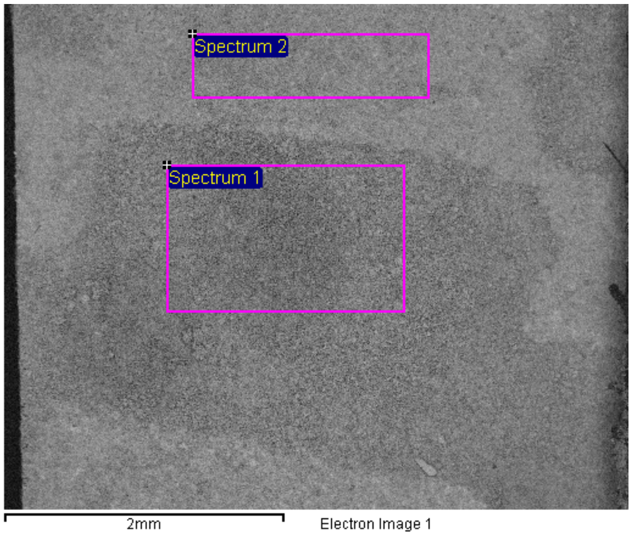

Figure 2-22. Cell Surface Analysis

The cell cross section analyses confirmed that there was no difference between 441 and Sanergy layers related to Cr or Ba diffusion. It is clear from Figure 2-23 that the middle of the stack had higher Cr and Ba diffusion. Higher temperature increased the rate of evaporation and diffusion. Most of the Cr must have originated from within the stack such as the flow plates.

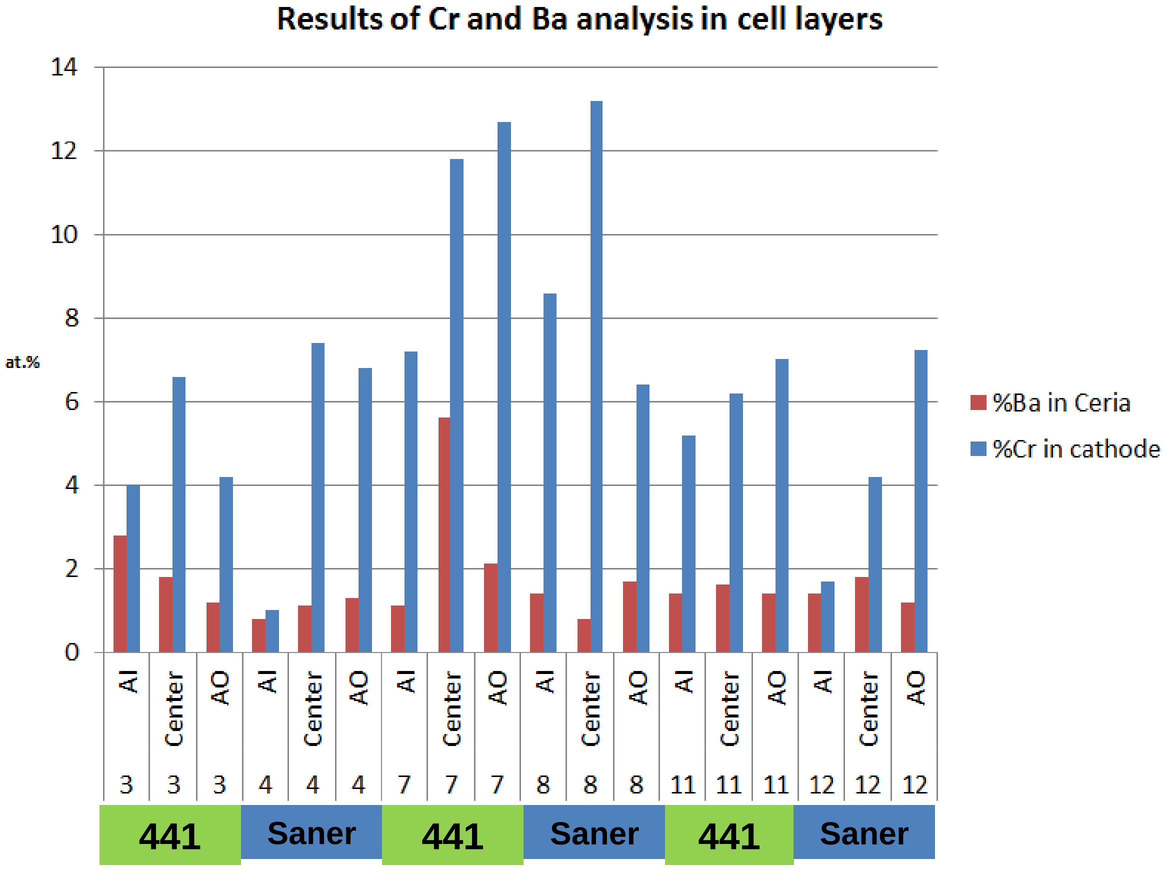

Figure 2-23. Elements Analysis in Cell Layers; Ba in Ceria and Cr in Cathode

The Co/Ce coated 441 alloy flow field analysis results presented in Figure 2-24 showed that the coating at the contact was dense. It was made of three layers: chromia and an inter-layer including Ce and a Co-Mn oxide. The coating in channel was broken with two layers: chromia and Co-Cr-Mn oxide. High chrome was present in all layers.

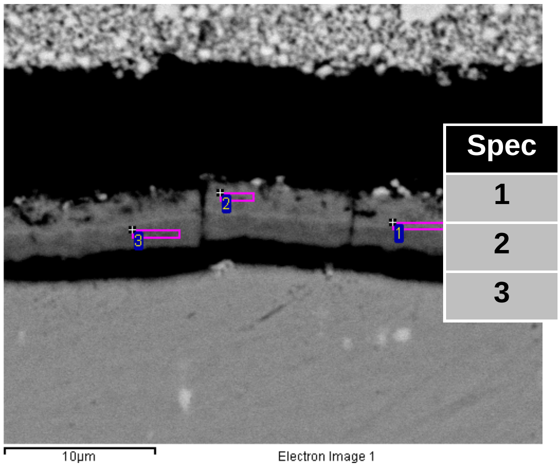

Spec	O	Ti	Cr	Mn	Fe	Co	Ni	La	Ce
1	53.3	0.5	9.0	7.0	2.4	27.3			0.5
2	51.5		0.9	7.8	2.1	34.3	2.9	0.5	
3	54.3		27.9	2.1	1.5	14.1			

Figure 2-24. Oxide at Contact Area for Co-Ce Coated 441 Alloy Flow Fields

The Co-coated Sanergy flow field analysis results presented in Figure 2-25 showed that the coating at the contact was dense. It was made of two layers: chromia and a Co-Mn oxide with a presence of chrome. The coating in channel was broken with two layers: chromia and a Co-Cr-Mn oxide. High chrome was present in all layers.

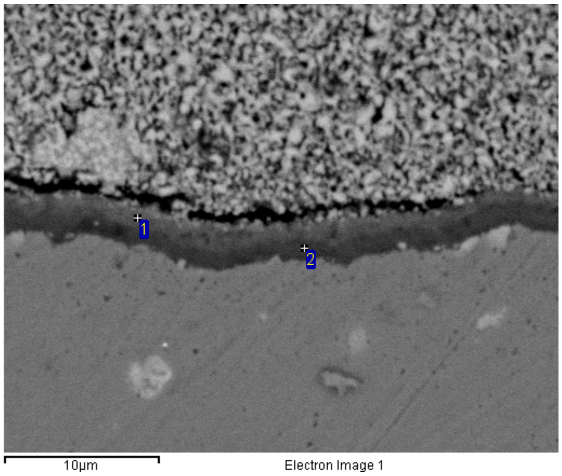

Spec	O	Cr	Mn	Fe	Co	Ni	La
1	46.8	5.8	11.7	4.0	25.0	5.4	1.1
2	49.7	42.5	1.5	3.1	3.3		

Figure 2-25. Oxide at Contact Area for Co-coated Sanergy Flow fields

The flow field top surface oxide had varying thickness from exposed channel to contact area. Also, the position (in the cell plane or the stack height) had an influence on that thickness. As shown in Figure 2-26, oxide was thicker in channel area compared to the contact area. Also, Sanergy flow fields had thinner oxides compared to 441 alloy flow fields.

Testing at 10% cathode gas humidity is very severe and requires protection of all metal surfaces. The stack results show the effect of chromium present in the cathode air stream on coatings and cells.

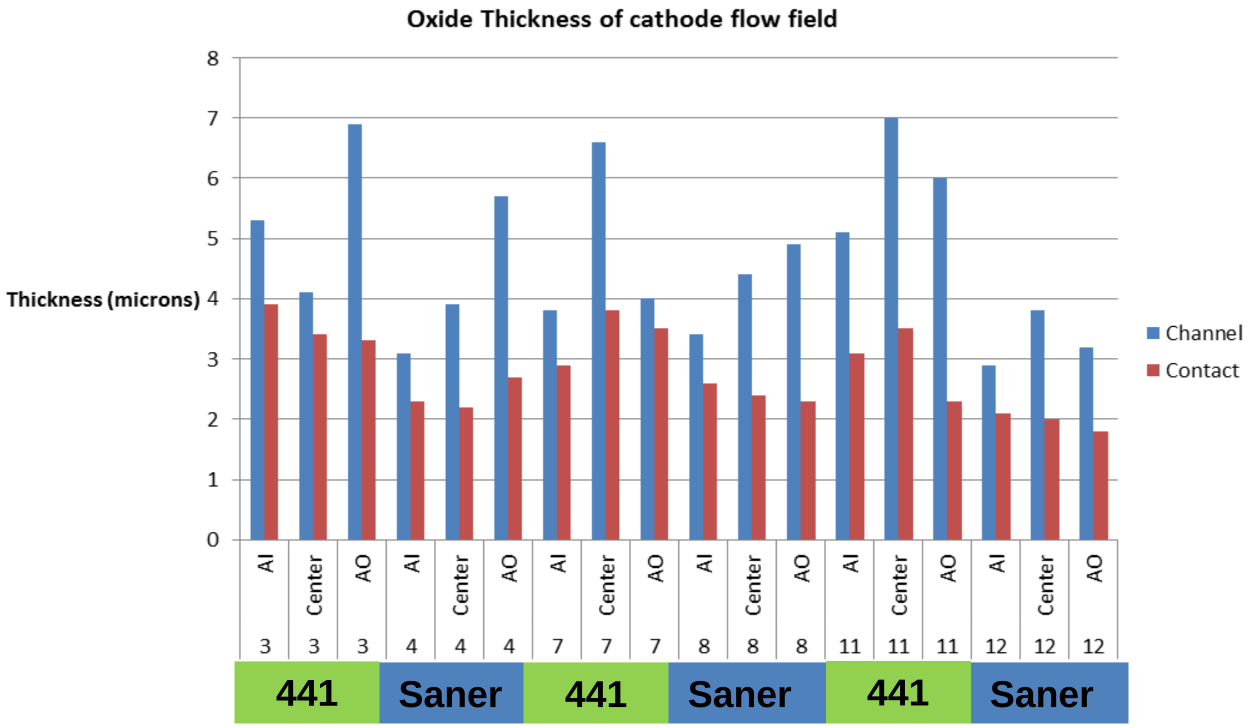

Figure 2-26. Oxide Thickness of Cathode Flow-Fields

In-house MCO Coating Development: A number of ZMG232G10 alloy coupons were dip coated. After coating, the heat treatment process was carried out including without reduction at 800°C for five hours then in air at 800°C for 500 to 1000 hours. Three different additives were used to modify the coating morphology and reduce the heat treatment temperatures. These additives had different influences on the oxide thickness and the coating morphology. Figure 2-27 shows the micrographs of cross-sections of coated coupons. Additive A affected the steel oxidation as seen by the thick oxide layer. Additive B led to a thinner oxide layer. Additive C was a good sintering aid as observed by the very dense coating. Combinations of two additives were also tried with different results. Also trials were performed to adjust the Mn to Co ratio in the coating to obtain a final composition close to $Mn_{1.5}Co_{1.5}O_4$. This composition offered the highest conductivity.

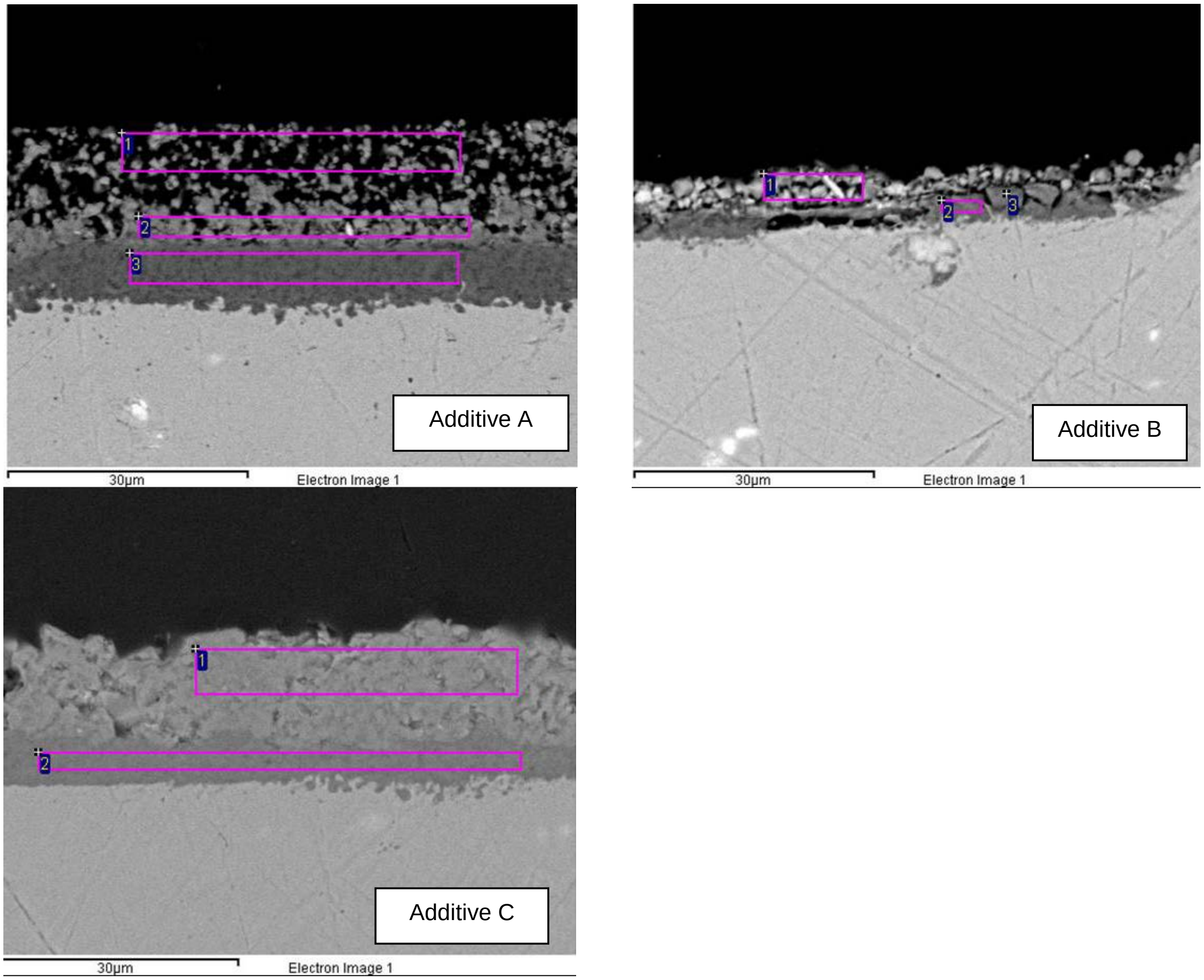

Figure 2-27. Post-test Micrographs of Cross Sections of Coated Coupons Prepared with Additives A, B, and C

Coating compositions were selected for single cell testing. The cathode jig was dip-coated and pre-fired before testing. Three representative single-cell tests were conducted. While the MCO coating sintered at 800°C became very dense with additive C, the cell degradation rate was higher. Test results with dry cathode air and humidified cathode gas are shown in Figure 2-28. MCO coatings with other additives were also tested. However, all of them exhibited higher degradation rates compared to the reference Co coated jig.

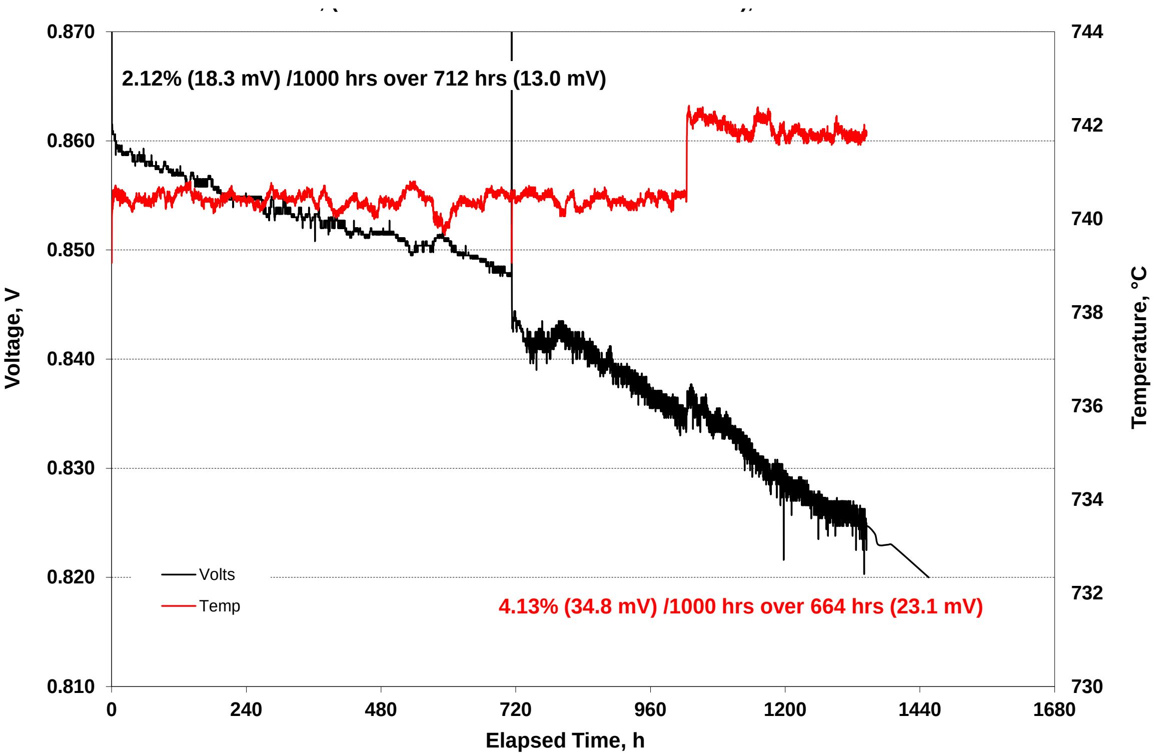

Figure 2-28. Single-Cell Test 101895 Evaluating MCO Coating with Additive C (Applied to Cathode Jig)

Subsequently, a two-layer coating (Co_3O_4 first and then MCO) was applied to a ZMG232G10 alloy jig. Additive B was added in both layers to facilitate sintering at 800°C. However, as shown in Figure 2-29, the cell exhibited high degradation rate while the initial performance was very good.

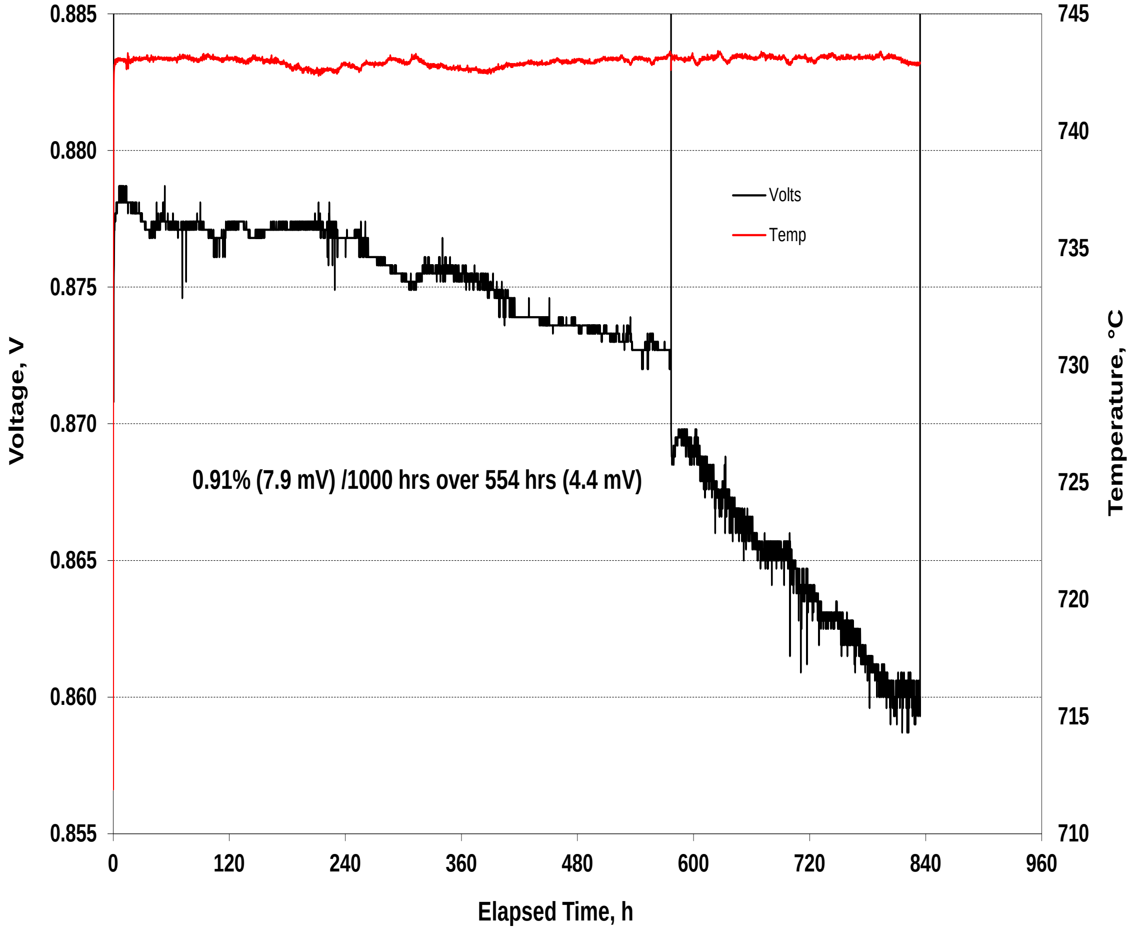

Figure 2-29. Single-Cell Test 101906 Evaluating Two-layer (Co and MCO) Coating with Additive B (Applied to Cathode Jig)

In the initial trials the representative coatings were all fired at 800°C. From SEM images, the coatings were found to be very porous while Cr species were not present in the coating. To further densify the MCO coating, the firing temperature was increased to 900°C with a two-layer coating. Figure 2-30 shows a micrograph of a two-layer coating sample coated first using additive B-MC1.5 then using additive D-MC1.5. A coupon test indicated there was no Cr in the coating layer and only about 2% Cr was present in the scale. As shown in Figure 2-31, the cell had very good initial performance (with dry cathode air). After changing to 10% cathode gas humidity, it showed a very linear degradation rate of 1.39% per 1000 hours for over 1500 hours of testing, which was very close to the degradation rate of cell with the reference Co coated jig (about 1.28%/1000h over 4942 hours of testing).

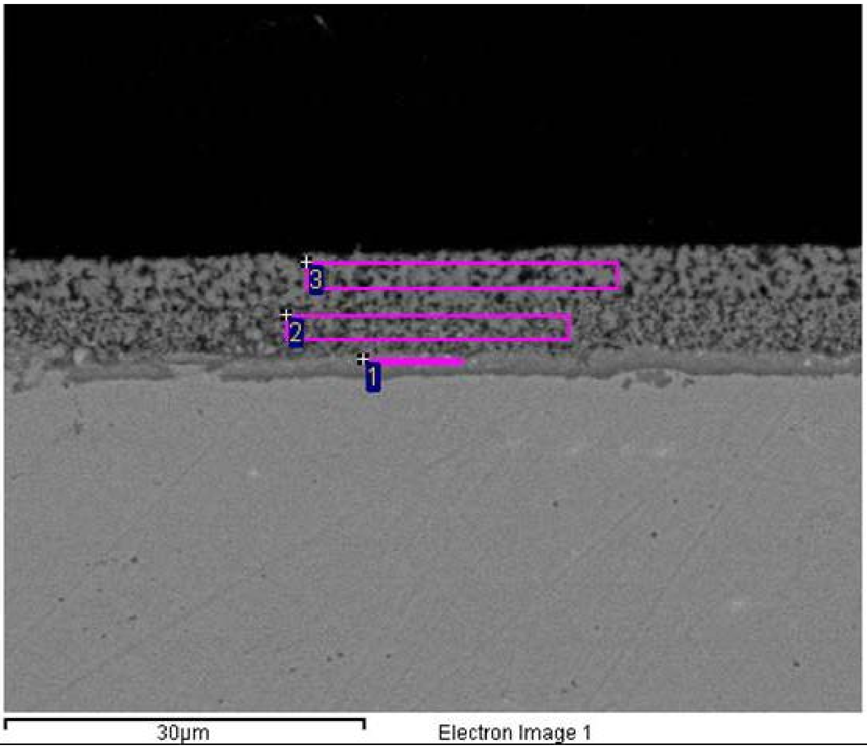

Figure 2-30. Cross Section of Coupon Coated (Two-layer) First Using Additive B-MC1.5 then Using Additive D-MC1.5

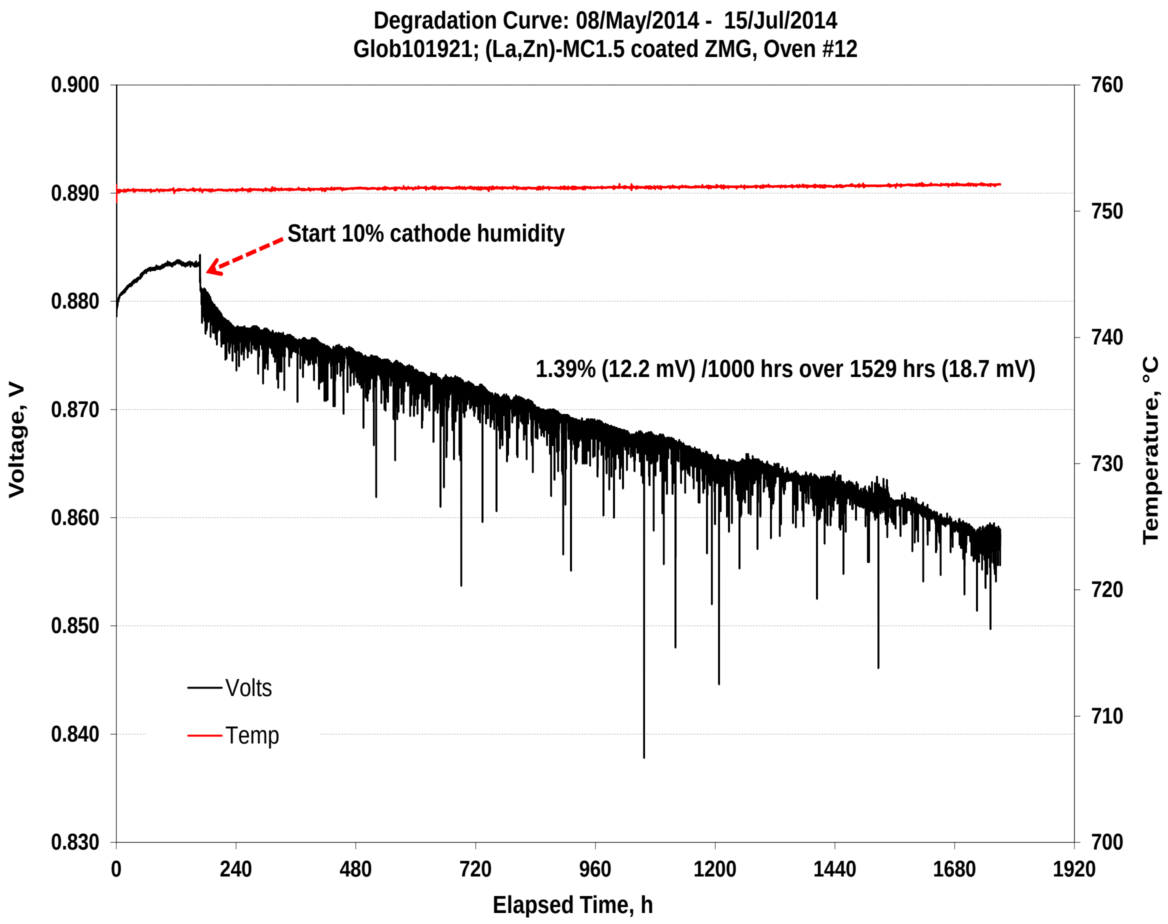

Figure 2-31. Single-Cell Test 101921 Evaluating Two-layer MCO Coating with Additives B-MC1.5 and D-MC1.5 (Applied to Cathode Jig)

After terminating the testing, the cell was examined by SEM-EDX. As shown in Figure 2-32, there were no Cr species detected in contact paste and cathode.

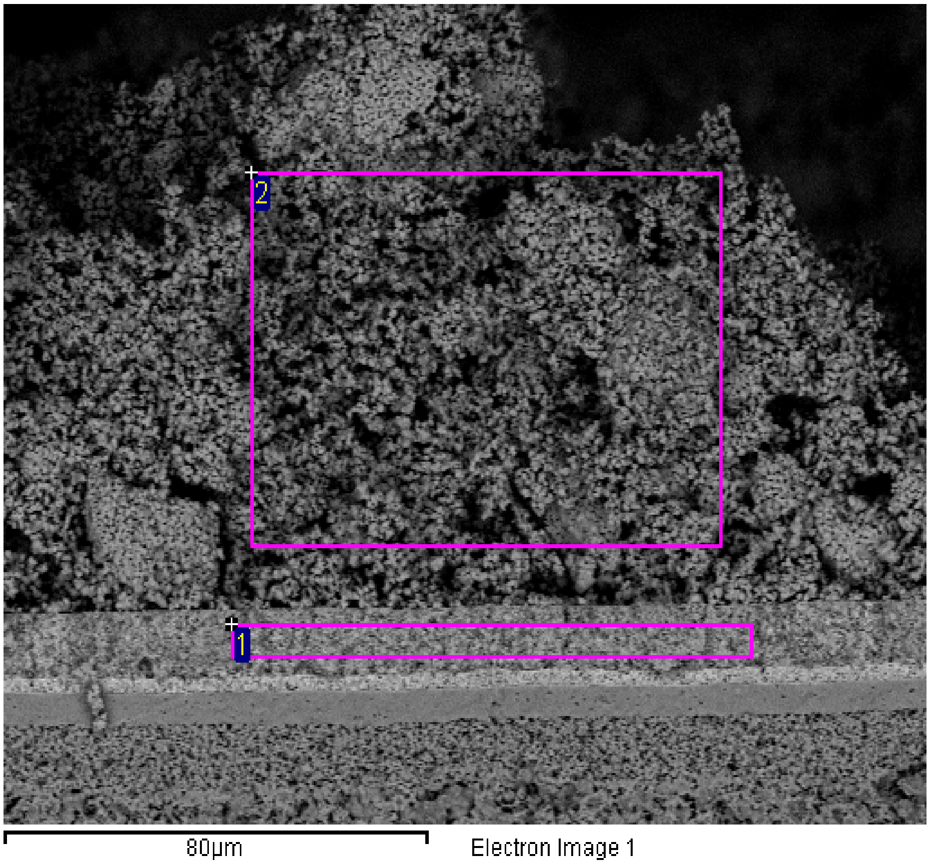

Figure 2-32. Micrograph of a Cross Section of Tested Cell GLOB 101921 (Chemical Analysis by EDX of two boxed areas showed no Cr in either area)

2.1.2. Cell Manufacturing Process Development and Fabrication

In order to support the SECA objective of demonstrating progress towards adequate stack life (≥ 4 years) and performance stability (≤ 0.2% per 1000 hours degradation), much work has been focused on cell and stack materials and designs including key cell issues related to material stability, cell robustness and performance degradation especially at system operating conditions. While this work continues at the cell level, efforts to improve life and reliability by addressing the issues of repeatability and quality control at the part manufacturing, cell assembly, and stack level are also critical to meeting the objectives. These efforts include:

- The use of statistical analysis tools to evaluate existing TSC-3 manufacturing process data, component tolerance variability, and cell testing data as part of Root Cause Analysis to identify key cell reliability, robustness, and endurance drivers.
- The use of process improvement tools, such as DMAIC (Define Measure Analyze Improve Control), Gage R&R's (Repeatability and Reproducibility) and fishbone diagrams, to further improve cell yield, shorten process pipeline, and reduce cell defects through improved process control.

The following sections summarize efforts to improve the quality and reliability of the stack.

Quality

A high level roadmap of a Quality Improvement Plan was created to guide efforts in developing a detailed quality program. The roadmap is shown in the Figure 2-33.

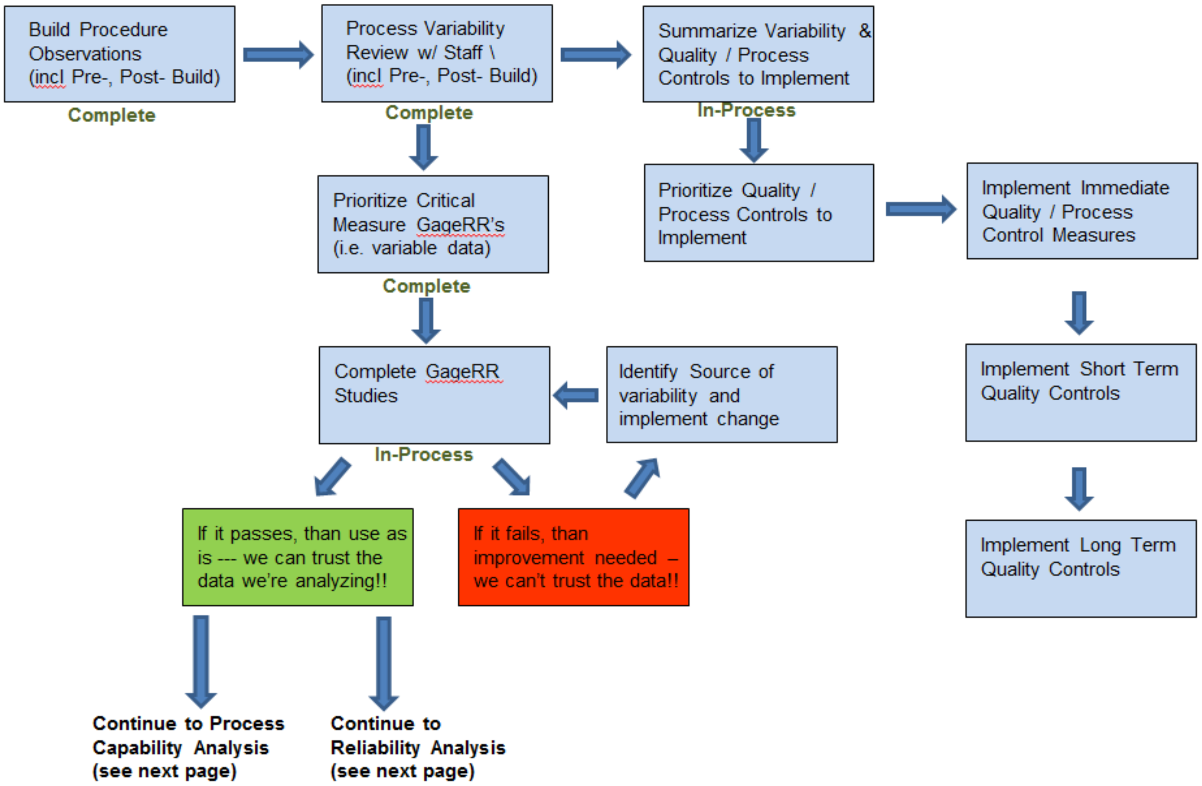

Figure 2-33. High Level Mapping of Quality Improvement Plan

The labels "Complete" and "In-Process" reflect the status of the activities. As shown, build procedure observations to identify elements of process variability was a critical first step in this process. Members of FCE's engineering research team visited the VPS pilot production facility in Calgary, Canada to assess the quality controls in place. The team worked alongside process operators and production managers, observing the procedures and making note of variables in need of improved process control. The effort included pre-build kitting (including component measurement), stack build, post-build test prep, and post-test packaging procedures. Subsequent to the observation period, meetings were conducted with individuals and small groups to review each process step to determine possible quality control measures to be pursued.

Gage R&R (Repeatability and Reproducibility) studies were initiated to determine whether the data obtained from production measurement systems (instrument, method, human, and environment) should be used for statistical analysis - process capabilities studies, hypothesis testing, control charts, or simply incoming inspection. The goal is to correct the measurement system where Acceptance Criteria is not met. Acceptance Criteria will be determined on a case-by-case basis but the goal will be to adhere to the following Automotive Industry Action Group (AIAG) MSA (Measurement Systems Analysis) Guidelines:

- Less than 10% - the measurement system is acceptable.
- Between 10% and 30% - the measurement system is acceptable depending on the application, the cost of the measuring device, cost of repair, or other factors.
- Greater than 30% - the measurement system is unacceptable and should be improved.

A more formal outline of a Quality Control Improvement Plan was reviewed and released. The tasks included: completing Gage R&R studies; recording measurements in proper locations;

providing specifications for manufacturing processes missing this information; replacing tasks requiring human judgment (may result in poor reproducibility) with calibrated equipment (which is reproducible); using jigs to assist assembly alignment; implementing traceability practices; updating drawing specifications where needed; process qualifications; etc. Tasks were grouped into three categories for activities to be carried out in parallel by the team: Measurement System Improvements, Documentation Control Improvements, and Process Control Improvements and Qualifications. High level activities for each of these groups are illustrated below:

1. **Measurement System Improvements**
   - Gage R&R's for Repeating Components
   - Gage R&R's for Cell Manufacturing
   - Gage R&R's for Stack Build / Assembly
   - Inspection Gage Calibration
   - Upgrade Non-conforming (<30% total Gage RR) Gages
   - Upgrade Non-conforming Attribute Analysis
2. **Documentation Control Improvements**
   - Documentation Tree / BoM Completion
   - Establish Engineering Specifications & Inspection Plans
3. **Process Control Improvements & Qualifications**
   - Inspection (First Article and Sustaining)
   - Material Prep & Stack Build
   - Test Prep Install Removal
   - Packaging & Shipping

Measurement System Improvements: Gage R&R studies for cell and stack manufacturing quality control measurements were conducted. There are several factors affecting a measurement system, including:

- Measuring instruments: the gage or instrument itself and all mounting blocks, supports, fixtures, load cells, etc.
- Operators: the ability and/or discipline of a person to follow instructions.
- Test methods: how the devices are set up, the test fixtures, how the data is recorded.
- Specification: the measurement is reported against a specification or a reference value. The range or the engineering tolerance does not affect the measurement, but is an important factor in evaluating the viability of the measurement system.
- Parts or specimens (what is being measured): some items are more easily measured than others.

Gage R&R, an important six sigma methodology, measures the amount of variability induced in measurements by the measurement system itself, and compares it to the total variability observed to determine the viability of the measurement system. There are two important aspects of a Gage R&R:

- Repeatability: The variation in measurements taken by a single person or instrument on the same or replicate item and under the same conditions.
- Reproducibility: the variation induced when different operators, instruments, or laboratories measure the same or replicate specimen.

Table 2-1 presents a summary of the status of the gage R&R efforts as a dashboard where green means the measurement data and method are acceptable. As shown in the table, needed improvements are either completed, or in process of being completed.

Table 2-1. Gage R&R Summary for Cell / Stack Quality Control

Gage R&R's	Collected	Data Analyzed	Results	Gage RR%	Tolerance to validate	Source(s) of Variation	Improvement	Results after improvement
Repeating Components								
Thickness, Anode Flow Field	Yes	Yes	> 30% Total GageRR	*54% (gage2), 57% (gage4)*	*0.0070"*	* Plates out of parallelism and flatness by up to .003" * req'd RR on individual gages (qty 4)	* Ground plates to flatness / parallelism of .001" MAX. * new method req's RR on measurements from all gages combined	< 30% Total GageRR
Thickness, Cathode Flow Field	Yes	Yes	> 30% Total GageRR	*36% (gage2), 34% (gage4)*	*0.0045"*	* Plates out of parallelism and flatness by up to .003" * req'd RR on individual gages (qty 4)	* Ground plates to flatness / parallelism of .001" MAX. * new method req's RR on measurements from all gages combined	< 30% Total GageRR
Width, Anode Flow Field	Yes	Yes	> 30% Total GageRR	*120%*	*.240"*	* Form of cut edge, both perpendicularity & profile * method required variable data	* Go, No-Go Gauge fabricated to capture both length and width * method requires attribute data	TBD
Width, Cathode Flow Field	Yes	Yes	> 30% Total GageRR	*382%*	*.764"*	* Form of cut edge, both perpendicularity & profile * method required variable data	* similar Go, No-Go gauge if Anode Flow Field passes * method requires attribute data	NR if Go, No-Go Gauge for Anode Flow Field passes
Thickness, Cell Holder (i.e. metal components)	Yes	Yes	> 30% Total GageRR	*49%*	*.0040"*	* Holding part stable / normal to anvil of measurement tool	* Updated flow field thickness measurement fixture to control applied force to plates (< 300; *see videos*) for use w/ cell holder	TBD
Thickness, Ceramic Seal	Yes	Yes	> 30% Total GageRR	*80%*	*0.0035*	* alignment of gage anvils / form of anvil head * mat'l compliant (durometer ~ hard rubber) * potential damage & tilt from platem shock load and/or tightening of set screw	* new compression plate fixture designed to capture thickness, w/ leak detection capabilities to screen for large localized variation	TBD
Cell Manufacturing								
Half Cell Thickness	Yes	Yes	> 30% Total GageRR	*49%*	*.126mm*	* end-user derived torque on micrometer thumb wheel * holding part stable / normal to micrometer anvil * operator fatigue	* new compression plate fixture designed to capture thickness, w/ leak detection capabilities to screen for large localized lip thickness variation (note: state of ironing process deem leak unnecessary)	TBD
Cell Layer Weights (Wet Paste)	Yes	Yes	< 30% Total GageRR	*6%*	N/A	N/A	N/A	N/A
Lip Depth of Half Cell	Yes	Yes	> 30% Total GageRR	*188%*	*0.30mm, USL*	* end-user derived torque on caliper rolled head * holding part stable / normal to caliper anvil * anvil wear from ceramic cell * operator fatigue	* new compression plate fixture designed to capture thickness, w/ leak detection capabilities to screen for large localized lip thickness variation (note: state of ironing process deem leak unnecessary)	TBD
Flex of Half Cell	Yes	Yes	< 30% Total GageRR	*25%*	*recommend 0.010" to 0.110"*	N/A	N/A	N/A
Leak Test of Half Cell	Yes	Yes	< 30% Total GageRR	*20%*	N/A	N/A	N/A	N/A
Width of Half Cell	Yes	Yes	< 30% Total GageRR	*8%*	N/A	N/A	N/A	N/A

Both the anode and cathode flow field measurements were improved by re-finishing of the platens used in recording the measurements via drop gages (see Figure 2-34). This device, when operated under a reduced compression force, is also used to measure thickness (height) of other metallic components such as cell holder and flow plates within the stack.

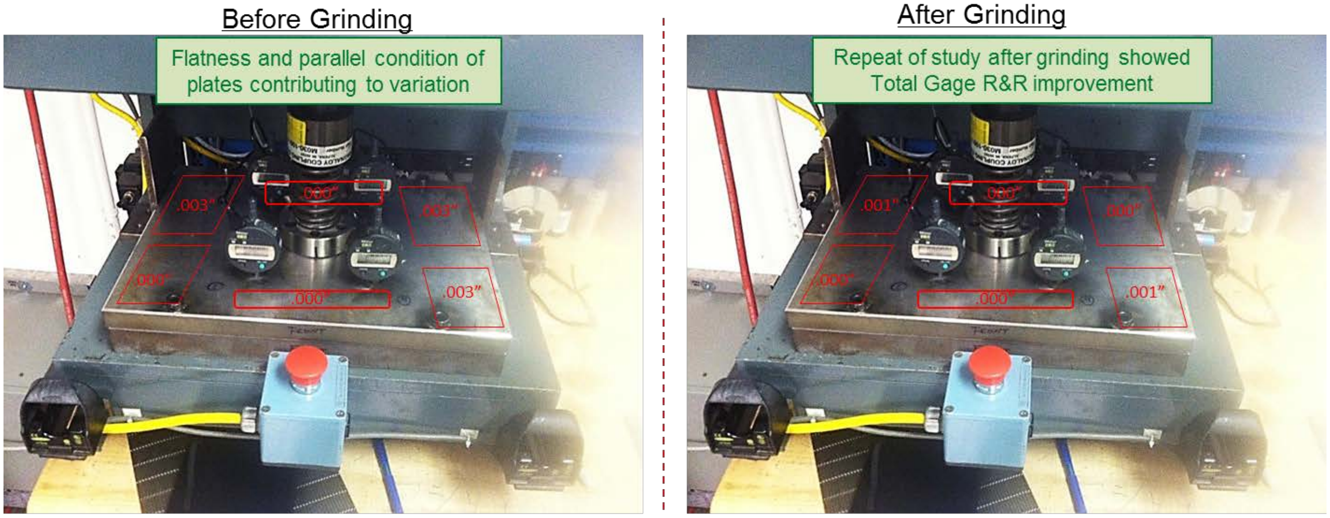
Before Grinding

Flatness and parallel condition of plates contributing to variation

After Grinding

Repeat of study after grinding showed Total Gage R&R improvement

Figure 2-34. Pressure Equipment Platen Gaps before (left) and after (right) Re-Grinding

Also, work was conducted for flow field width and length measurements. Prior to this, measurements were taken by hand using a micrometer. In an effort to improve design and process with the gage R&R, flow field cutting by laser and water jet was explored through local vendors. Laser cutting was selected and now the parts are able to hold a ±0.025” tolerance. Figure 2-35 shows a flow field component cut to width. A Go / No-Go Gage was also designed and procured to implement an acceptable technique to QC the flow field width.

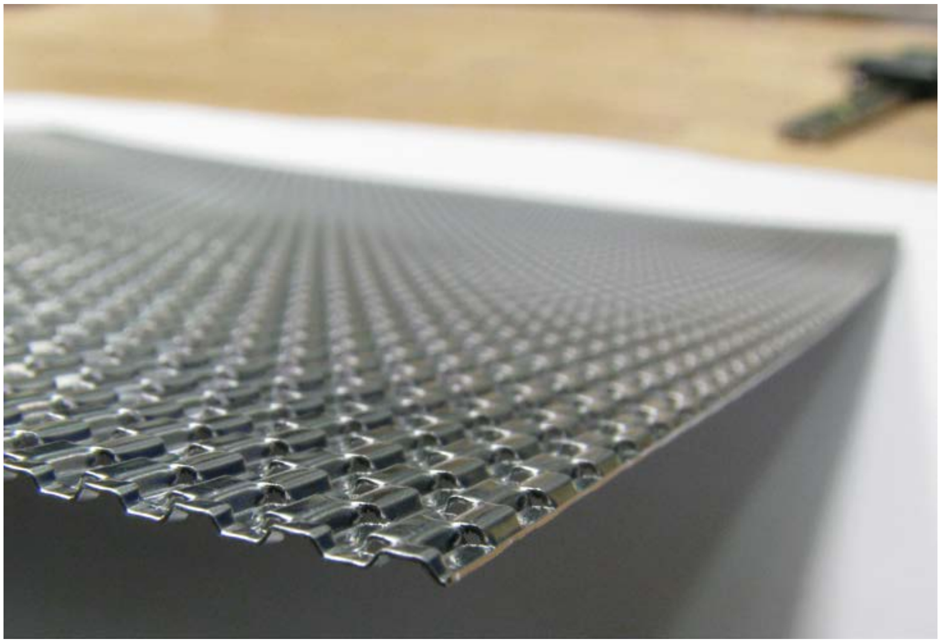

Figure 2-35. Flow Field Cut to Width

In an effort to further improve the measurement of flow field width and length, the anode go/no-go gage was evaluated. Two action plans generated were to provide training materials on how to use the anode go/no-go gauge properly and re-design the gauge to have an additional reference line to check for anode flow field length below the lower specification limit (LSL) in addition to the mechanical notch already included in the design. Figure 2-36 shows the new design of the Anode Flow Field Go No-Go Gauge.

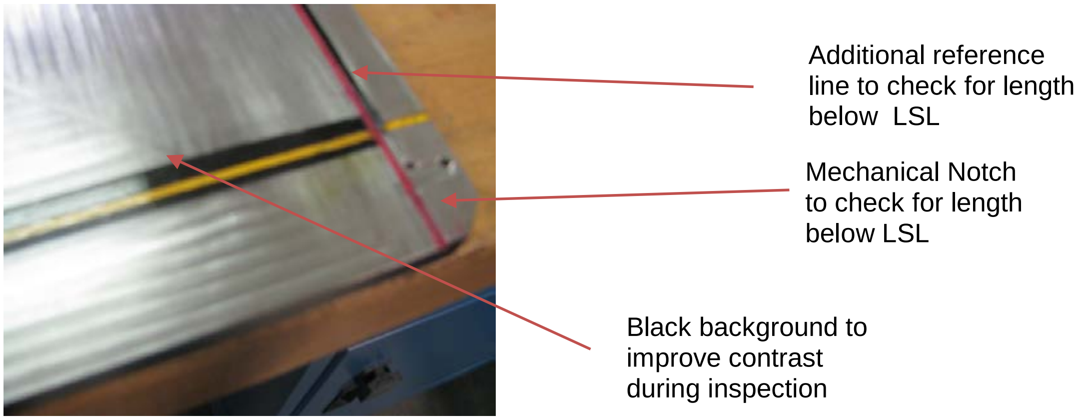

Figure 2-36. New Design of Go No-Go Gauge for Anode Flow Field

Due to the result of the gap analysis conducted for anode and cathode flow fields, the team decided to adjust the tolerance for both width and length after analyzing the historical data when rolling the flow fields. The changes in limits required a modification to the anode go/no-go gauge and another attribute GR&R study. The anode flow field go/no-go gauge was modified and GR&R study was conducted.

It was decided to have separate go/no-go gauges for cathode flow field width and length (as shown in Figure 2-37) to eliminate subjectivity by relying on only mechanical notches and guides for testing for outliers. The cost of the two gauges is much higher but yields better quality control than one gauge for both flow field width and length.

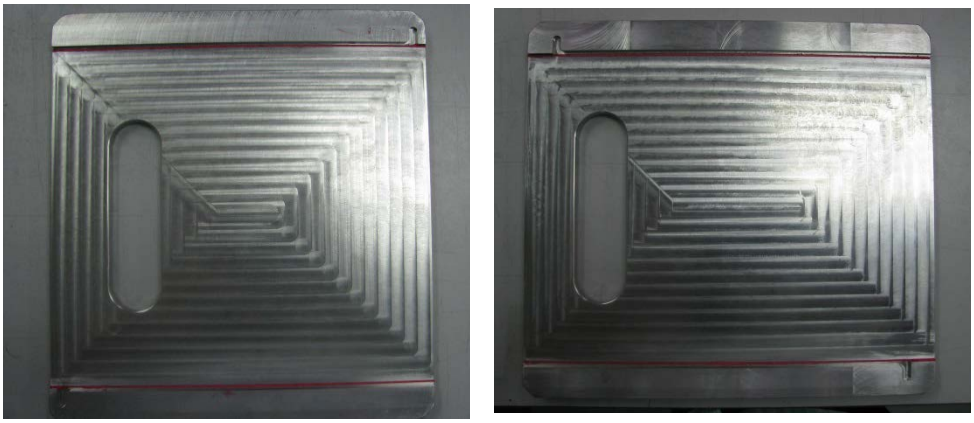

Figure 2-37. Go/No-Go Gauges for Cathode Flow Field Length and Width

An attribute GR&R study was conducted for the two go/no-go gauges for cathode flow field. The GR&R studies for the anode and cathode flow fields passed the tests, meeting requirements of kappa >75% for attribute output response and <30% for variable output response.

Accurate seal thickness measurement is critical to the stack design and a difficult task to perform. It is critical because the seals are the components that absorb the tolerance accumulation of the other components in the stack, yet the seals have only limited useful compliance. Size them too thin and inadequate sealing or even gaps will result. Size them too thick and they will not deform (thin) enough to enable proper electrical contact between components. Figure 2-38 shows the general seal shape after cutting.

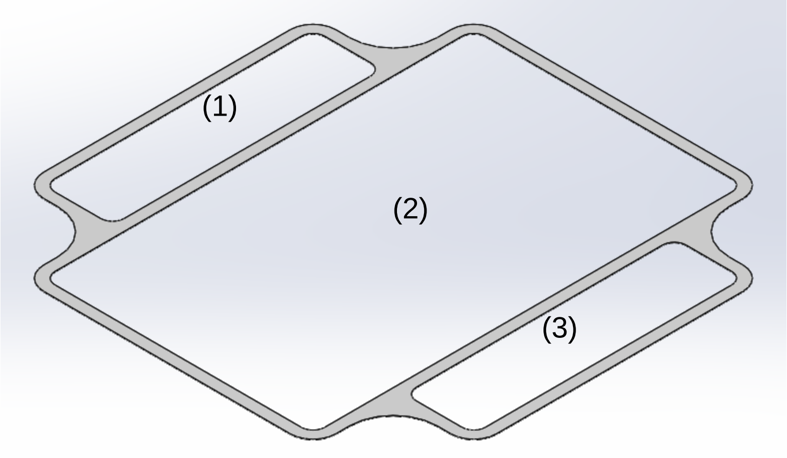

Figure 2-38. General Seal Shape after Cutting

The key QC (quality control) questions are:

- What is the nominal thickness of the seal?
- Are there any low points anywhere in the seal material that could result in cross leak or external leak?

Gage R&R evaluation of the existing seal thickness device was not satisfactory, with 5.15 standard deviations (99% confidence interval) corresponding to 80% of the tolerance band. The measurement device did not zero consistently. An examination of the device revealed some weaknesses as follows:

- The stops that set the reference plane from which all measurements were taken were over constrained. As a result there was inconsistency in the location of the reference plane. The moving plate in the down position can rock or move between several stable positions.
- The setup was sensitive to the perpendicularity of the measurement gauges. The micrometer mounting did not ensure good perpendicularity and may have damaged the probes
- Some of the linear gauges on the device were damaged. The gauges were not rated for shaking or impact loading. Shock loading at the end of travel may have damaged the probes.

Solutions to the above problems required significant rework of the device. After consideration, an alternative approach was proposed based on the idea of using flow measurement to detect low points in the seal, while using contact between flat plates to identify the nominal high points. This has the advantage of evaluating the full seal area rather than 13 discrete points around the circumference of the seal. The new method is more likely to detect local flaws and low spots than the prior method. Some experimentation will be required to determine how much leakage flow, if any, corresponds to a functional and acceptable seal.

The proposed approach to answering the second QC question above was to lightly compress the seal between platens then sequentially pressurize cavity #2 (numbered in Figure 2-38), then cavities #1 and #3, and check for leaks at each step. Any leakage will be due to local low points in the seal body. The nominal seal thickness will be measured as the distance between the platens when they are compressing the seal.

The seal material is not easy to handle after it is cut to shape. Hence, grooves matching the seal shape are required to be machined into one of the platens (main platen), while the other is left flat. The resulting device is shown in Figure 2-39. In order to maintain platen flatness without requiring heavy structural platens, a distributed loading strategy was pursued. An array of nine pneumatic cylinders shares a pressurization source. The system automatically distributes load between cylinders independent of any deflection of the mounting frame. Alignment couplers at the end of the cylinders prevent any binding from occurring. The main platen motion is controlled by the upper cylinders.

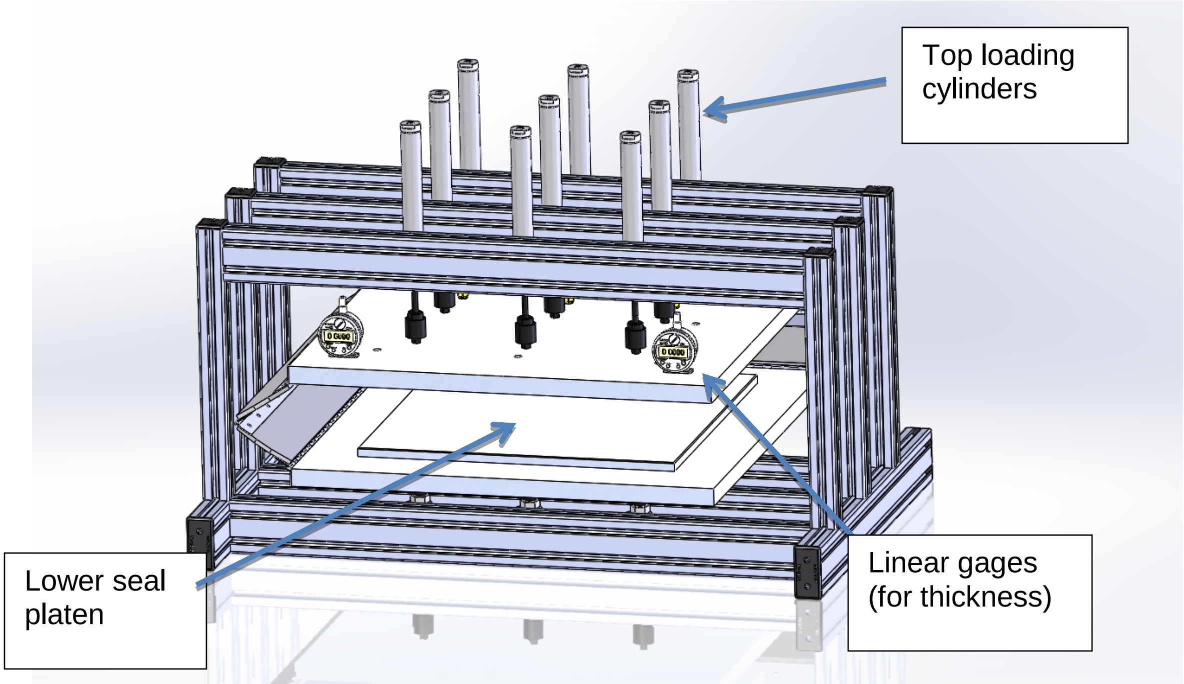

Figure 2-39. Seal Thickness Measurement Device (shows lower platen)

The upper and lower platens are linked through a Sarrus linkage which ensures they travel nominally parallel to each other. Inevitable hinge slop will result in some lack of parallelism, but the goal is to prevent substantial side motion after the platens first come into contact and the linkage should be adequate for that purpose.

By using this strategy of decoupling the framing of the device from the measurement locations, low displacement is achieved with relatively thin platens. The relative displacements at the four corners are all less than 2.5 micron (0.0001”).

The new device could be implemented at a cost comparable to what would be required to address the issues with the current seal measurement device. It should ultimately provide more useful data than the existing device. The new device will require some experimental/commissioning work to identify target tolerance limits as well as cycle conditions (loads, pressures, and timing) that give the most relevant results. This device will result in improvements to the gauge R&R. It does avoid the problem of poorly controlled reference surfaces for the measurements. It will incorporate shock absorbers to reduce any impact loading experienced by the linear gages. A proposal to purchase and assemble a new measurement device as shown in Figure 2-40 to address the gage R&R issues for seal thickness was finally approved.

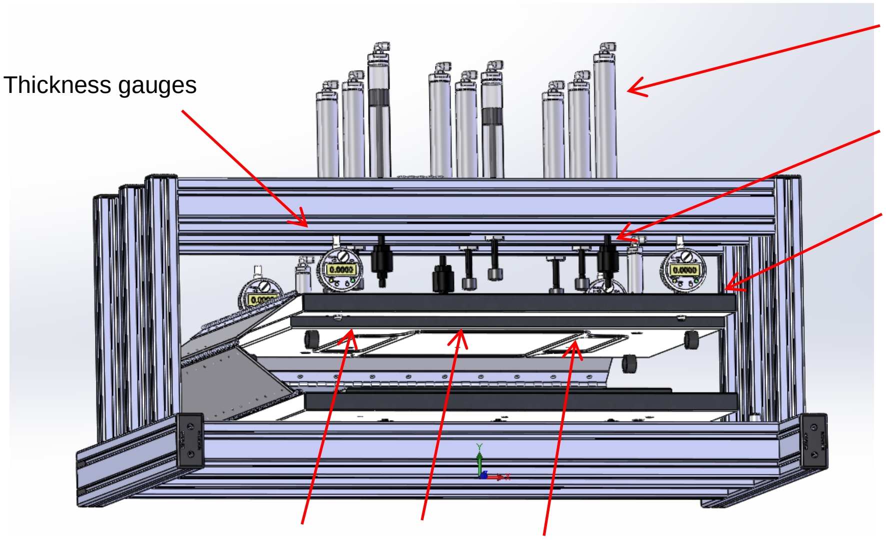

Thickness gauges

Distributed compression
cylinders on common pressure
source (top and bottom)

Floating connections limit
transferred strain

Test platens
(Upper platen incorporates
negative of seal shape)

Leak test these cavities to assess seal uniformity

Figure 2-40. New Design Measurement Device for Seal Thickness

For the Corner Seal Visual Inspection Attribute GR&R, another GR&R study was needed because the Attribute GR&R evaluation result was under 75% (kappa). Gap analysis was performed to understand the issue. A review meeting on corner seal visual quality was conducted with the operators, and every specification in the work instruction was discussed. This activity was very instrumental in addressing miscorrelation issue regarding the rejects. The team is planning another Attribute GR&R study.

The assembly of the new seal measurement device was completed and the equipment was successfully commissioned. An overview photo is shown in Figure 2-41. Cavities are formed into the upper platen in such a way as to generate sealing areas that follow the final seal geometry and these are visible in the view shown in Figure 2-42. The cavities are individually tested for leak with a simple pressure decay methodology: pressurize, close, monitor pressure decay over time, and reject if pressure decays too rapidly. This geometry allows seals to be tested while still in sheet form (before cutting), a state in which they are more quickly and easily handled. The lower platen is sized to the blank seal to ensure relatively repeatable positioning.

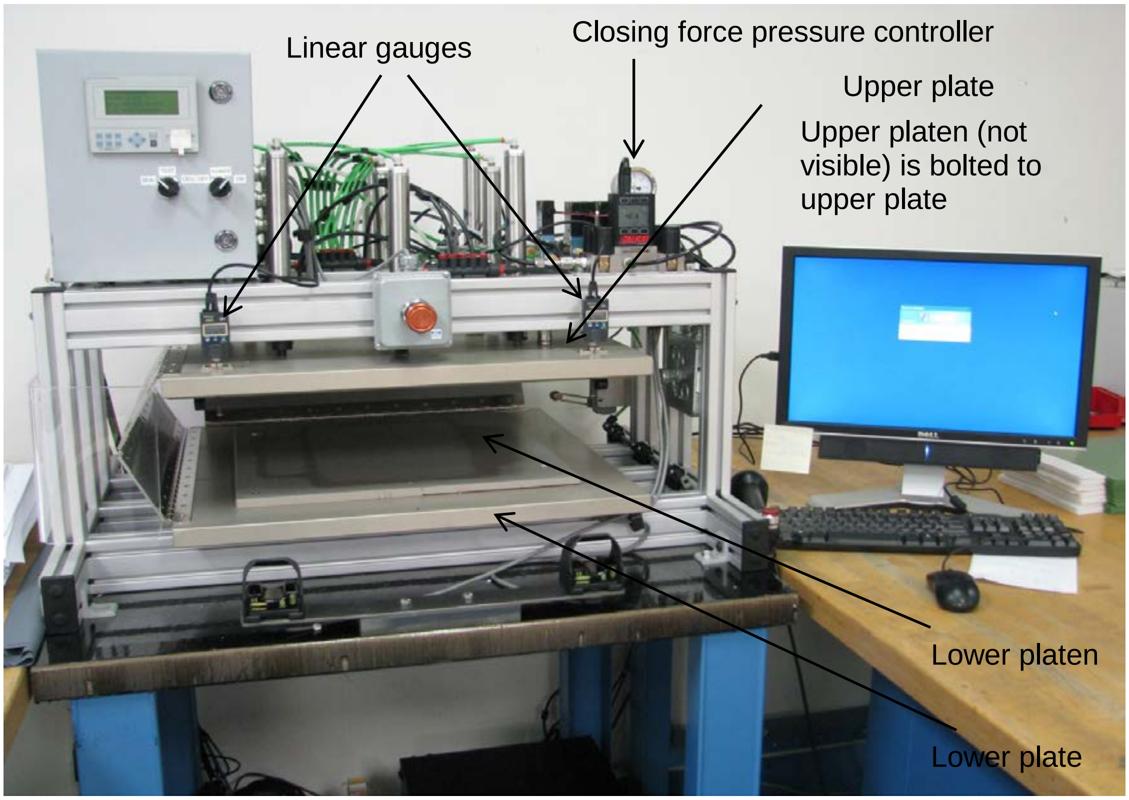

Figure 2-41. Seal Thickness Measurement Device View Looking Down

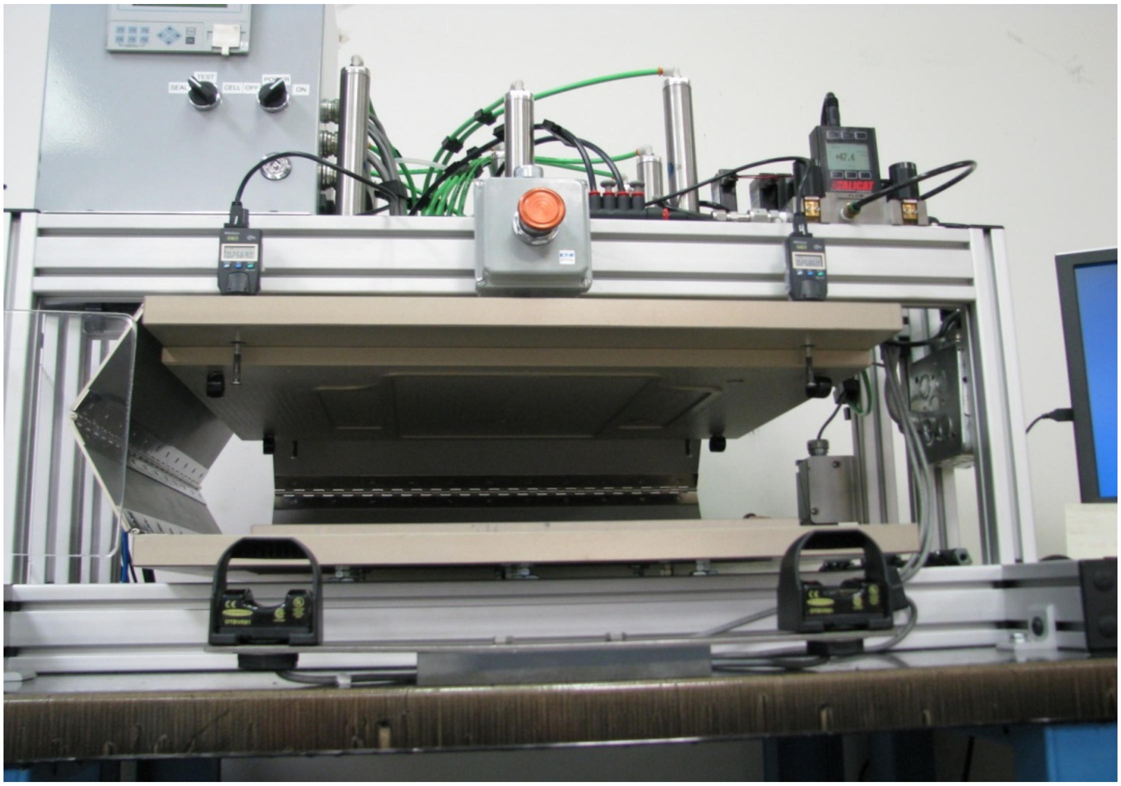

Figure 2-42. Seal Thickness Measurement Device View Looking Up

The distributed support strategy has proven effective. Both the top and the bottom platens are relatively thin and lightweight aluminum, free floating, and each supported on an array of nine cylinders. During the test cycle, the platens are pressed together with 2200 N (500 lbf) force and the array of nine cylinders distributes the force across the platens to minimize the resultant deflection. The platens are fully isolated from the framing which allows the framing to be relatively lightweight (and somewhat flexible) without introducing distortions to the platens. Figure 2-43 shows FEA results on the platens with 2700 N base closing force which is higher than the current test force of 2200 N, cavity pressure of 6900 Pa (1 psi) which is used for detecting flow/leak, and 790 N additional closing force to compensate for the cavity pressures. Under these conditions, the four corner mounting points for the linear gauges are in regions that deflect less than 2.5 micron (9.8 x 10^{-5} in). Additionally, the deflection is somewhat repeatable so that the same deflection occurs during zeroing as well as during measurement. The result is a setup that has theoretical potential for positioning accuracy approaching one micron.

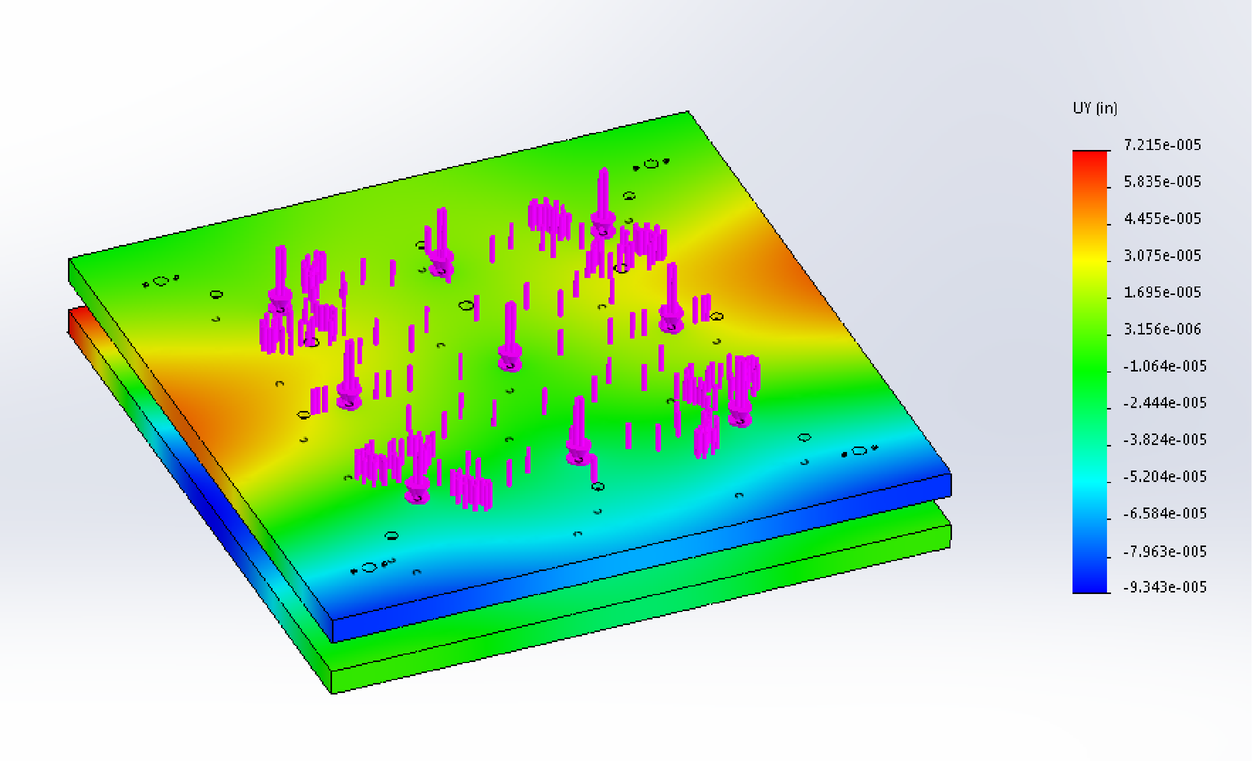

Figure 2-43. Platen Displacement under Load (FEA results)

Initial commissioning trials showed less improvement than was expected in terms of repeatability and reproducibility as well as the tendency to consistently report a low corner. The source was traced to a flaw in one of the platens where a local bump approximately 0.25 mm (0.010 inch) high was causing the platen to bend where it was mounted to the upper moving plate. The problem was corrected by removing the bump in the platen and inspecting and cleaning the top and bottom platen interfaces.

After correcting the problem platen, the GR&R results improved and there was no longer any detectable systemic difference in measurements from the four corners. Figure 2-44 shows data from five seal samples that were measured in four orientations (a through d), rotating the sample by 90 degrees between the measurements. The data set for each sample was repeated to check for reproducibility of measurements. There was a relatively large deviation at corner ‘C’ on seal #1 in orientation ‘b’. With the exception of that point the measurement consistency was good independent of part orientation within the measurement device. There was real and significant within-part variation on some parts (e.g.: samples #1 and #3) where the lowest corner was 38 to 50 microns (0.0015 to 0.0020 in) shorter than the highest corner.

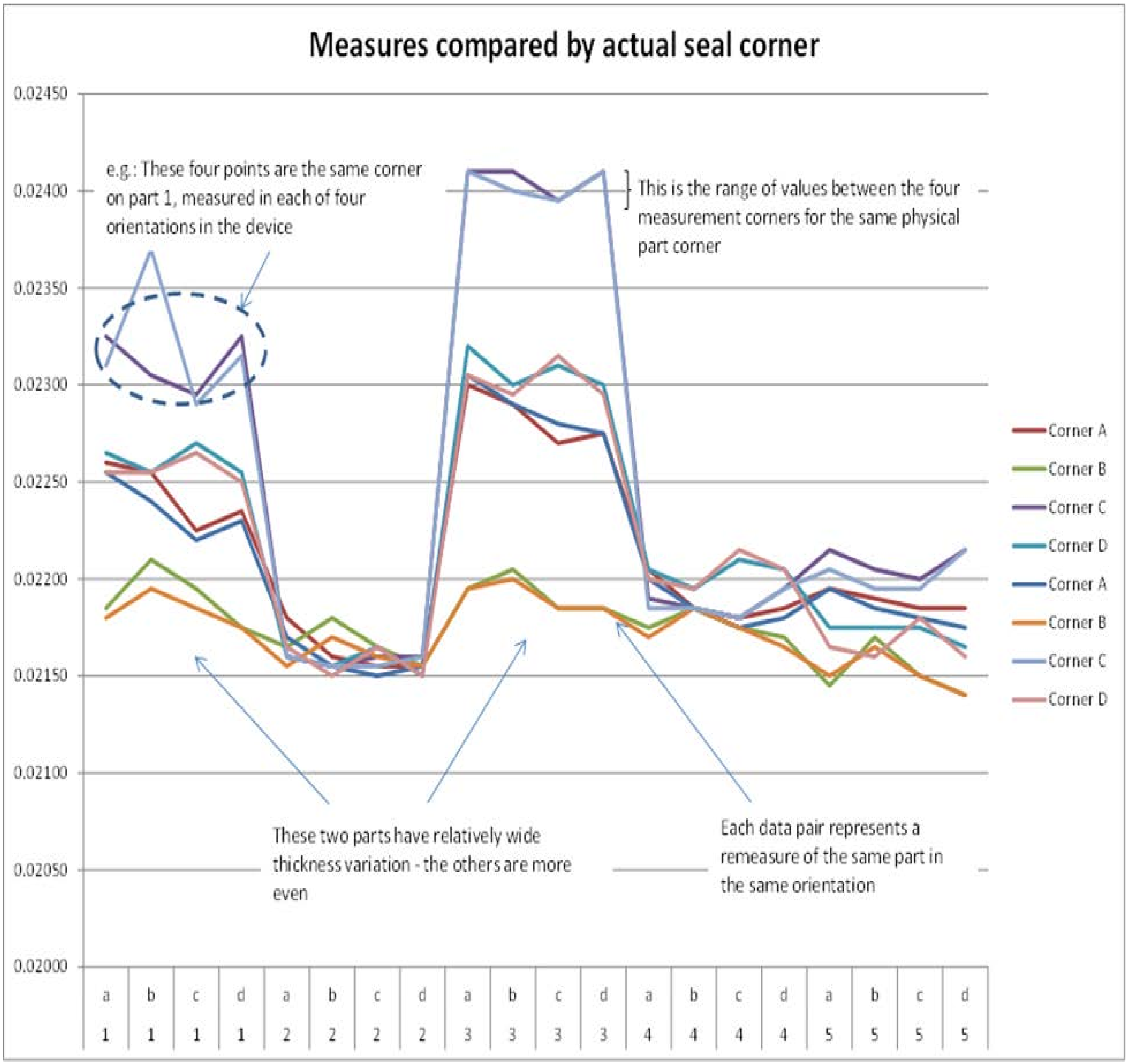
Measures compared by actual seal corner

e.g.: These four points are the same corner on part 1, measured in each of four orientations in the device

This is the range of values between the four measurement corners for the same physical part corner

These two parts have relatively wide thickness variation - the others are more even

Each data pair represents a remeasure of the same part in the same orientation

Figure 2-44. Consistency of Seal Corner Thickness Measurements in New Device (thickness shown in inch)

A GR&R was carried out for nine parts, with two operators, taking three measurements each over two days. The result was a gauge contribution[1] of 20% of tolerance given a ±13 micron (±0.0005 inch) tolerance band. This is well within the 30% gauge contribution target. The previous device had a GR&R result of 80% as well as had intermittent consistency problems that were not captured by the GR&R. These results refer to the average thickness measurement.

---

[1] This and all GR&R results in this section are based on a 95% confidence interval (±5.15 standard deviations)

The leak/flow test portion of the device is implemented as a go/no-go. The device is controlled by a PLC that monitors the pressure decay and punches marking holes in the seal if the pressure decay is less than a preset threshold. These holes (outboard of the useful seal area) become the indicators that the seal has passed leak test. The threshold leak was set somewhat arbitrarily as approximately double the leak observed on ten sample pieces that were selected as representatives of good parts. Qualitatively, the leak test results appear consistent. In the first batch of one hundred seals only one failed leak. There has been discussion of adding sensors and data acquisition to the device to monitor and record the pressure decay results along with the dimensional feedback.

Seals that fail leak test are set aside for further examination. Less seals were rejected through the leak check than had previously been rejected (on the old machine) due to measurement variations. The seals that are rejected for leak do not have visually obvious leak paths. A preliminary assessment of these observations suggests that the old method may have been rejecting more seals than it needed to. The new jig replicates the seal interfaces of the stack better than the old jig. Also, some relatively minor flaws in the seal that are not at all obvious in visual inspection are sufficient to cause higher than normal leakage. These may not have been detected by the old 13-point measurement system. Further review is needed.

The first 100 parts measured on the new machine were also measured on the old machine. This was to determine if there was a shift in reported average thickness between the two machines. Although there was a slight shift in between the means it was less than 2.5 microns (0.0001 inch) and not sufficient to warrant changes to the seal thickness that is targeted. Comparing the data sets as though they were two separate populations, the difference is minor compared to the population variance.

Finally, the cycle time on the new machine is longer than the old machine. The new machine has an operational cycle (close-to-open) of approximately eleven seconds. The old machine operational cycle was approximately six seconds. Both have similar load/unload operations that add ten to fifteen seconds to the overall cycle. The total cycle time has therefore increased from about sixteen seconds (old device) to twenty one seconds (new device), a 30% increase. The increased test time is driven primarily from the pressure decay, which requires a delay time for each test cavity. Repeatable results in twenty-one seconds have more value than non-repeatable results in sixteen.

Considering that this new measurement tool is more stable, VPS is planning to qualify other metallic parts using this tool.

Cell holder thickness and cell thickness are considered critical product characteristics for stack assembly. Matching the two is one of the check points and the allowable mismatch is being controlled to ±0.0006”. The current method of measuring cell thickness is using micrometer caliper, at nine points. The use of a compression type measurement fixture for cell holder thickness measurement was discontinued because it was discovered that the readings were not comparable to those taken using a micrometer caliper. The average reading taken using this fixture was 0.0005” to 0.001” lower compared to the average reading taken when using a micrometer caliper. Decreasing the top load pressure to lessen the compression on the cell holder did not improve the situation.

Another issue found on the current compression type measurement fixture was that the gap between the top and bottom platens cannot be corrected. A simulation was conducted and a significant difference in readings between the front and rear digital meters was found when operating at a 200 pound top load.

The difference in readings increased when the top load was set to zero pounds. This indicated that there was an inherent problem with the compression type measurement fixture.

Along the left side, the top platen could be moved from its original position indicating that there was a planarity problem even after grinding the bottom platen. A meter mounting holder prevented the grinding of the top platen.

A short-term corrective action comprising four-point measurement using a micrometer caliper was implemented for cell holder thickness. GR&R was performed using this method and it passed the %GR&R criteria (<30%). The %GR&R for four-point measurement was at 22.51% but when using one-point measurement, the %GR&R was only 89.07%. This method, however, was time consuming and very difficult to manage. Another concern when using the four-point measurement using a micrometer caliper was that it was a repetitive activity and can cause wrist and finger injury when holding the parts and when rotating the thimble of the caliper as shown in Figure 2-45.

Figure 2-45. Cell Holder Thickness Measurement Using Micrometer Caliper

A long term improvement plan was to evaluate cell holder thickness measurement using a modified version of the new tool for seal thickness measurement. This new seal measurement tool had already passed the GR&R study for seal thickness and the result was very satisfactory. A flat top platen is ready and will be installed in the machine in Q4 2014. The new tool will then be qualified for cell holder and other metallic parts.

Documentation Control Improvements: The team reviewed the materials specifications, engineering (drawing) specifications, and work instructions required to complete in-house processes and assembly of a PCI stack. A formal Documentation Tree was created and released as a top level document outlining all drawings, specifications, and work instructions. A portion of these documents was categorized as High Priority. The effort was focused on gathering historical dimensional data of critical components for gap analysis, revising specific drawing dimension tolerances based on current process capability and quality consideration, updating or generating work instructions based on the new format, and providing quality review of documents. A total of 19 documents (36%) were approved and released. The remaining 34 documents are undergoing reviews and pending approval. Some are dependent on the team's decision on configuration numbering format which can lead to consolidation of related drawings. A new cell engineering specification was generated and is undergoing review. This covers different materials comprising a cell and their Min-Max requirements. The approval of this document will result in consolidation of eight cell-related drawings. The Stack Assembly Build Sheet was revised and approved. It includes Build and Conformance Record, information of validated measurement tools, traceability of metal components for its heat number, vendor lot number, and purchase order number.

The documentation tree is undergoing revision to make it more manageable. It will be broken into three different document trees covering cell manufacturing, seal fabrication, and stack assembly and test. Also, corrections will be made on some document numbers, process flow charts, and material combinations. A Quality Control Plan will also be included. A Quality Control Plan (QCP) is a quality matrix summary for every process defining the critical process or product characteristics, their criteria or specification limits, measurement tools and techniques to be used, inspection and sampling plans, owner, control method, and reaction for out of control.

Process Control Improvements & Qualifications: The process control improvements and qualifications activities are on-going and will be rolled into the PCI revision controlled documentation if needed to complete in-house processes and assembly of a PCI stack (via process qualification, best practice, or other).

Reliability

Adequate performance of the SOFC system is measured by the life (years running) and the stability (voltage degradation rate). In order to demonstrate progress towards specified goals, the reliability of the system, especially the multi-cell stack, will be monitored and improved over time. The reliability is ultimately measured as a percentage confidence that a minimum percentage of systems will meet the target performance measures. In regards to the stack, the focus of reliability improvements will be on identifying the variables that cause a cell to perform poorly (low voltage output, high voltage degradation rate) – as it has been shown that this can affect the overall performance of the stack (i.e. - reducing the reliability of the stack).

As part of the established stack Factory Acceptance Testing procedures, a newly-built cell stack is placed in a test stand to perform conditioning (burn-in), fuel utilization testing, and steady state performance testing. If one or more cells are performing poorly, the engineering staff at the production facility typically conducts a failure investigation on the stack. These investigations include review of test results, review of manufacturing process records, non-destructive diagnostics and invasive post-test examination, resulting in a summary report.

A significant amount of data has been collected from the production team. This data includes stack test performance results; most recent failure investigation results; dimensional inspection results, in-process measurement results, and stack build specifications. Forthcoming root cause determination work will include hypothesis testing (using prior recorded data and data from new lab tests on smaller sized stacks); post-test examinations; and material testing to better understand high temperature stiffness characteristics. Once a root cause variable has been confirmed, a Design of Experiments will be completed to optimize a design or process improvement to mitigate the influence of the variable.

Development of Flow Field Pressure Drop Measuring Device

Anode and cathode flow fields are fin materials formed of ferritic stainless steel sheet metal. VPS flow fields are purchased from outside manufacturers and processed in-house with operations including final rolling, cutting to size, cleaning, annealing, and quality control. Quality control of the fin components entering Versa Power Systems has focused mostly on dimensional checks (overall dimensions as well as uniformity) and qualitative assessments of the form quality (e.g., the quality of openings at sheared edges). The general expectation was that as long as the part dimensions were within specification, the pressure drop characteristics for all parts would be consistent. Limited preliminary testing suggested that there might be large differences in pressure drop between different fin components. This concern prompted the development of a device to accurately and consistently measure cold flow field pressure drop with the flow field constrained in a manner similar to the way it is constrained within a stack.

The flow field pressure drop measurement test jig design was completed and the jig was procured. The manufactured jig is shown in Figure 2-46, along with key features of the test setup. In the jig, an even flow of nitrogen is generated over the flow field and the resulting pressure drop is then measured. The flow field to be tested is placed below a one inch thick acrylic plate inside a soft seal whose dimensions replicate the total contained width in a real stack. The transparent cover plate allows verification that the flow field is properly positioned within the closed jig.

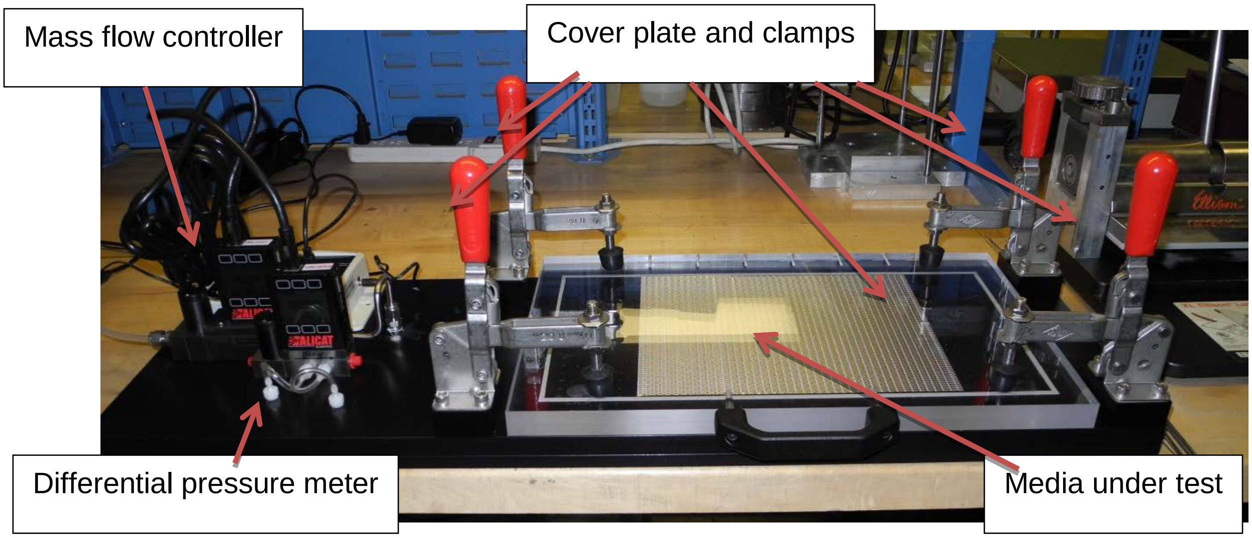

Figure 2-46. Pressure Drop Testing Jig

Figure 2-47 shows the flow ports and pressure sensing ports relative to the flow field under test. The flow ports are located 50 mm away from the pressure sense ports to enable fully developed flow when passing the pressure sense ports.

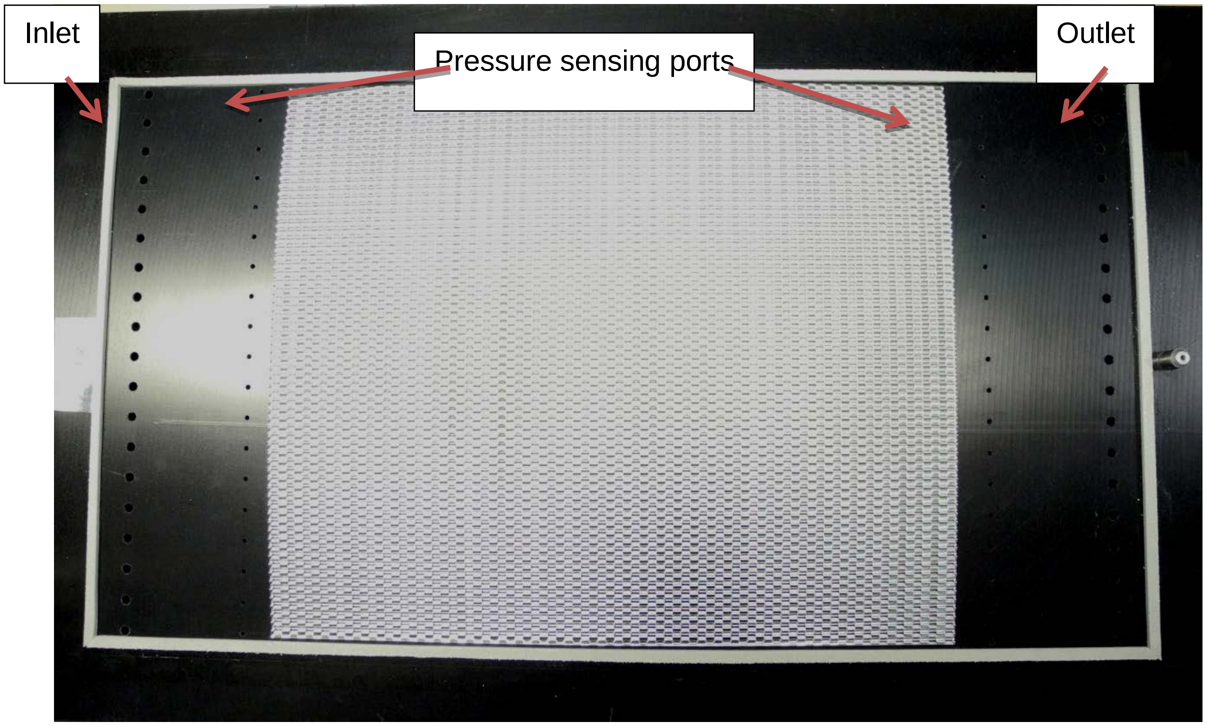

Figure 2-47. Flow Field Mounted in the Test Jig and Locations of Flow and Pressure Ports

The pressure sense ports are located approximately 10 mm from the edges of the flow media. This was an estimate of the distance necessary to limit any flow induced pressure disturbances from the flow field in test, while minimizing the contribution of the jig pressure drop to the resulting measurement. Test operation is controlled from a laptop computer programmed with a custom Excel code. The operator defines a sequence of flows and durations through a configuration spreadsheet. Once configured, a button press triggers test execution. The Excel code runs the test sequence, collects the pressure and flow data, and plots the results.

The jig design was validated first in model space through CFD analysis, then physically by running blank tests and comparing results to the flow/pressure results predicted (by calculations). The primary goal of the device is to provide comparative data between different flow fields. Normally a Reynolds number matching strategy would be used and that is a viable strategy in this case. However, the Reynolds number is low (about 6.4) for reformate flowing through the anode flow field, treating the flow passage as a parallel plate for the purpose of determining the hydraulic diameter. This is well into the laminar regime and it seemed plausible that the flow rates could be increased without unduly affecting the comparative results.

As a first test of the device, anode flow field components to be used for stack GT057235-0103 were characterized showing some interesting results. Figure 2-48 presents the results including two extra parts that were evaluated for comparison and show up as major outliers. A large variation in flow field pressure drop was observed for the parts that had been prepared for the stack. Repeated testing of the parts showed good consistency of results. The two major outliers are a piece of anode flow field with 0.010" base material (the past standard, replaced in this stack with 0.008" base material flow field), and a piece of 0.008" base material flow field before final sizing operations (which reduce the height of the flow field).

Figure 2-49 shows the pressure drop through each flow field component as a percentage of the average pressure drop. The 1 and 2 slpm flow rate cases are omitted because there was insufficient resolution to differentiate between the flow fields. It can be seen that pressure drop deviations can be as high as about 10% above and below average. Noting that the flow pressure drop relationship is nearly linear, this means that for a given pressure drop condition in stack, the flows through individual layers might deviate by an amount approaching ±10%.

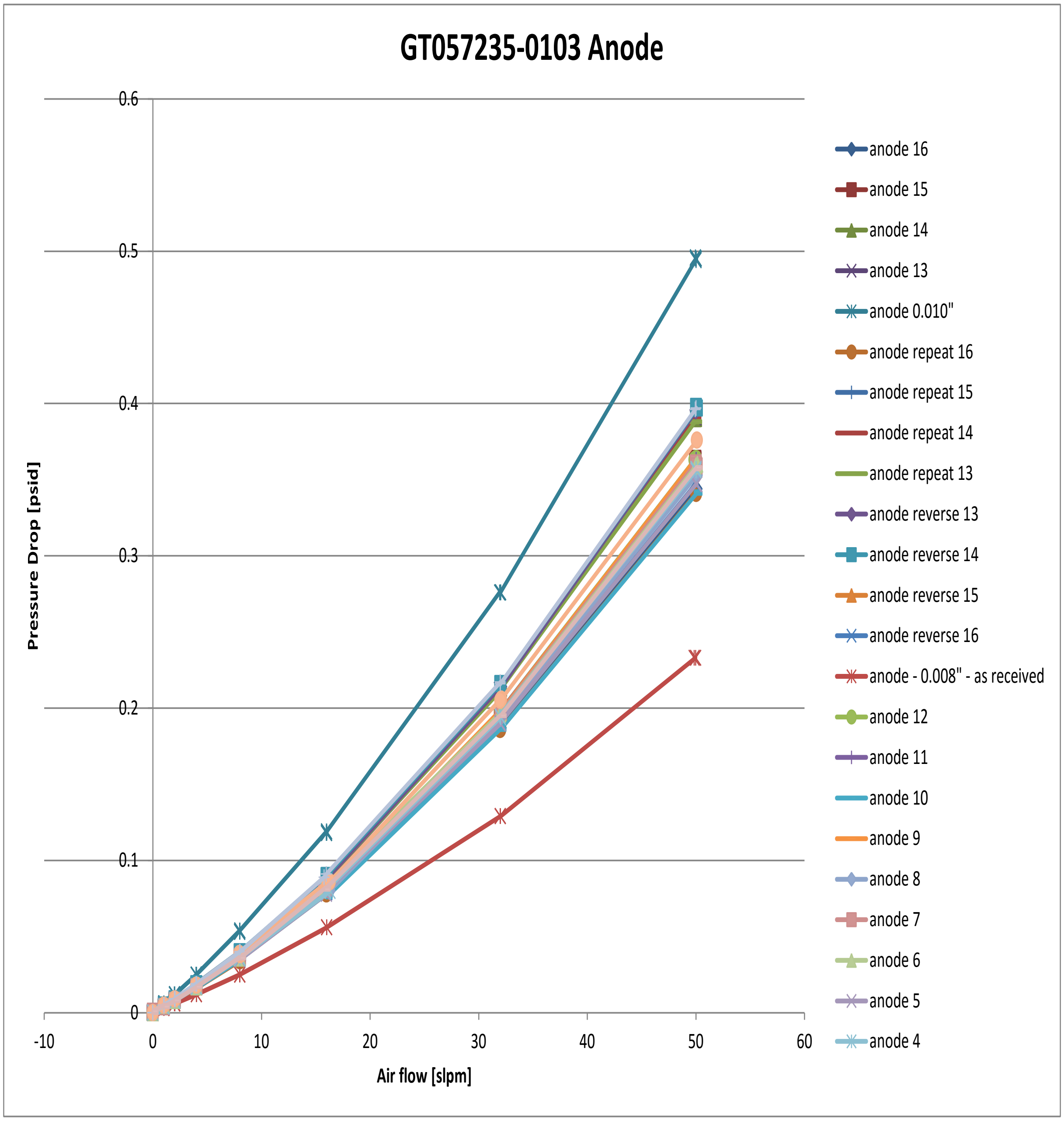

Figure 2-48. Pressure Drop Characterization of Anode Flow Fields to be Used in Stack GT057235-0103

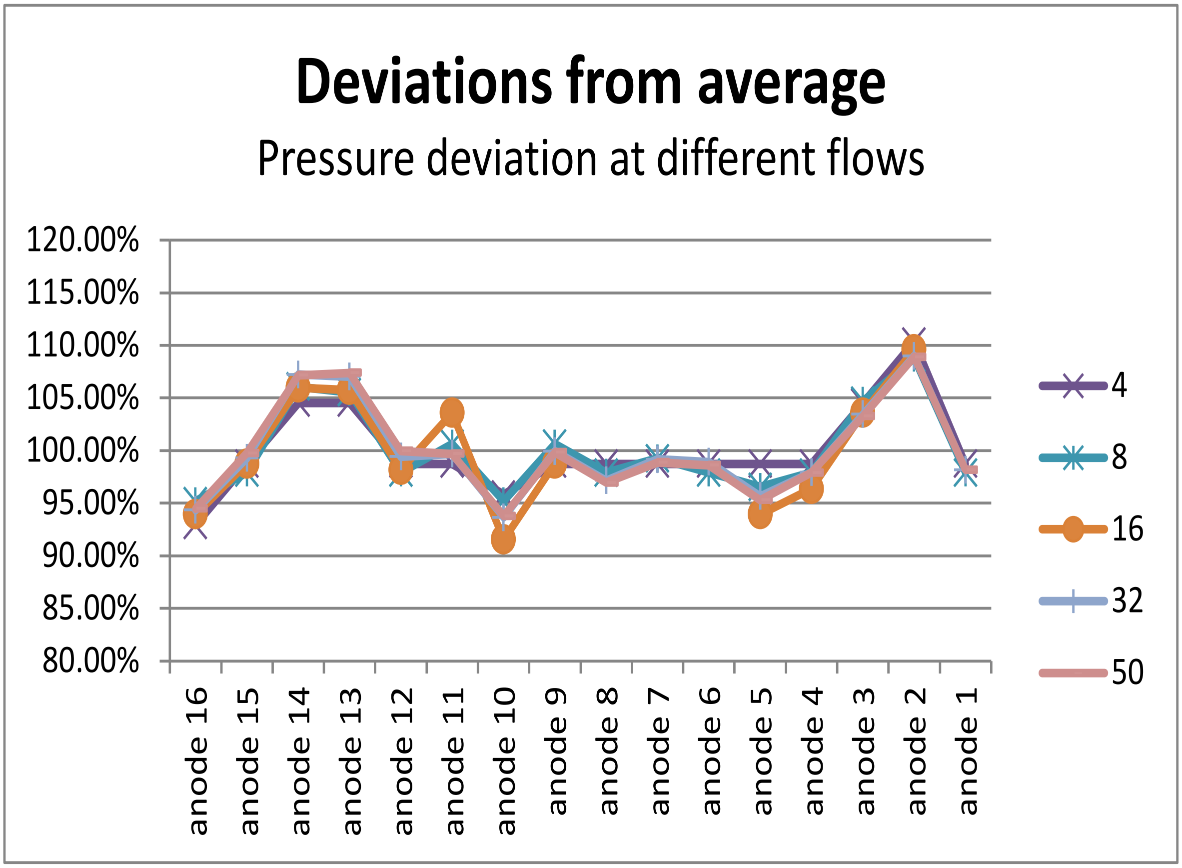

Figure 2-49. Deviations from Average Pressure Drop for Anode Flow Fields Selected for Use in Stack GT057235-0103 (Flow rate in slpm)

Figure 2-50 shows the reproducibility of the results (at 50 slpm flow rate) for flow fields 13 through 16. Each was characterized and removed from the jig. The cycle was repeated, re-installing each flow field in the same orientation and nominally the same position within the jig. These form the first eight measurements (in the figure). The cycle was then repeated, this time reversing orientation of the flow field (end-for-end) to see if there was any impact of orientation on the results. From these results it seems that:

- Measurement repeatability is acceptable, certainly much better than the part to part variation.
- Repeatability problems are not a plausible explanation for the observed part-to-part variation.
- There does appear to be a small orientation effect on pressure drop (note: orientation is not controlled in the production process, the flow field is treated as symmetrical).
- The orientation effect is not sufficient to explain the observed part-to-part variation.

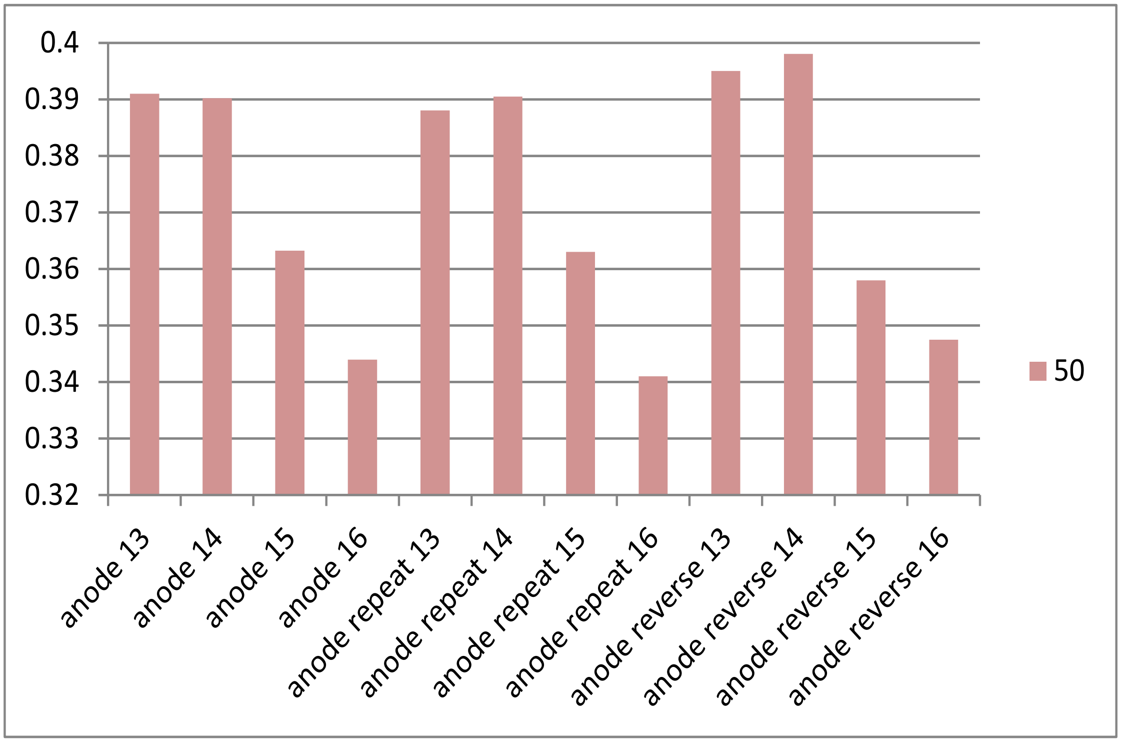

Figure 2-50. DP Measurement Consistency at 50 slpm Flow Rate (DP in psid)

Referring back to Figure 2-48, it is interesting to observe the significant impact of base material thickness and of final sizing operations on the flow field pressure drop. For example, the 0.008” (0.2 mm) thick base material fin had a pressure drop approximately 25% lower than that of the 0.010” (0.25 mm) thick base material fin. This was a larger reduction in pressure drop than desired, as it can influence the flow distribution within the stack. Also of interest was the roughly 50% increase in pressure drop of the 0.008” thick base material fin when it was brought to final height, an operation that consisted of lowering the height from the as-received height of about 0.041” (1.05 mm) to a final height of about 0.035” (0.9 mm). If a 0.15 mm decrease in height results in a 50% increase in pressure drop, then maybe it is not surprising that a ±0.04 mm tolerance band is sufficient to allow ±10% variation in pressure drop between flow fields. Analysis of data showed that there is some correlation between measured height and the resulting pressure drop.

In summary, a device had been built that measured individual flow field pressure drop as a function of flow rate and can be used to assess variability between flow field components, to assess the impact of changes in flow field design and in stack design that relates to flow. Preliminary testing suggested that the device had the resolution necessary to differentiate between flow fields. Initial results suggested that there was more variation between flow fields than was desired. This may be due to the allowable tolerance range selected for part height. Next steps will include evaluation of the cathode flow fields and as-received components to see how they compare with the components after re-sizing. If parts need to be controlled to the nearest 0.0005” (0.013 mm) to give acceptable pressure drop consistency, then alternate manufacturing methods may need to be considered. It was recommended that a standardization calculation be developed that allows part comparisons over time and provides results in units of pressure drop which have more meaning to designers. Standardization is required to compensate for any ambient pressure effects (jig outlet is not pressure controlled).

Development of a Cell (Edge Deformation) Measurement Device

Gage R&R studies showed weaknesses also in the cell QC process, particularly in relation to the measurement of “edge lip.” Edge lip is a cell characteristic that arises from the structure of the cell and the stresses imposed by the firing process. The unbalanced stresses at the cell edge cause local curvature on the outer 10 to 20 mm of the cell edges. If excessive or of too small a local radius, the edge lip can cause local stresses in the cell (used to build a stack). Empirical experience has shown that if the edge lip is below a certain value then cells do not break when built into a stack. Edge lip is measured at the half cell level, and if found to be excessive, the cell is simply routed through an additional high temperature ironing step before being re-measured. Measuring edge lip is a relatively low cost way to catch problem cells and process drift before stack assembly as the consequences would be the likely loss of the stack.

Figure 2-51 shows the method used to measure edge lip. This measurement is repeated at three places along each cell edge for a total of twelve measurements. If the maximum of those measures minus the average cell thickness exceeds a limit of 0.15 mm, the cell is sent for ironing.

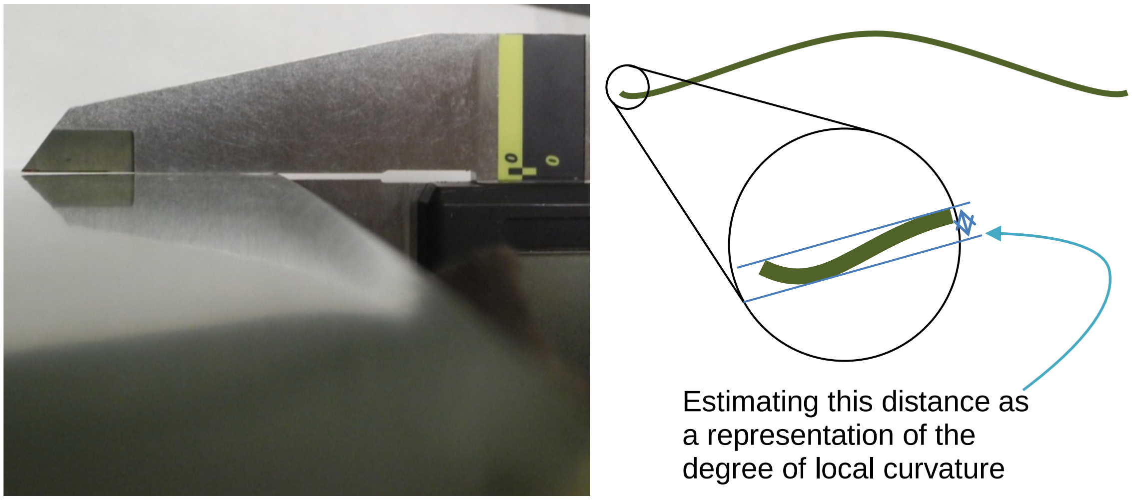
Estimating this distance as a representation of the degree of local curvature

Figure 2-51. Cell Edge Lip Measurement

A gauge R&R showed that this measurement was not repeatable. Nine parts measured three times by each of three operators had a study variation (at 99% confidence interval) of 188% of the tolerance limit. That is to say, 5.15 times the standard deviation of the measures was almost 1.9 times the tolerance limit. Cells not breaking in the stack shows that the tolerance limit is conservative and that additional ironing steps are being carried out but not strictly necessary. It does not mean that the tolerance limit can be relaxed. To do so without risking cell failure in stack would require improved measurement accuracy.

A large part of the R&R results observed is thought to be due to the relatively complex geometry at the cell edges. The exact shape of the cell edge varies from cell to cell, and varies even along the cell edge. Also, it is a measure at twelve points around the cell edge, where the theoretical goal is to ensure that no point around the cell edge exceeds some limit. The location of the peak of the local curvature can vary as can the location of the tip of the cell, cell thickness, etc. These all make it challenging to get a consistent measurement. After consideration, it seemed that the path to improvement was not through modifications to the existing measurement approach. Instead a form of go-no/go testing was suggested where the cell is loaded in a manner representative of the loading expected in-stack. If the cell breaks it is discarded. This approach has the advantage (and it may be an important one) of testing the whole cell edge rather than twelve discrete points.

In order to limit the additional work imposed by the test, it was proposed to integrate it into leak testing. The cell will be exposed to loads and geometry representative of a real stack and leak tested. If it passes the leak test and exits the leak test fixture undamaged, there can be confidence that it will not crack in a real stack. This strategy (integration with leak testing) was detailed in CAD space and FEA modeling of the structure was carried out. In order to load the cell in a manner similar to how it is loaded in a stack, the leak testing apparatus had to be redesigned from the ground up. The compressive loads on the cell during leak testing increase from a few hundred points against soft seals to two thousand points with the cell compressed between steel plates. The test jigs required a redesign, and a heavier press was required to handle the higher loads. The end result is a design illustrated in Figure 2-52. The operator loads the cell with the help of retracting alignment pins. Two handed actuation triggers the press closure. As the press closes the full cell comes into contact with the press platens, except at the cell edges where rubber seals are sized to reproduce loading similar to that expected in a real stack. These seals also form the basis for leak testing. After the leak test cycle, the press is opened and the cell extracted. If the cell passed the leak check, a visual inspection of the cell edge is carried out and the cell is ready for the next process step. If it fails leak test and/or cracks, the cell is discarded. Integrated into the leak test platens are mounts for four linear gauges, which will provide new information on the nominal cell thickness when the cell is loaded. This would be of interest in setting target thicknesses for seals in the stack.

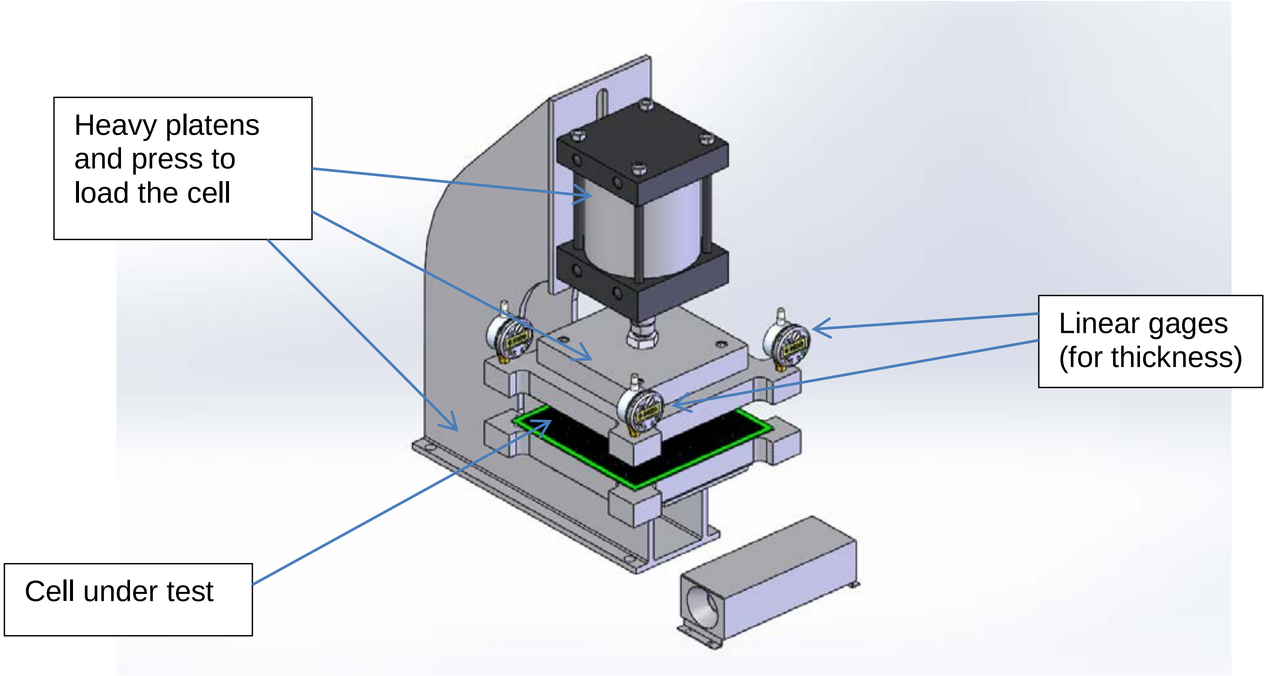

Figure 2-52. Cell Leak Test and Edge Lip Checker

FEA results for the platens (and the overall structure) at 2000 lbf closing force (the maximum compressive load exerted on a real stack) showed that the deflection of the plates (which is relevant to the cell thickness measurement) was the limit of what is acceptable (total differential deflection at the gauge locations approaching 0.0005”). Careful zeroing and calibration of the device should reduce the real error relative to that limit and there can be some expectation that the deflection will be relatively constant between tests. The new method offers an opportunity to improve the leak test resolution, and provide additional cell thickness data not previously available.

The device was built and is shown in Figure 2-53. It is centered around leak testing (a relatively slow process), but simultaneously measures cell thickness and checks for cell flatness (for a low risk of cell breaking in a stack). The device is intended to replace three of the existing measurement steps:

- Cell thickness – 9 hand measures with micrometer
- Edge lip – 12 hand measurements with caliper
- Cell leak – 1 measurement read from rotameter

Figure 2-53. Cell Leak, Thickness, and Flatness Checker

It is attractive to have all three measures performed simultaneously using a semi-automated method and within the time period it takes to perform the leak test.

The principle of the device is to compress the half-cell (fired anode + electrolyte) between hard stops, with the cell edges captured in compliant polymer seals in a way that loosely represents the geometry and loading the cell will encounter in a real stack. The existing nine-point cell thickness measurement is replaced by the average of four measurements of the distance between the upper and lower platen when pressed into the cell. The old cell lip measurement is replaced by a go/no-go condition between the edge seals. If the cell can be pressed flat with seals mimicking the loading in the real stack without breaking then it is presumed to be capable of being similarly loaded in the stack. Instead of taking 12 points and hoping to find the maximum, the new device tests the entire perimeter. When the press closes on the cell to take the measurements, the perimeter polymer seals allow leak testing of the cell electrolyte to occur. In this way, three measurement steps are replaced by one.

Initial gage R&R (Repeatability & Reproducibility) for cell thickness measurement led to very promising result of <10% (compared to gage R&R target of <30% for variable output response) as shown in Figure 2-54.

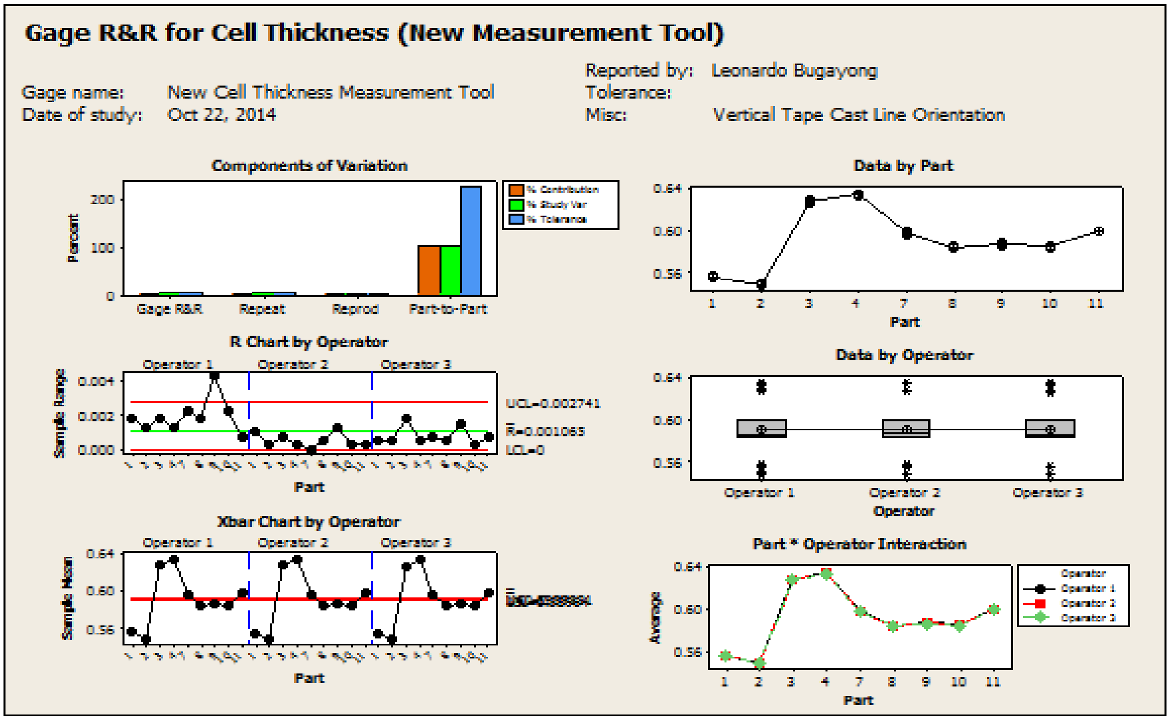

Gage R&R for Cell Thickness (New Measurement Tool)

Gage name: New Cell Thickness Measurement Tool
Date of study: Oct 22, 2014
Reported by: Leonardo Bugayong
Tolerance:
Misc: Vertical Tape Cast Line Orientation

```
                          %Study Var                      %Tolerance
Source                          (%SV)       95% CI        (SV/Toler)        95% CI
Total Gage R&R                   2.53   ( 1.30,   5.89)         5.69   (  4.93,  13.04)
  Repeatability                  2.43   ( 1.25,   3.74)         5.47   (  4.69,   6.55)
  Reproducibility                0.70   ( 0.00,   5.23)         1.57   (  0.00,  11.81)
    Operator                     0.70   ( 0.00,   5.23)         1.57   (  0.00,  11.81)
Part-To-Part                    99.97   (99.83,  99.99)       225.08   (152.03, 431.21)
Total Variation                100.00                         225.15   (152.13, 431.25)


Number of Distinct Categories = 55
95% CI = (23.9650, 108.531)
```

Figure 2-54. Summary of Initial Gage R&R for Cell Thickness Performed Using New Measurement Tool

Parametric Study For Optimization of TSC-3 Cell Anode Substrate

In order to further optimize TSC-3 cell anode substrate, it was decided to investigate the effect of cell (component) density and thickness on cell performance in the temperature range of 650 to 800°C and up to high fuel utilization at fixed conditions of 750°C, 0.5 A/cm^2 and 25% Uo (dry air). Anode supported cells with thickness of approximately 0.6 mm were sintered to slightly different temperatures to yield cells with densities of 5.25, 5.48 and 5.75 g/cm^3 for single-cell testing. Figure 2-55 shows the porosity (for both oxidized and reduced volume forms) and Ni and YSZ volume percentage against the measured cell density with the parameters for these three cells highlighted by vertical lines.

In addition, a 0.3 mm thick cell with density of 5.45 g/cm^3 that had previously been produced using a slightly modified anode substrate to enable lower sintering temperature was tested under the same conditions to investigate anode substrate thickness effects at an average density. This cell was developed for reversible SOFC operation and is referenced as an RSOFC-7 cell. The AFL, electrolyte, and cathode side of the cell comprise the same materials and are processed in the same way as TSC-3 cells, the only material difference is the anode substrate. Power curves at low utilization were generated for temperatures from 800 to 650°C covering current densities up to 0.74 A/cm^2 for the 0.3 mm thick cell with average density and three 0.6 mm thick cells with low, average and high densities. Power curves for the 0.3 mm thick cell are shown in Figure 2-56 as an example. Power densities approaching 0.7 w/cm^2 were observed. Figure 2-57 shows a comparison of cell performance characteristics at 750°C for the four cells. It can be seen that while there is only 4 mV difference in OCV for these cells, the cell voltage at 0.74 A/cm^2 varies significantly (53 mV) with the thinner anode substrate cell having highest voltage and the thicker and higher density anode substrates having lowest cell voltage. Table 2-2 and Table 2-3 show the effect of cell density and thickness on the cell voltage at 0.5 A/cm^2 and various fuel utilizations of up to 90% Uf before and after thermal cycle, respectively. The same trend is clear with the highest voltage at high utilizations exhibited by the cell with thin anode substrate and the lower density cell showing higher cell voltage at high fuel utilizations than higher density cells. Clearly, for improved cell performance at high current density and/or high fuel utilization, it is advantageous to use a thin anode substrate and target cell densities of under 5.5 g/cm^3.

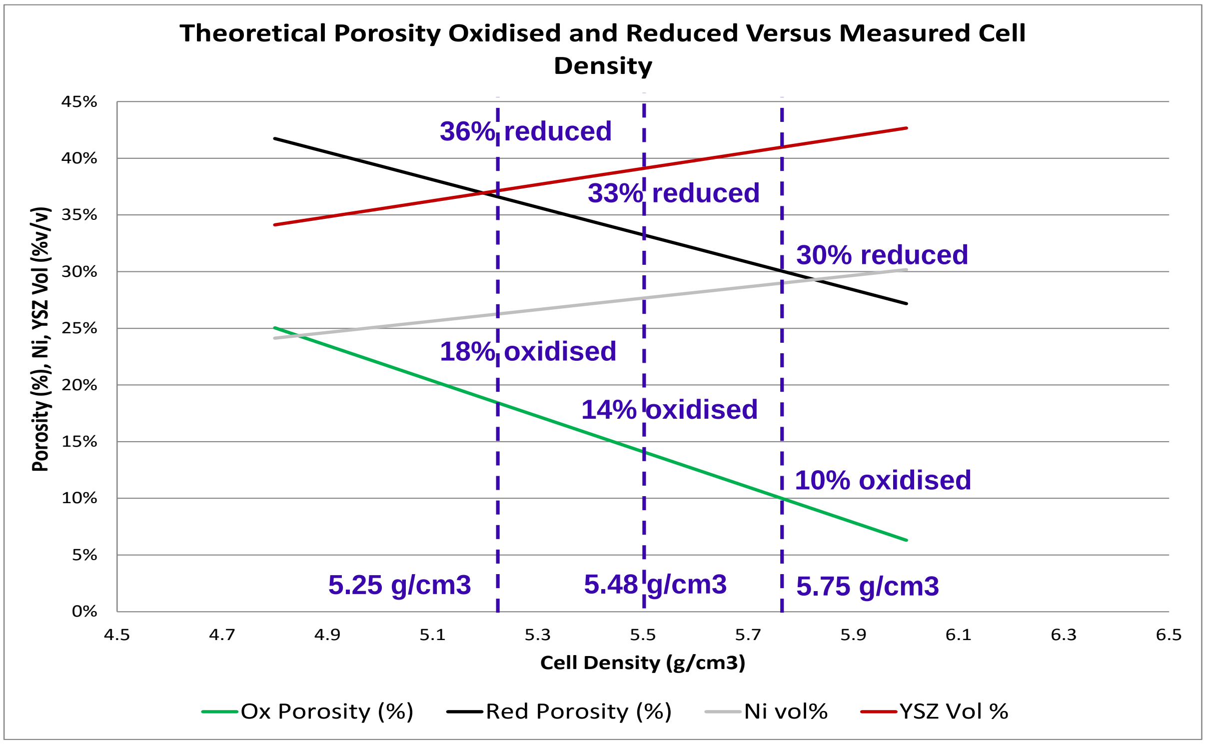

Figure 2-55. Theoretical Porosity (oxidized and reduced) and Ni and YSZ Volume % vs. Measured Cell Density

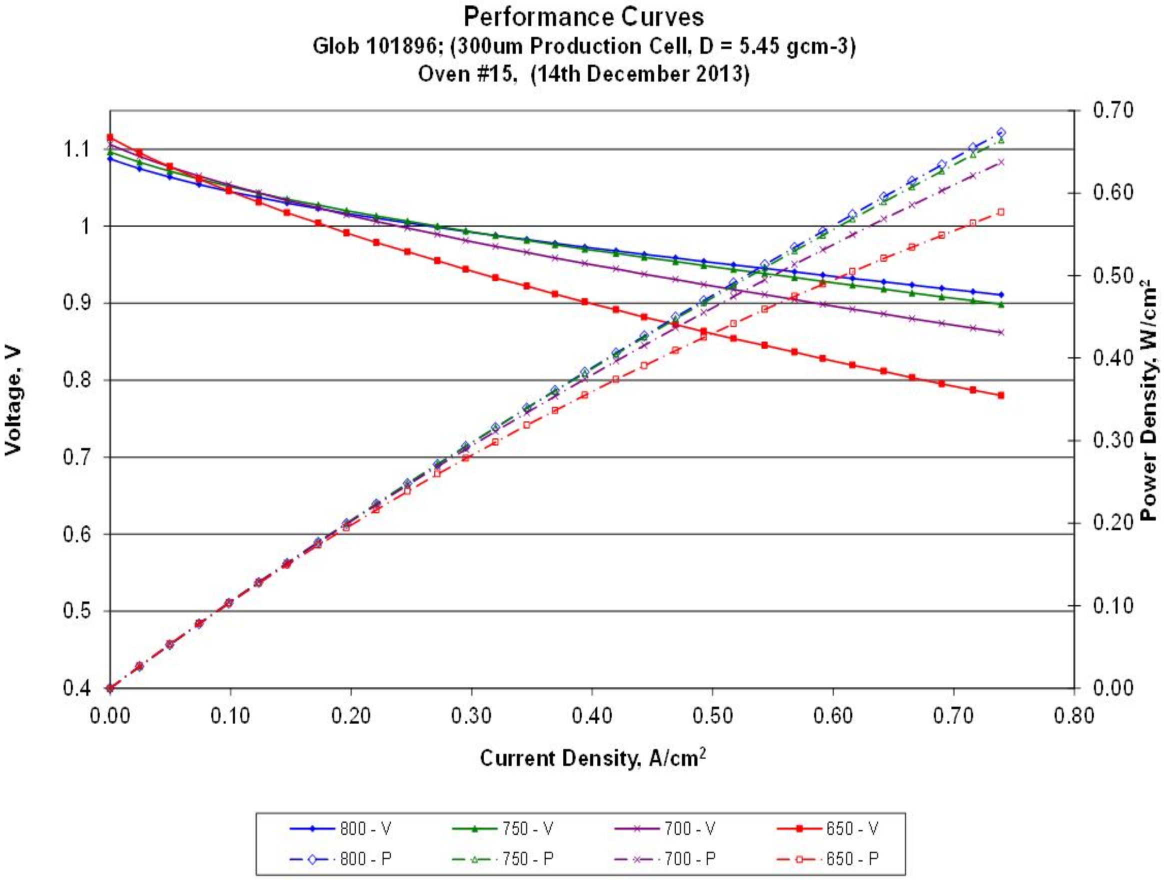

Figure 2-56. Performance Characteristics and Power Curves of GLOB 101896 0.3 mm RSOFC-7 Cell in Temperature Range of 650-800°C

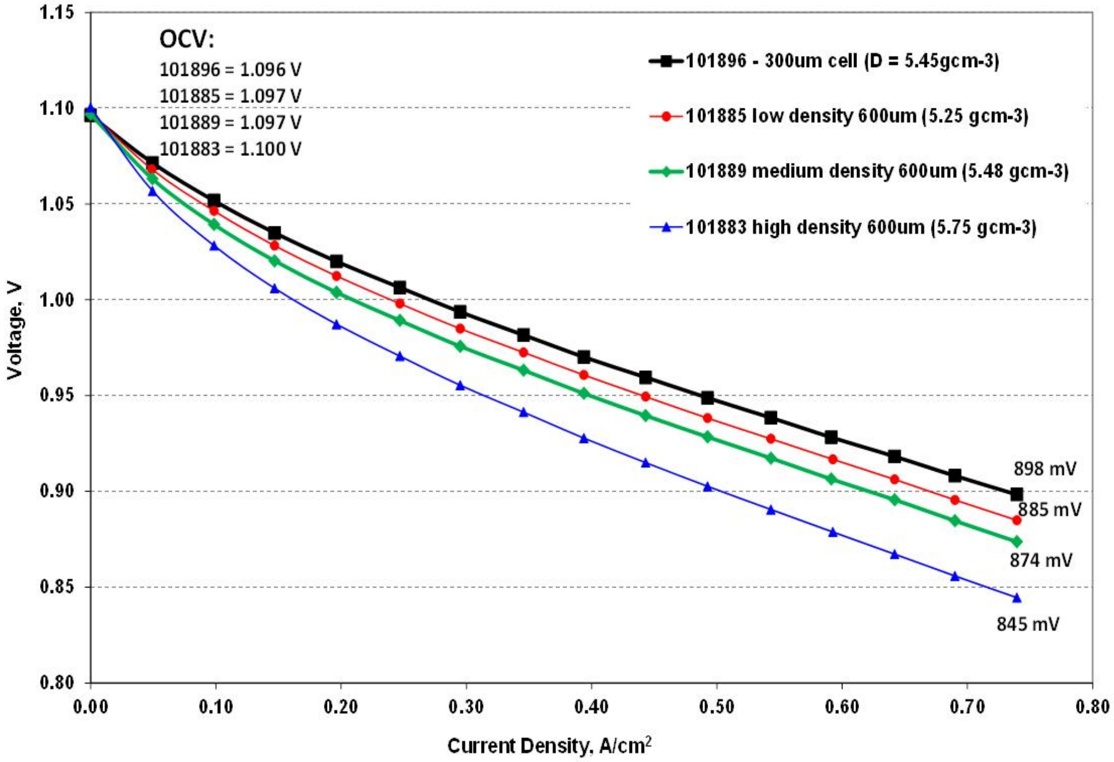

Figure 2-57. Comparison of Performance Characteristics at 750°C for 0.6 mm TSC-3 Cells at Three Densities and a 0.3 mm RSOFC-7 Cell at Average Density of 5.45 g/cm^3

Table 2-2. Effect of Cell Thickness and Density on Performance at 750°C, 0.5 A/cm^2, 25% Uo and 50-90% Uf (before thermal cycle)

Test No.	101896	101885	101889	101883
Cell Thickness (um)	300	600	600	600
Cell Density (g/cm3)	5.45	5.25	5.48	5.75
V at 50% Uf (mV)	890	879	867	838
V at 60% Uf (mV)	878	869	855	827
V at 70% Uf (mV)	862	852	839	808
V at 80% Uf (mV)	833	828	811	773
V at 85% Uf (mV)	811	798	781	730
V at 90% Uf (mV)	715	681	670	Fail

Table 2-3. Effect of Cell Thickness and Density on Uf Performance at 750°C, 0.5 A/cm^2, 25% Uo and 50-90% Uf(after one thermal cycle)

Test No.	101896	101885	101889	101883
Cell Thickness (um)	300	600	600	600
Cell Density (g/cm3)	5.45	5.25	5.48	5.75
V at 50% Uf (mV)	894	879	871	850
V at 60% Uf (mV)	880	868	858	838
V at 70% Uf (mV)	868	852	842	822
V at 80% Uf (mV)	846	828	819	793
V at 85% Uf (mV)	826	803	788	758
V at 90% Uf (mV)	785	692	665	652

The excellent performance of 0.3 mm cells led to further exploring the maximum power density for the cell design. Due to the test equipment limitation, a smaller square cell (25 cm^2 active area) was used in this test. As shown in Figure 2-58, the cell demonstrated maximum power density of over 2 W/cm^2 at 800ºC. Even at lower temperature of 650ºC, the maximum power density of 0.8 W/cm^2 was reached.

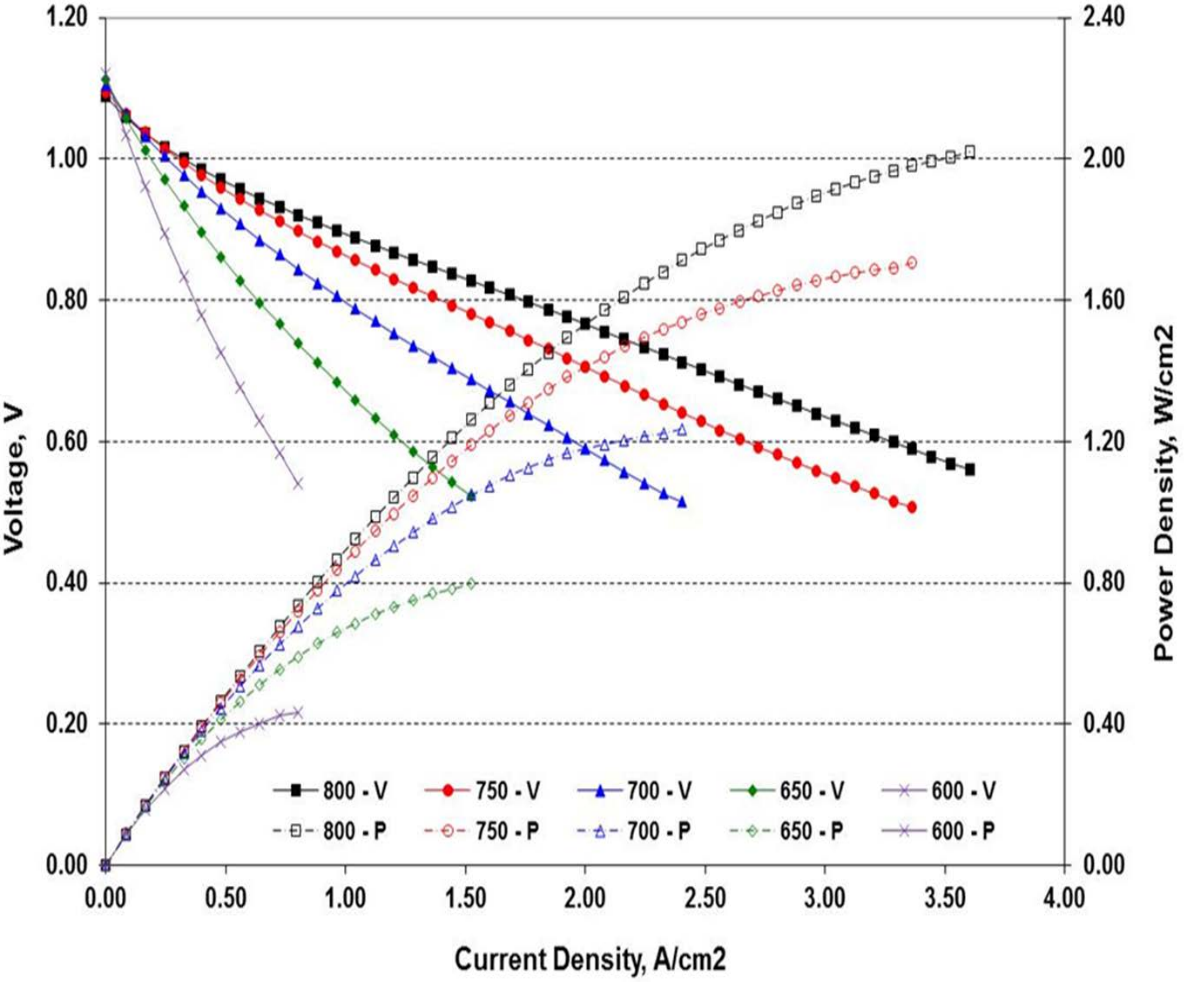

Figure 2-58. Performance Characteristics of a 0.3 mm TSC-3 cell (in Temperature Range of 600 – 800ºC)

Cells with different NiO/YSZ ratios and different densities were also tested. Anode substrates with 50, 60, and 65% w/w NiO (standard is 57% w/w) were prepared and fired at different temperatures to obtain different cell densities. Cells with two different densities for each NiO content were prepared and tested with the exception of 65% w/w NiO at the higher density (as some cells had to be fired at too high a sintering temperature to give acceptable leak rates due to low shrinkage of the substrate). Figure 2-59, Figure 2-60, and Figure 2-61 show the Ni and YSZ volume percent and porosity for both oxidized and reduced forms vs. the measured cell density for 50, 60, and 65% w/w NiO anode substrates, respectively. Single-cell tests were conducted. The higher NiO content cells show some promise in terms of performance, however, the shrinkage is too low at standard cell firing temperatures so some formulation changes are required. Next, tests to increase cell shrinkage at lower firing temperatures allowing production of dense electrolytes will be conducted by blending different particle sizes of nickel oxide.

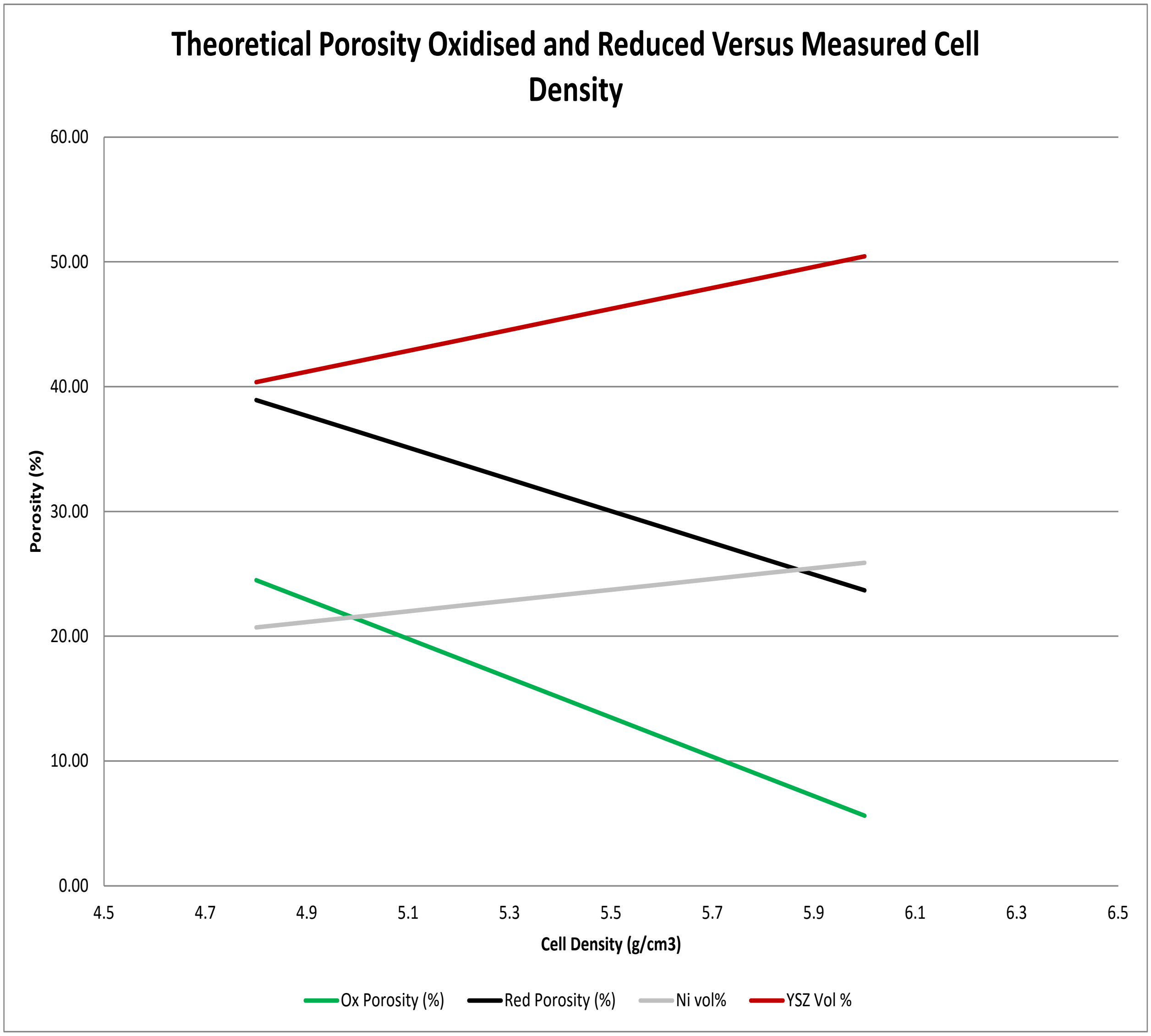

Figure 2-59. Theoretical Ni and YSZ Volume Percent, and porosity (oxidized and reduced) vs. Measured Cell Density for 50% w/w NiO Anode Substrate

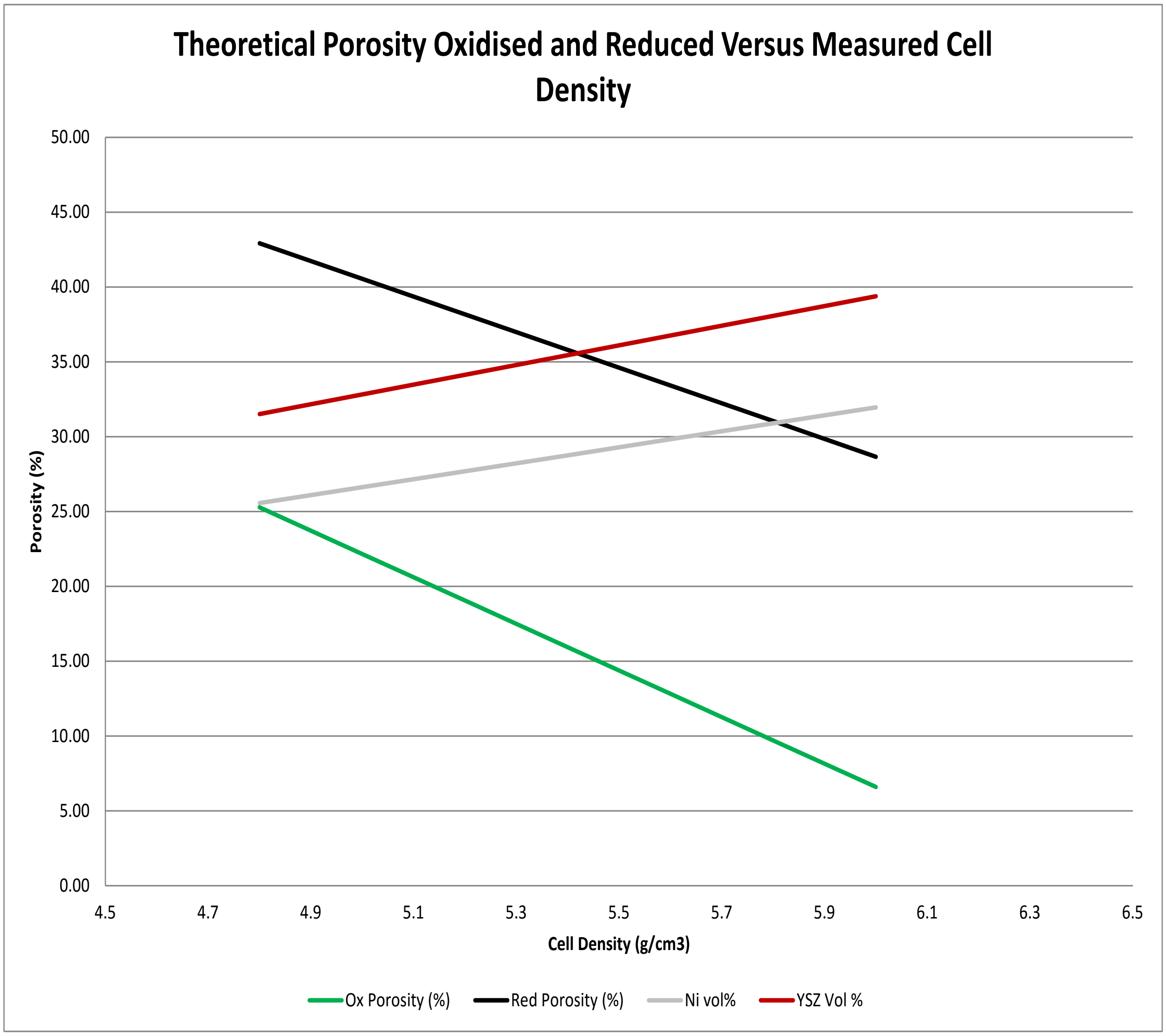

Figure 2-60. Theoretical Ni and YSZ Volume Percent, and Porosity (oxidized and reduced) vs. Measured Cell Density for 60% w/w NiO Anode Substrate

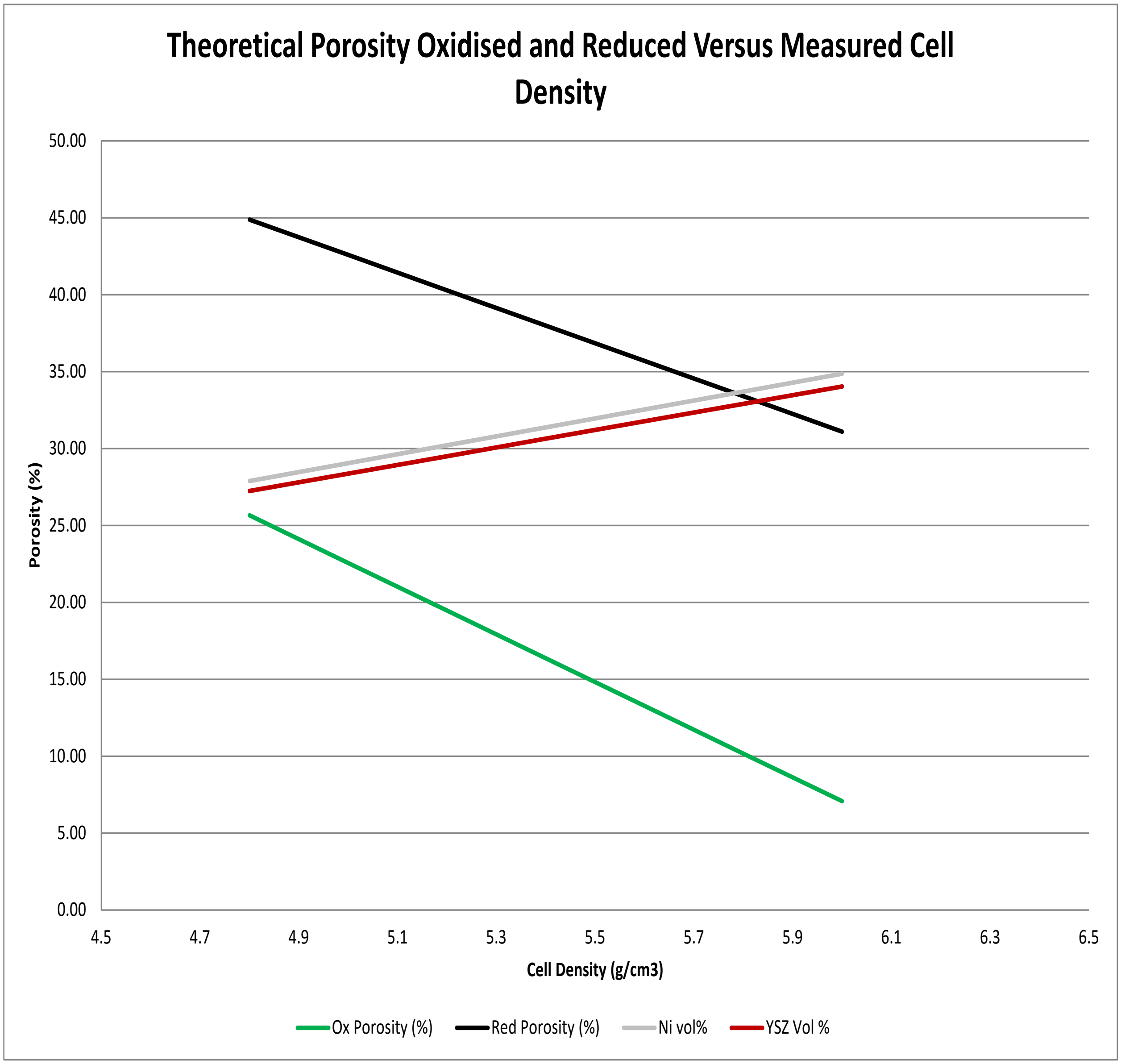

Figure 2-61. Theoretical Ni and YSZ Volume Percent, and Porosity (oxidized and reduced) vs. Measured Cell Density for 65% w/w NiO Anode Substrate

2.2. Stack Technology Development

Stack development focused on several key areas, including the following:

- Continued development and advancement of the baseline stack block design
- Delivery of SOFC stacks for 50 kW system test
- Continued development of the In-Cell Manifolding (ICM) stack block design

2.2.1. Stack Design & Modeling

VPS's baseline stack block design, as shown in Figure 2-62, consists of 96 TSC-3 cells that are 25.4 cm by 25.4 cm (each cell 0.06 cm thick) with an active area of 550 cm^2, which leads to a total of 52,800 cm^2 (or 5.28 m^2) of active area for each stack block.

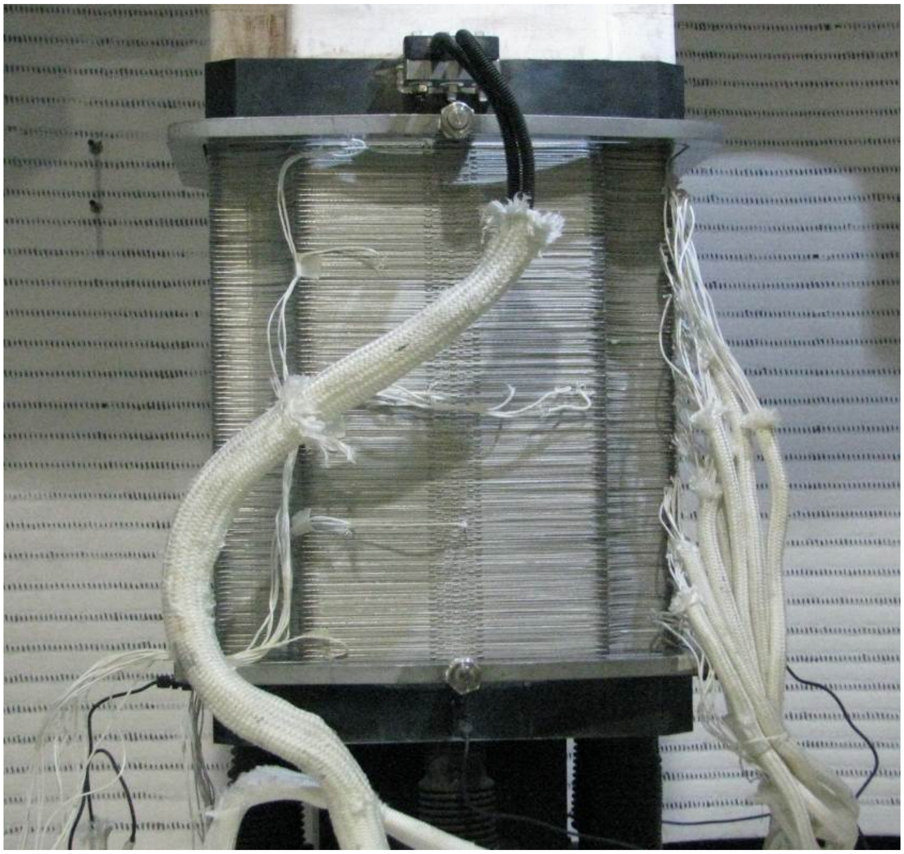

Figure 2-62. 96-Cell Baseline Stack Block

A stack is under development from a number of different perspectives including technology, engineering, and manufacturing (quality). From a reliability perspective and for obtaining technical and operational understanding, computational fluid dynamics (CFD) and finite element analysis (FEA) are important tools. This is especially true as the stack operates at 650 to 800°C and direct stack sensing is difficult. An important design objective is to make the operating conditions for each cell (within the stack) as uniform as possible. As for the stack, all cells are electrically in series, thus one weak performing or high degrading cell can affect the operation and life prospects for the entire stack. From a thermal-fluid flow or CFD perspective, some of the goals are to provide equal flow (mass flow) to each cell and have uniform temperature profile (T_{min}, T_{max}, and distribution) for the stack.

VPS completed CFD studies in a customized ANSYS FLUENT environment on the baseline stack as well as a newly developed advanced stack termed the In-Cell Manifold (ICM) stack.

Figure 2-63 shows a picture of a development stack (left) with the right view showing the cell design with the cathode area (black) and through cell fuel manifolding. The cell for early development had a 440 cm^2 active area.

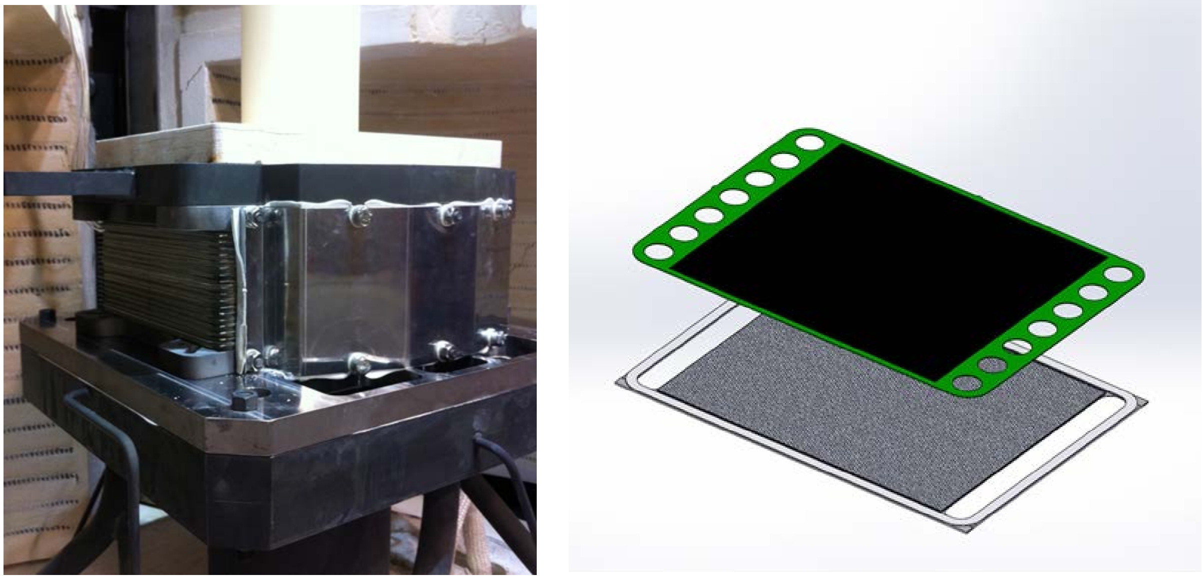

Figure 2-63. In-Cell Manifold Stack

80-cell ICM Stack Analysis: Detailed three-dimensional CFD modeling work was conducted on an 80-cell ICM stack in an effort to evaluate scalability to the tall stack level. The key objectives were to investigate key factors contributing to stack flow distribution and potential fine tuning of flow field components to improve stack operation. The modeling results indicated that variances of geometry, tolerance, hydraulic resistance of anode and cathode flow fields affect the stack flow distribution. Additionally, the stack thermal distribution (hot core, cold ends) also significantly affects the stack flow distribution.

As a potential solution for the stack thermal profile, a non-uniform anode flow field design (in the vertical z-direction) was proposed. Based on analysis using a uniform porous media model, a simplified fourth-order polynomial model was developed for the anode flow field height as a function of position where the flow fields at the cold ends were of a shorter height (higher pressure drop) and core cells were more uniform. It is difficult to implement such a solution - make different flow fields with high precision heights for a smooth distribution. VPS rolls down the flow fields from a 0.042” as-manufactured height to a 0.0355” final height.

As an alternate approach, fine tuning of the anode flow field in flow direction (flow path length) was also analyzed using a simplified polynomial model as shown in Figure 2-64. The flow field length (shown in mm) distribution for the 80 cells in the ICM stack is shown on the left side, whereas, the velocity (shown in m/s) distribution computed by CFD analysis is shown on the right side.

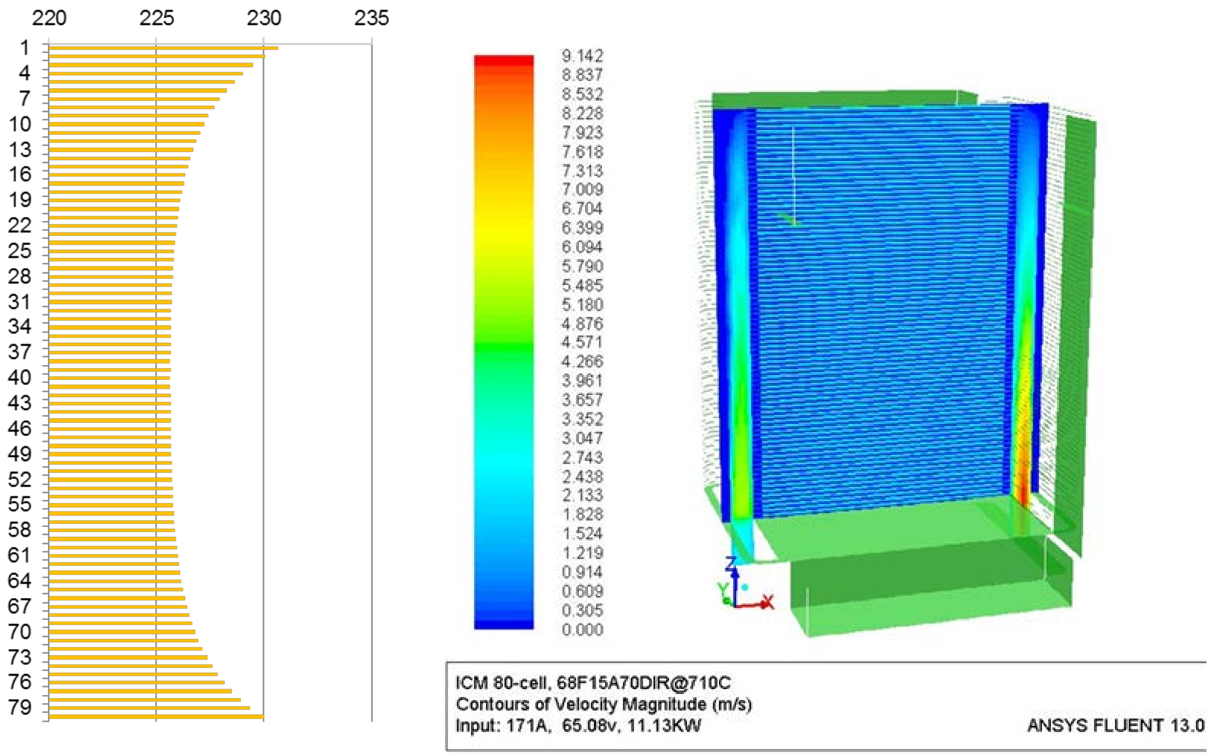

Figure 2-64. Conceptual Design of Non-Uniform Anode Flow Field Media Length for 80-Cell ICM Stack

Flow Field Gap Bypass Estimate: Analysis was also conducted in order to evaluate the fit as well as the gap created between the edge of the flow field and the flow shim assembly. A gap is needed to avoid interference between the two parts in stack assembly. The gap is in the direction of the reactant flow, and it was thought that the gap may play an important role in stack flow distribution and performance due to the fuel gas or air internal bypasses.

A detailed unit-cell assembly was fully modeled. Gap sensitivities (symmetrical on both sides) were explored ranging from 0 mm (no gap) to 4 mm per side for both the anode and cathode flow fields. An assumption for this level of analysis was made that dimensional tolerance is uniform and the anode flow fields are perfectly square.

Modeling results in general indicated that the large area stack needs to maintain a gap less than about 1.5 mm for both anode and cathode flow fields to maintain flow by-pass at reasonable levels (less than 5% bulk flow passing through the formed channel). The unit cell analysis for operation under conditions of 68% fuel utilization, 70% in-stack reforming, and 15% air utililzation at 200 A was performed. Cell temperature and pressure drop profiles predicted by the model are shown in Figure 2-65 and Figure 2-66, respectively.

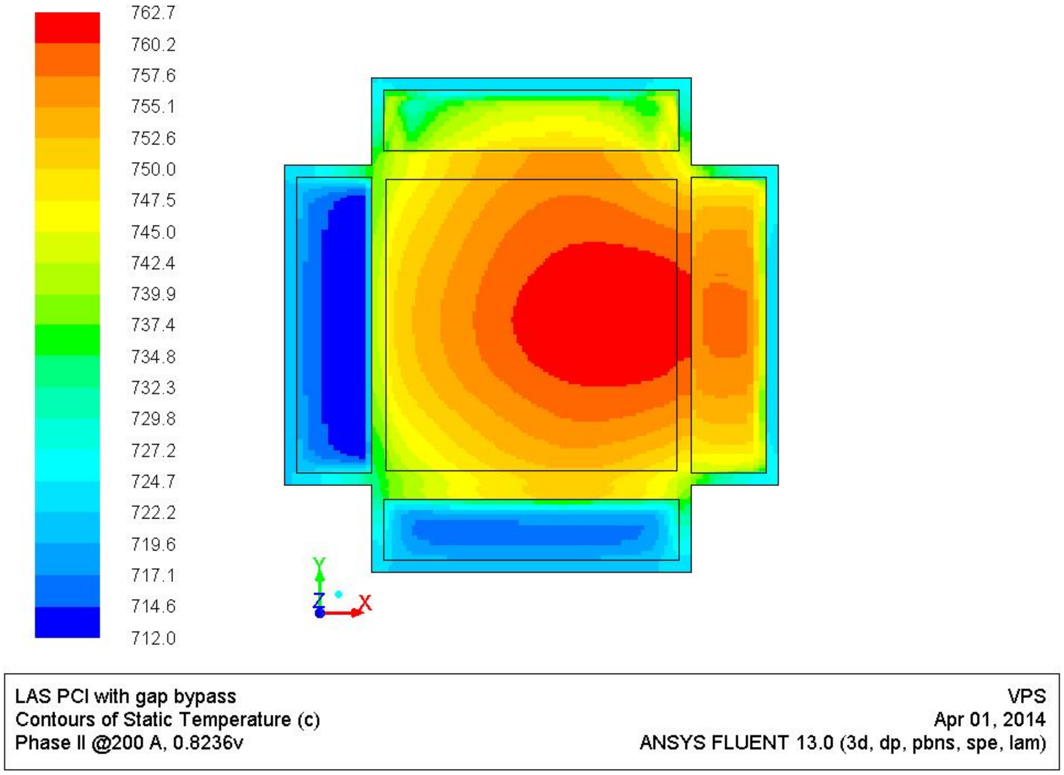

Figure 2-65. Large Area Stack Unit Cell Temperature Profile

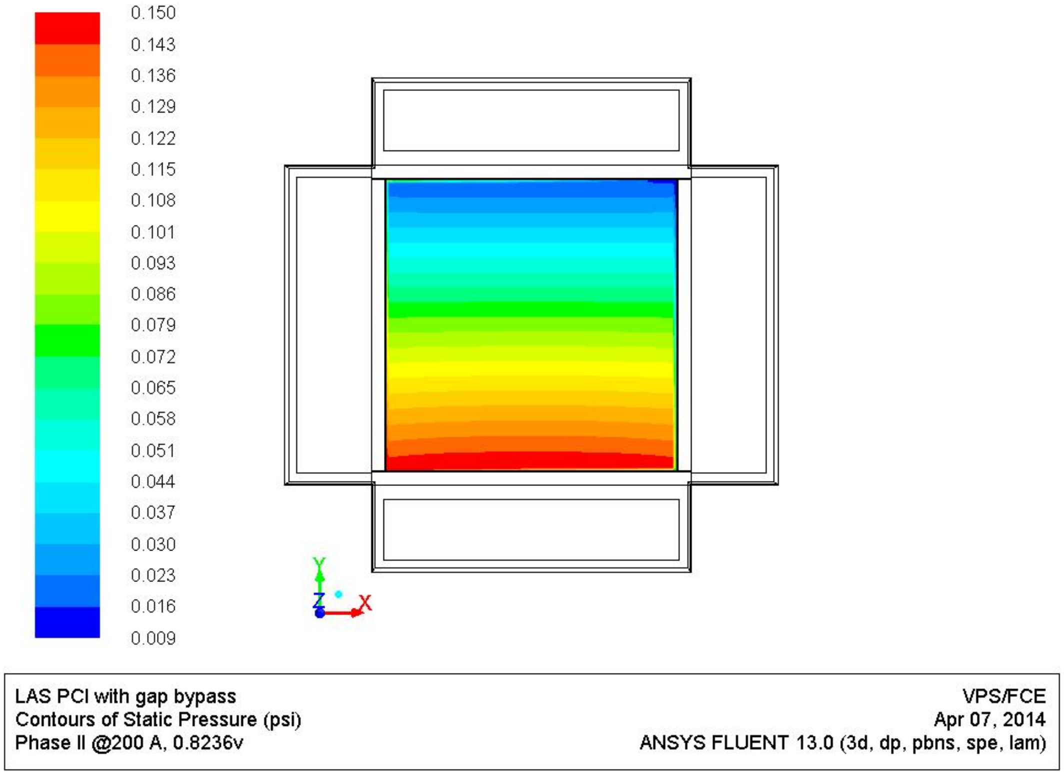

Figure 2-66. Large Area Stack Unit Cell Pressure Drop Profile

The CH_4 concentration profiles for the gap areas at inlet and exit (left side of cell anode) were analyzed.

The profiles of CO and H_2 concentration resulting after reforming reaction along the gap were also generated (assuming no fuel is leaking into cathode doman in the model). The H_2 concentration profile for the cell anode area is shown in Figure 2-67. The figure shows that the fuel penetrates into the anode layer (at the left corner).

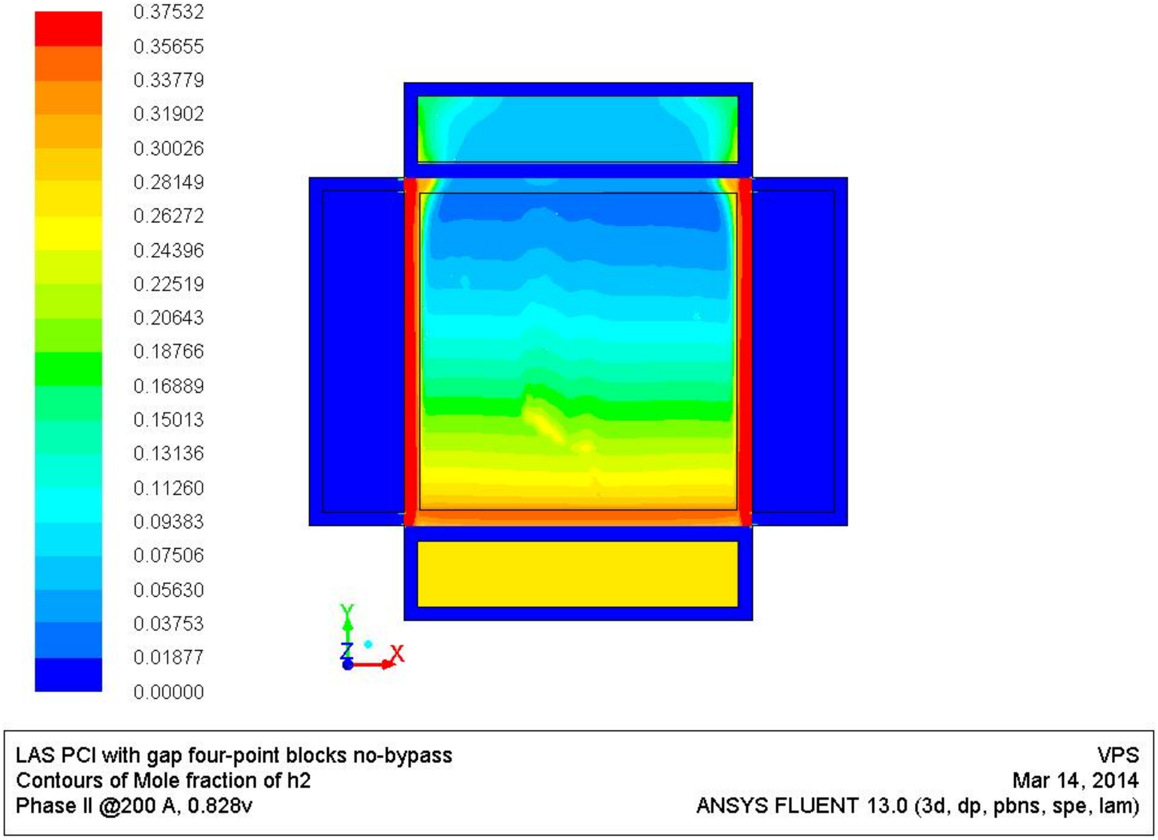

Figure 2-67. H_2 Profile on the Anode Layer

Also, the hydrogen concentration in the gap channel is actually higher than in the fuel in manifold (shown as bottom), as the methane contained in the fuel stream is steam reformed and converted to hydrogen and carbon monoxide. The Nernst potential and current density distributions for the cell are illustrated in Figure 2-68.

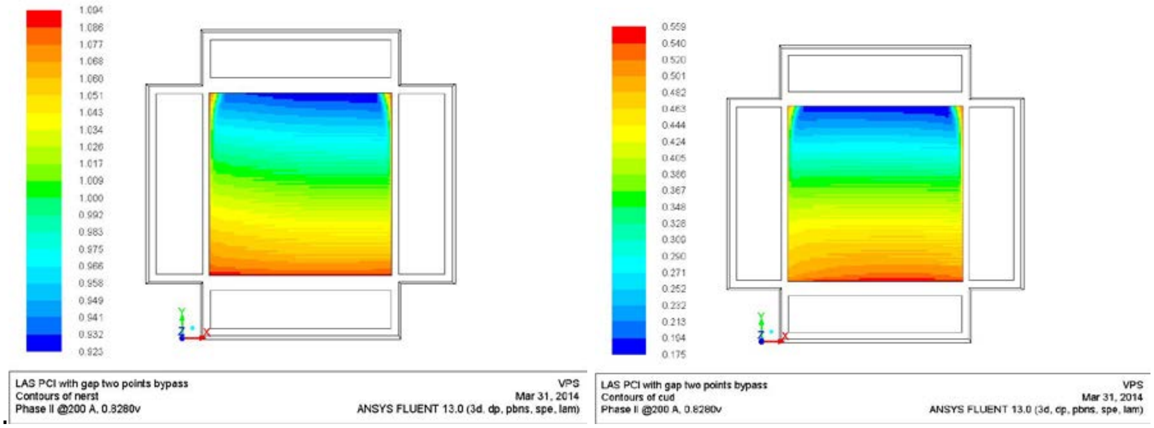

Figure 2-68. Nernst and Current Density Profiles

There are a number of technical recommendations under consideration to prevent by-pass. However, modeling analysis is still investigating the degree of participation of the reactant in the fuel cell reactions and the performance / cooling penalty of bypass.

Split Cathode Flow Media Design and Modeling

In order to reduce the in-cell hotspot temperature as well as the in-cell temperature gradient, a new concept using a split cathode contact media (like a split cathode flow media G2) has been proposed to allow more air flow through the hotspot region.

To characterize split G2 media hydraulic performance, the in-house pressure drop test jig as shown in Figure 2-69 was used to study the relationship between the pressure drop and the slot size of the split G2.

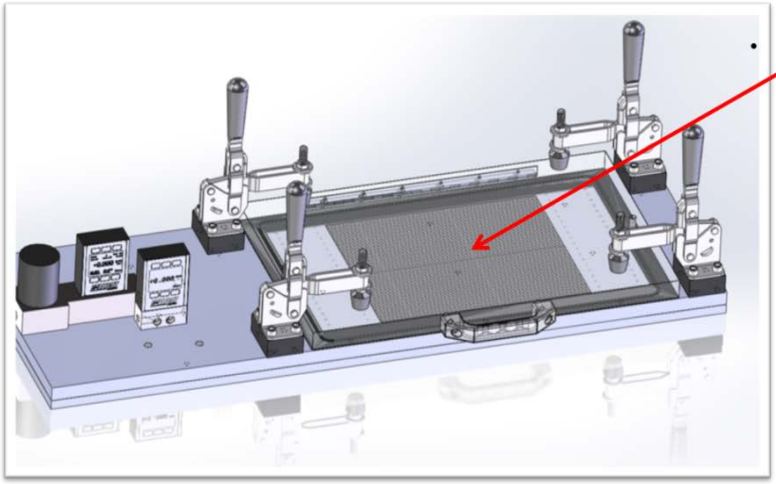

- Shear cut to produce open slot in the middle
  - 0 mm
  - 0.5 mm
  - 1.0 mm
  - 1.5 mm (dP ~ < -2%)
  - 2.0 mm
  - 2.5 mm
  - 3.0 mm (dP ~ -8%)
  - 3.5 mm
  - 4.0 mm
  - 4.5 mm
  - 5.0 mm (dP ~ -15%)

Figure 2-69. Pressure Drop Testing Jig for Cathode Flow Media G2 with a Split Slot in the Middle

All specimens of cathode flow media G2 were cut by using an in-house shear cutting machine. The precision of shear cutting process is relatively lower than that achievable by laser cutting. As the largest slot site is 5 mm, the shear cutting was considered to be acceptable. All design variations were tested, and the results of 12 cases are presented in Figure 2-70.

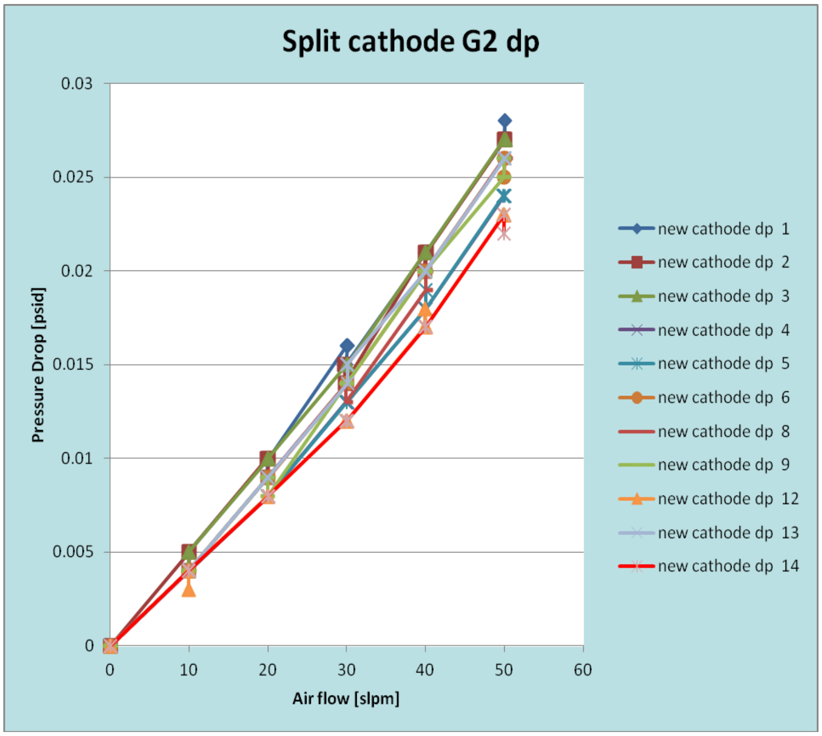

Fuel composition
(simulated at VPS)

14.51% CH_4
25.17% H_2
38.00% H_2O
22.32% N_2

Figure 2-70. Pressure Drop vs. Split Slot

The testing results indicated when the slot is less than 1 mm, the change in pressure drop is insignificant.

Meanwhile, a three-dimensional, fully coupled modeling case with 3 mm split cathode G2 as shown in Figure 2-71 was studied to investigate the impact on stack performance.

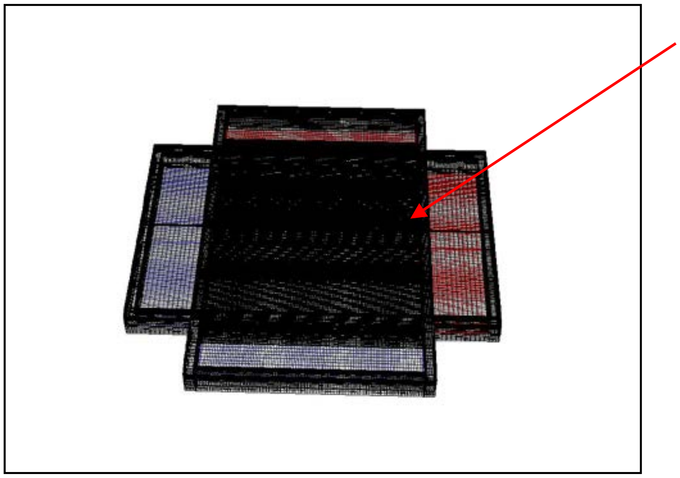

Open slot (3 mm) in the middle / central line
Of the cathode contact media G2

Figure 2-71. 3-D modeling of a repeat layer with split cathode G2.

The case comparison of original cathode G2 and split G2 by 3D modeling is made in Figure 2-72 and Figure 2-73.

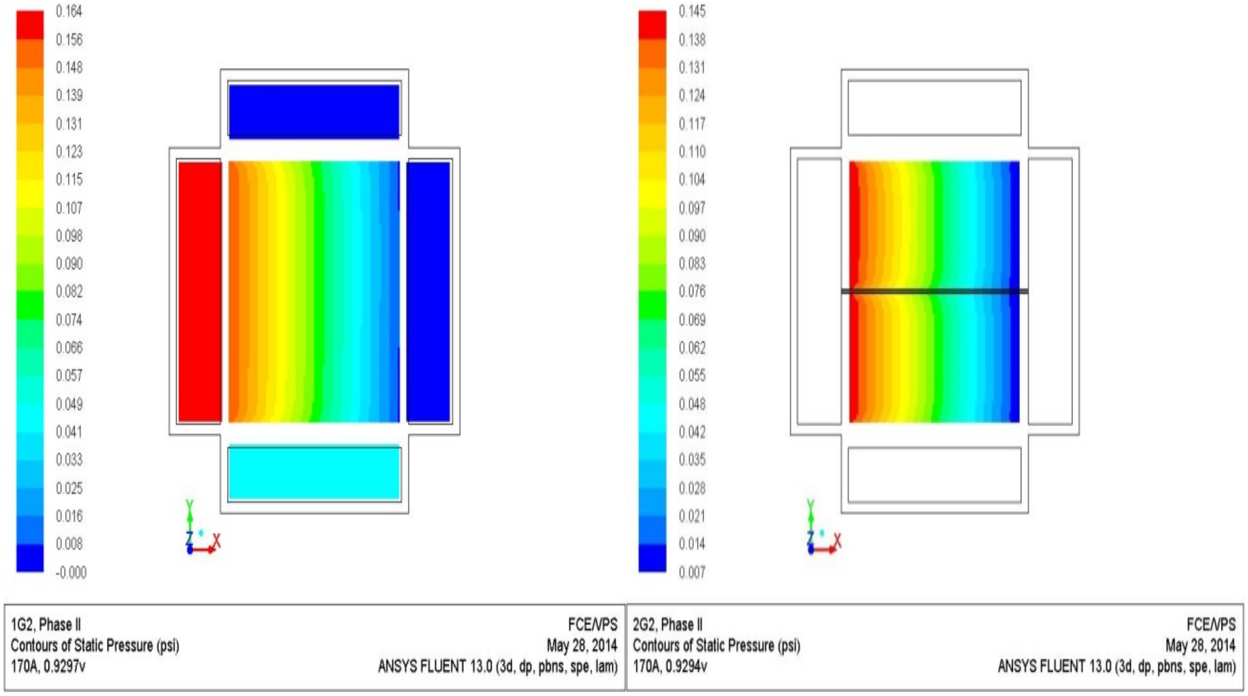

Figure 2-72. Split Cathode G2 (3 mm slot) has 6.8% Less Pressure Drop (right side)

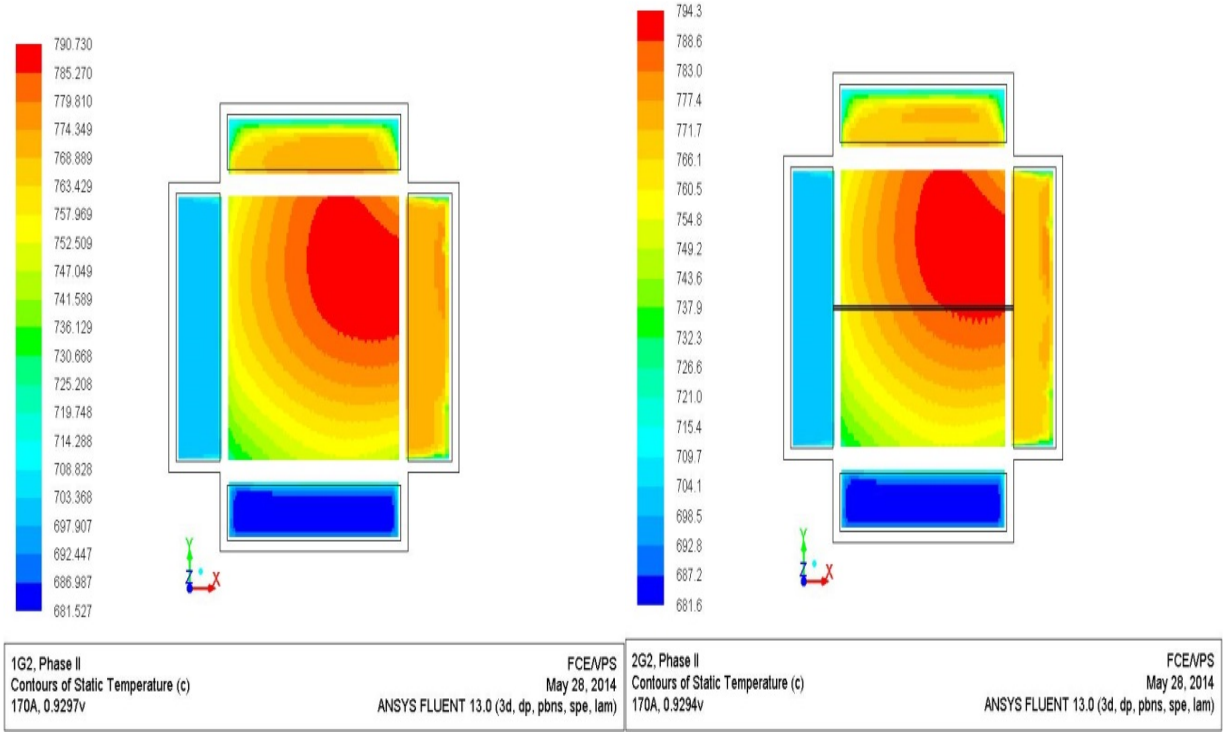

Figure 2-73. Split Cathode G2 (3 mm slot) has 3.5°C Temperature Increase in Hotspot (right side)

Modeling indicated that the split G2 may not be effective for hotspot cooling as the cell voltage decrease during operation will generate more heat. It explains why the hotspot temperature increases (not decreases as expected) 3.5°C for the 3 mm split G2 case.

Nickel Mesh Interconnection Layers: For the stack end plate design used in the 50 kW stack module, stack power take-off or current collection moves away from the exterior current collection ring which is more suitable for test stand setup compared to more compact through-end plate configuration. To perform the electrical connection of the stack end plate to the stack module end plate, two thin nickel mesh layers were sandwiched together and are in direct contact with the stack and stack module compression plates. As nickel will fully oxidize over time in a free oxygen environment, a fuel bypass and seals were added to this interconnection zone to maintain the nickel in a reduced state resulting in high electrical conductivity and low ohmic losses with a small amount of fuel bypass (around the stack) as this flow path is in parallel with the stack.

A computational fluid dynamics model was constructed to estimate the effective fuel bypass around each 120-cell stack. Two nickel mesh interconnection layers were used at each stack end as shown in Figure 2-74.

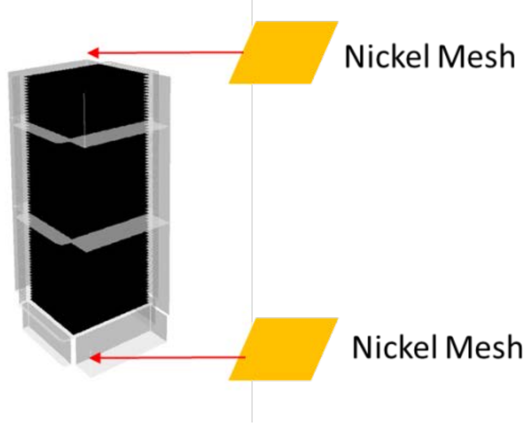

Figure 2-74. Nickel Mesh Interconnection Layers in a 120-Cell Stack

The nickel mesh hydraulic properties of viscous resistance and inertial resistance, applied as nickel mesh modeling parameters, were measured in the lab. The characteristics of nickel mesh hydraulic performance were measured using the in-house d*P* jig. This is the same jig that is used to measure the anode flow field pressure drop.

For testing, double layers of nickel mesh (0.0085" thickness each) were assembled in a cross orientation to avoid the nickel meshes nesting with each other. Testing was performed at ambient (room) temperature utilizing nitrogen gas. Meanwhile, a 3D CFD model was built to simulate the double-layer nickel mesh exposed to the same test conditions. The modeled nickel mesh was treated as a porous media with viscous resistance and inertial resistance parameters as input. The modelled pressure drop profile of the nickel mesh cross-section in the test jig was generated. Since there were no gaps between the nickel mesh side edges and jig side walls in the test setup, there was no gas bypass through the nickel mesh side edges. However, it was found that there was significant bypass along the top and bottom contact area between jig and nickel mesh layer. Therefore, a mechanical load of 60 kg was added to the top plate of the testing jig.

The experimental and CFD modeling results are compared in Figure 2-75 (Test 1 without load, Test 2 with load). Based on the relationship between the pressure drop and the flow rate, the nickel mesh viscous resistance parameter of Cx = 1.15 x 10^9 (1/m^2) and inertial resistance parameter of Cy = 0 (1/m) were estimated for the model.

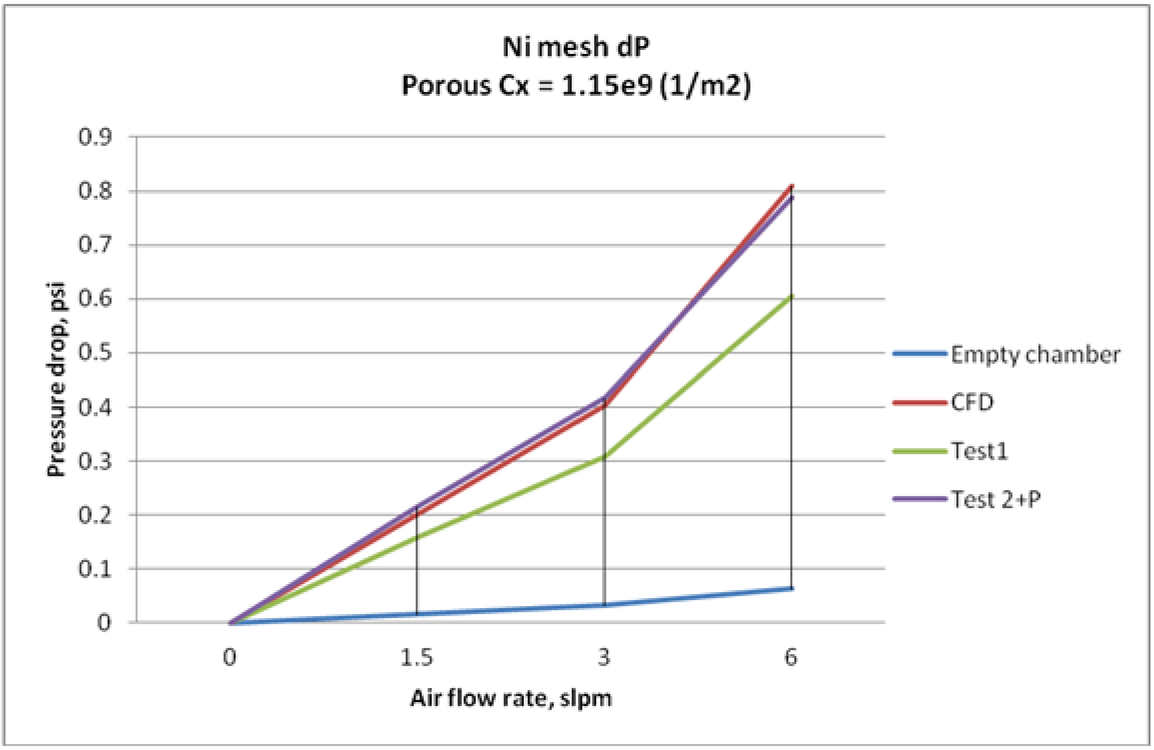

Figure 2-75. Modeled vs Measured Pressure Drop Profiles of Nickel Mesh

To estimate the fuel gas bypass through the nickel mesh layers, different fluid conditions were setup for a sensitivity analysis.

- Case 1: 120-cell stack, air, room temperature
- Case 2: 120-cell stack, SECA Phase 1 system condition, 200 Amps
- Case 3: 120-cell stack, SECA Phase 2 system condition, 200 Amps
- Pressure drop range: 0.05 to 0.5 psi (anode stream)

Gas compositions are listed in Table 2-4.

Table 2-4. Modeled Gas Compositions

	Ph1	Ph2
	61.5% uf	68.0% uf
Species	mol %	mol %
CH_4	0.049	0.126
H_2	0.586	0.218
H_2O	0.200	0.560
N_2	0.165	0.096
Total	1.0	1.0

A sensitivity analysis was performed to examine how the bypass fuel flow rate changes with pressure drop in the gas stream across the 120-cell stack. The CFD modeling results are presented in Figure 2-76. The results indicated that the overall gas bypass rate will be small-less than 0.3% under an extreme condition of 0.5 psid stack dP. This means that the effect of fuel bypass due to nickel mesh layer on the anode fuel utilization will be small. It is also interesting that cold nitrogen, hot Phase 1 fuel, and hot Phase 2 fuel have the similar bypass percentage versus pressure drop characteristics in the stack pressure drop range from 0.05 psi to 0.5 psi.

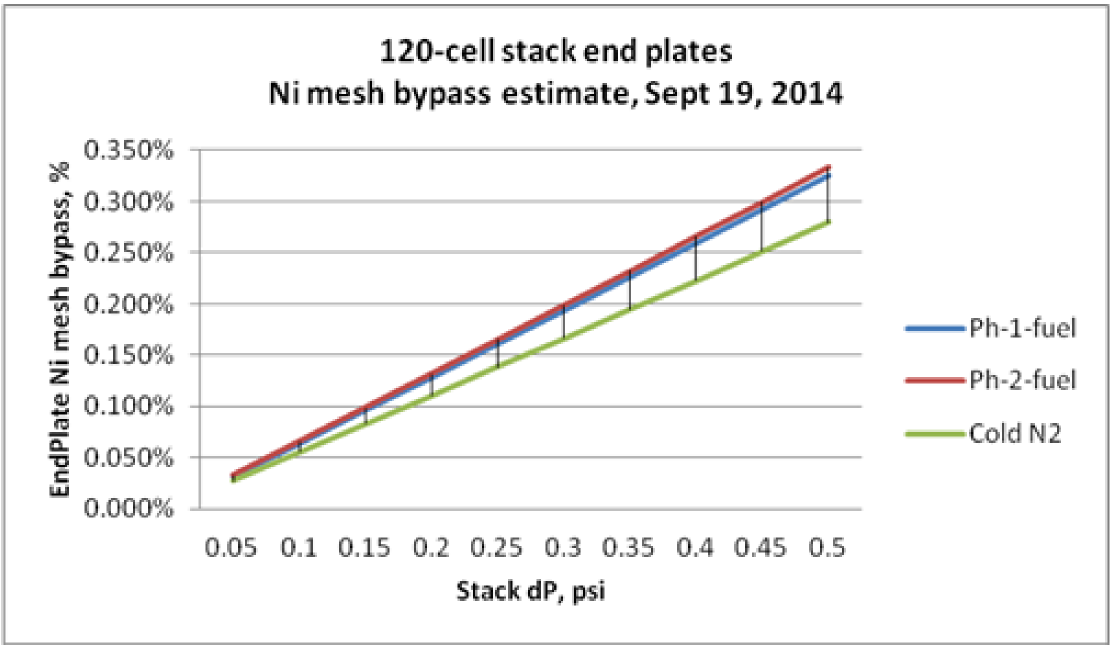

Figure 2-76. Gas Bypass Due to Nickel Mesh Interconnection Layers

For a 120-cell stack, the normal operating pressure drop in the anode fuel manifold is around 0.2 psi, so the bypass of fuel through the nickel mesh layer will be around the order of 0.12%, or 0.24% for two stack interconnections.

2.2.2. Stack Component Development

2.2.2.1. Development of Repeat Components

Advanced Seal Development

A new glass-ceramic from NYG, called NYG-353, was evaluated to see if it is feasible for use in stacks. Initially, this material was tested in a single-cell with the cathode jig machined so that a glass-ceramic seal could be used on both the cathode and anode side. The material has reasonably high boron content [4], so it was important to evaluate the effect on degradation rate. Cell test GLOB101881 with NYG-353 seals on both cathode and anode sides was conducted. Figure 2-77 shows the cell voltage vs time trend at 750°C, 0.5 A/cm^2, 50% Uf (hydrogen + 3% water), and 25% Uo (air). The degradation rate was 0.5% per 1000 hours over 12,701 hours operation including ten thermal cycles. Clearly the material did not cause an increase in degradation rate. The material can be used to seal the edge of the cell anode substrate (as a more stable alternative to the commercially available coating used in Thermicullite 866LS (discussed later in this section). By applying this material to standard Thermicullite 866, it may be possible to tailor compressibility and have a stable hybrid seal for the stack.

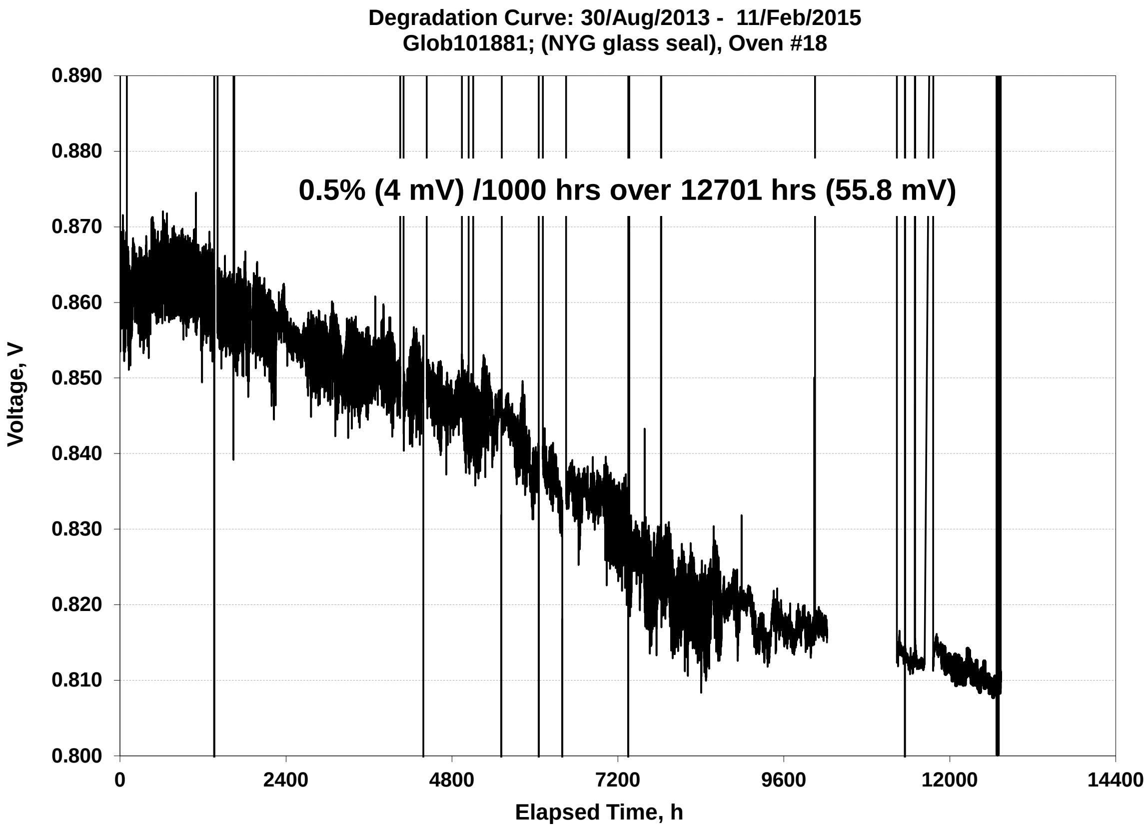

Figure 2-77. Performance Stability of Cell GLOB 101881 Containing NYG-353 Glass-ceramic Seals

Post-test analysis of the cell was carried out. SEM/EDX analysis was performed on five samples taken from fuel inlet (FI), fuel outlet (FO), air inlet (AI), air outlet (AO), and center of the cell active area. Figure 2-78 shows an SEM image of the sample taken from AO region and showing all functional cell layers. Figure 2-79 shows an SEM image of the cell to glass-ceramic seal interface at the anode substrate FO region. EDX analysis was performed at multiple locations for all five samples and there was no evidence of any significant reaction or diffusion of glass components into the cell materials which is consistent with the low degradation rate observed over 12,700-hour test period. This glass-ceramic seal is suitable for long-term use in anode-supported SOFC stacks so long as the operation of the stack does not lead to stresses that exceed the mechanical strength of the seal or cell components.

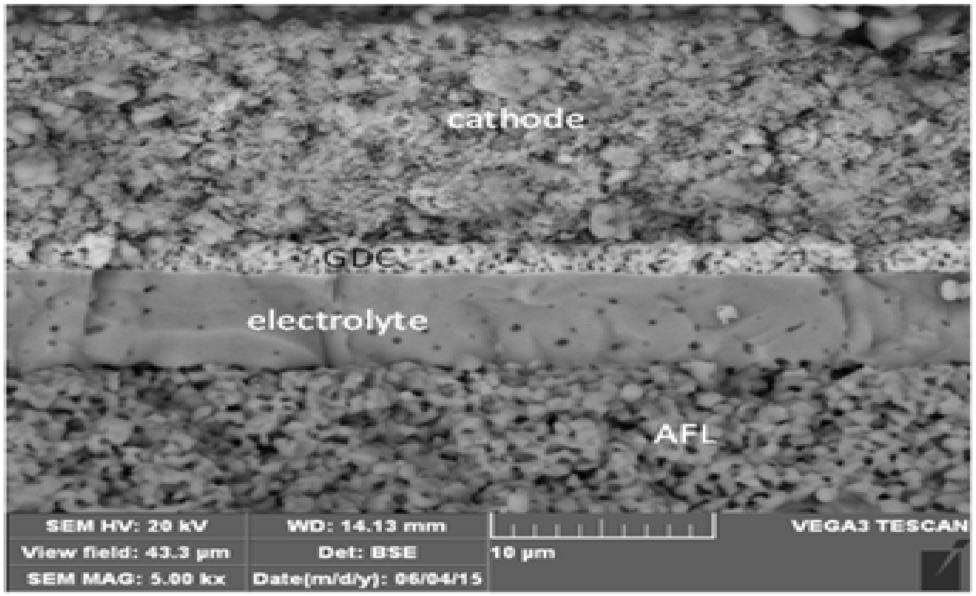

Figure 2-78. SEM Image of Sample Taken from AO Region of Cell GLOB 101881

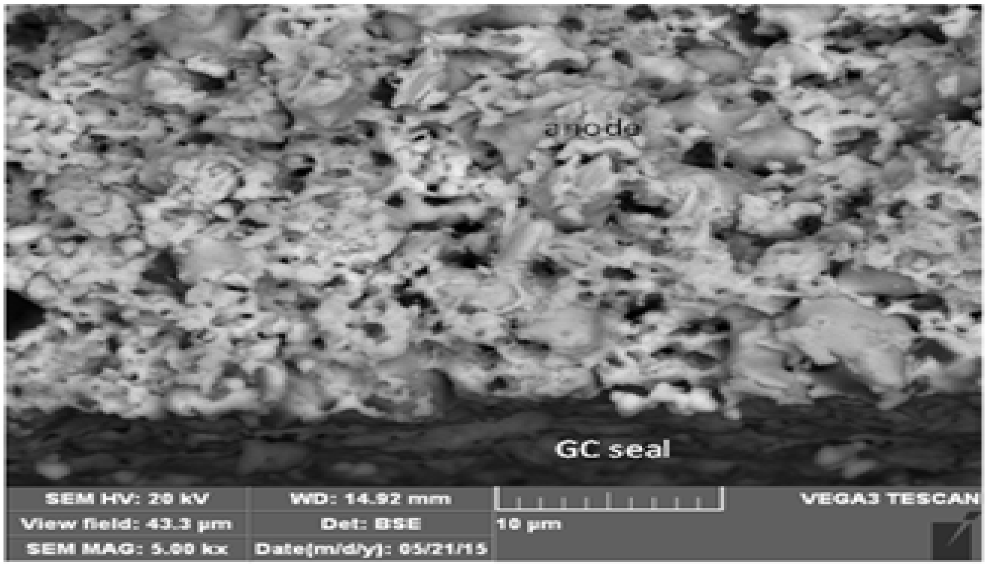

Figure 2-79. SEM Image of Anode to Glass Seal Interface at FO Region of Cell GLOB 101881

Flexitallic provided Thermicullite 866 LS seal material for testing. This material comprises chemically and thermally exfoliated vermiculite seal with a low viscosity glass coating on both surfaces. Figure 2-80 shows the leak rate comparison of two Flexitallic seals compared with two standard seals at 750°C. The test gas in each case was air at 0.5 psi and the initial and final thickness measurements of the seals are noted in the figures. Compressibility appears similar at these thicknesses even with the relatively low compressive loads used. Post-test analysis showed that the glass layer had bonded the seal to both of the 430SS test jig plates and the seal broke within the Thermicullite as desired (meaning interfacial leakage is eliminated).

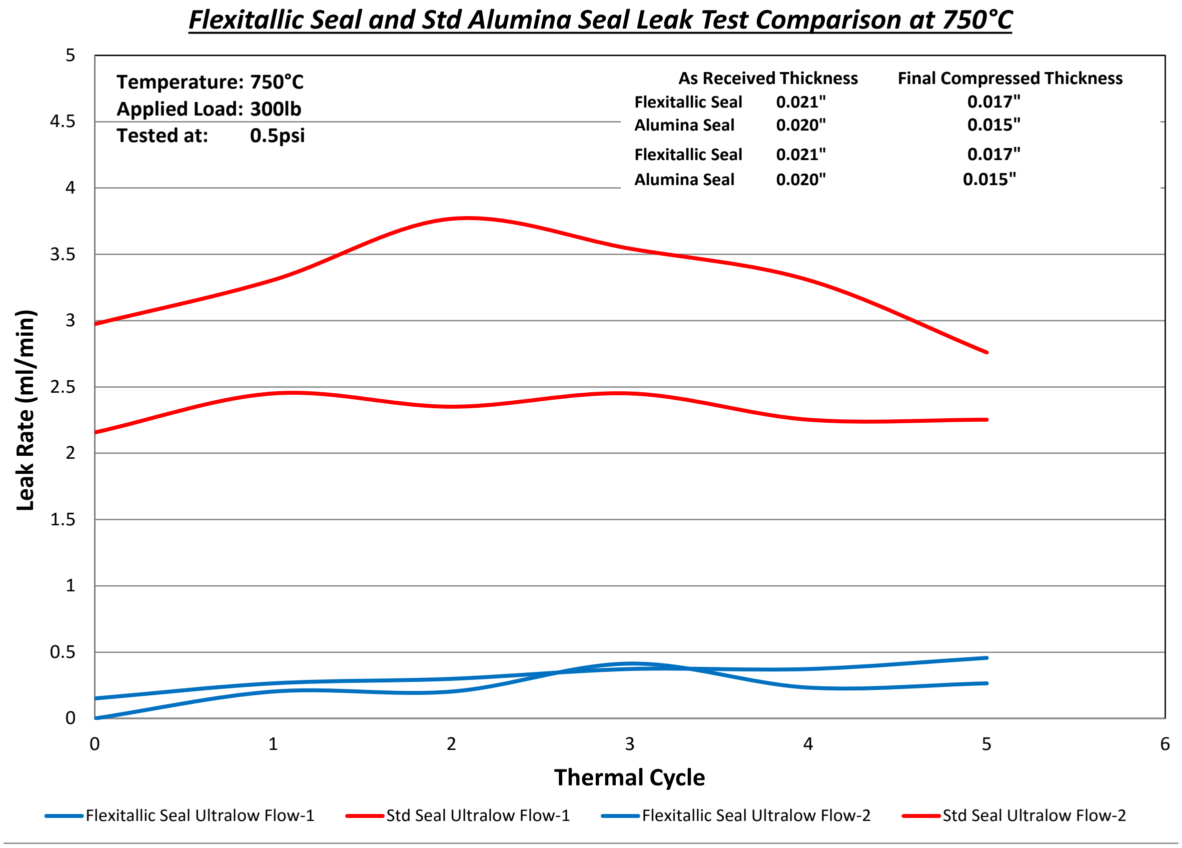

Figure 2-80. Leak Rate at 750°C and 0.5 psi Air of Thermicullite 866 LS (blue) and Standard Seals (red)

Figure 2-81 shows the leak test plates with seal bonded to both sides by the glass coating. SEM of the cross-section of the seal broken away showed that no glass was present (it remained bonded to the plates and the seal fractured within the Thermicullite at both interfaces).

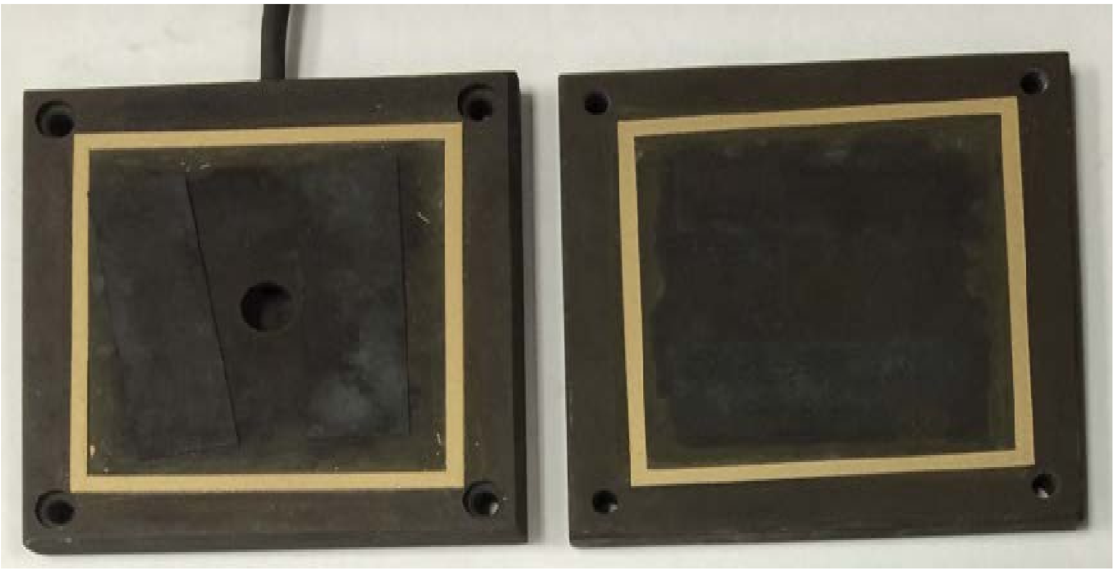

Figure 2-81. Post-Test Leak Test Plates with Thermicullite Seal Bonded to Both Sides by the Glass Coating

For the purposes of stack testing it was necessary to investigate compressibility with thicker seals. Since the sheets were only available in one thickness, it was decided to stack them to increase thickness. Figure 2-82 shows leak rate vs. initial seal thickness at 750°C and room temperature for one seal layer (~0.020” height), two seal layers (~0.040”), three seal layers (~0.060”), and four seal layers (~0.080”). Upon initial testing at 750°C, the leak rate hardly changed with seal thickness which is very promising. However, when cooled to room temperature and leak tested again, the four-layer seal had a significantly higher leak rate suggesting the thicker seals failed on thermal cycling.

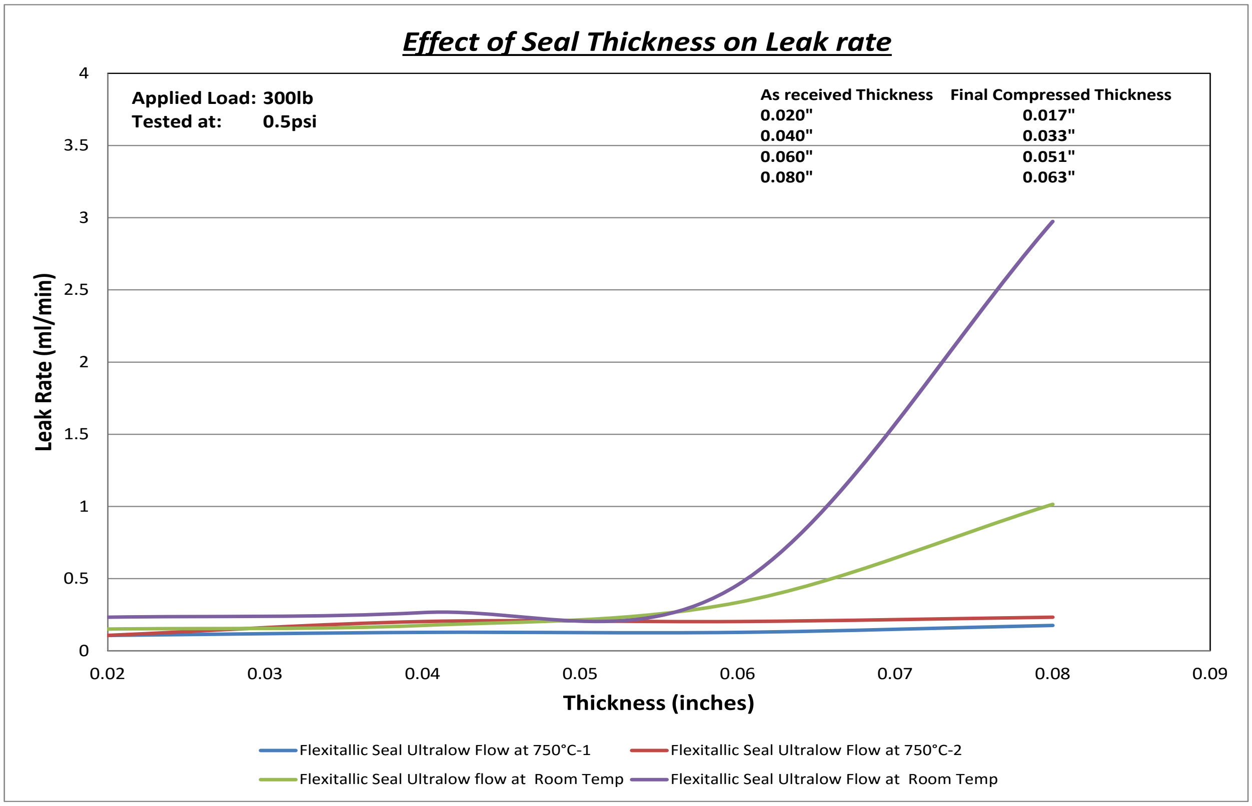

Figure 2-82. Effect of Seal Thickness on Leak Rate for Flexitallic Thermicullite 866 LS Seals

Figure 2-83 shows an SEM of the cross-section of the four-seal stack after leak testing. The glass had bonded the seals to the plate at the interfaces for the main part and the seals were well bonded together by the glass coating. However, the high leak rate suggests the seals failed on thermal cycling.

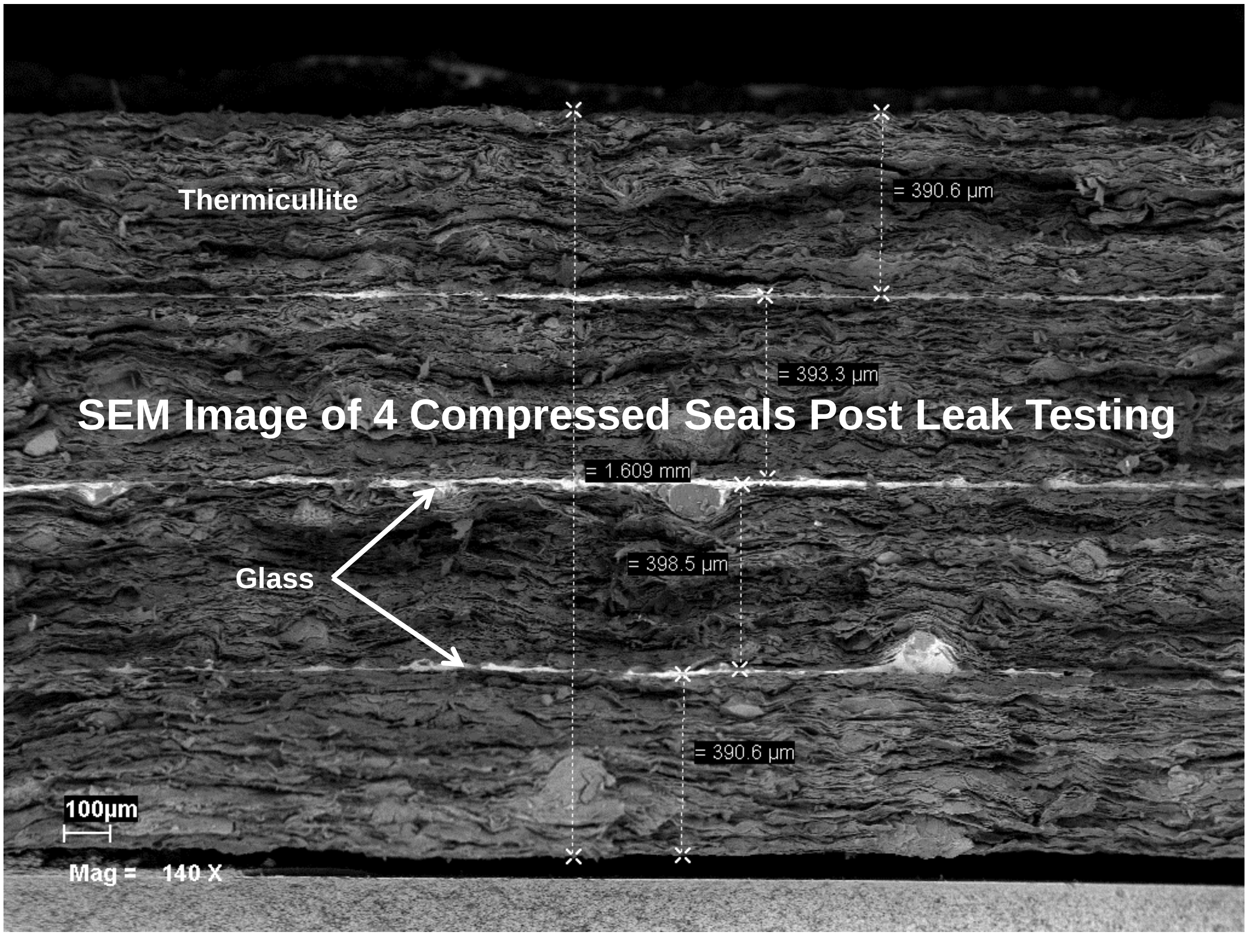

Figure 2-83. SEM Cross-Section of Thermicullite Seal Broken Away from the Jigs

Following this testing, a single-cell test was conducted with a Thermicullite 866LS seal on the anode side. Figure 2-84 shows performance characteristic curve comparisons at 750°C up to 0.74 A/cm^2, including three thermal cycles. The cell voltage was high at 0.74 A/cm^2, showing that the seal compressed sufficiently in-situ to make good contact in the active area. Almost no change in cell voltage over three thermal cycles showed no cycling issues with the seal material. In addition, the test was run up to 90% Uf without incident, indicating reasonable sealing. However, post-test analysis revealed that the seal failed within the glass layer in the fuel environment, which was not seen with leak testing in the air environment. More testing was required to see if it was possible to use a 0.080” or thicker seal as would be preferred for the large area stacks and to resolve why the glass seal coating failed in the fuel environment. It was suggested to coat with a different glass that has been investigated in-house (NYG-353) that might have improved stability.

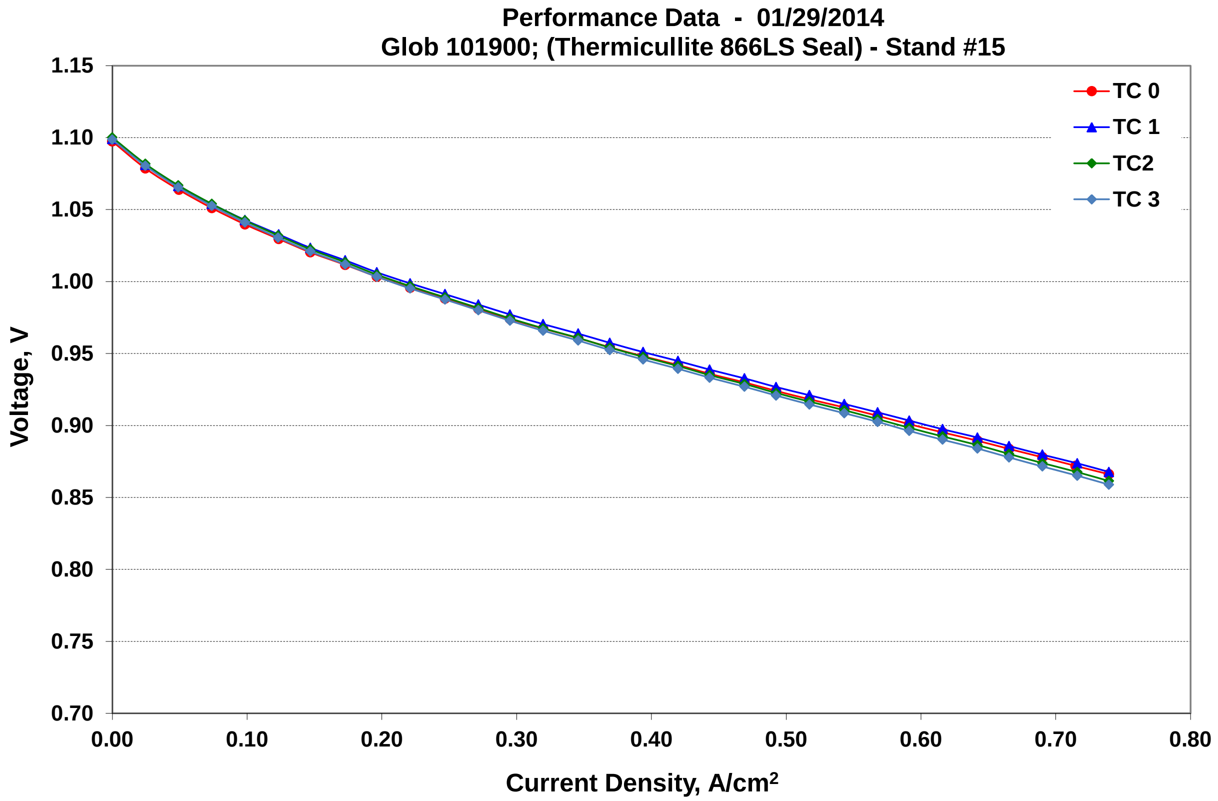

Figure 2-84. Power Curve Comparison of Cell with Thermicullite 866LS Seal on Anode

Samples of 0.7 mm thermicullite were coated by screen printing with NYG-353 glass powder paste and leak tested at room temperature and 0.5 psi air after a glass heat treatment. The leak rate at this point was below detection limit (the same as one of the thermicullite 866 LS seals reported above). During thermal cycling a furnace failure caused damage to the test and no further leak rate data were obtained. Figure 2-85 shows the seals after leak testing with seal material clearly bonded to both stainless steel jig surfaces and fracture occurring within the thermicullite 866 layer as is desirable (leaving the interfaces in-tact). This indicated that the combination of NYG-353 and thermicullite 866 was capable of lowering leak rate in a similar manner to thermicullite 866LS reported above. This glass ceramic has been shown to be stable in SOFC operating conditions. To proceed with this configuration it was decided to test a six-cell stack with 121 cm^2 active area cells. Thermicullite 866 sheets were punched to the seal dimensions for a PCI stack. Dispensing trials were conducted to apply NYG-353 to both surfaces to make a composite seal.

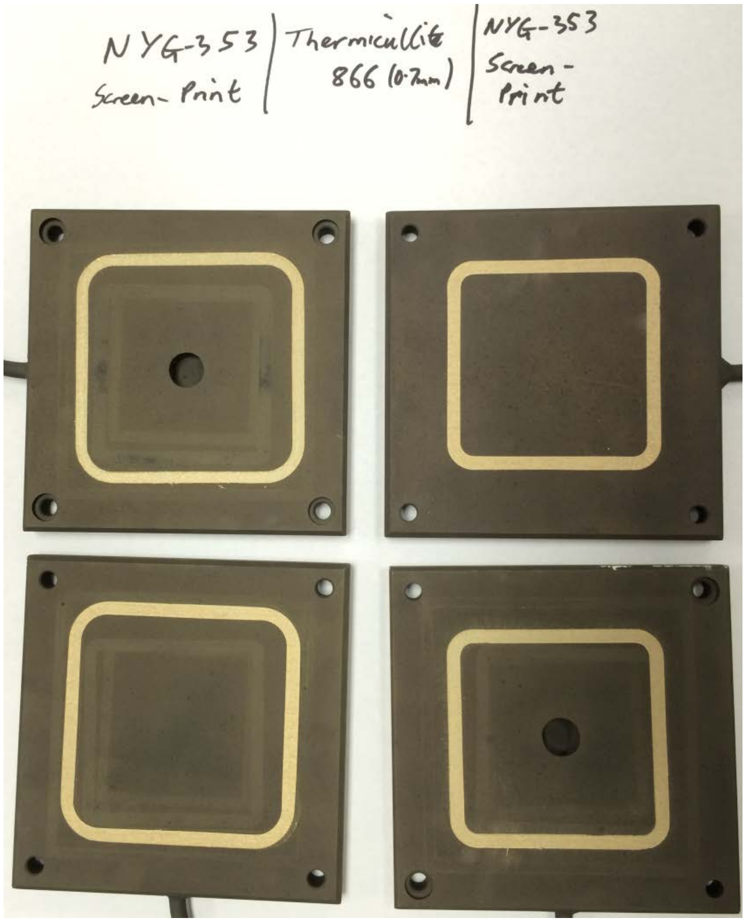

Figure 2-85. NYG-353 | Thermicullite 866 | NYG-353 Seals after Leak Testing

Figure 2-86 shows samples of initial dispensing trials obtained with different nozzle sizes and dispensing rates. These trials were repeated for each of four different formulations developed to provide a suitable dispensable paste. Figure 2-87 shows dispensing of seals on cardboard sheets (cut into the shape of stack seals) while developing the dispensing program to deposit seals onto the final Thermicullite part for use as a hybrid stack seal. Figure 2-88 shows the first attempt at dispensing onto the final Thermicullite seals to confirm that the bond and drying conditions of the dispensed glass seal are suitable.

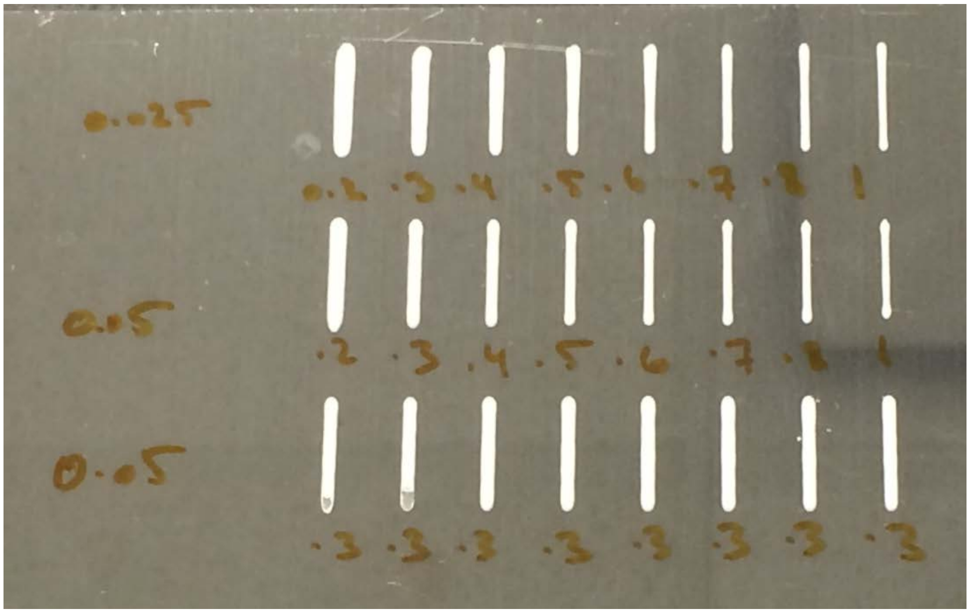

Figure 2-86. Dispensing Trials with Different Dispense Rates and Nozzle Sizes for Hybrid Seal Fabrication

Figure 2-87. Dispensing Trials on Cardboard Blanks to Define the Automated Program

Figure 2-88. Dispensing Trials on Thermicullite Seal to Verify the Process

The dispensing trials to apply NYG-353 to both surfaces to make a composite seal were completed. The final parts were dispensed with the optimized program and formulation, and three mock stacks were built. The first stack used the hybrid seal between current collector and compression plates since these were made of different materials (430SS and Inconnel 600) and therefore had different coefficients of thermal expansion (CTE). A modified heat up was used to incorporate tape-cast alumina seals in some parts of the test stand and because of the glass seal heat-treatment profile required to form the optimum ceramic phases in the crystalline glass-ceramic. The assembly was then leak tested. The leak rate was high, and testing with snoop revealed that the majority of leakage was from the corners. Post-test examination showed that the seals were cracked in the corners. As shown in Figure 2-89, the interface between glass and Thermiculite was intact in all cases. But, as shown in Figure 2-90, the bulk Thermiculite seal itself had cracked in almost all corners for these larger seals.

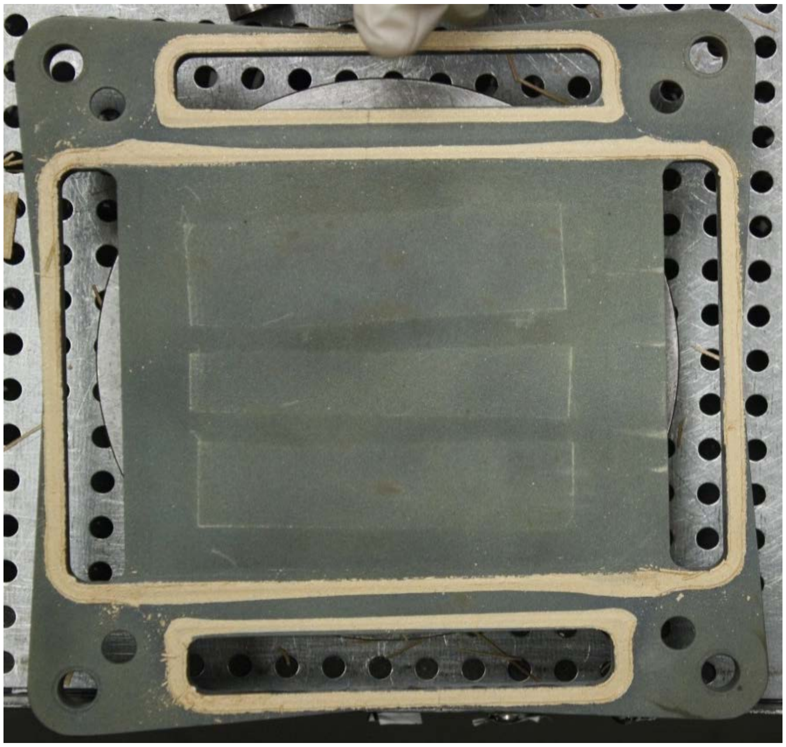

Figure 2-89. Compression Plate after Thermiculite Seal Removed Showing Good Interfacial Bonding of the Glass Seal to the Inconnel 600 Compression Plate

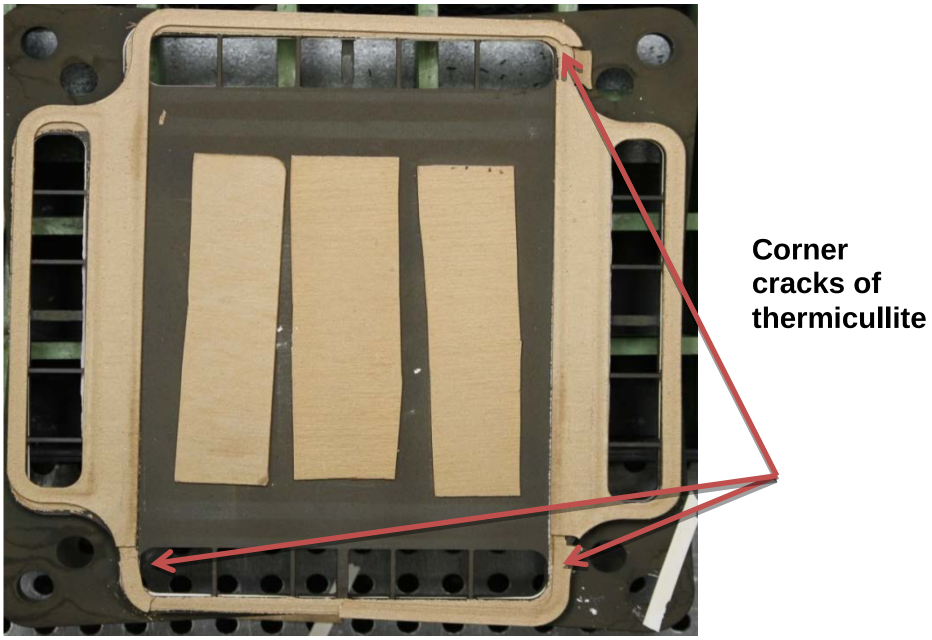

Corner cracks of thermicullite

Figure 2-90. Thermiculite Seal on Current Collector Showing Significant Cracking (especially at corners) of the Thermiculite Seal

The trial was repeated using only 430SS current collector parts so that there was no mismatch in CTE and the same result was found. Leak rate was high and mostly from the corners and post-test examination again showed good interfacial contact with the bulk Thermiculite seal fractured in the corners. It should be noted that after the initial heat treatment, the Thermiculite seal is very brittle in contrast to the initial somewhat flexible nature of the material.

These results showed a fundamental problem with this approach. Using glass-ceramic seals alone can result in a hermetic seal; however, they are brittle and prone to failure. A hybrid compression seal with the interfaces bonded using glass-ceramic can overcome these failings, however, Thermiculite is also very brittle after a single thermal cycle leading to failure of the seal when using large parts. Tape-cast alumina seals in place of the Thermiculite can be evaluated since they are more resilient after thermal cycling.

2.2.2.2. Development of Non-Repeat Components

Existing Non-Repeat PCI and ICM Stack Component Development

Efforts to improve documentation and communication related to non-repeat components were carried out. As part of a broader activity to improve quality and documentation for the entire large area stack assembly process, drawings for stack assembly components were reviewed and updated. Stack assembly procedures are in the process of being documented and reviewed. Further coordination between the VPS and FCE teams is anticipated to ensure alignment of non-repeat components within multi-stack module designs.

Design and Development of Chromium Filter in Stack

An on-cell Cr-filter had demonstrated technical success in single cell testing as well as large area stack testing with a wet cathode gas environment. As an extension of this technology, a stack chromium filter was under development to remove gas-phase chromium species from the cathode air flowing into stacks. The concept was to use the same filter materials that had been successfully utilized within the stack.

Samples of Cr-filter materials were received and tested for stability in oven bench tests. A suitable stable material was selected which survived thermal cycle testing. A filter cartridge design was pursued to create a prototype Cr filter that can be installed in the existing 16-cell (large area) stack test stands #25 and 26 that have the cathode gas humidity test capability.

Calculations showed that due to the small quantity of Cr and high take-up ability of the materials, design consideration should not be reactant mass but rather space velocities and ultra-low residence times. Key design considerations included:

- Use existing manifold base and change inlet tubing
- Container must be able to be removed to change out support media
- Should be easy to disassemble to inspect support media
- Container must have a volume of at least 4.5 L of support media
- Investigate the best metallic material and coating for the lining of the container
- Low pressure drop

A conceptual design of the filter is shown in Figure 2-91.

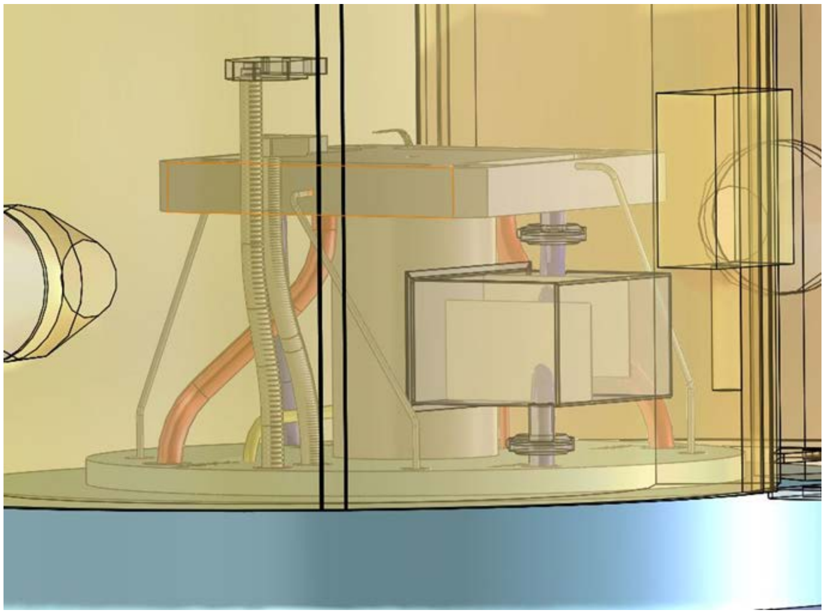

Figure 2-91. Conceptual Design of Cr-filter Box for Stack Testing

Further discussions and testing revealed a concern that the Cr-getter material will break down into fine powder and may clog downstream filter or stack. This can result in a high pressure drop and prevent adequate flow to the stack. Before fabrication for full integration in the test stand, it was decided to confirm this issue by testing the material itself.

The test plan included thermal cycling the material ten times from 750°C to 150°C with 15 SLPM air flow (10 mol% moisture added by passing through a water bath). The test setup was a simple design as shown in Figure 2-92. It consisted of a 1.5” diameter by 12” long Inconel 600 tube that was welded to plate with a machined through hole. The tube was first filled with chrome chips up to 3/8” depth and then topped off with Cr-getter material.

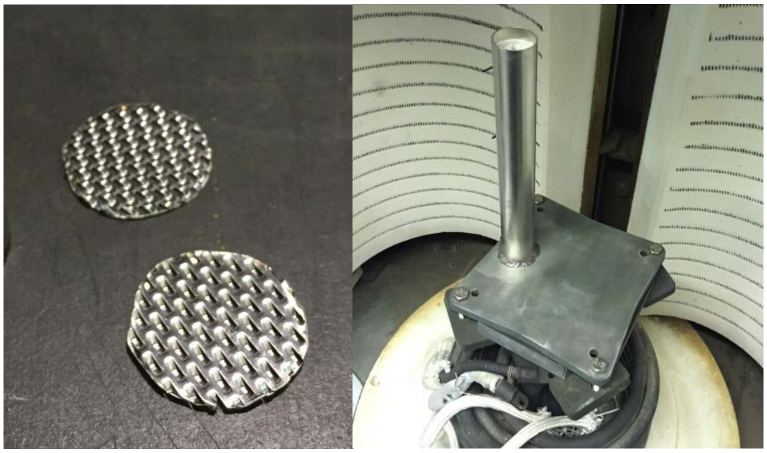

Figure 2-92. Proof of Concept Cr-Getter Filter Test Apparatus

Flow media (corrugated) were placed on both sides to separate the chrome chips from the Cr getter chips and to keep the chrome chips from falling out through the hole in the plate. To prevent flow media from reacting with the Cr getter material, 1/16” thick alumina felt was placed on top. In addition, felt lined the complete tube section that was filled with the Cr getter material. This test jig was then bolted on to the stack manifold with tape cast seals.

Two tests were completed. The first test was very aggressive. Humidity was introduced into the air stream during the initial heat up. The Cr getter chips absorbed water in as they were heated to 750°C. The Cr getter was reduced to powder and scattered and deposited throughout the furnace enclosure.

The second test included a hold at 110°C (during initial heat up) for four hours to allow the Cr-getter material to dry, then heat up to 750°C. This test also included downstream getter filter/containment with a piece of expanded metal (exmet) loosely spot welded on the top of the tube. Once at 750°C, humidity was introduced and the test proceeded to complete ten thermal cycles. The final result with this less aggressive test was similar to the first test where the Cr getter chips also turned to powder and deposited in the furnace. Approximately 30% of the openings of the exmet were blocked with the powder. The material breakdown is a concern as this powder can clog or block any type of filter. If the filter did fail, it would allow powder to flow through the stack and potentially block channels in the stack cathode flow field or cathode electrodes. Removal of the material from the tube proved to be very difficult and required a chisel and hammer (Figure 2-93).

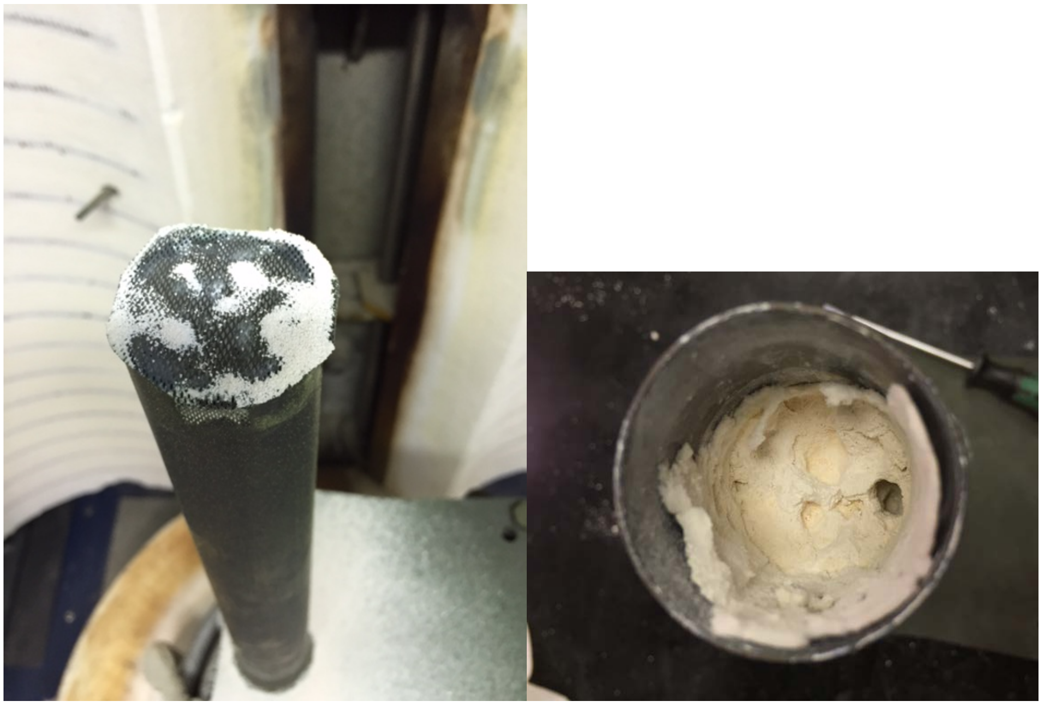

Figure 2-93. Proof of Concept Cr-Getter Filter Test #2 – Post-Test

The Cr getter technology developed and implemented in the stack had been so effective at lowering degradation rate that it was decided to try and implement a Cr filter to be placed in front of the cathode inlet manifold in the hot module using similar technology. Although calcium-based compounds are not suitable to be applied on cell due to materials compatibility issues, they are effective Cr getter materials. Calcium carbonate, in the form of limestone, is available in relatively high purity (>99%) at very low cost. Initial trials centered around this material configured as a packed column type filter. Tests were performed to ensure that the material stays intact and absorbs Cr, in a tube furnace over Cr pieces for 1000 hours at 800°C (using dry air as the humidified air test facility was already in use).

Figure 2-94 shows limestone pieces (marble chips), calcium carbonate powder, and Cr-getter material Gb powder after 1000 hours of testing in dry air at 800°C, showing clear discoloration as they reacted with Cr species (confirmed later by SEM/EDX analysis). The materials were tested in presence of Cr pieces to provide exposure to Cr species. Following this, marble chips packed in a tube were tested using 15 slpm nitrogen containing 10% water vapor and thermal cycled ten times between 150 and 750°C to check the integrity of the limestone. It was found that the limestone breaks down under these conditions to powder. This will significantly increase pressure drop through the filter. The test was repeated with carefully dried limestone, and although a little better than the undried limestone, there was some breakdown to powder as well as some fusing of the material. XRD analysis showed calcium hydroxide was formed and thermodynamic calculations suggested calcium carbonate will be converted to calcium oxide on heating, then to calcium hydroxide on cooling with humidity present. Although a low cost option, this material is not suitable for this type of packed column filter where consistent pressure drop is required.

Figure 2-94. Cr Getter Materials Tested for 1000 Hours at 800°C in Dry Air over Cr Pieces

At this point, a literature survey was conducted for common supports for calcium oxide and it was found that there has been a lot of research on CO_2 removal using supported CaO. Samples of calcium oxide infiltrated into four common substrates were provided by the vendor for testing. All four samples were placed in crucibles over Cr pieces and heated to 750°C in air with 10% humidity for 1000 hours. Figure 2-95 shows the samples after testing. Analysis of test results showed that 10% CaO on alpha-alumina picked up the most Cr on the surface, followed by 21% CaO on gamma-alumina, 15% CaO on Zeolite-5A, and finally no obvious Cr deposits on 13% CaO on silica gel.

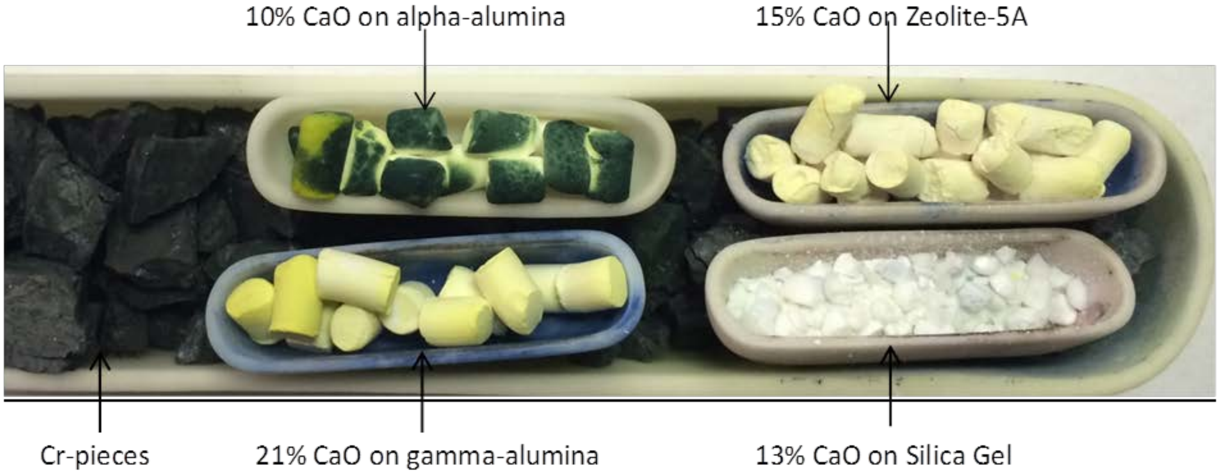

Figure 2-95. CaO Cr Getter Supported on Various Materials Tested for 1000 Hours at 750°C in Air with 10% Humidity

Figure 2-96 presents a comparison of low magnification SEM images for the four samples showing the integrity of the beads after the heat-treatment and Cr vapor exposure. Both alumina beads were mainly intact, the Zeolite bead had significant cracking, and the silica gel beads had all cracked and broken extensively. Figure 2-97 shows SEM/EDX analysis of 10% CaO on alpha alumina after exposure to Cr vapor. Significant amount of Cr was found in areas with high CaO content (10 to 11 atomic percent (at%) Cr). Also, areas with high alumina content had lower Ca and Cr content indicating no significant reaction between the filter material and substrate at 750°C over 1000 hours. SEM/EDX analysis of 15% CaO on Zeolite-5A sample showed that Ca and Si contents trended together and, where these were high, there was a distinct microstructure change most likely due to calcium silicate formation. Where Ca content was lower, Si content was lower and the other Zeolite elements had higher concentrations. No Cr was found associated with Ca, and only small amounts (under 1 at%) were found in the sample. These appeared to be associated with Na (also likely to react strongly with Cr vapor). Figure 2-98 shows SEM/EDX analysis of 21% CaO on gamma alumina. Some Cr was found and it appeared to be associated with Ca, but maximum Cr content was 2.5% which is quite low. SEM/EDX analysis of 13% CaO on silica gel sample showed no Cr, so this material is not an effective Cr getter. In addition, two phases appeared to be present, most likely silica and calcium silicate.

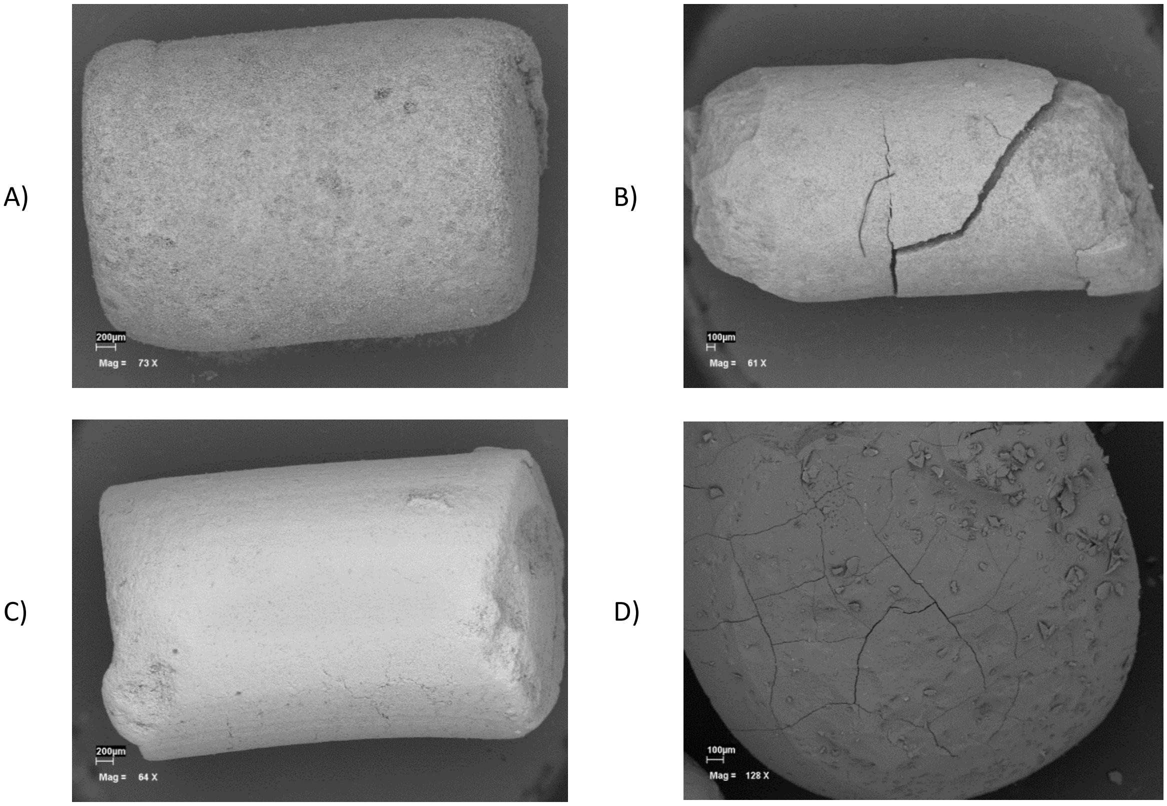

Figure 2-96. SEM Images of Samples taken from Materials shown in Figure 2-6

A) 10% CaO on alpha alumina, B) 15% CaO on Zeolite-5A,
C) 21% CaO on gamma-alumina, D) 13% CaO on silica gel

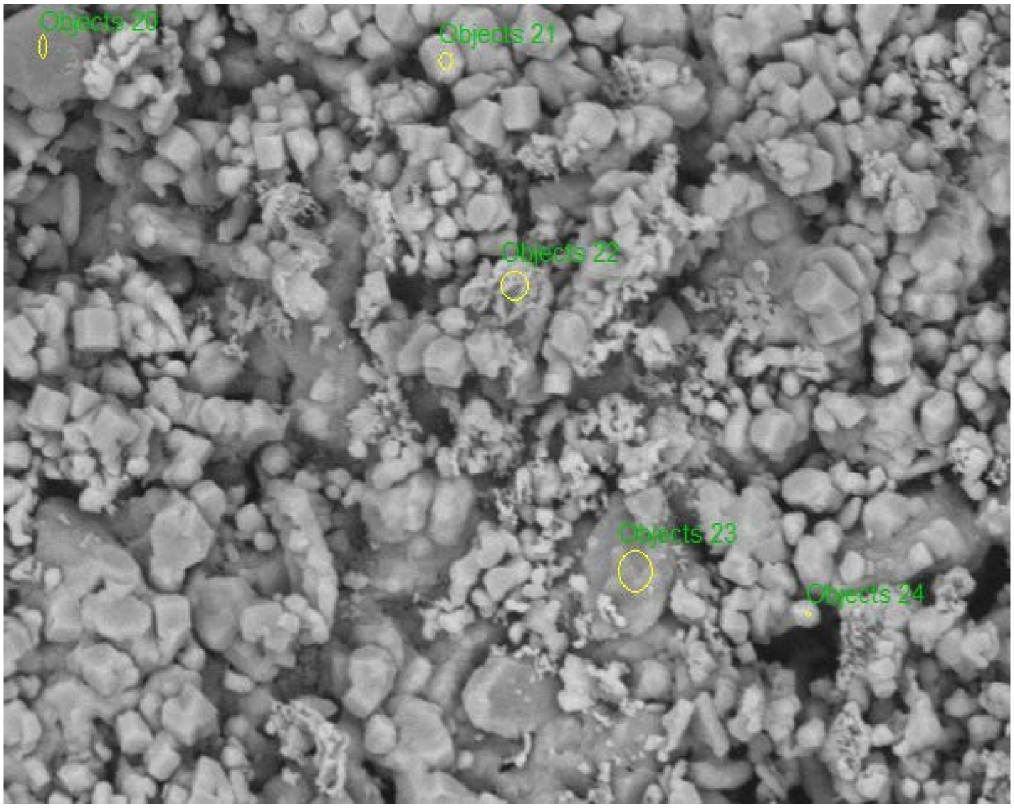

```
Atomic percent (%)

Spectrum         C      O     Al    Si     Ca     Cr    Au
------------------------------------------------------------
Objects 20   84.39  10.52      -  0.97   1.96   0.34  1.82
Objects 21    7.81  52.02      -  2.13  24.23  10.32  3.49
Objects 22    6.11  45.48   1.13  3.15  30.20  10.34  3.60
Objects 23    3.88  48.65  32.26     -   8.43   2.80  3.98
Objects 24    6.05  50.58      -  1.92  27.57  10.88  2.99
------------------------------------------------------------
```

Figure 2-97. SEM/EDX Analysis of 10% CaO on Alpha Alumina

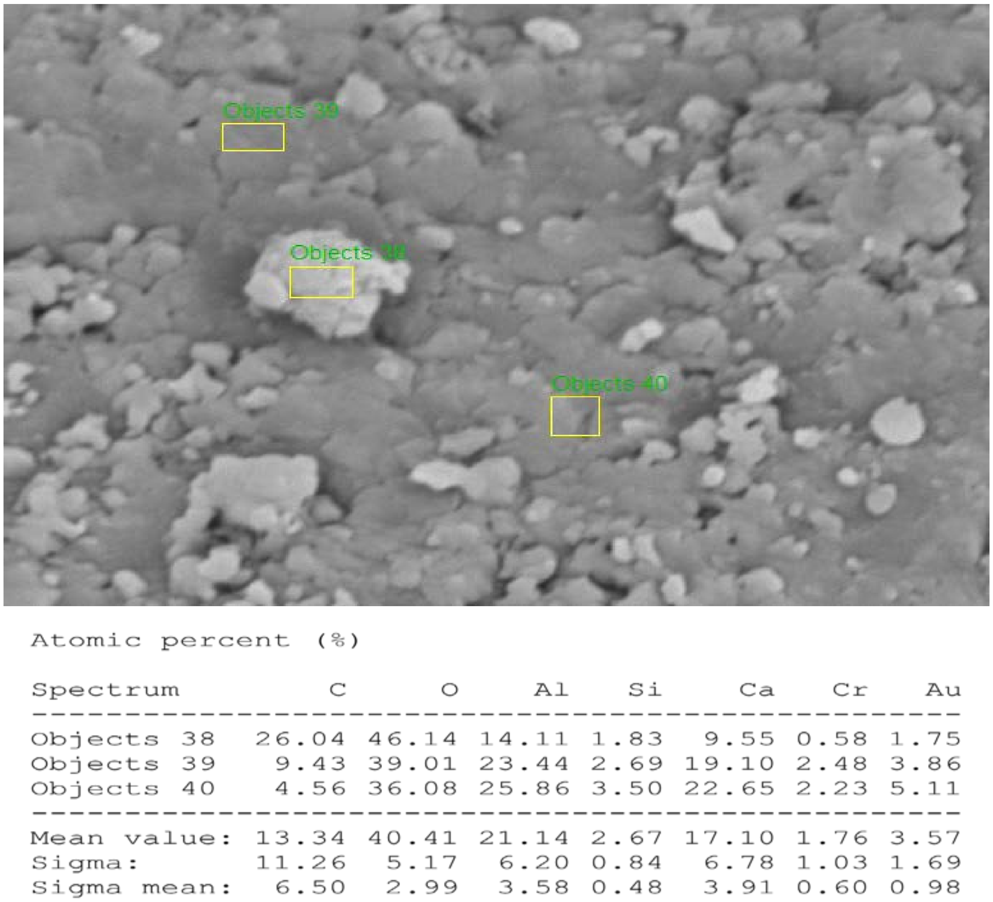

```
Atomic percent (%)

Spectrum         C       O      Al     Si      Ca     Cr     Au
------------------------------------------------------------------
Objects 38   26.04  46.14  14.11  1.83    9.55  0.58  1.75
Objects 39    9.43  39.01  23.44  2.69   19.10  2.48  3.86
Objects 40    4.56  36.08  25.86  3.50   22.65  2.23  5.11
------------------------------------------------------------------
Mean value:  13.34  40.41  21.14  2.67   17.10  1.76  3.57
Sigma:       11.26   5.17   6.20  0.84    6.78  1.03  1.69
Sigma mean:   6.50   2.99   3.58  0.48    3.91  0.60  0.98
```

Figure 2-98. SEM/EDX Analysis of 21% CaO on Gamma Alumina

The samples packed in a tube were also tested using 15 SLPM nitrogen containing 10% water vapor and thermal cycled ten times between 150 and 750°C to check integrity. Figure 2-99 shows a comparison of the as-received samples with samples after the cycles (packed in a tube to simulate reactor/filter conditions). The silica gel sample showed significant change. This, coupled with the lack of Cr absorption and (likely) reaction to form calcium silicate indicated by SEM/EDX analysis, eliminates the silica gel as a viable substrate. All other samples showed little visible change after this test from the as-received material. However, the Zeolite-5A had some cracks on the surface of the beads when examined under SEM and also showed likely reaction to form calcium silicate where CaO was infiltrated in SEM/EDX analysis after the 1000-hour test. So this substrate is also eliminated. The alpha alumina and gamma alumina samples are both viable supports for a CaO-based Cr filter.

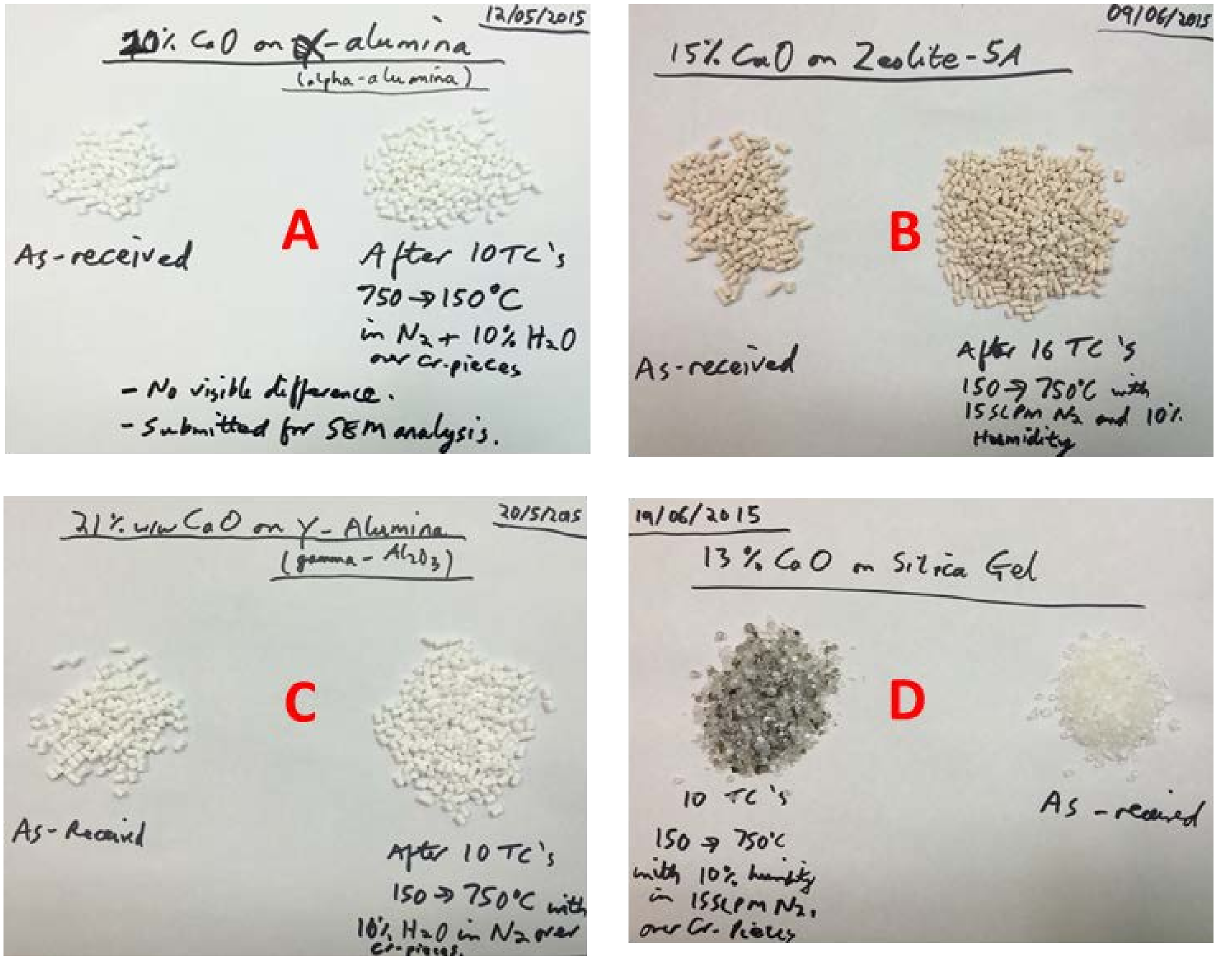

Figure 2-99. Samples Before and After Thermal Cycling with Humidified Nitrogen

(A) 10% CaO Cr Getter supported on alpha alumina
(B) 15% CaO Cr Getter supported on Zeolite-5A
(C) 21% CaO Cr Getter supported on gamma alumina
(D) 13% CaO Cr Getter supported on silica gel

The samples were examined after 1000 and 2000 h of exposures at 750°C in humidified air (10% water) over Cr-pieces. SEM/EDX analyses of the cross-sections of the two alumina based beads (10% CaO on alpha-alumina and 21% CaO on gamma-alumina) and the Zeolite bead (15% CaO on Zeolite-5A) were performed to see how far CaO infiltrated into the beads and how much Cr was deposited throughout the cross-section. Both alumina beads were in-tact, while the Zeolite bead had significant cracking. The gamma-alumina bead showed clear signs of an expanded reaction zone of Cr with CaO penetrating into the bead from the outer surface, compared to the 1000 hour-exposed sample.

Figure 2-100 shows the sample arrangement and results after 5000 hours of testing. The discoloration (yellow) indicates the extent of interaction with Cr-species. It appears that 10% CaO on alpha-alumina picked up the most Cr on the surface, followed by 21% CaO on gamma-alumina, 15% CaO on Zeolite-5A, and finally 13% CaO on silica gel with no obvious Cr deposits. Based on the previous results, it was deemed unnecessary to perform analysis on the silica gel and Zeolite samples. CaO in both was seen to react with silica in the support, most likely forming calcium silicate and leaving little to no CaO free for reaction with chromium vapor species.

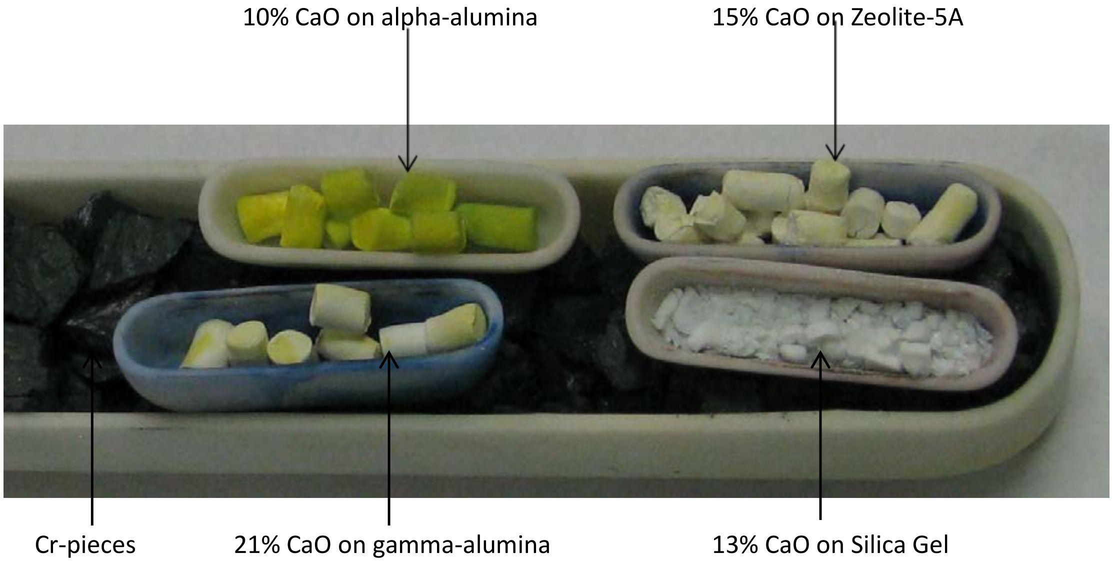

Figure 2-100. CaO Cr-Getter Supported on Various Materials and Tested for 5000 Hours at 750°C in 10% Humid Air Over Cr-pieces

The other two (alumina) samples were epoxy mounted and polished. Figure 2-101 shows an optical micrograph of the polished sections after 5000 hours of exposure. It can be seen that, compared with 2000 hour samples, the Cr-species have migrated much further into the sample. This is evidenced by yellowing all the way through the cross-section of the gamma alumina sample and all except a portion of one quadrant of the alpha alumina sample (possibly due to being in contact with another bead in this location). SEM/EDX analysis results of the 5000 hour tested samples can be seen in Figure 2-102 and Figure 2-103 for the alpha alumina and gamma alumina support material, respectively. In both cases it was confirmed that Cr was found and always when Ca levels were higher (i.e., the Cr is associated with Ca as expected).

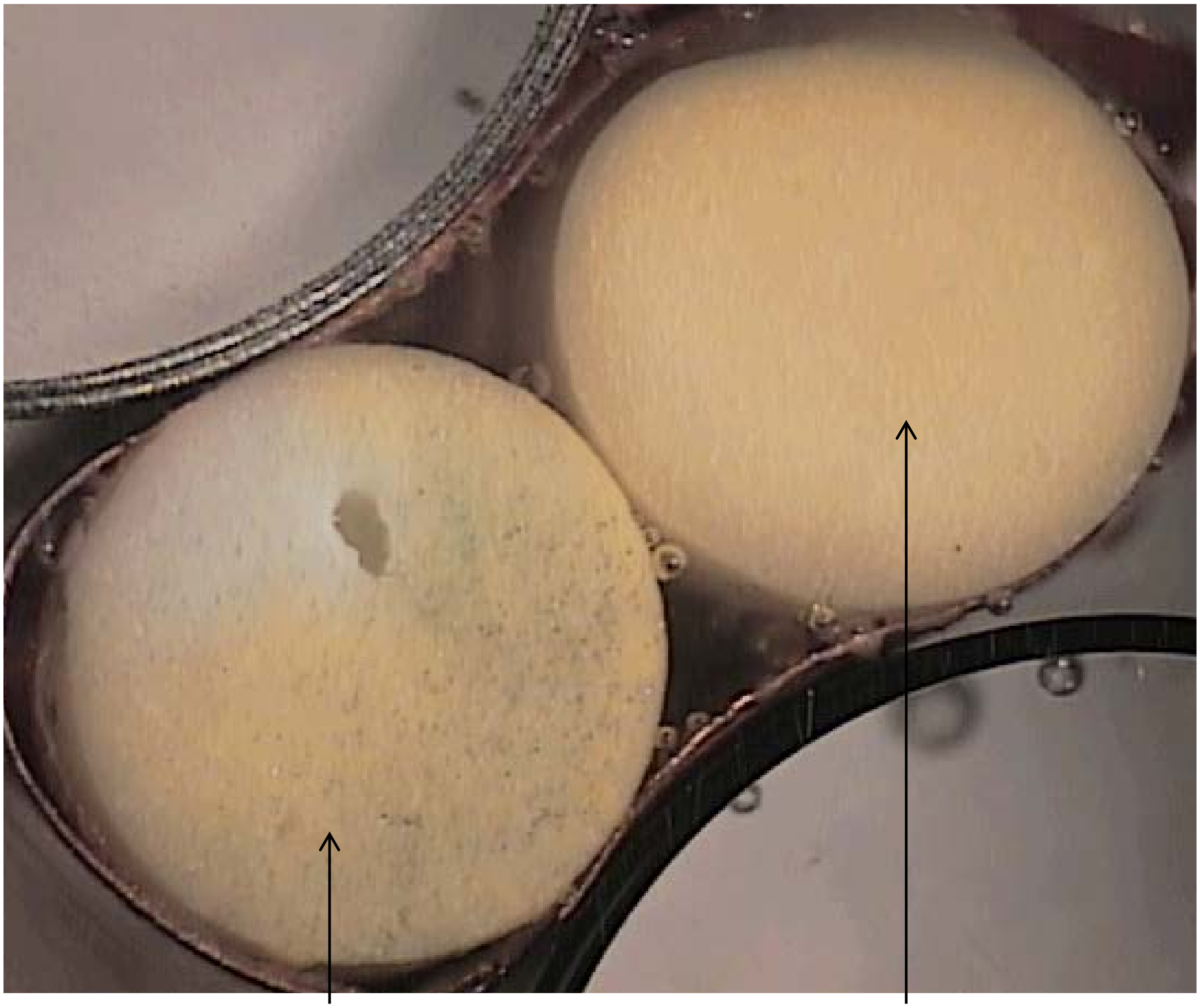

Figure 2-101. Micrograph of Alumina-supported CaO Samples After 5000-Hour Test: Showing Discoloration Due to Cr-Species Interaction

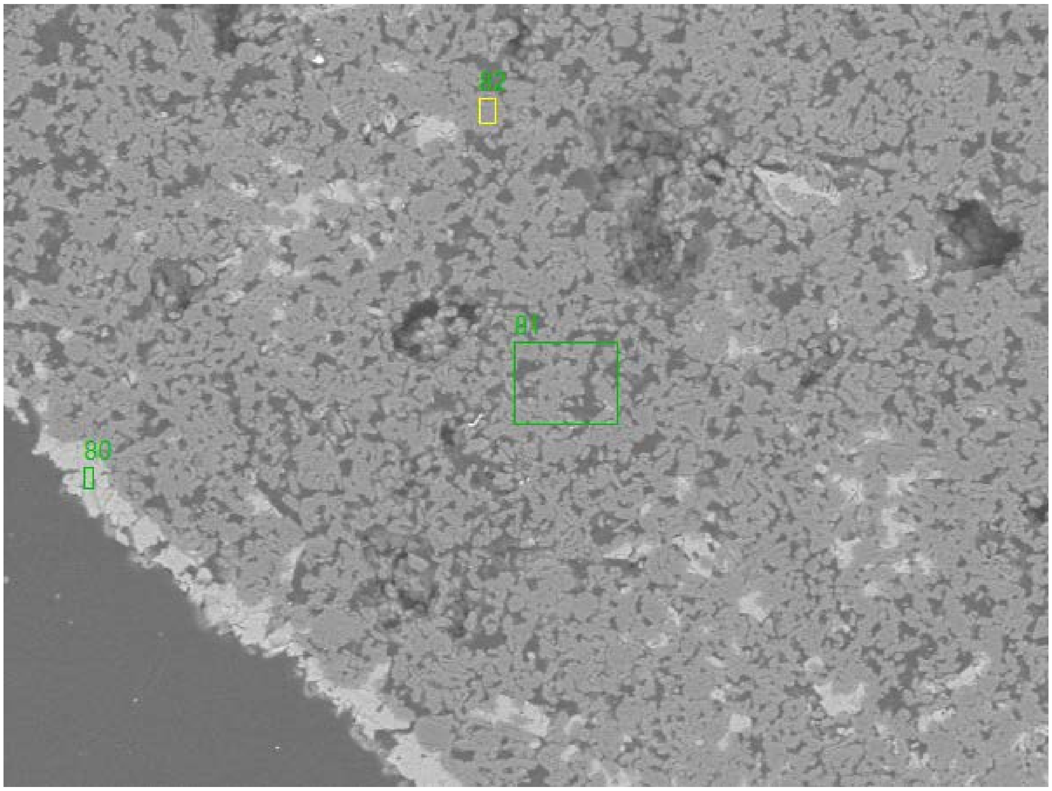

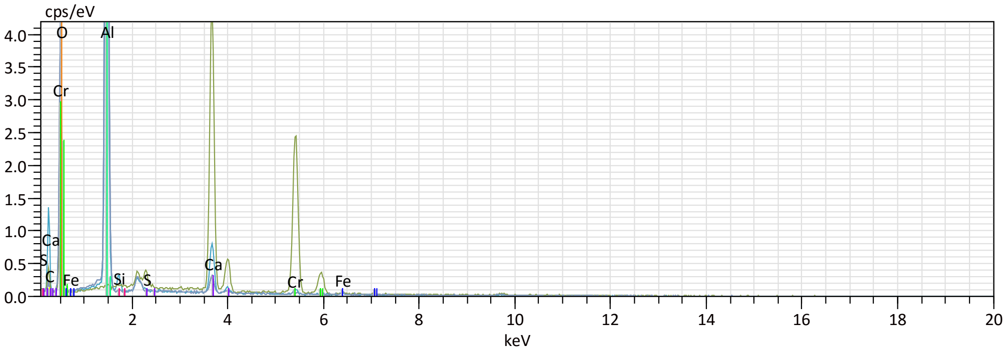

```
Atomic percent (%)

Spectrum        C     O    Al   Si    S    Ca    Cr   Fe
-------------------------------------------------------
 80         10.76 57.69     -    - 0.87 16.69 13.99    -
 81         43.10 36.97 16.77 0.62    -  2.22  0.24 0.09
 82         10.24 53.45 35.20    -    -  1.11     -    -
-------------------------------------------------------
Mean value: 21.37 49.37 25.98 0.62 0.87  6.67  7.11 0.09
Sigma:      18.82 10.95 13.03 0.00 0.00  8.69  9.73 0.00
Sigma mean: 10.87  6.32  7.52 0.00 0.00  5.02  5.62 0.00
```

Figure 2-102. SEM/EDX Analysis of Alpha Alumina-supported CaO After 5000-Hour Test Showing Cr Associated with Ca

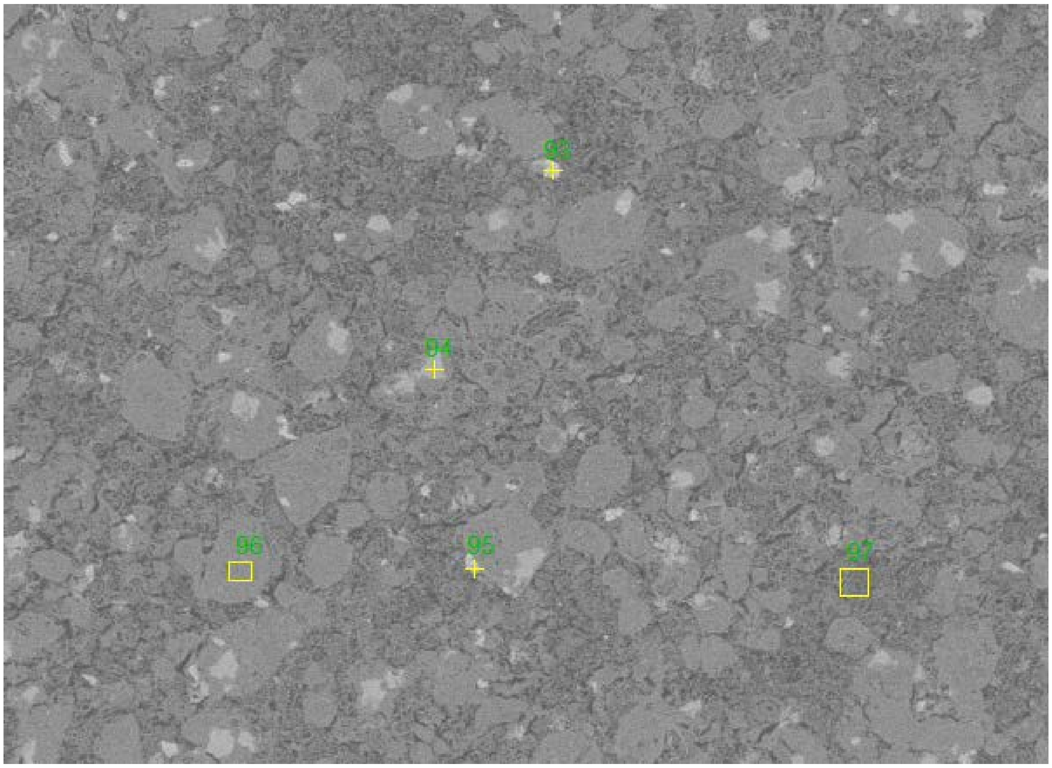

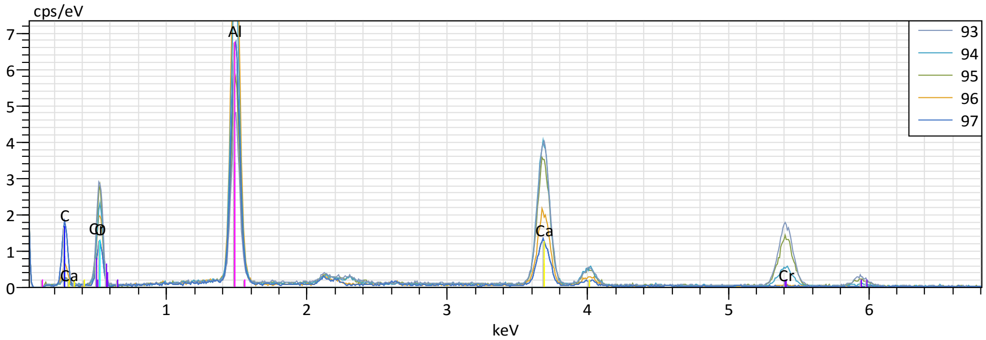

```
Atomic percent (%)

Spectrum        C      O     Al     Ca    Cr
----------------------------------------
 93          5.94 59.13 12.50 13.91 8.52
 94          7.94 53.44 21.02 14.76 2.84
 95          9.02 56.76 14.52 12.45 7.25
 96         27.70 42.81 21.19  8.30    -
 97         54.42 28.92 12.86  3.80    -
----------------------------------------
Mean value: 21.00 48.21 16.42 10.64 6.20
Sigma:      20.63 12.46  4.35  4.56 2.98
Sigma mean:  9.23  5.57  1.94  2.04 1.33
```

Figure 2-103. SEM/EDX Analysis of Gamma Alumina-supported CaO After 5000-Hour Test Showing Cr Associated with Ca

Improve Z Direction Thermal and Flow Uniformity

Related to the modeling discussion presented earlier in this report, technical design approaches to improve the z-direction thermal uniformity of the stacks have been discussed and include:

- Design and installation of an end plate heat exchanger to recover exhaust heat from the cathode outlet stream to maintain thermal uniformity across the stack.
- Keeping the end plates well insulated using additional insulation, or embedding insulation into a new end plate design.
- Installing electrical heaters within the stack endplates (or attached to the stack end plates). External power source required.
- Installation of a resistive heating layer against the stack end plates which utilize the power generated within the stack to heat the layers.

Among the possibilities shown above, it has been determined to design and implement an end plate heat exchanger to recover the exhaust heat from the cathode outlet stream to ensure that the stack ends remain hot and z-direction stack flow uniformity is maintained. Further design and selection of a prototype is planned and will be followed by assembly and testing in a large area 32-cell stack in the near future.

Chromium *Evaporation* Rate Study

In the Cr evaporation rate study being conducted at FCE (Danbury), Cr evaporation rate from five sets of material samples were investigated. The materials studied included Alloy A (austenitic stainless steel), aluminized Alloy A, Alloy B (ferritic stainless steel), aluminized Alloy B, and Alloy C (ferritic stainless steel). The experimental conditions were consistently set to be T=850°C, air flow rate=5300 sccm, and humidity=12%. The experimental setup is demonstrated in Figure 2-104. The experiment duration was about 16 days and Cr evaporation rate was measured at mid-test and at the end of each test. These conditions are extreme in terms of Cr volatility and are expected to far exceed the actual environment, thereby providing an accelerated test. The evaporation rates are summarized in Table 2-5. As observed, austenitic stainless steel Alloy A has a relatively high tendency to lose Cr, which is expected because of the high Cr content in this alloy (about 25%).

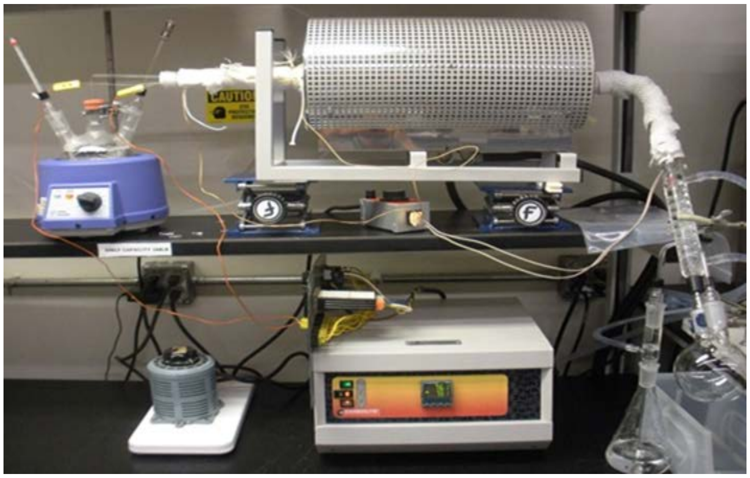

Figure 2-104. Experimental setup for Cr evaporation rate evaluation

Table 2-5. Cr evaporation rates for the alloys studied

Alloy	Test Duration (h)	Elapsed Time (h)	Evaporation Rate (each rinse, $kg \cdot m^{-2} \cdot s^{-1}$)	Evaporation Rate (cumulative, $kg \cdot m^{-2} \cdot s^{-1}$)
Alloy A	184	184	54.8E-11	54.8E-11
	232	416	42.5E-11	49.5E-11
Al-Alloy A	190	190	1.70E-11	1.70E-11
	193	383	0.28E-11	0.99E-11
Alloy B	190	190	18.2E-11	18.2E-11
	190	380	6.04E-11	12.1E-11
Al-Alloy B	190	190	1.34E-11	1.34E-11
	190	380	2.10E-11	1.72E-11
Alloy C	192	192	24.9E-11	24.9E-11
	191	383	19.1E-11	22.0E-11

On the other hand, ferritic stainless steel Alloy B, which contains only about 11% Cr, showed much lower Cr evaporation rate (about three times less than Alloy A). Aluminization was found to be an effective way to limit the Cr loss. Aluminized Alloy A and aluminized Alloy B similarly showed very low Cr evaporation rates.

2.2.2.3. Stack Tower and Stack Module Components Development

Integrated Fuel Radiator and Pre-Reformer: Based on a strategy similar to the concept of the Catalytic Heat Exchanger for the 50 kW Proof of Concept Module system, a design change was made to combine the functionality of the fuel pre-reformer and fuel radiator (pre-heater) into a single device. Figure 2-105 shows a schematic of the integrated unit. The fuel radiator is an X-shaped heat exchanger that fits in the space between the four SOFC stacks. Fuel to the anodes is introduced at the bottom of two arms and passes upwards through heat exchange channels. At the top, the flow turns downward through the remaining two arms. By installing reforming catalyst into the heat exchange channels, the following benefits are expected:

- Consolidating space in the equipment arrangement by using one less reactor vessel
- Avoiding addition of a pre-reformer heater by using heat transferred from the SOFC stacks
- Driving the reformer reaction further to equilibrium by continuously replacing heat used in the endothermic reaction. This results in lower on-cell reforming which is expected to decrease on-cell thermal gradients and improve SOFC reliability and robustness.

- **First pass:**
  - **16 channels**
  - **Cross Sectional Area = 8 in^2 total**
- **Second pass:**
  - **14 channels**
  - **Cross Sectional Area = 7 in^2 total**

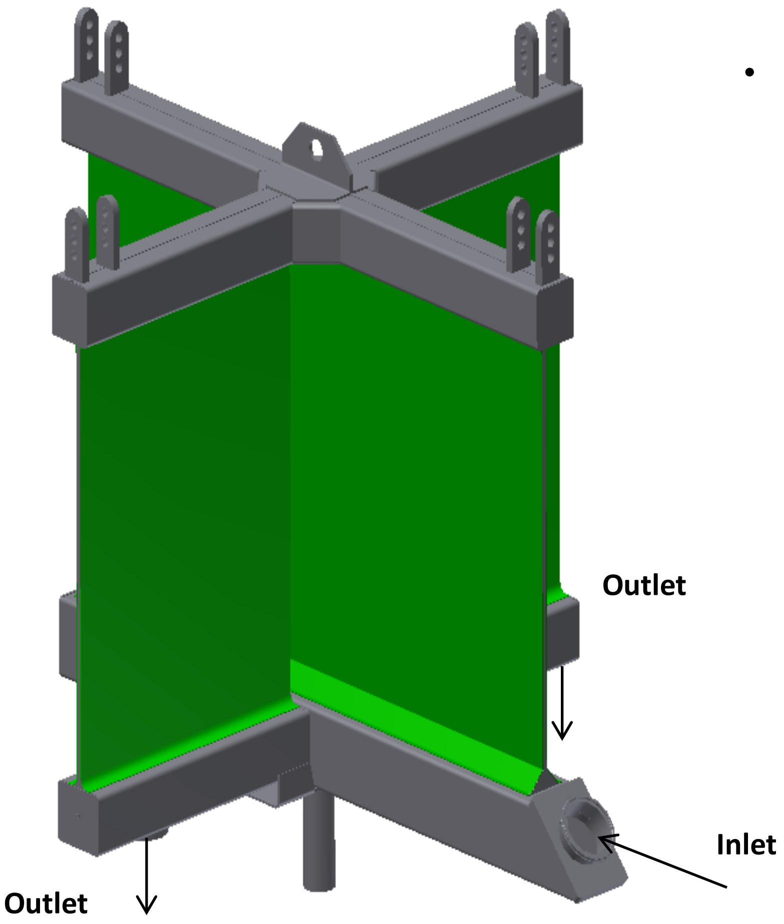

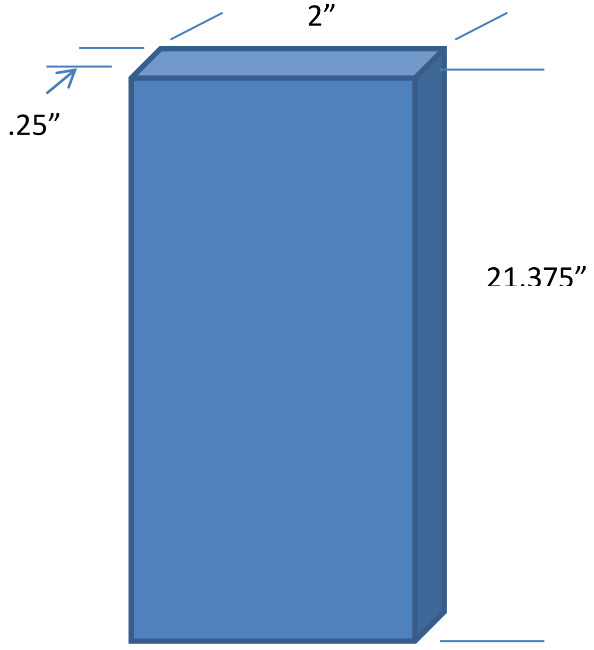

Channel Dimensions

Figure 2-105. Schematic of Integrated Fuel Radiator and Pre-Reformer Unit

Computational fluid dynamics (CFD) analysis was performed to evaluate the 50 kW reforming radiator concept. A CFD model was developed for the previous generation radiator that was tested with Stack Module 60kW-1. The model boundary conditions were validated by comparing the experimental results of 60kW-1 Test to the model results. After the boundary condition validation, a CFD model was developed for the proposed second generation radiator design that includes corrugated inserts, coated with reforming catalyst (integrated reformer radiator). The energy consumed by the endothermic reforming reaction was subtracted from the model as a heat sink and is shown as Reforming Energy in Figure 2-106. The CFD results showed that the amount of reforming energy does not have a large impact on the sensible heat picked up by the anode gas. Based on the CFD results the reforming radiator is being designed for incorporation into the module and should reform more methane than an external radiator because of the higher temperature inside the module and simultaneous heat transfer to drive the reforming reaction towards completion.

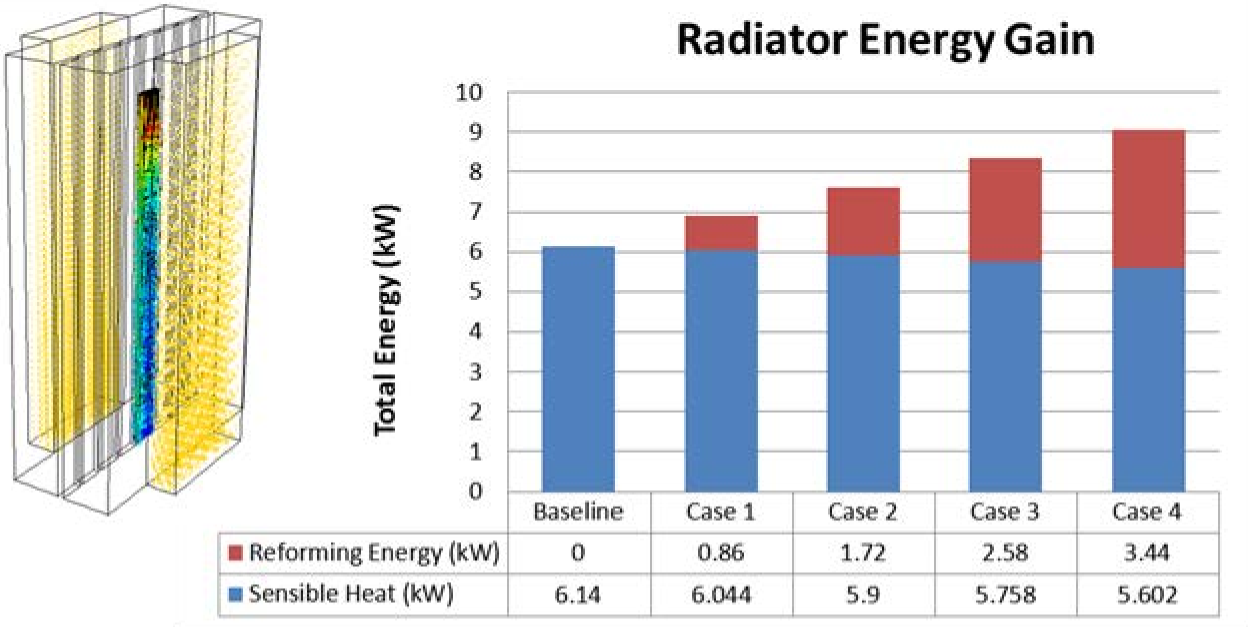

	Baseline	Case 1	Case 2	Case 3	Case 4
🟥 Reforming Energy (kW)	0	0.86	1.72	2.58	3.44
🟦 Sensible Heat (kW)	6.14	6.044	5.9	5.758	5.602

Figure 2-106. CFD Analysis Results for 50 kW Reformer - Radiator

Catalytic Heat Exchanger (Cathode Air Preheater): The catalytic heat exchanger (for the PCM system) combines the functionality of two pieces of equipment (the catalytic oxidizer and cathode air heat exchanger) into a single high-performance multi-functional device. Design of a second generation catalytic heat exchanger has been commissioned incorporating lessons learned from the prototype testing. Functional areas addressed include:

- Initiating oxidation reactions from a cold start up.
- Limiting CO emissions to 10 ppmv.
- Withstanding high temperature excursions brought about by upstream combustion.
- Achieving more uniform gas distributions.

To facilitate cold start up, an ignition device and/or heater will be integrated into the heat exchanger body. To reduce CO emissions, the exhaust-side baffle will be re-designed to significantly reduce the potential for gas bypass.

A number of features are being incorporated to improve resistance to temperature excursions or mitigate their occurrence. These include improved joint design, increased weld penetration and size, improved oxide and/or catalyst removal from weld area, and use of heavier gauge material. Finally, to achieve more uniform gas distribution, the startup gas connection will be relocated upstream of its current position to permit more mixing with anode exhaust gas.

In addition, progress on related common areas, such as Cathode Thermal Diffuser and Radiative Fuel Reformer is also reported in Section 3.1 and 5.1, respectively.

2.2.3. Stack Fabrication and Testing

16-Cell Stack Testing

The 16-cell 550 cm^2 large area stack (LAS) was continued to be used as a development platform for the stack building block and expected 120-cell stacks for the 50 kW stack module.

Stack GT057235-0097: Steady state testing of Stack GT057235-0097 (started earlier under DOE project DE-FC26-04NT41837) was continued. Stack -0097 was built with thicker wet cathode contact paste in each cell. The testing was conducted at Phase II system operating conditions of 68% fuel utilization, 70% in-stack reforming, 15% air utilization and 200 A current (364 mA/cm^2). Figure 2-107 presents the test results. Under these conditions, the stack demonstrated 0.73% (6.2 mV) per 1000 hours degradation rate over 767 hours after first thermal cycle and 0.54% (4.5 mV) per 1000 hours degradation rate over 4173 hours after the second thermal cycle.

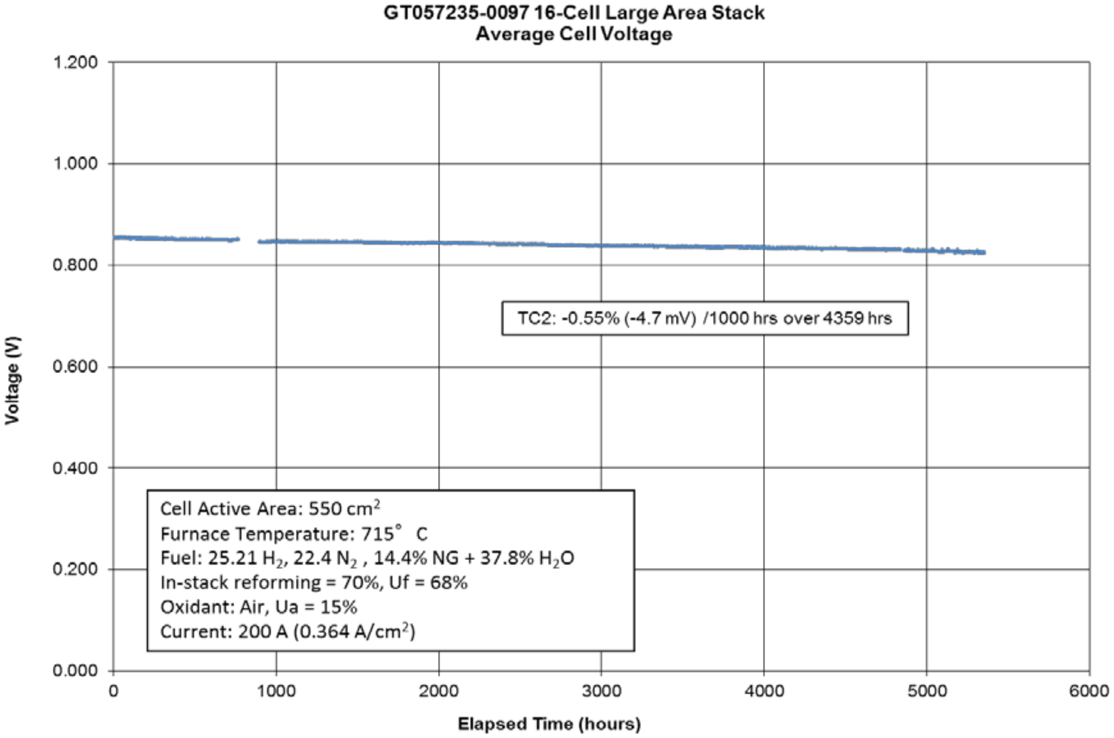

Figure 2-107. Average Cell Voltage of 16-Cell Stack GT057235-0097

Figure 2-108 shows the performance trends of individual cells. The cells voltages were uniform (stayed grouped together) throughout the duration with less than 20 mV voltage spread.

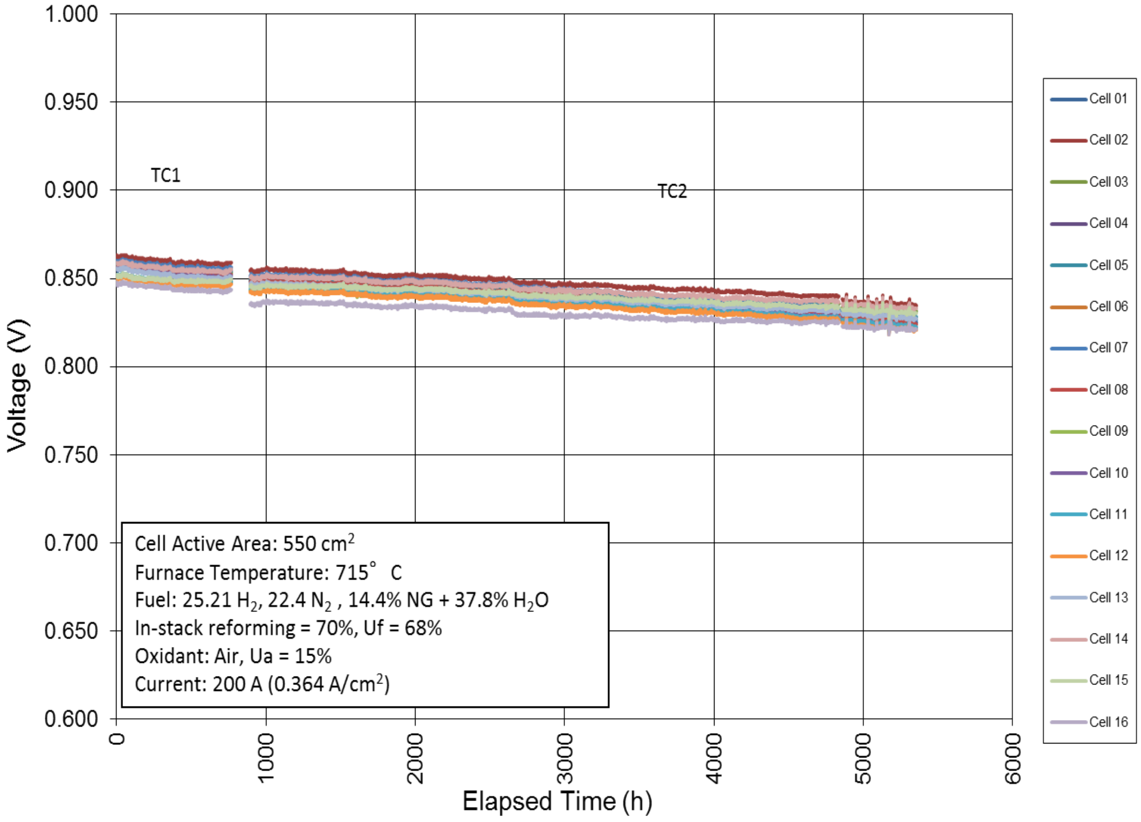

Figure 2-108. Individual Cell Voltages of 16-Cell Stack GT057235-0097

Figure 2-109 shows the cell by cell performance degradation rate before and after the second thermal cycle. The cell degradation rates remained quite uniform throughout the stack as desired for the technology.

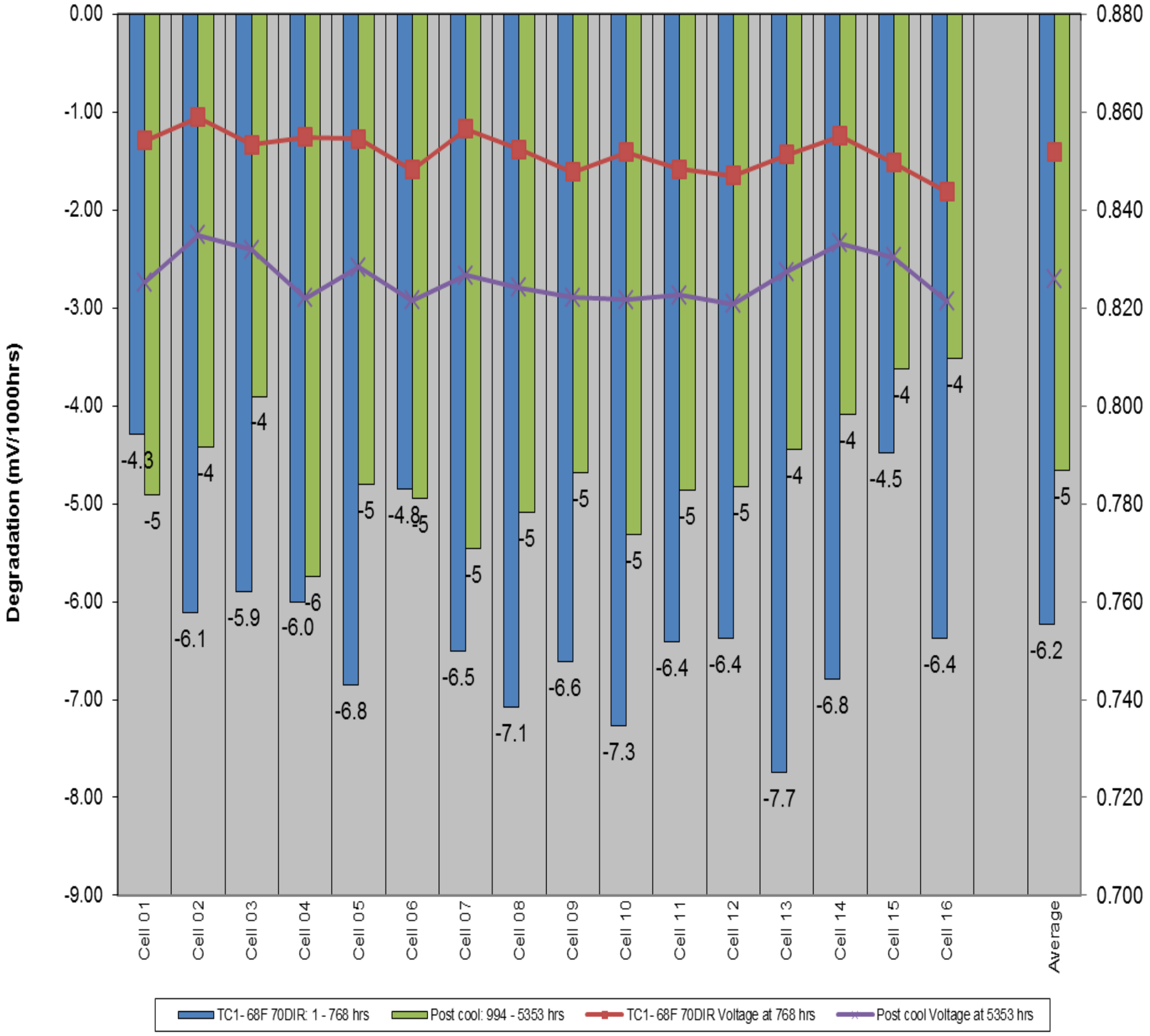

Figure 2-109. Distribution of Performance Degradation Rates for Stack GT057235-0097 at Phase II System Operating Conditions

Stack GT057235-0099: Stack -0099 was built for another test of thicker cathode contact paste with Cr getter loading of 20% by volume. The cell voltages were stable at 80% Uf (fuel utilization) during performance testing before and after thermal cycling. However, random cells in stack 0099 were observed to droop in voltage and quickly recover during test transitions such as introducing or making a significant flow change of natural gas as shown in Figure 2-110.

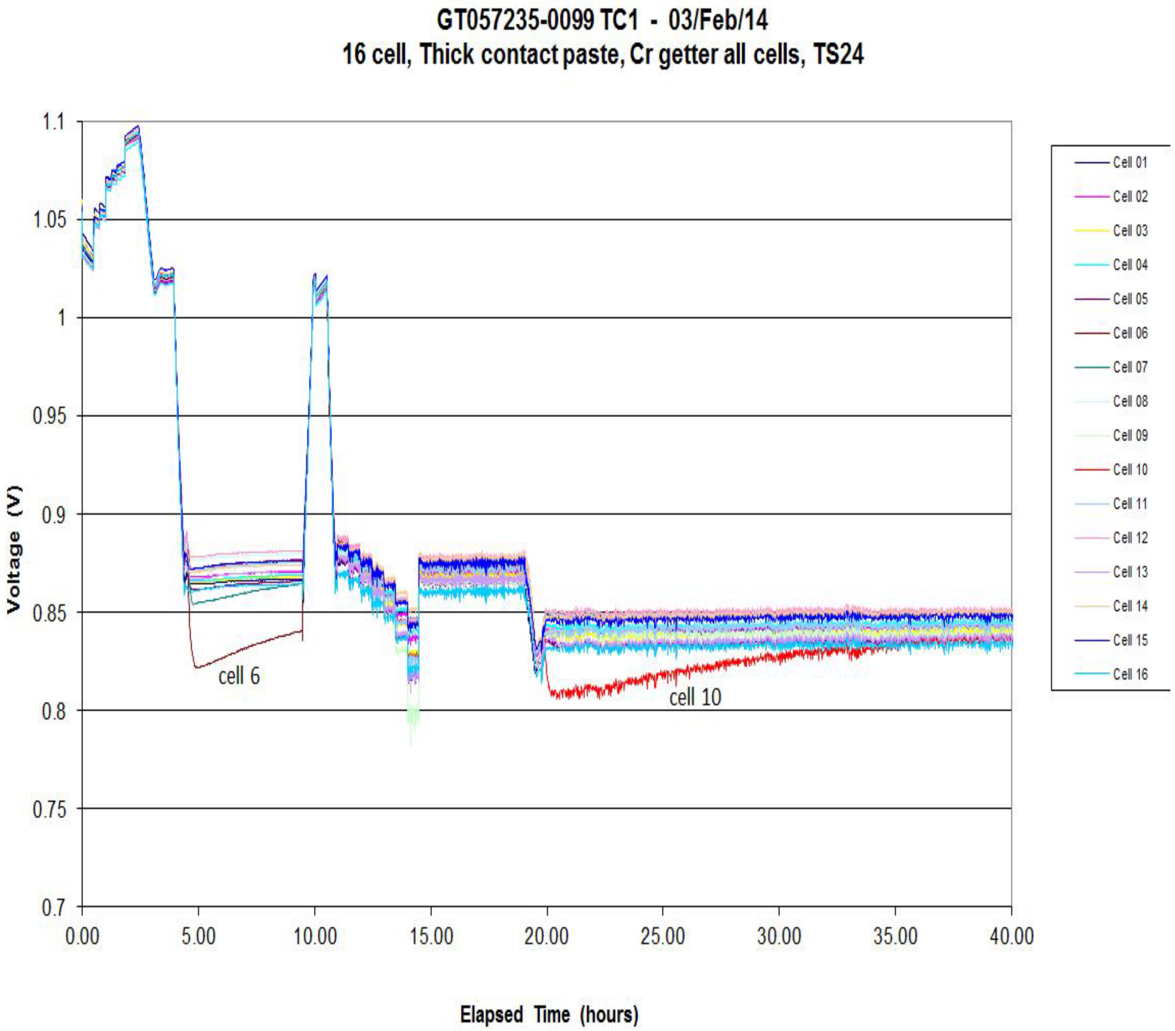

Figure 2-110. Stack GT057235-0099 – Random Drooping of Cells after One Thermal Cycle

In comparison to this stack, Stack GT057235-0097 (with thick contact paste) did not contain Cr getters and did not exhibit the voltage drooping with random cells. This issue was analyzed and it was decided that the random cell droop may be due to the high Cr getter loading on cell. Stack -0099 was held only for 85 hours at Phase 2 system conditions prior to shutdown in order to make room for stack -0100.

Stack GT057235-0101: Stack -0101 was built with lower Cr getter loading (% by volume). Fuel utilization Performance tests had stable cell voltages at 80% Uf before and after thermal cycle. Cell 11 voltage drooped 25 mV during performance characterization before thermal cycle. After one thermal cycle, the same cell (cell 11) drooped again during performance characterization and during the Phase 1 to Phase 2 system condition transition. Cell 11 voltage recovered fully within 24 hours during the Phase 2 system condition hold as shown in Figure 2-111.

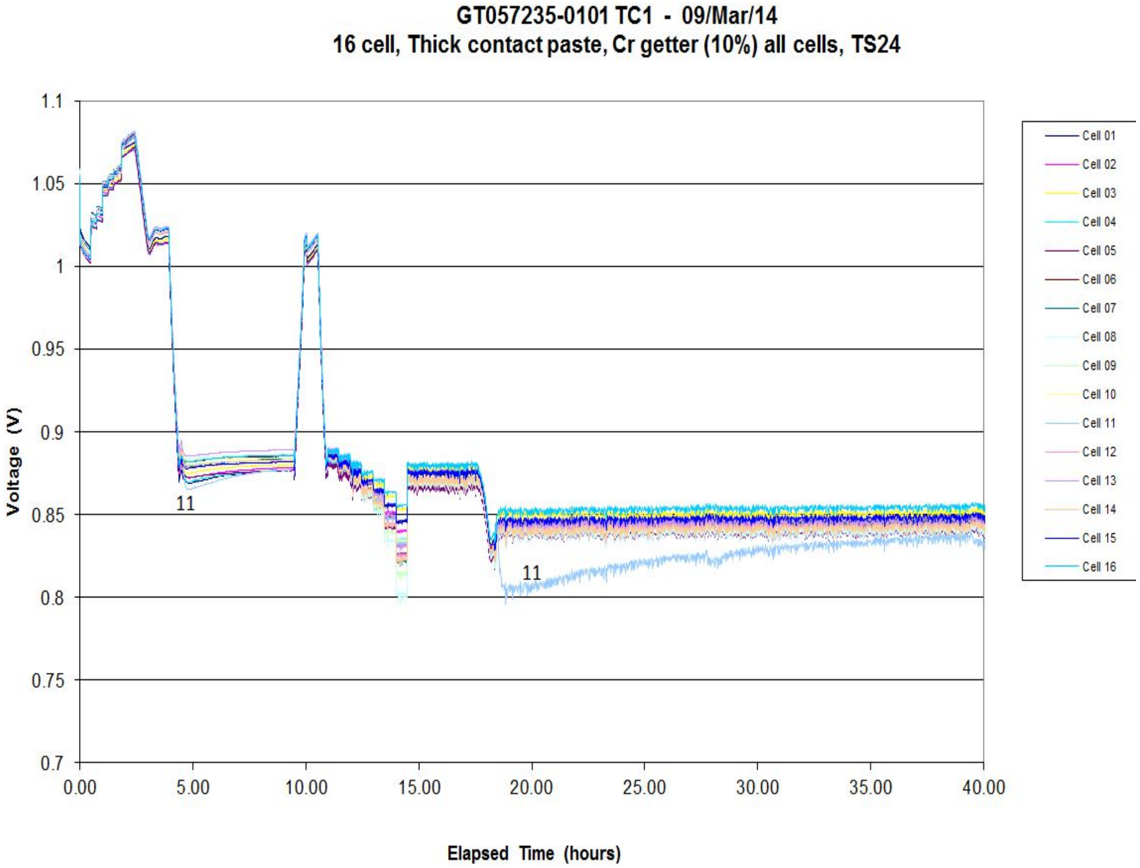

Figure 2-111. Stack GT057235-0101 – Cell 11 Voltage Drooped During Performance Characterization and Recovered During Steady-State Hold after One Thermal Cycle

A plan was made to test the stack at system representative conditions corresponding to the 50 kW system (and 60 kW stack module). VPS Gas Replacement (GR) composition was created to replace the CO_2 with nitrogen. Figure 2-112 displays the intended gas compositions and testing conditions, labeled as VPS GR and FCE GR.

VPS GR:
-68%u_f, 15%u_a, 36.4% DIR
-CH_4: 6.37%
-H_2: 44.43%
-N_2: 23.26%
-H_2O: 25.94%
-Furn Temp 710C
-Anode Preheat 655C
-Cathode Preheat 655C

FCE GR:
-68%u_f, 15%u_a, 25.7% DIR
-CH_4: 4.32%
-H_2: 50.1%
-N_2: 2%
-CO_2: 32.35%
-H_2O: 11.69%
-Furn Temp 710C
-Preheat 653C

Figure 2-112. VPS Gas Replacement (GR) and FCE GR Test Conditions

Prior to the heat up of this stack, a CO_2 mass flow controller was installed for FCE gas replacement condition testing. Test stand 24 was previously used to run electrolysis testing and used the CO_2 solenoid as a switch to reverse polarity for electrolysis. The stack had to be cooled down for the second thermal cycle to correct the CO_2 test stand functionality.

Cell 11 voltage along with voltages of cells 4 and 7 drooped during the performance characterization after the second thermal cycle. Stack was then tested at VPS GR conditions and testing at 200, 160 and 110 A current was performed. Figure 2-113 shows the results. Cell 11 voltage drooped when the stack current was reduced during each step of the VPS GR condition testing, then quickly recovered once the flows changed. Test condition was then changed to FCE GR conditions. During testing at FCE GR conditions, stack current was increased in steps to 160 and 200 A. Figure 2-114 shows the results. Cell 11 voltage drooped when flows changed on each step of the FCE GR testing, then quickly recovered once the electric load increased.

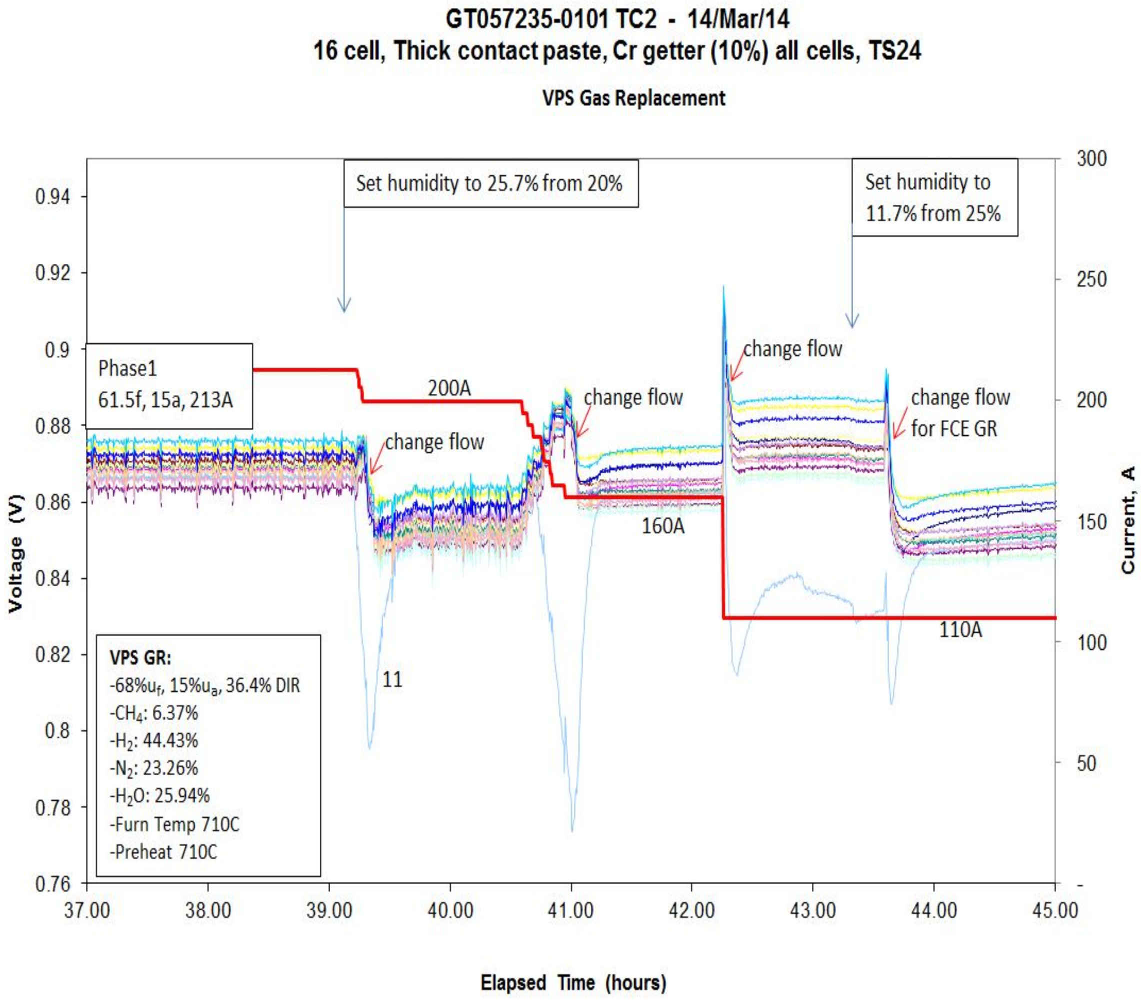

Figure 2-113. Stack GT057235-0101 – Testing at VPS GR Conditions (after Two Thermal Cycles)

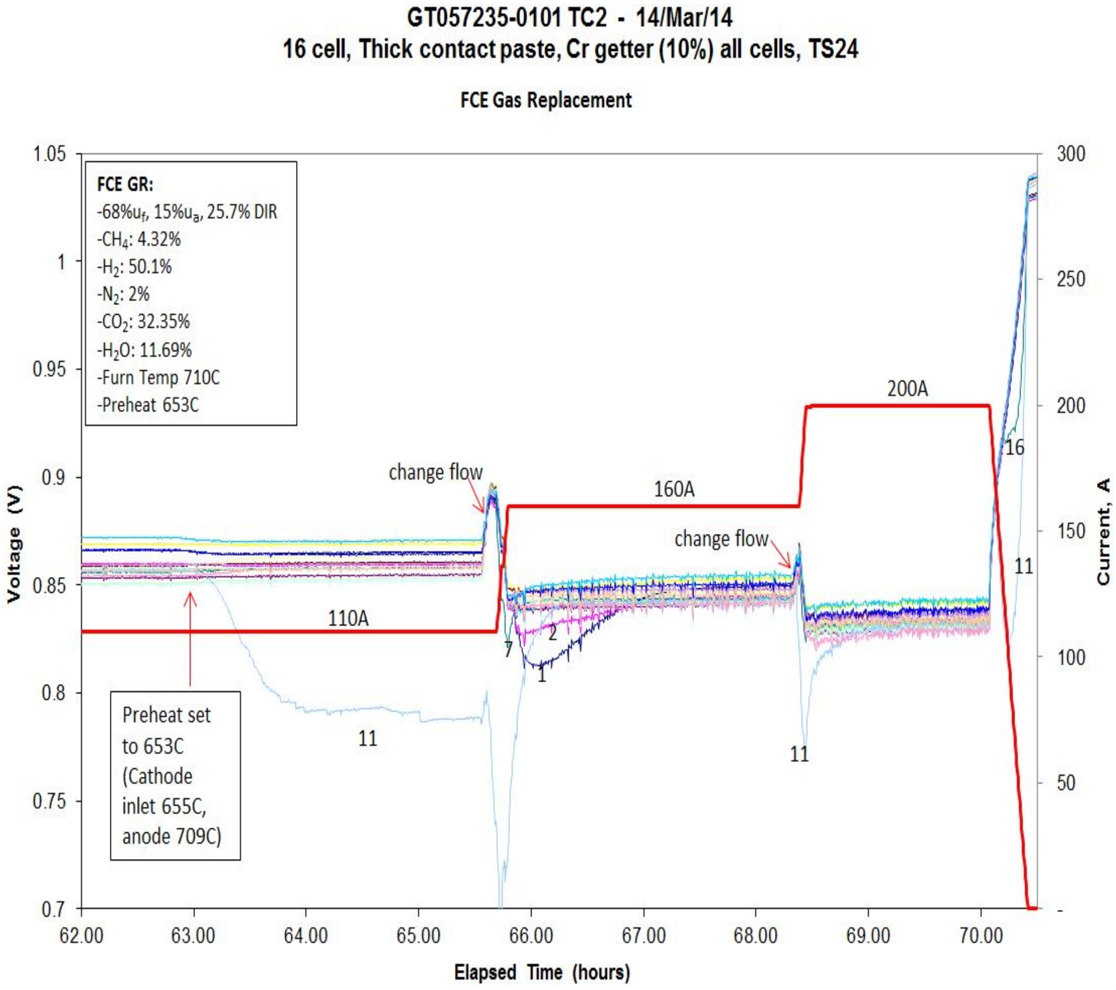

Figure 2-114. Stack GT057235-0101 – Testing at FCE GR Conditions (after Two Thermal Cycles)

Stack GT057235 -0101 was cooled after FCE GR condition testing to build and install stack -0102 into the same test stand (TS24). It was decided test stack- 0101 with cathode gas humidity, in test stand 26.

In test stand 26, Stack -0101 completed same tests as those conducted in test stand 24 without any cells drooping. Cells also had a reduced voltage band (more uniform) of ~15 to 18 mV. Test results are presented in Figure 2-115.

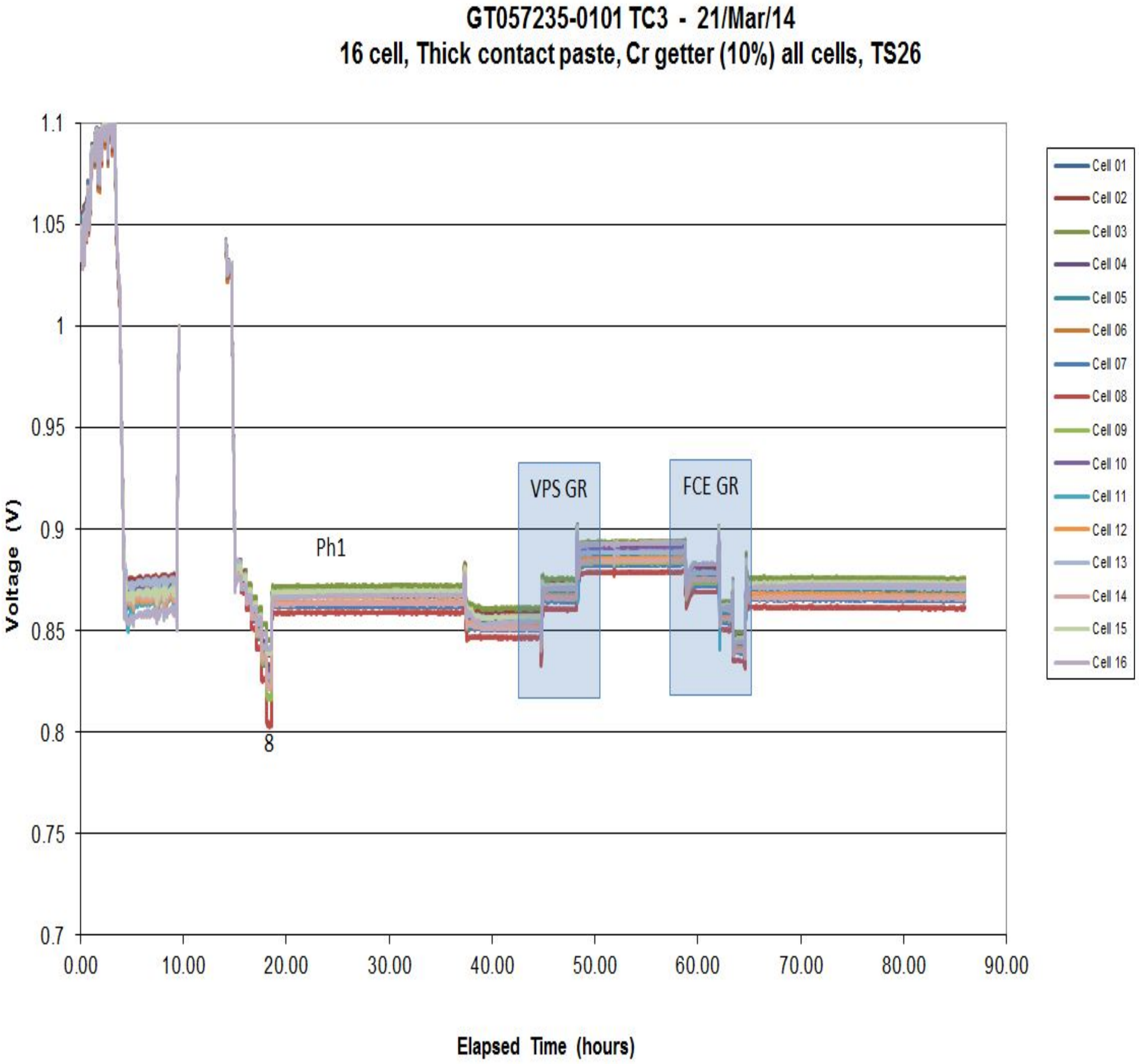

Figure 2-115. Stack GT057235-0101 – Testing in Test Stand 26 (after relocating from Test Stand 24)

After some investigation, it was discovered that the anode and control temperatures in Test Stand (TS26) were higher than temperatures in Test Stand (TS24). However, anode inlet temperatures were approximately 25°C-30°C lower in TS26.

Both test stands 24 and 26 have different means of preheating the inlet gases. Anode and cathode preheaters in TS26 are decoupled and have individual in-line heaters. Whereas TS24 preheaters are coupled in the same clamshell heater environment with gases flowing through two tube preheat coils. The voltage drooping of cells may be caused by high anode inlet temperatures that may result in increased reforming. Increased reforming could cause higher temperature deltas (differentials) in the stack and/or across the cell plane. Table 2-6 compares key temperatures for the two test stands. Temperatures are in °C. Electrical load (Eload) is in Amps.

Table 2-6. Stack GT057235-0101 Temperature Comparison During Performance Characterization in TS24 and TS26

		TS24	TS26
Power Curve	Stack Furnace	691	700
	Anode Preheat	712	730
	Cathode Preheat	712	730
	FI	731	705
	FO	740	751
	AI	690	707
	AO	730	745
	ELoad	272.4	273

Phase 1	Stack Furnace	696	700
	Anode Preheat	712	730
	Cathode Preheat	712	730
	FI	724	699
	FO	734	736
	AI	696	706
	AO	749	749
	ELoad	212.4	213

Stack GT057832-0005 (32-cell Stack): Stack GT057832-0005 was a 32-cell stack built with cells containing Cr-getter configuration 2 (C2) and 0.008” thick anode flow field base material. For stacks greater than 16 cells in size, fuel utilization testing is conducted only up to 75% level. Cell voltages were stable at 75% fuel utilization for utilization tests before thermal cycle (TC0) and after thermal cycle (TC1). Figure 2-116 shows the results after thermal cycle as an example.

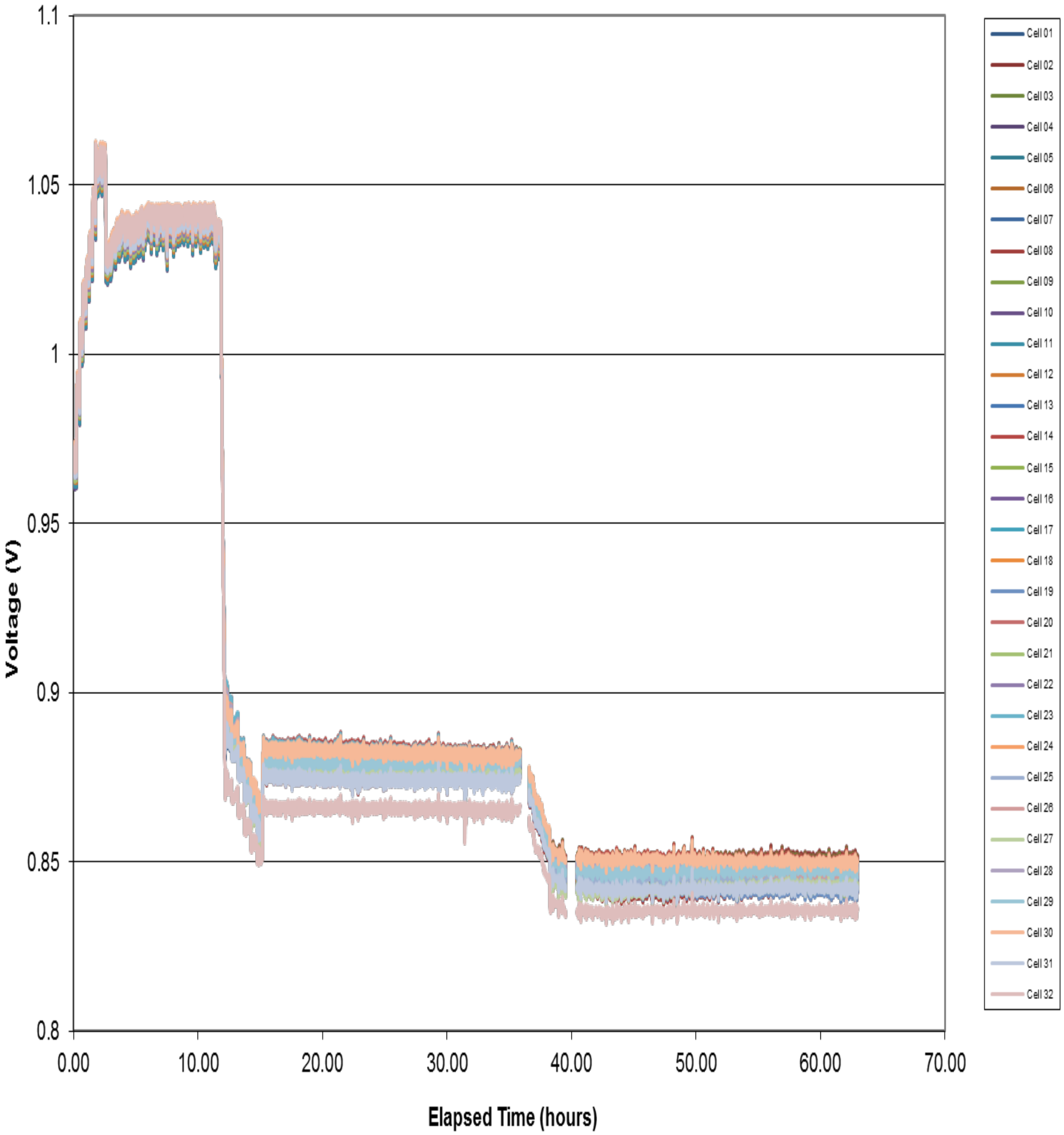

Figure 2-116. Stack GT057832-0005 Fuel Utilization Test After First Thermal Cycle

Stack -0005 was tested at Phase II system operating conditions with dry cathode air (this test stand was not capable of supplying cathode gas humidity) and had a high performance degradation rate over the initial 190 hours. After investigating the cause of the high degradation, it was discovered that the anode inlet temperature was approximately 635°C. Inlet temperatures should be at least 655°C. Heat was lost due to long tubing runs between the stack inlet and inline preheater. Because the anode preheater was already at its maximum operating temperature of 750°C (and increasing the preheater temperature above 750°C has potential to damage the preheater heating elements), nitrogen flow was increased to 50 slpm from 3.8 slpm to carry more heat to the stack. This increased the anode inlet temperature to 656°C. The increased nitrogen flow significantly decreased degradation rate. Figure 2-117 shows the average cell voltage and change in degradation rate with the added nitrogen flow. The degradation rate of 0.83% per 1000 hours was observed over the 1267-hour period.

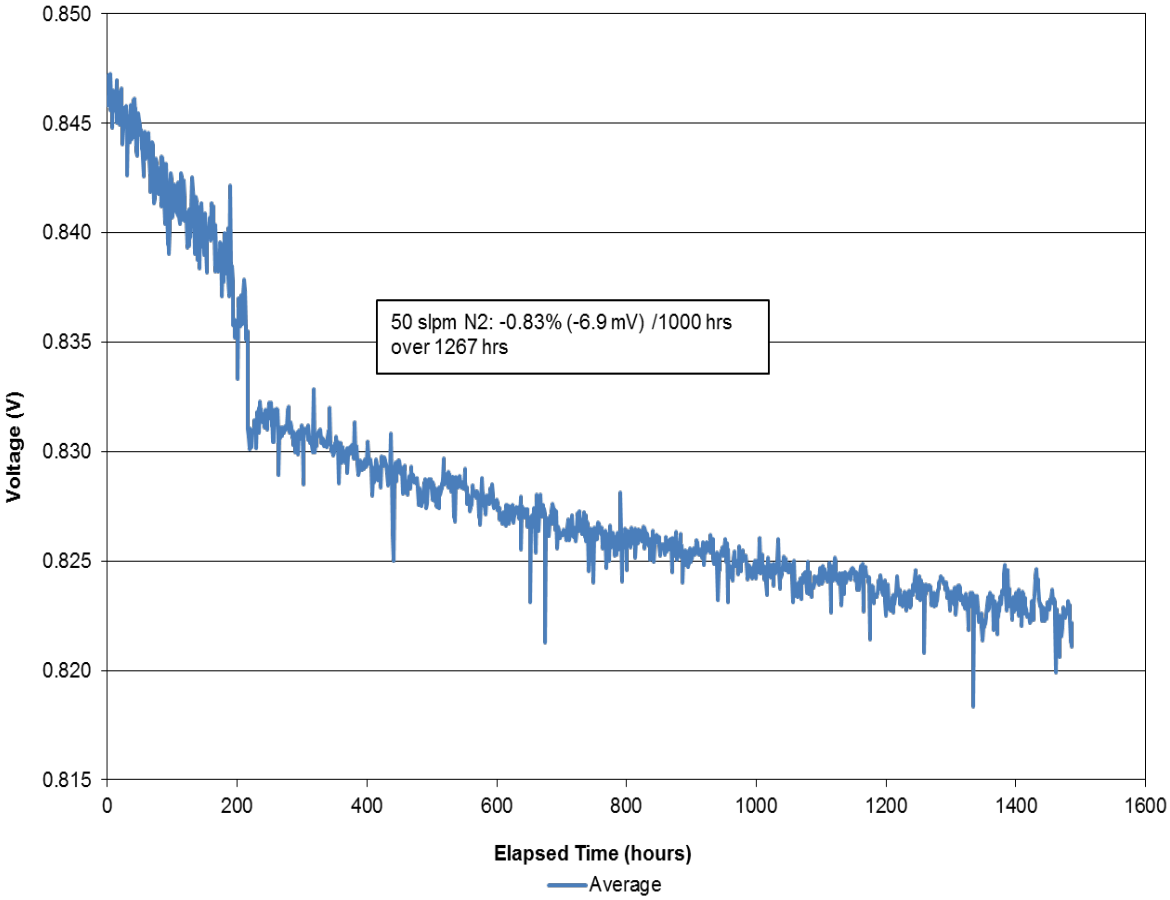

Figure 2-117. Stack GT057832-0005 Performance at Phase II System Operating Conditions (with increased N_2 flow)

This stack also had on-cell thermocouples in the stack. The stack had lower thermal gradients across the cell as well as from top and bottom of the stack with the increased nitrogen flow. Figure 2-118 shows the thermal map before (left) and after (right) nitrogen flow increase.

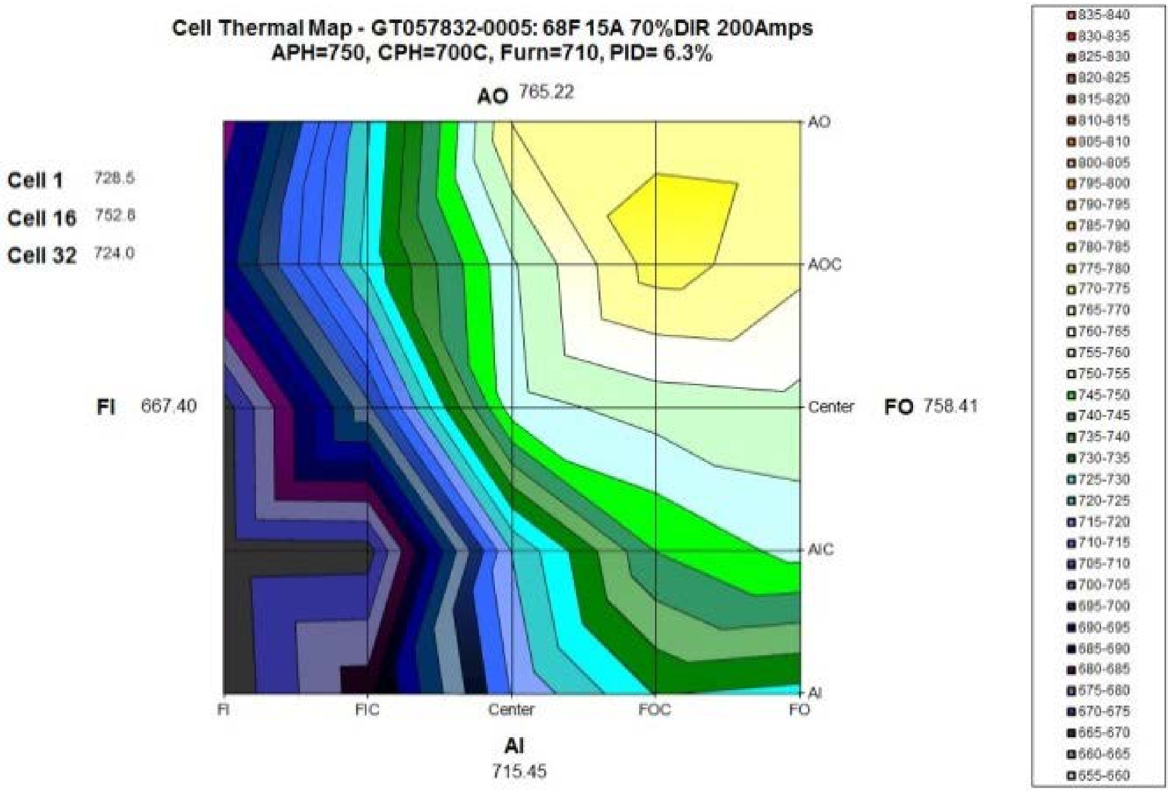

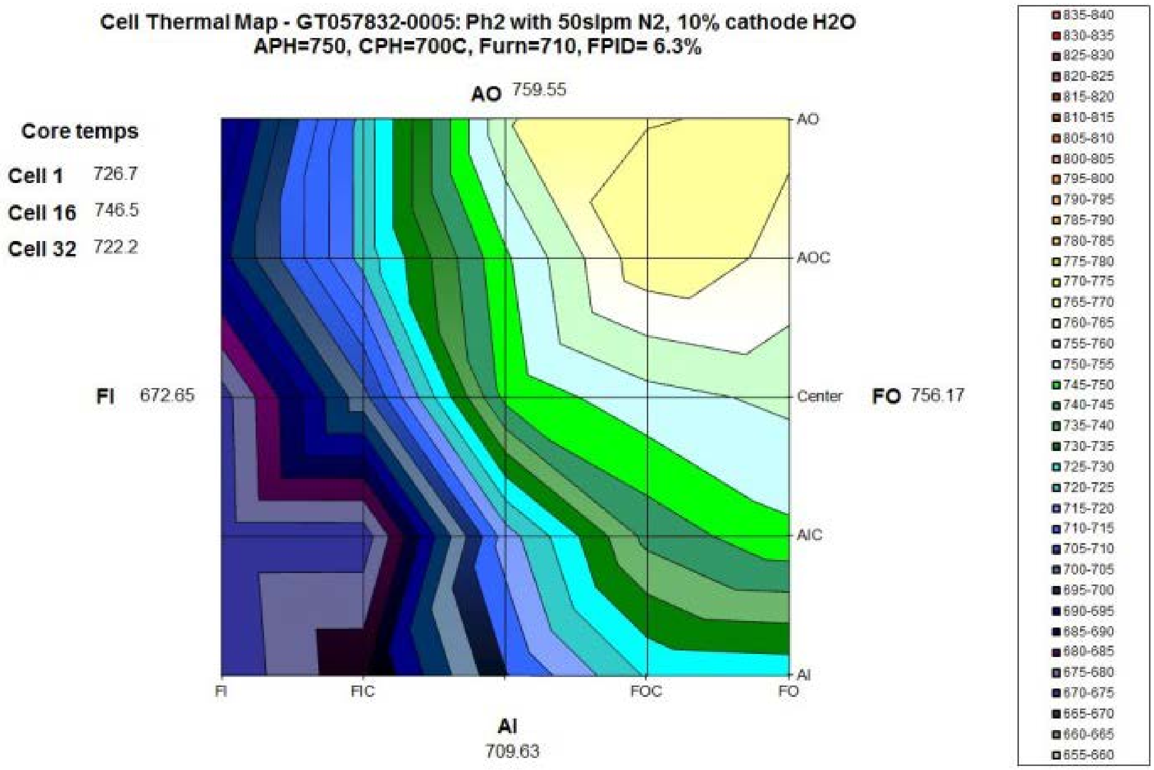

Figure 2-118. Stack GT057832-0005 – Thermal Maps Before (top) and After (bottom) N_2 Flow Increase at Anode

Testing was continued at Phase 2 system conditions with increased nitrogen flow. The test was interrupted by failure of an interlocked facility (dilution) fan. Before the fault, stack -0005 had a degradation rate of 0.65% (5.4 mV) per 1000 hours over 2388 hours. The facility trip placed the stack in hot standby mode condition. The standby mode did not flow cathode purge resulting in cathode preheater failure. After cathode preheater repair, the stack was heated back up and was operated at the same conditions as before the fault (Phase 2 system conditions with increased nitrogen flow). Figure 2-119 presents the test results showing significant decrease in cell voltages after the fault. Investigation revealed that all flows, temperatures, and current were the same as before the fault.

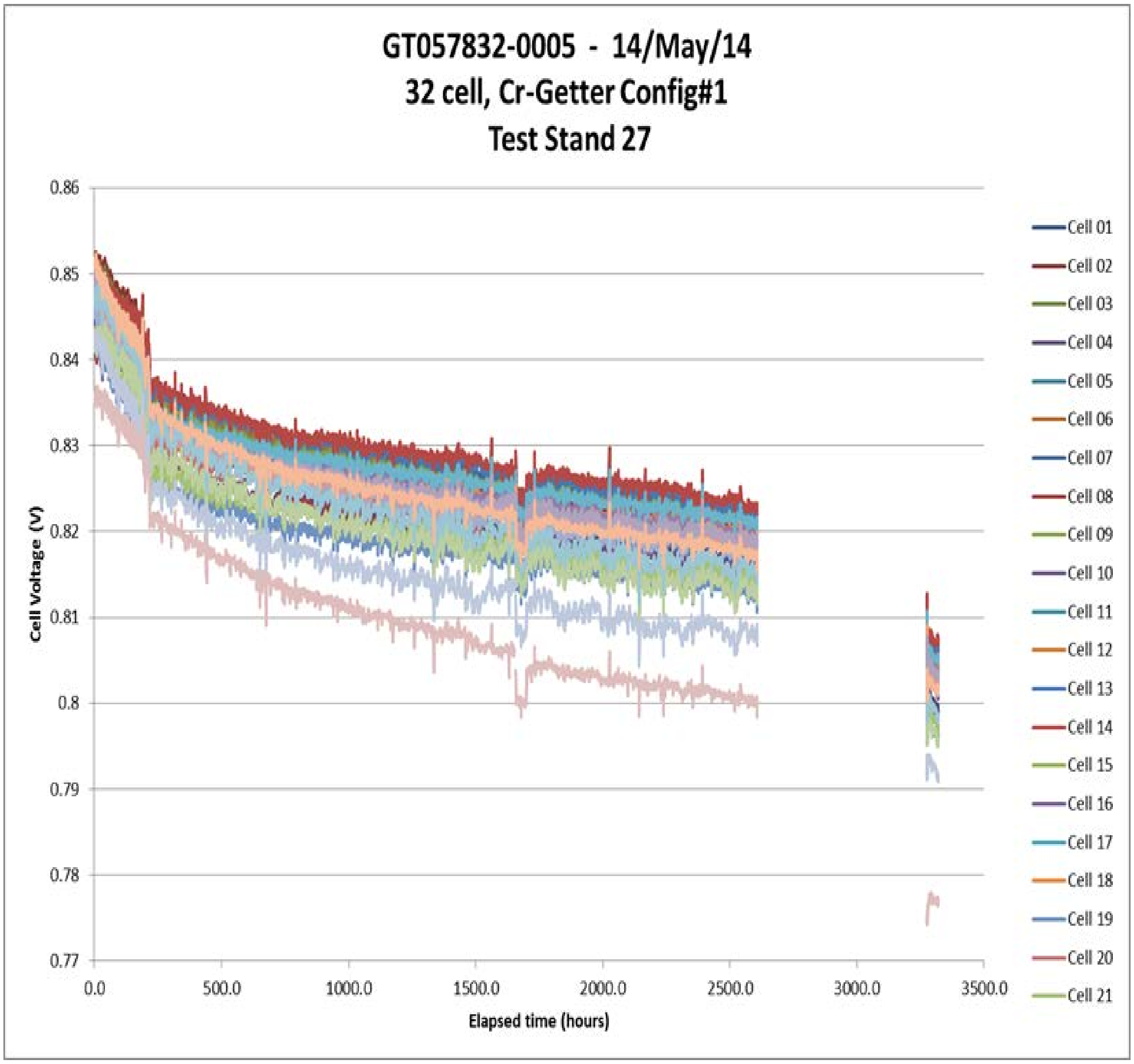

Figure 2-119. Individual Cell Performance Trends of Stack GT057832-0005 at Phase 2 System Operating Conditions (with increased N_2 flow)

Figure 2-120 shows average cell voltage and cathode exhaust humidity trends. The decrease in cell voltages after the fault may be explained by the increase of humidity in the cathode exhaust from 0.2% to 1.4%. This is indicative of cross leakage and possible damage to the stack.

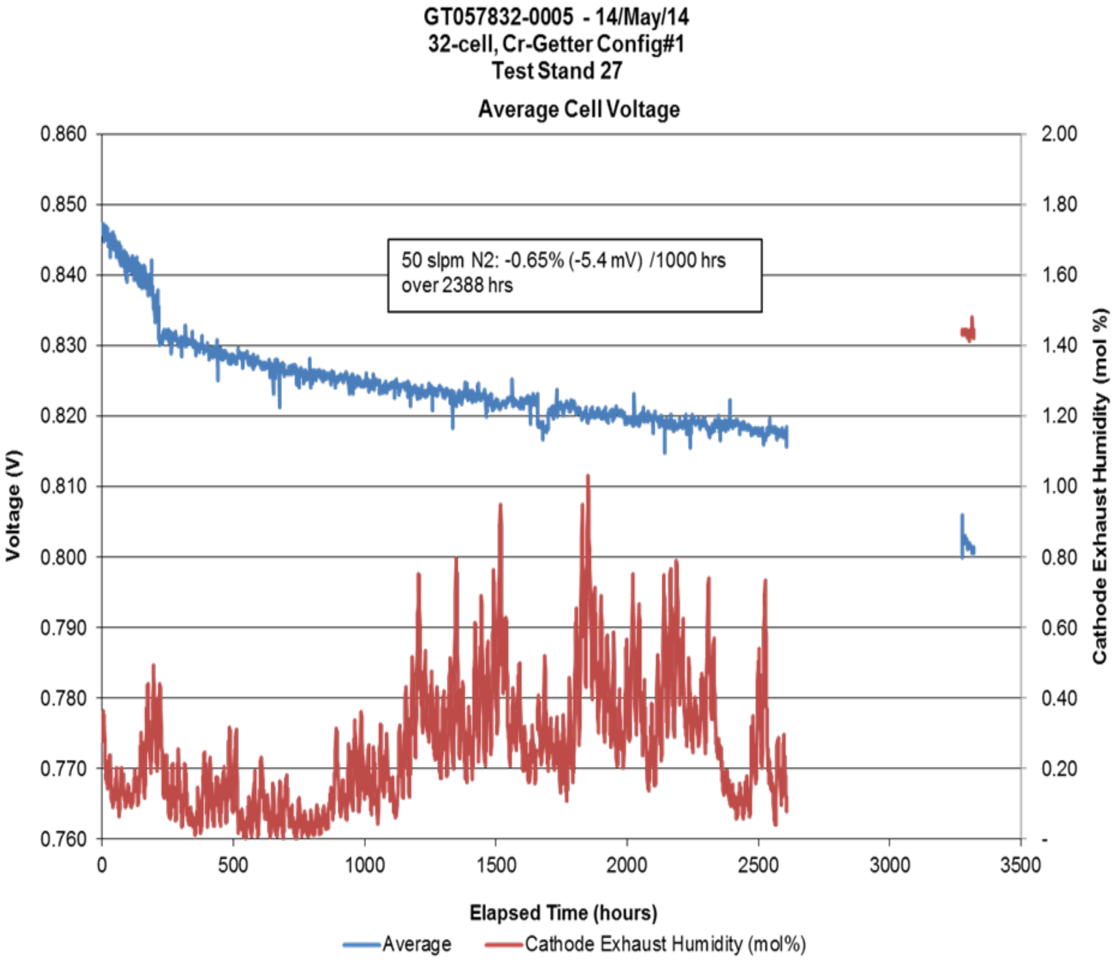

Figure 2-120. Stack GT057832-0005 Performance Stability at Phase 2 System Operating Conditions (with increased N_2 flow)

Stack GT057235-0108: Stack -0108 was a 16-cell large area stack containing cells with Cr-getter Configuration 2 (C2) and anode flow fields utilizing a base material of 0.010” thickness. This stack was stable at 80% fuel utilization during fuel utilization testing after thermal cycle (TC1, Figure 2-121). During fuel utilization testing before thermal cycle (TC0) there was a cathode preheater failure and the stack had to be shut down to replace the preheater.

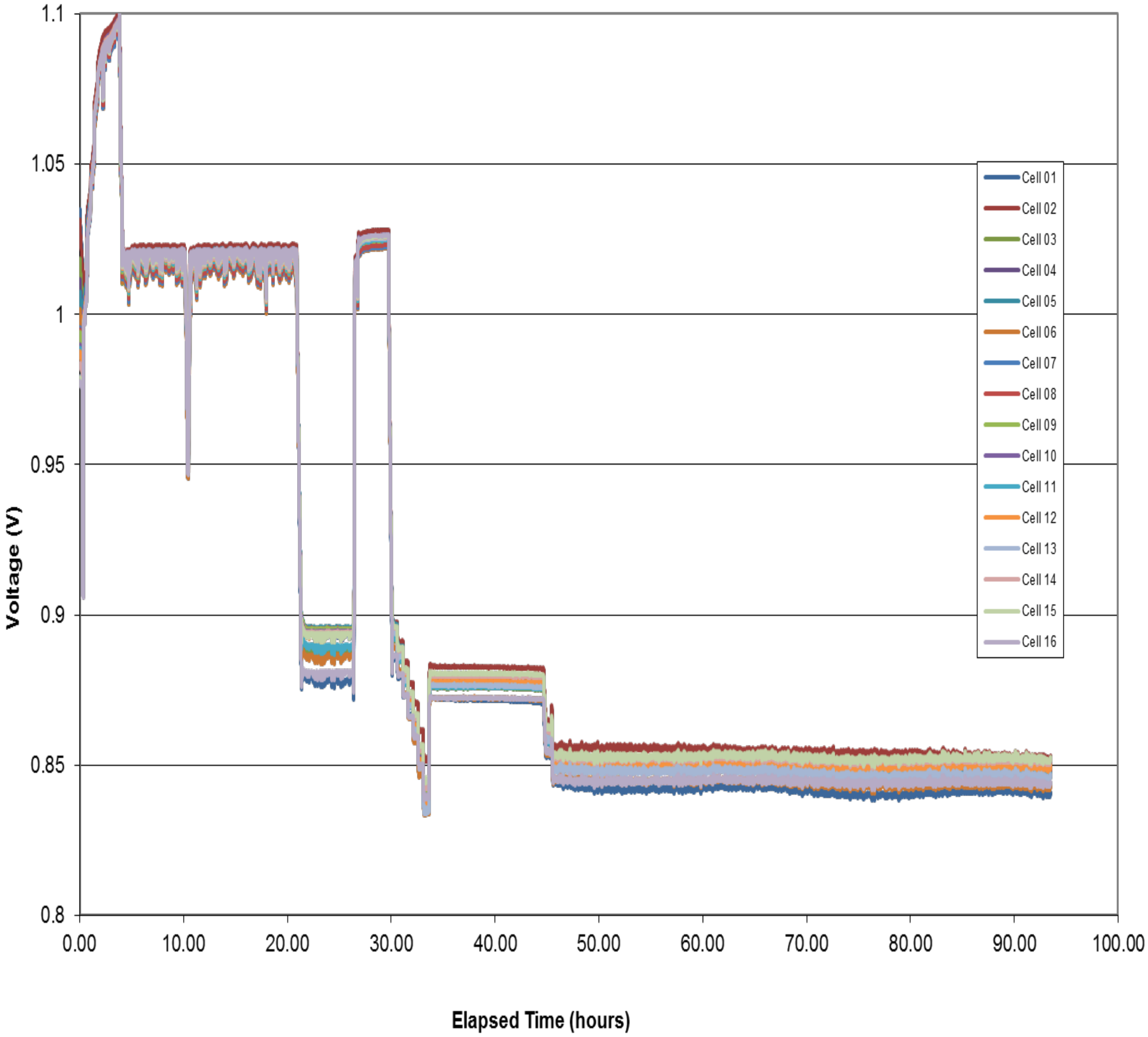

Figure 2-121. Stack GT057235-0108 Fuel Utilization Testing After First Thermal Cycle

The stack was tested at Phase 2 system operating conditions (68% fuel utilization, 70% in-stack reforming, 15% air utilization and 388 mA/cm^2) for 741 hours. It had a high initial degradation rate of 2.3% (20 mV) per 1000 hours.

After this period, humidity was introduced on the cathode side and the stack operated for additional 628 hours with a degradation rate of 1.7% (14 mV) per 1000 hours. Figure 2-122 presents the test results.

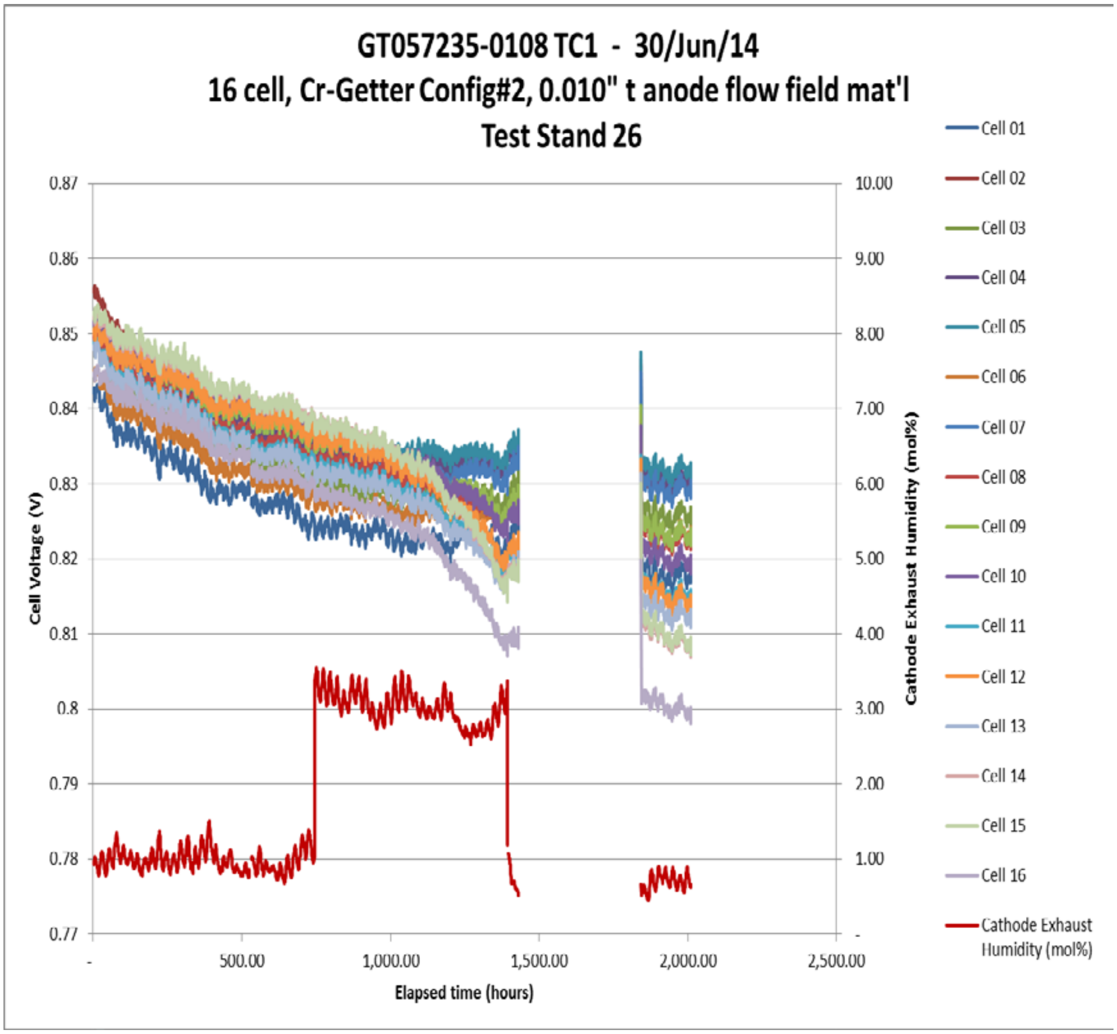

Figure 2-122. Individual Cell Performance Trends for Stack GT057235-0108 at Phase 2 System Operating Conditions

While testing under the cathode gas humidity test condition, degradation rate increased in the bottom half (eight to nine cells) of the stack while degradation rate decreased in the top half. Figure 2-123 shows a comparison of individual cell performance and degradation rates, before and after this transition.

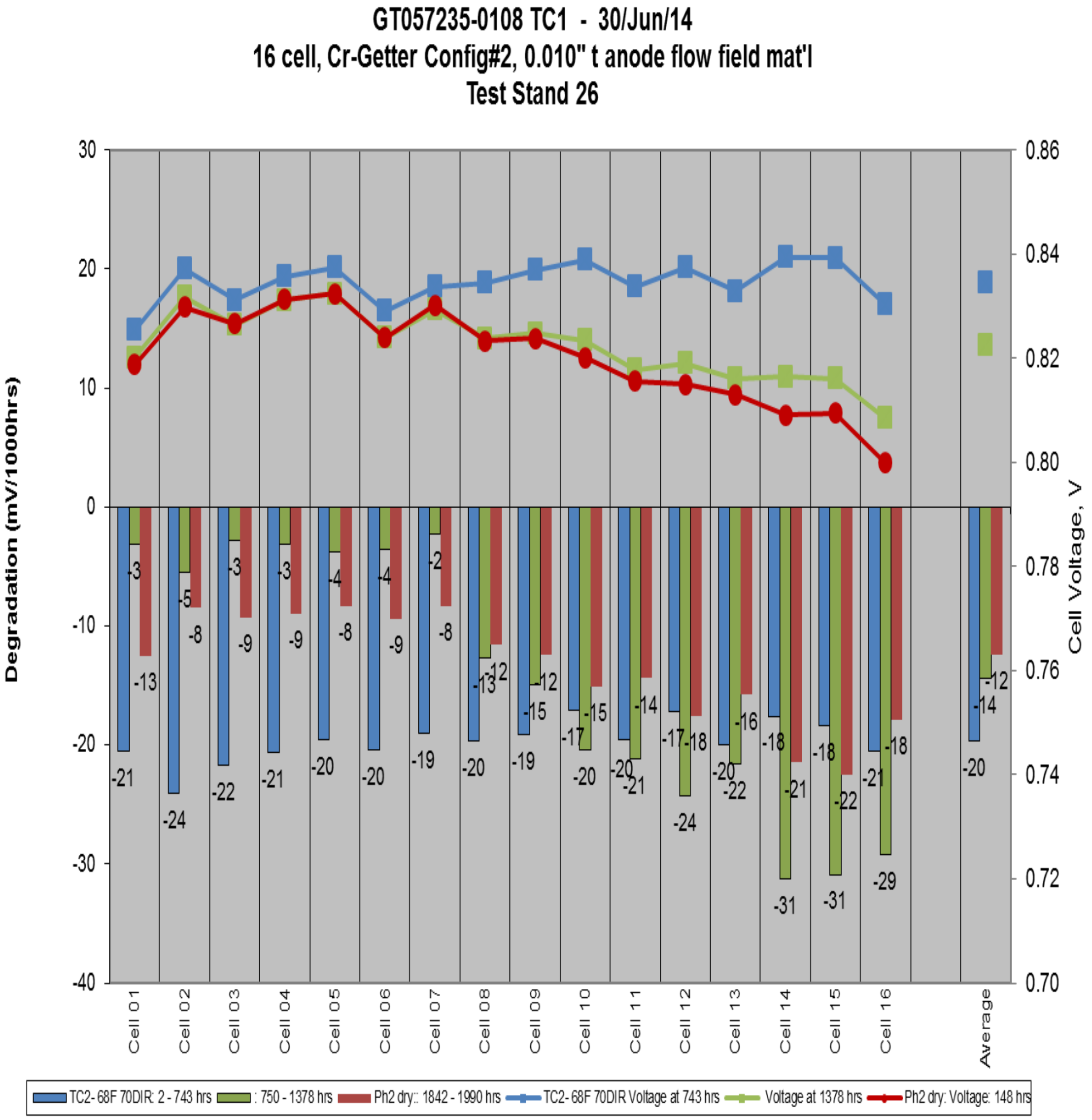

Figure 2-123. Individual Cell Performance and Degradation Rates in Stack GT057235-0108 at Phase 2 System Conditions

The test was interrupted due to failure of a solid state relay (SSR) module for the 24-volt power supply. The stack had to be cooled to room temperature to replace the part. Degradation rate after the repair was 1.5% (12.4 mV) per 1000 hours for 148 hours operation with dry cathode air. It was decided to terminate this test.

It seems that the anode flow field may not be the main driving factor for higher degradation of the most recent stacks. The test results indicate that Cr getter configuration C2 is the main cause.

Stack GT057235-0109 (Cr-getter C1): The lead Cr getter configuration, C1, was incorporated in stack GT057235-0109. Stack -0109 cell voltages were stable at 80% Uf during characterization testing before and after thermal cycle.

Steady-state testing was initially conducted at Phase 2 system operating conditions. Over the course of the steady-state testing, Stack- 0109 (and Test Stand 24) encountered several interruptions and issues. There was a facility fire alarm at 240 hours that cut off fuel gases. Stack -0109 remained hot and at OCV without hydrogen at the anode. At 962 and 1289 hours, the test stand control computer spuriously turned off and forced the test stand into an uncontrolled (e-stop type) shutdown. With the second event, the computer could not be recovered and the stack underwent a thermal cycle.

Operation during first 240 hours at Phase 2 system conditions showed a degradation rate of 0.87% (7.3 mV) per 1000 hours. After the fire alarm the degradation rate increased to 1.0% (8.7mV) per 1000 hours over 832 hours. The cell voltages increased when the stack was transitioned from Phase 2 system conditions to a drier (corresponding to higher Nernst potential) and lower current VPS gas replacement (VPS GR) condition comparable to what the stacks will see in the 50 kW stack module / system.

After 7942 hours of runtime (6562 hours of operation at VPS GR conditions), the stack test was shutdown to accommodate continued testing of new development Technology Stacks. Stack -109 demonstrated a very low performance degradation rate of 0.26% (2.2 mV) per 1000 hours over the 6562-h period as shown in Figure 2-124. The distribution of individual cell degradation rates was quite even throughout the entire stack with no cells exceeding 2.6 mV per 1000 hours as shown in Figure 2-125(secondary y-axis shows cell performance in volt).

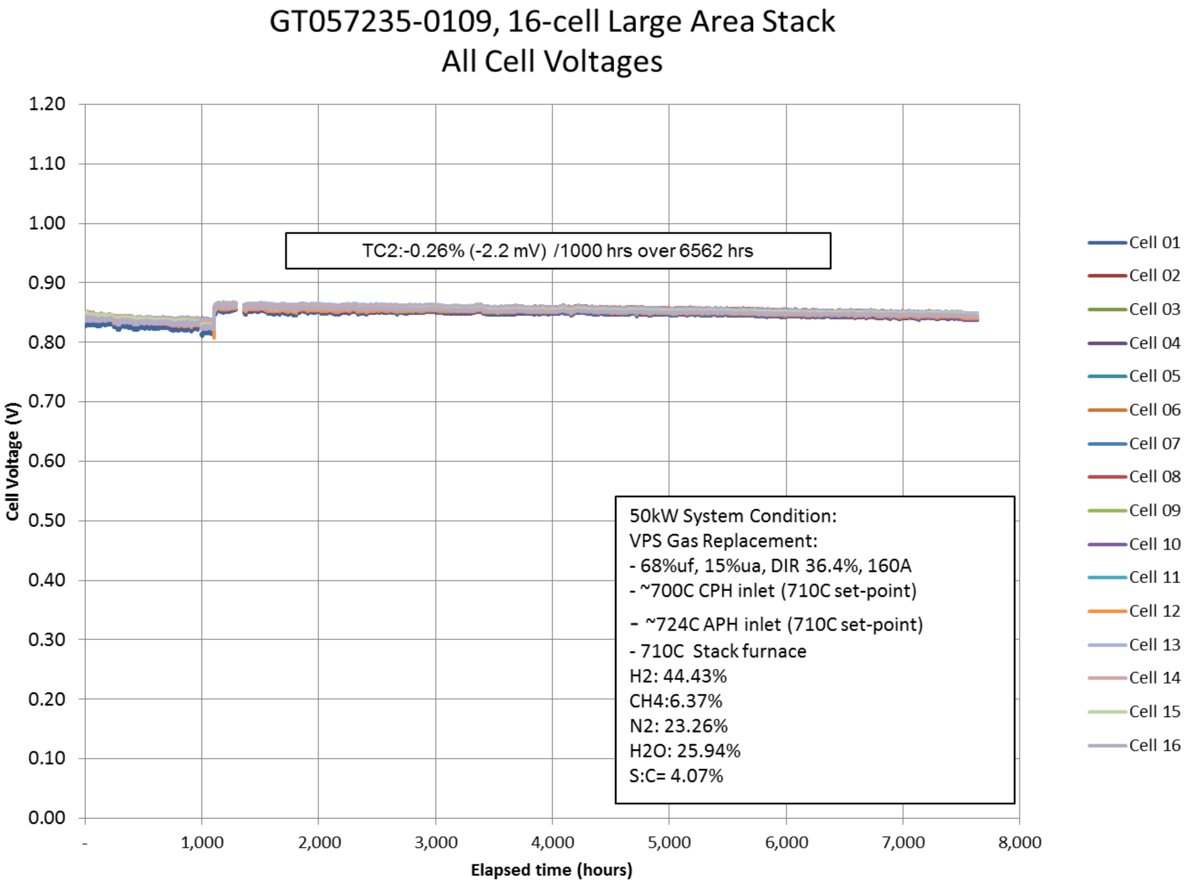
GT057235-0109, 16-cell Large Area Stack
All Cell Voltages

TC2:-0.26% (-2.2 mV) /1000 hrs over 6562 hrs

50kW System Condition:
VPS Gas Replacement:
- 68%uf, 15%ua, DIR 36.4%, 160A
- ~700C CPH inlet (710C set-point)
- ~724C APH inlet (710C set-point)
- 710C Stack furnace
H2: 44.43%
CH4:6.37%
N2: 23.26%
H2O: 25.94%
S:C= 4.07%

Figure 2-124. Stack GT057235-0109 Performance at VPS GR Conditions

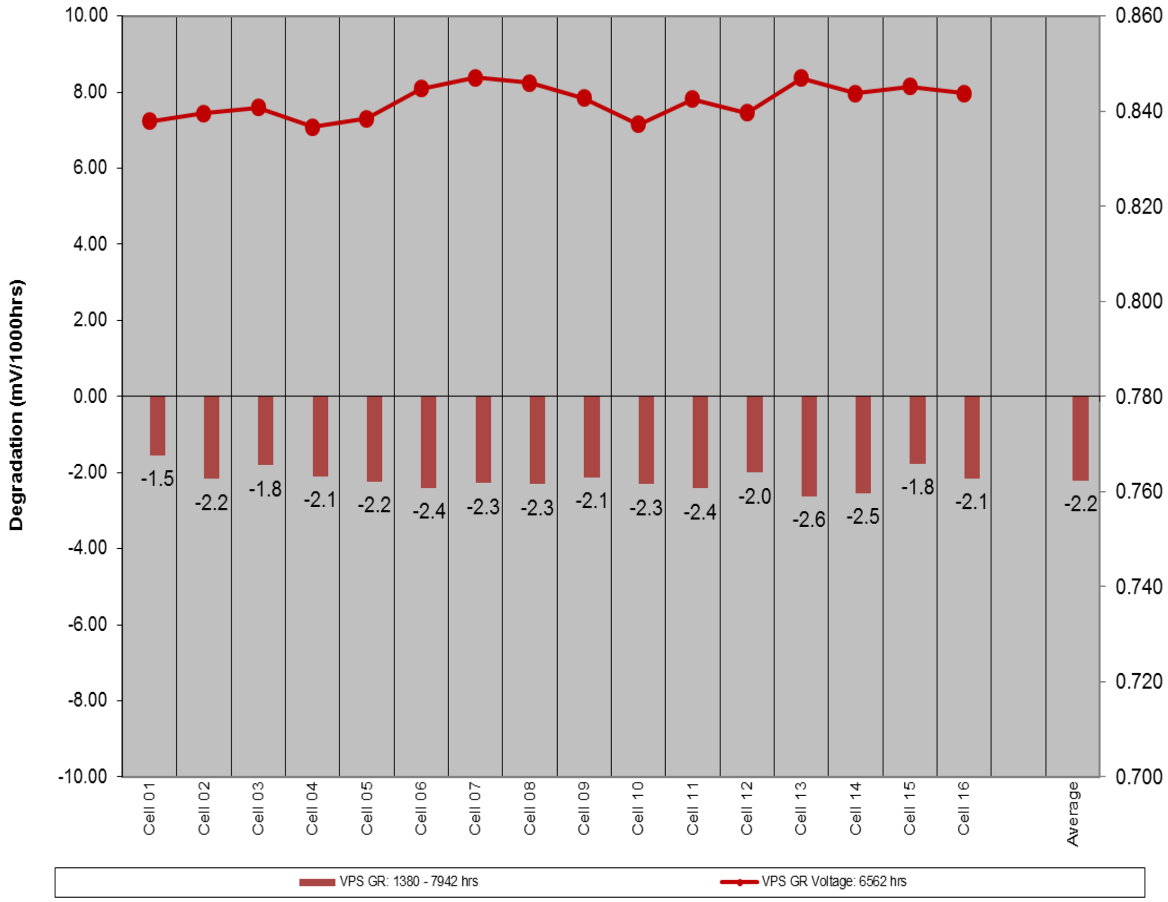

Figure 2-125. Individual Cell Performance Degradation Rate Distribution for Stack GT057235-0109 at VPS GR Conditions

VPS GR is a milder operating condition compared to Phase 2 system conditions. The degradation rate was reduced by more than the ratio of the two current densities.

Stack GT058139-0002 (64-Cell Stack, Cr-getter C1): The larger 64-cell version of stack GT057235-0109 was built to verify the performance with a taller stack (for 50 kW SOFC system stack validation). This stack was operated at a lower current density (~290 mA/cm^2) and fuel utilization (limited to 70%) in characterization tests to mitigate potential damage prior to steady state hold. Cell voltages were stable at 70% Uf during characterization tests before and after thermal cycle.

Steady state testing was conducted at VPS GR conditions (291 mA/cm^2, 68% fuel utilization, 36.4% in-stack reforming). Figure 2-126 presents the test results.

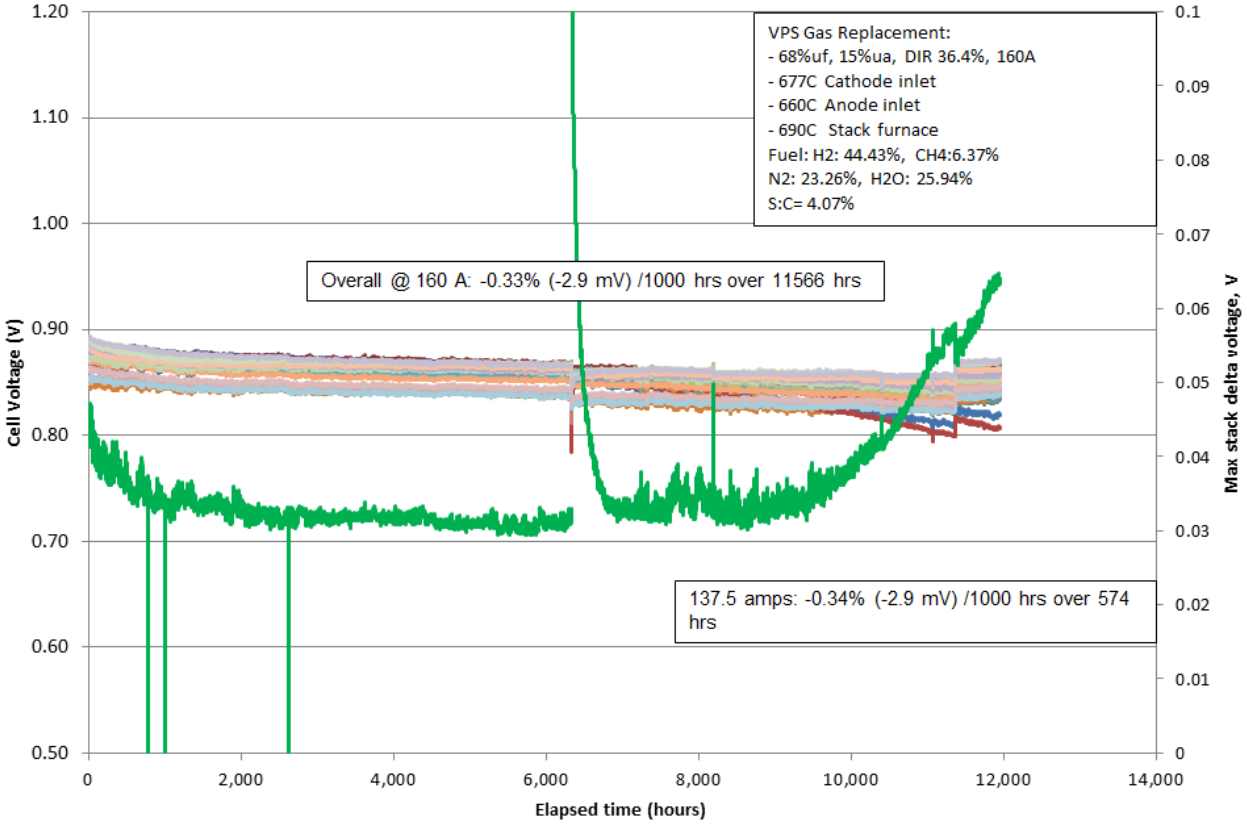

Figure 2-126. Performance Stability of Stack GT058139-0002 at VPS Gas Replacement Conditions

Degradation rate over 11566 hours was 0.33% per 1000 hours. The overall voltage spread from the highest to the lowest performing cell was ~39 mV. This confirmed the stack -0109 performance at low current density and that the VPS GR composition relates to the low degradation rate.

At approximately 10,200 hours, degradation rate for Cells 24 and 25 accelerated. It was decided to de-rate the current at 11,618 hours in an attempt to slow the degradation. As shown in Figure 2-127, the ten cells at each stack end improved in degradation rate and some of these cells were appreciating in voltage rather than degrading. Max dV increased to 64 mV. Degradation rate at 137.5 Amps was 0.34% (2.9 mV) per 1000 hours over 574 hours.

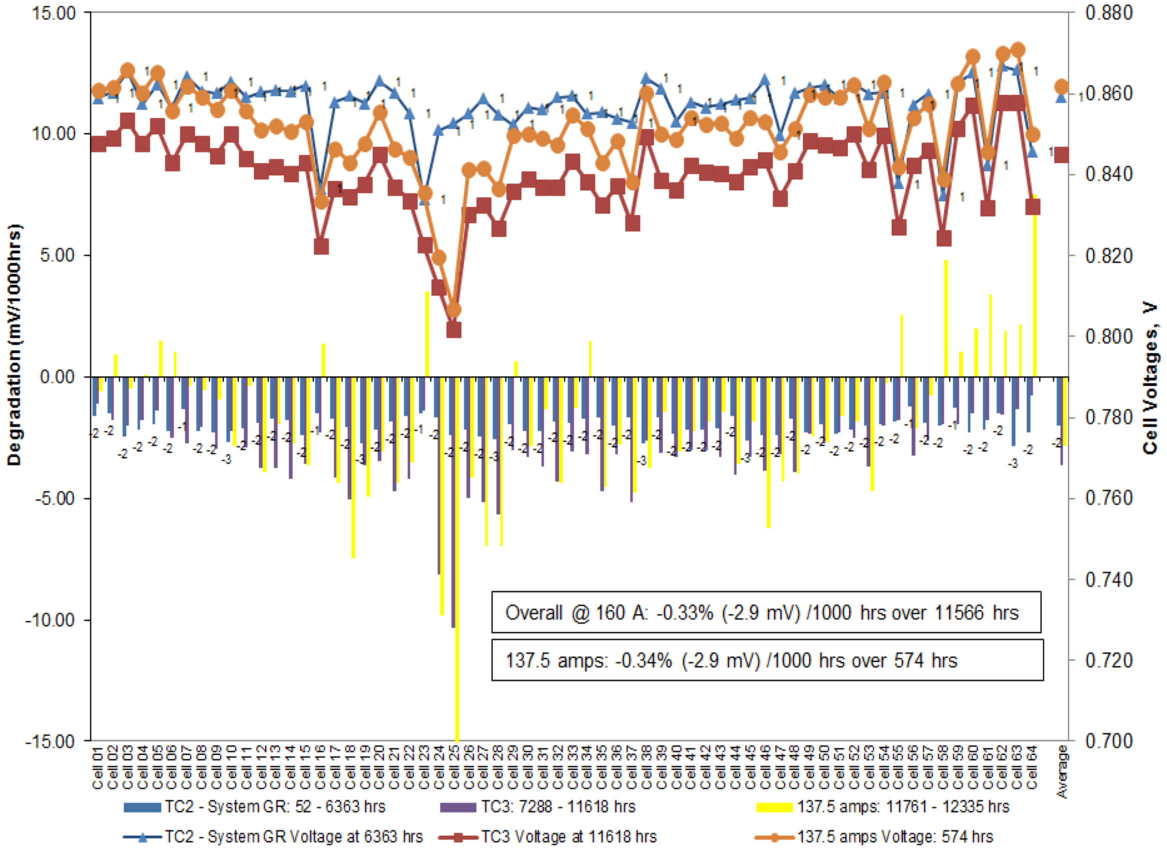

Figure 2-127. Distribution of Individual Cell Performance Degradation Rates for Stack GT058139-0002 at VPS Gas Replacement Conditions

Stack GT057235-0111 (Cr-getter C3): Stack GT057235-0111 was the first stack evaluating new Cr-getter Configuration 3 (previously tested at the single-cell level) at the large area stack level. As an added feature of this stack, a thin cobalt-coated insert was used in the cathode chamber to isolate an uncoated chromium source within the stack (uncoated ferritic stainless steel). In order to accommodate this 0.005” thick insert, the cathode flow field component was reduced in height via pinch rolling.

Stable individual cell voltages were observed up to 80% fuel utilization during characterization tests before and after thermal cycle.

The stack was initially tested at Phase 2 system operating conditions using dry cathode air for 519 hours. The cathode gas humidity condition was then adjusted from dry (~0.1 mol%) to 10 mol% for accelerated testing. Figure 2-128 presents the test results. The stack accumulated 1634 hours of testing at 10% cathode air humidity conditions showing an overall average cell performance degradation rate of 0.85% (7.1 mV)/1000 hours. As apparent from the figure, the degradation rate had increased to 1.64% (13.5 mV)/1000 hours at ~1569 hours. It is speculated that the Cr getters were saturated at this point of testing. It was decided to examine the degradation rate without the humidity addition. The performance degradation rate after restoring dry cathode air condition was ~0.4%/1000 hours.

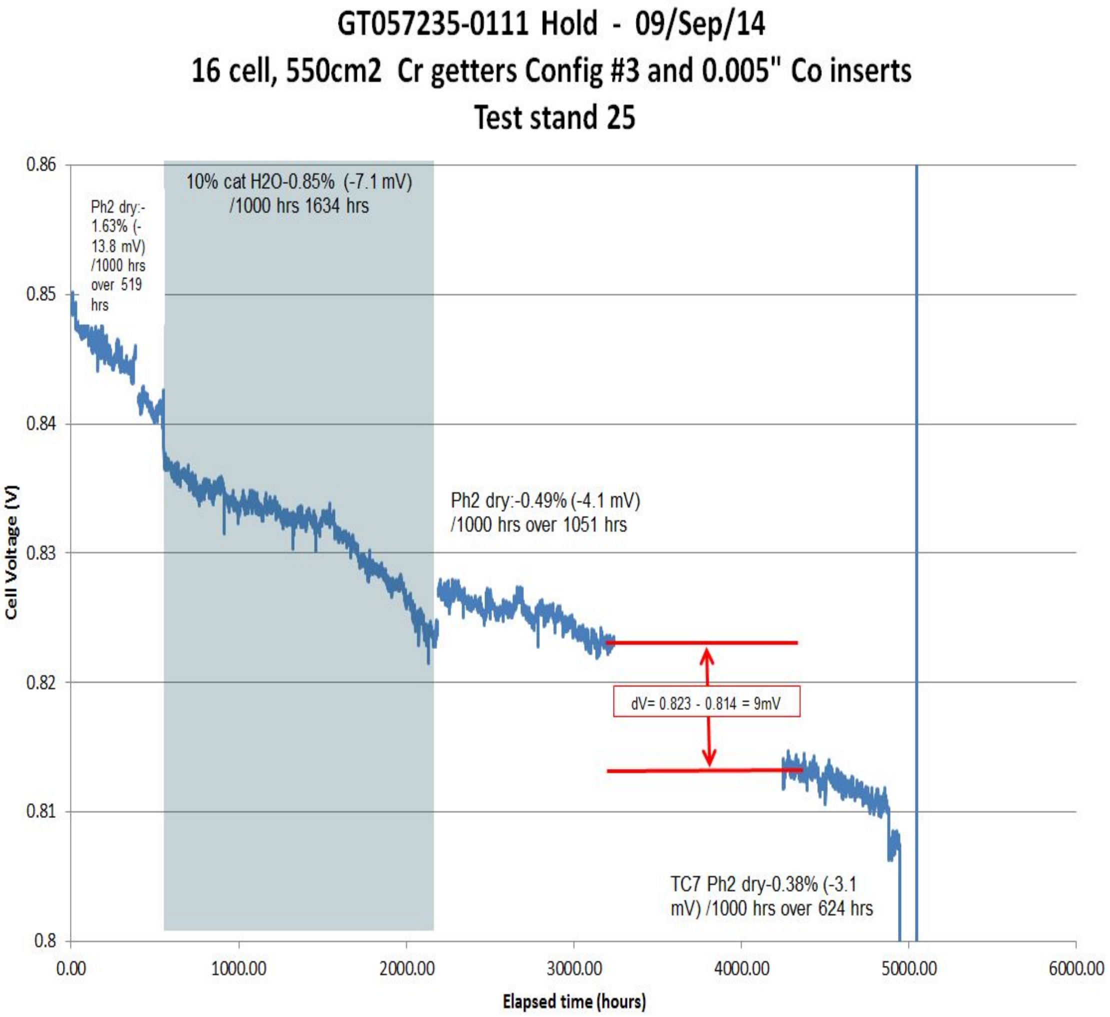

Figure 2-128. Performance Stability of Stack GT057235-0111 at Phase 2 System Conditions (with dry cathode air and with 10% cathode gas humidity)

The stack test was terminated due to rapid degradation observed in Cell 9 to 15 voltages.

Stack GT057235-0112 (No Cr-getters): Stack GT057235-0112 was an attempt to repeat the performance and degradation of stack GT057235-0097. Average cell voltages for characterization testing (both TC0 and TC1) were somewhat lower than those for stack -0097.

The stack completed over 1760 h of steady state testing at Phase 2 system conditions. As shown in Figure 2-129, the stack exhibited a performance degradation rate of 0.81% (6.8 mV)/1000 hours over the 1769- hour period. This is very close to 0.73%/1000 h degradation rate observed earlier in similar stack GT057235-0097 over 767-h period at Phase 2 system conditions. Figure 2-130 shows individual cell performance and degradation rate distribution (secondary y-axis shows performance in volt).

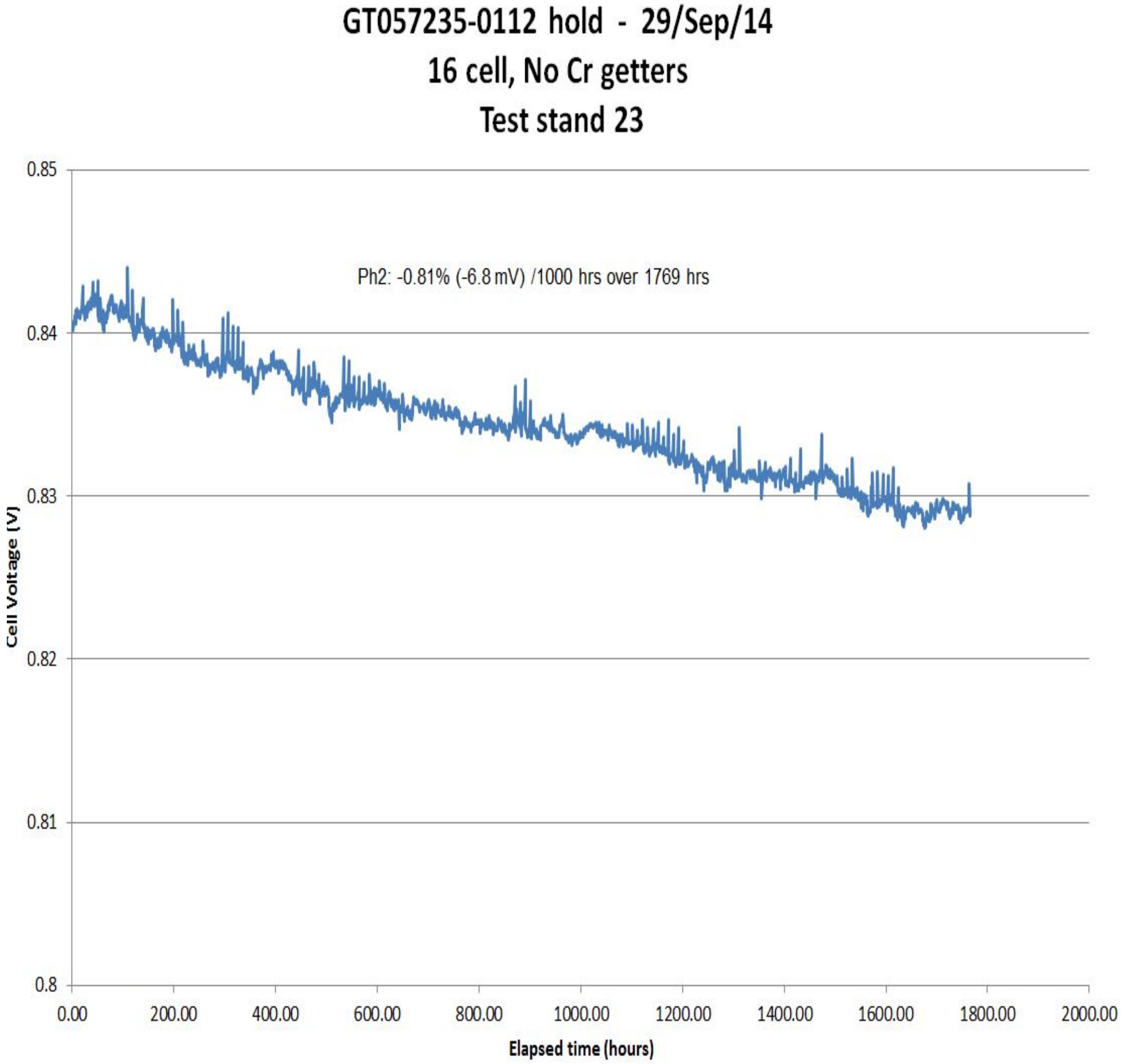

Figure 2-129. Performance Stability of Stack GT057235-0112 at Phase 2 System Conditions

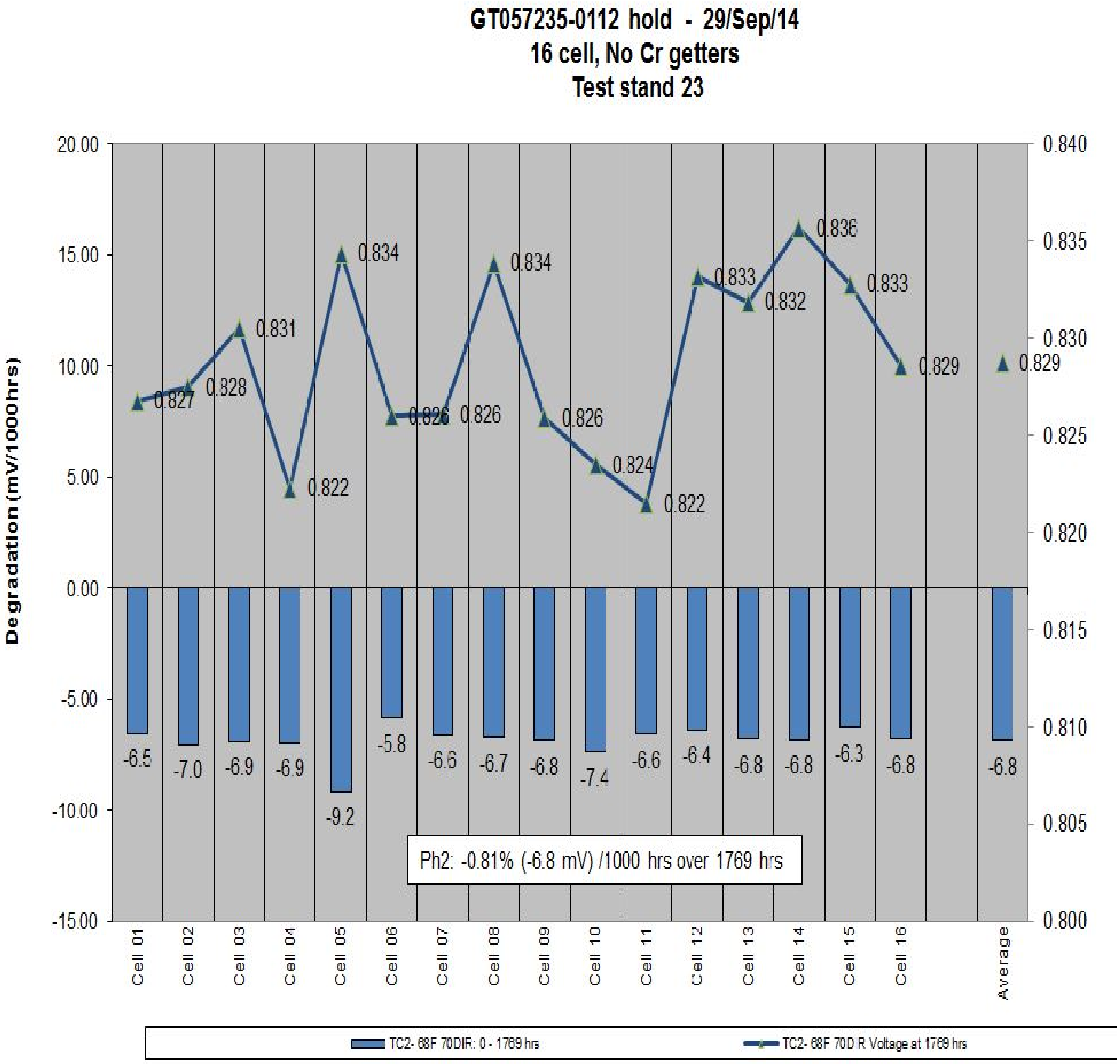

Figure 2-130. Degradation Rate Distribution in Stack GT057235-0112

Develop Test Stands for Cathode Humidity Tests

Two test stands were modified to allow testing of SOFC large area (550 cm²) stacks in size (cells/stack) up to 16 cells with cathode gas humidity. VPS test stands #25 and #26 use a new (dew-point based) humidifier system purchased from an outside vendor. Figures 2-131 show the photographs of the test area. Modifications to the existing automated test stand software were necessary to fully integrate the controls for the new humidifier system. A new software version was installed on both test stands and commissioning of test stands was carried out. The design of the humidifier allows precise control of cathode stream moisture content between 0 and 10 mole percent up to a maximum flow rate of 500 SLPM of air. Humidity below 3 mole percent is achieved by blending with dry air (using a second air mass flow controller to dilute the humidified air). The automated software controls the dew point of the air stream exiting the humidifier and then controls the blend of the humidified air and dry air to achieve accurate humidity levels. From the results of the commissioning tests it was determined to add further automation to the blending control for water vapor below 3 mole percent. Currently some manual control is required by the operator. The new software versions are validated on Test Stand #25 followed by deployment in stand #26.

Figure 2-131. Test Stand Cathode Gas Humidifier Upgrade (left) with In-Stand Dew-Point Humidifier Vessel (right)

A final software version was completed to improve some of the automated transitions between diluted and non-diluted air (for flows with less than 3 mole% humidity). It was observed through some of the tests that the airflow can momentarily drop when turning on the cathode humidifier (due to the re-direction of airflow through the humidifier instead of the humidifier bypass). Some stack performance loss can occur if the stack is under electrical load during these transitions. A testing sequence was developed to turn on the cathode dilution air during this transition to minimize the momentary loss of airflow. If the proper sequence is followed to transition to humidified air, then there is no performance loss during the switch. Both test stands are operating with Integrity Version v4.11.067.

Reliable Test Stand Development

VPS Test stand #28, which is capable of up to 25 kW size stack testing, was identified for improved reliability in order to run a two-year test of a 10+ kW stack. All high risk items were identified and tabulated. A summary of high risk items and proposed solutions include the following:

- Install manual pressure regulator and valves for pneumatic load. This will allow for improved reliability of stack compressive loading.
- Install improved cooling of electronic components to reduce possibility of component failure during a test. This is also expected to improve accuracy of some analog input channels.

- Install new cathode and anode preheaters to be consistent with preheater design installed on Test stand #27. New heaters will reduce risk of heater failure during the next test run.
- Overhaul of test stand computer and data acquisition system components. (i.e., new hard drives, new power supply, etc.).
- Calibrate components prior to test run (mass flow controllers, pressure transmitters, etc.).

Modification of VPS test stand #28 to improve test stand reliability was completed. The improvements are expected to reduce the likelihood of unintended shutdowns during the two-year test planned on a 10+ kW stack. Modifications completed include the following:

- Installed a manual pressure regulator and valves for the pneumatic load. This will allow for improved reliability of stack compressive loading. Additionally, the rubber seals in the pneumatic loading cylinder were replaced as a preventative measure and a cooling fan was added to provide local cooling of the pneumatic cylinder. The current-to-pressure controller was also replaced with a new unit as a preventative measure.
- Removed the old anode and cathode preheaters. Welding modifications were performed to the piping to allow for the installation of the new Sylvania heaters that have been successful on the other two large stack test stands (#27, #29). A new anode preheater phase-angle-fired SCR controller was also installed to provide better control of the heater and to be consistent with the controls on the other test stands. Highly efficient microporous and aerogel based insulation was installed on the piping and preheaters after pressure testing the heater and welded pipe assemblies to reduce heat loss. Figure 2-132 shows the photograph after the replacement of preheaters.
- Removed the high-temperature fiber insulation from the cathode recuperator and replaced with higher efficiency microporous and aerogel based insulation. This will reduce heat loss from the recuperator and reduce surface temperatures. A CO gas sensor in the vicinity of this recuperator which previously was getting hot was re-located to a cooler area. The improved insulation and relocation of the sensor will reduce the likelihood of heat related failures of the gas sensor.
- Inspected and cleaned (dust removed) the test stand computer and PXI real-time controller chassis. A newer model of the PXI chassis was installed and the hard drive on the PXI controller was replaced. The computer hard drives were also replaced and all software reloaded.
- Calibrated the analog voltage and temperature channels using an external voltage reference and allowed for compensation of the signals through the entire DAQ system (voltage isolators + cables + DAQ Terminal + cables +DAQ SCXI Card + cable + DAQ PXI card).
- Replaced the heat damaged thermocouple cables with cables rated for higher temperature.

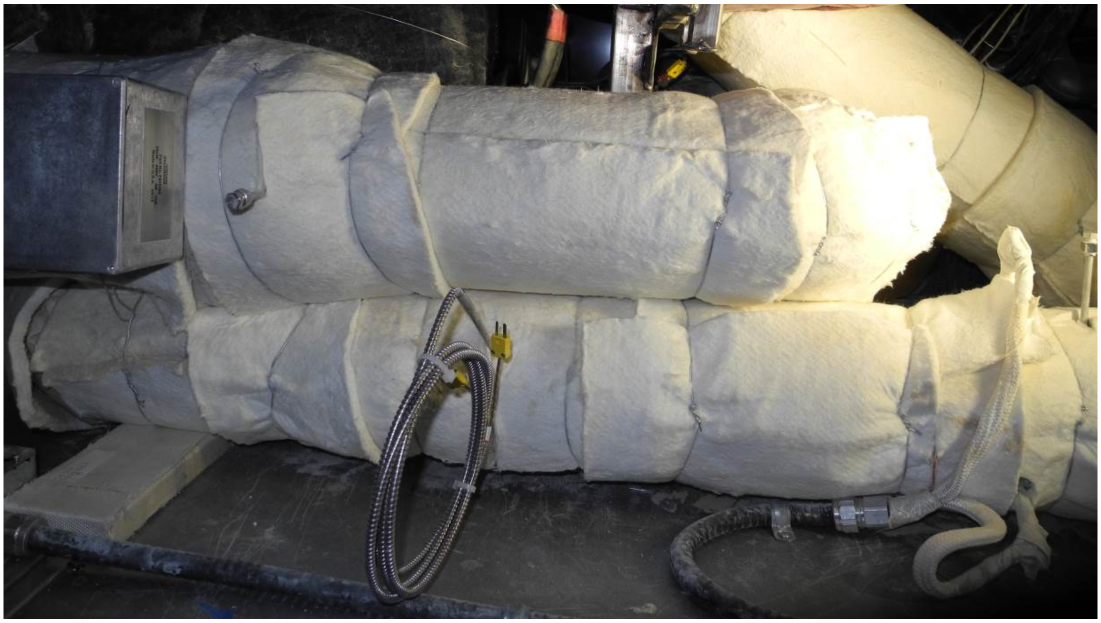

Figure 2-132. Newly Installed Cathode and Anode Preheaters after Insulation Work in Test Stand #28

- Installation of higher resolution current shunt (0-400 A) for improved feedback on electrical current.
- Calibration of humidifier water pumps for anode humidification
- Replacement of control thermocouples on stack furnace.

A short commissioning test to prove preheater operation and the stability of the humidity system was completed before the installation of a large area 64-cell stack. Stack GT058139-0002 was installed in August. The stack test in the facility has already accumulated 1500 h of operation.

Emergency shutdown sequence files

A review of the emergency action sequence files in the Integrity software was performed to understand the actions taken during various test stand shutdown scenarios. This was prompted by cathode preheater failure on another test stand (#27) during a safety shutdown caused by a plant ventilation alarm.

During the review, it was determined that in two out of the seven possible emergency shutdown sequences, the air flow was fully interrupted and the cathode heaters were simply allowed to free cool with no air flow. Due to the order and timing of the shutdown sequence, there was also a two second delay (after air flow was stopped) before the preheater set-points were set to zero. It was widely agreed among the team that these sequences place great strain on the cathode preheaters and could be the cause for some of previous failures).

As a result, the emergency action sequence files were revised (to Version 1.4 of the emergency actions spreadsheet) to increase protection of the cathode and anode preheaters. Changes include ensuring that cathode purge is turned on in cases where the air is shut off. The timing was updated to ensure that heaters are turned off first before any changes to flow are made in the emergency shutdown.

The updated emergency action sequences were tested to ensure functionality on TS#27 and then deployed to all other large area stack test stands (#25, #26, #28, and #29).

Testing at FCE Danbury

Stack Performance Degradation Rate Demonstration

Preparations for the steady state stack performance degradation rate demonstration were carried out. Necessary facility maintenance was performed along with a hot-test in the 30kW-5 test facility in Danbury. The hot-test was used to verify the functionality of all major equipment prior to the installation of the test stack. A 16-cell large area stack, GT057235-0100, was installed into the 3 kW thermally self-sustaining module, shown in Figure 2-133. Testing was performed at a system-relevant condition representative of the 50 kW PCM system.

Figure 2-133. 3 kW Thermally Self-sustaining SOFC Stack Module Installed in FCE Danbury Test Facility TF-30kW-5

The anode feed gas simulated the expected gas temperature and composition at the outlet of the radiative fuel reformer. Since this anode composition would result in less direct internal reforming and the radiative reformer was not being used (in the 16-cell stack test module) to draw heat away from the stack, the stack temperature was managed by increasing the cathode air flow. To begin with, the fuel utilization was controlled to 70% and the oxygen utilization was controlled to 10% by means of mass flow controllers. These flows were adjusted (minor changes) midway through testing based on gas chromatograph analysis, to ensure the utilizations were correct. Throughout the testing at FCE, the current density was held constant at 273 mA/cm^2. Additional minor changes to cathode and anode inlet temperatures were made to meet simulated system requirements.

The demonstration was completed at the end of March, 2015. The average cell voltage and current can be seen over the course of time in Figure 2-134. The stack had been on load for 6255 hours total, including 6014 hours at FCE under the system conditions. There were three steady state holds of at least 900 hours. The first hold was for 1135 hours and experienced an overall degradation rate of 0.85%/1000 hours. The second hold was for 930 hours and the overall degradation rate had decreased to 0.51%/1000 hrs. The third steady state hold lasted 2715 hours and had an overall degradation rate of 1.10%/1000 hrs with an accelerating degradation. Overall, the stack operated at simulated system relevant conditions for more than 4500 hours with an average degradation rate below 1%/1000 hrs.

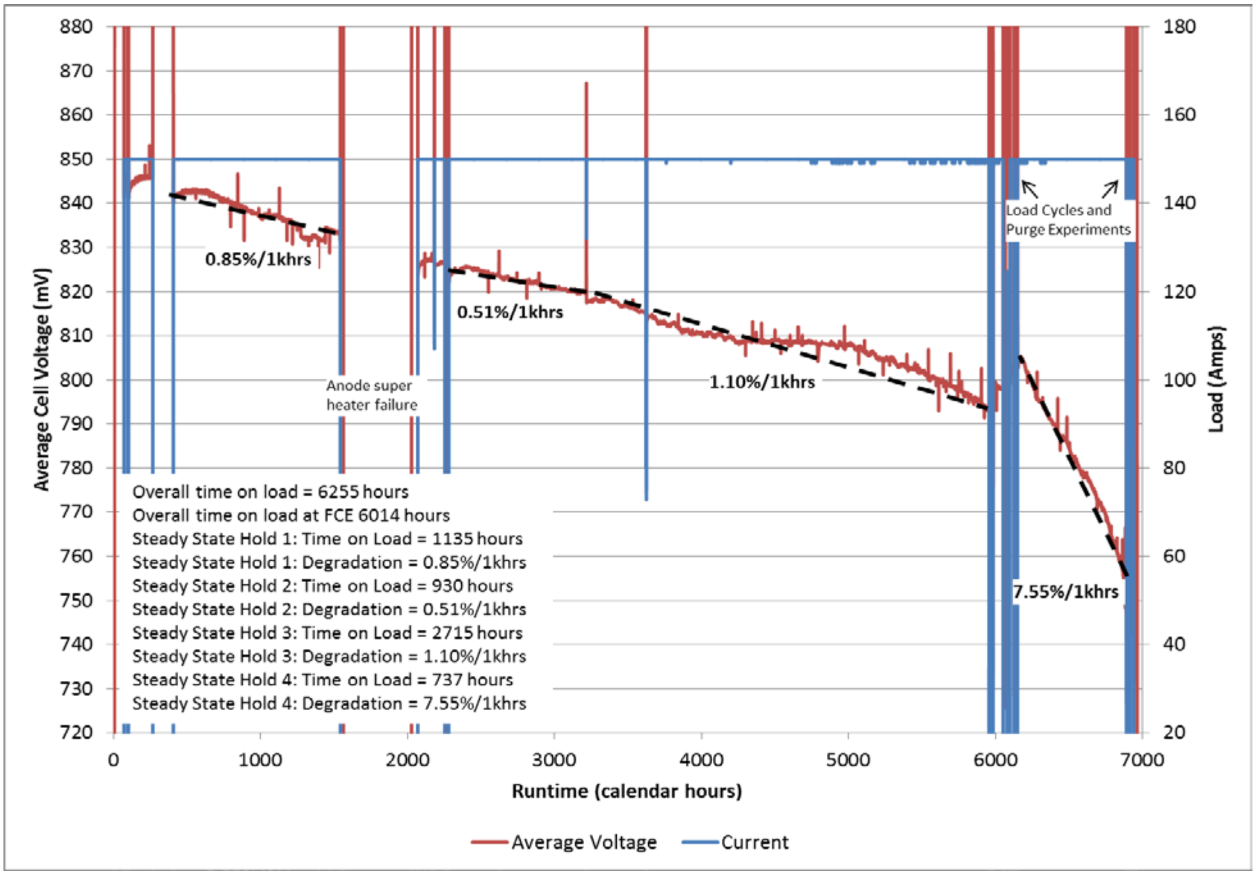

Figure 2-134. Average Cell Voltage and Stack Current During 16-Cell Stack Test GT057235-0100

While the stack was operating on load, an anode heater failure forced a shutdown. After shutting down the stack, a replacement anode heater was installed. The stack was then returned to the same operating conditions and was running steadily.

As shown in Figure 2-135 the cell voltages were very uniform through the first steady state hold, with the exception of Cell 16, which had a much lower voltage from the start of testing, likely due to electrical contact issues. In the second hold, Cells 1 and 3 began to degrade at an advanced pace. Cell 1 continued to degrade in the third steady state hold while Cell 3 began to level out. In addition Cell 5 started to degrade at a high rate. Throughout these holds, Cell 16 voltage either remained constant or improved, potentially due to contact improvement from increased heat generation caused by stack degradation.

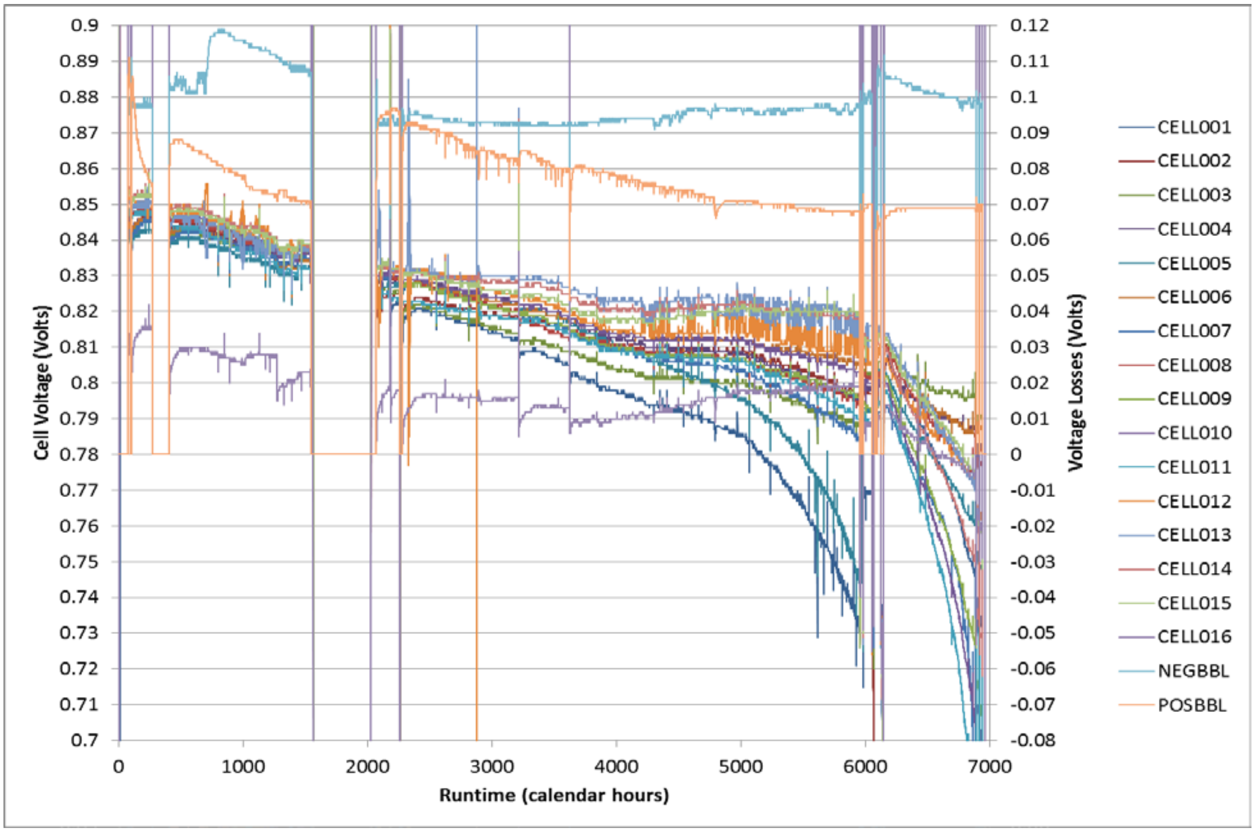

Figure 2-135. Individual Cell Voltages and End-Losses During 16-Cell Stack Test

A couple adjustments were made to the cathode and anode heaters after roughly 1000 hours of operation. After the changes, the stack manifold temperatures increased relatively slowly through the first three steady state holds. The average manifold temperature increase was 0.98°C/1000 hrs. As shown in Figure 2-136, after the first four load cycles, the manifold temperatures began to increase more rapidly due to stack degradation.

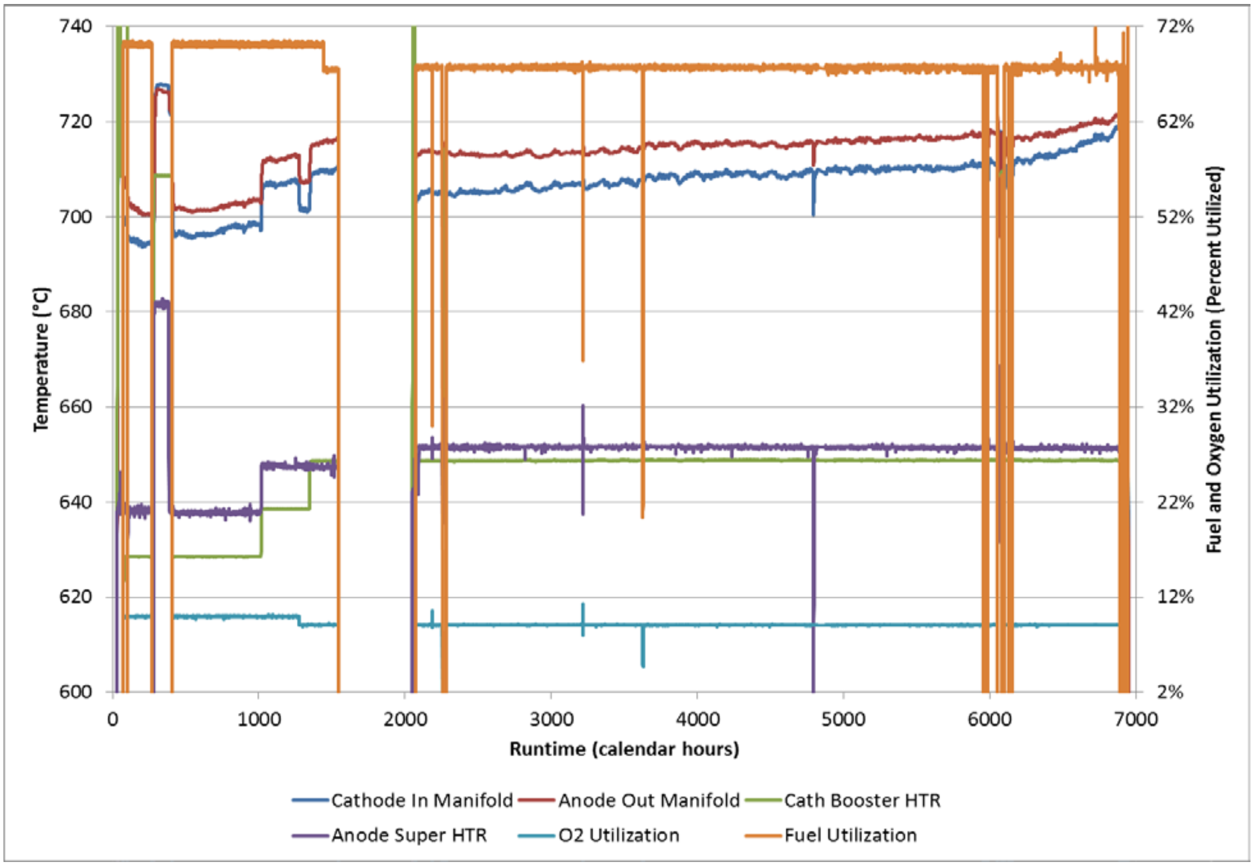

Figure 2-136. Manifold and Heater Temperatures and Reactant Utilizations During 16-Cell Stack Test

Initially, the system was set up using back-pressure valves to maintain the cathode inlet and outlet manifold pressures to be slightly above the anode manifold pressures. The pressures were observed to increase rapidly over the first 750 hours of testing before suddenly dropping. This was caused by water condensation accumulation in the exhaust piping and was resolved by decreasing the quench air flow to the oxidizer. This increased the oxidizer combustion temperature, maintaining all water in the vapor phase. Throughout the first three steady state holds, the cathode pressures remained fairly constant while the anode inlet, anode outlet, and anode pressure drop all slowly increased, exceeding the cathode pressures. The trend plot is shown in Figure 2-137.

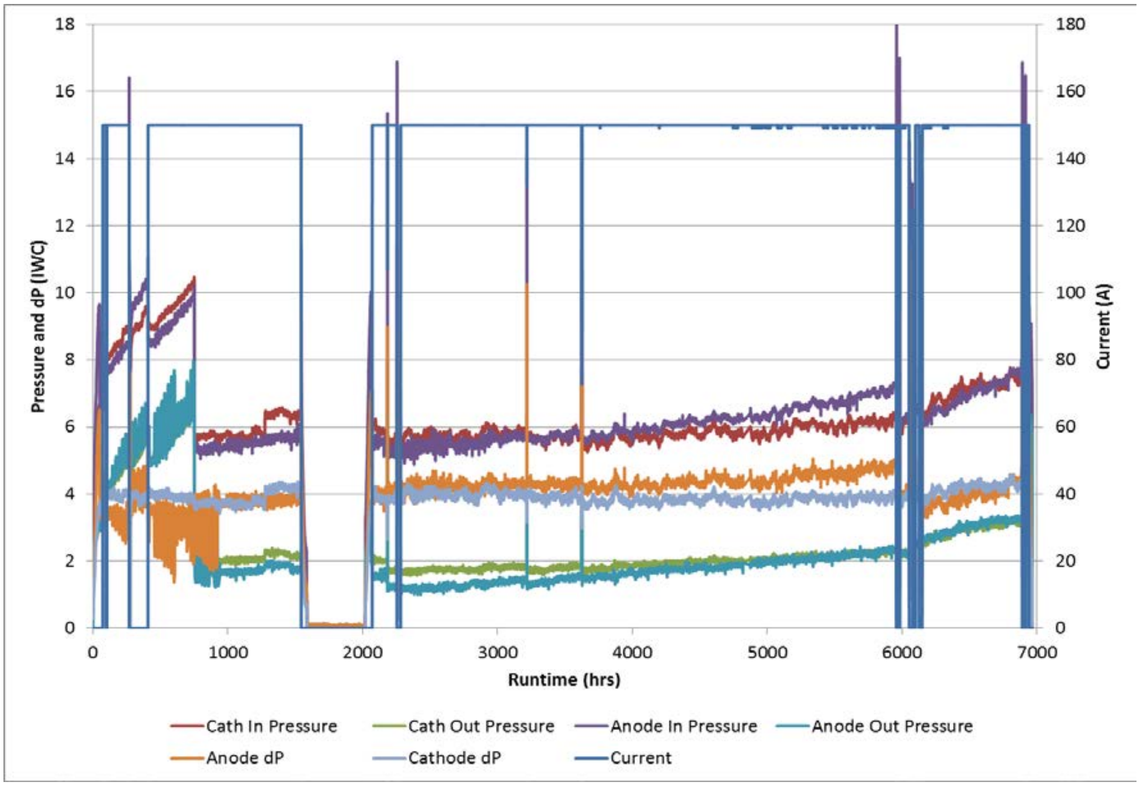

Figure 2-137. Manifold Pressures and Cell Pressure Drops During 16-Cell Stack Test

Once the degradation rate exceeded 1%/1000 hrs in the third steady state hold (just prior to 6000 hour runtime, caused primarily by the degradation of Cells 1 and 5), steady state testing was concluded. Several load cycles were performed for evaluation of potential system shutdown conditions. In the event of loss of fuel, a purge gas is required to prevent anode oxidation. Typically, a gas mixture containing 4% hydrogen in nitrogen is used. However, the use of pure nitrogen would be a cheaper and simpler alternative. To prevent oxidation, the anode would be pressurized with nitrogen to prevent cathode air from leaking to the anode. To evaluate this condition, the stack was ramped down to OCV condition and allowed to stabilize. Anode water and hydrogen were shut off, the anode nitrogen flow was increased to 4.5 scfm, and the cathode air flow was decreased from 16.7 scfm to 5 scfm. The anode back pressure valve was closed; increasing the anode outlet manifold pressure to ~0.5 iwc above the cathode inlet manifold pressure, ensuring the entire anode was at pressure above cathode-in pressure. After variable amounts of time, the stack was returned to normal OCV conditions and ramped back on load to the steady state conditions previously demonstrated. This served as the worst-case scenario by maintaining high temperatures at OCV condition, in a real system, this condition would only occur in a situation when the stack is cooling down. Additionally, this was considered a worst case scenario based on facility limitations to fully pressurize the anode well above the cathode. This procedure was performed four times; lasting for 40 minutes, 90 minutes, 13.7 hours, and 20.5 hours, respectively.

During the first two load cycles and nitrogen purges, the cell voltages decreased from OCV and held at ~735 mV for the duration of the purge. This voltage was expected based on the electrochemical potential between oxygen and reduced nickel in the anode. The third purge was meant to run for a full day, however after a number of hours, the voltage of Cell 2 began to decrease suddenly, indicating potential anode oxidation. On returning to load, there was no noticeable damage to Cell 2. So the fourth purge was performed for a full day, in which all of the cell voltages dropped after holding at ~735mV for several hours as shown in Figure 2-138.

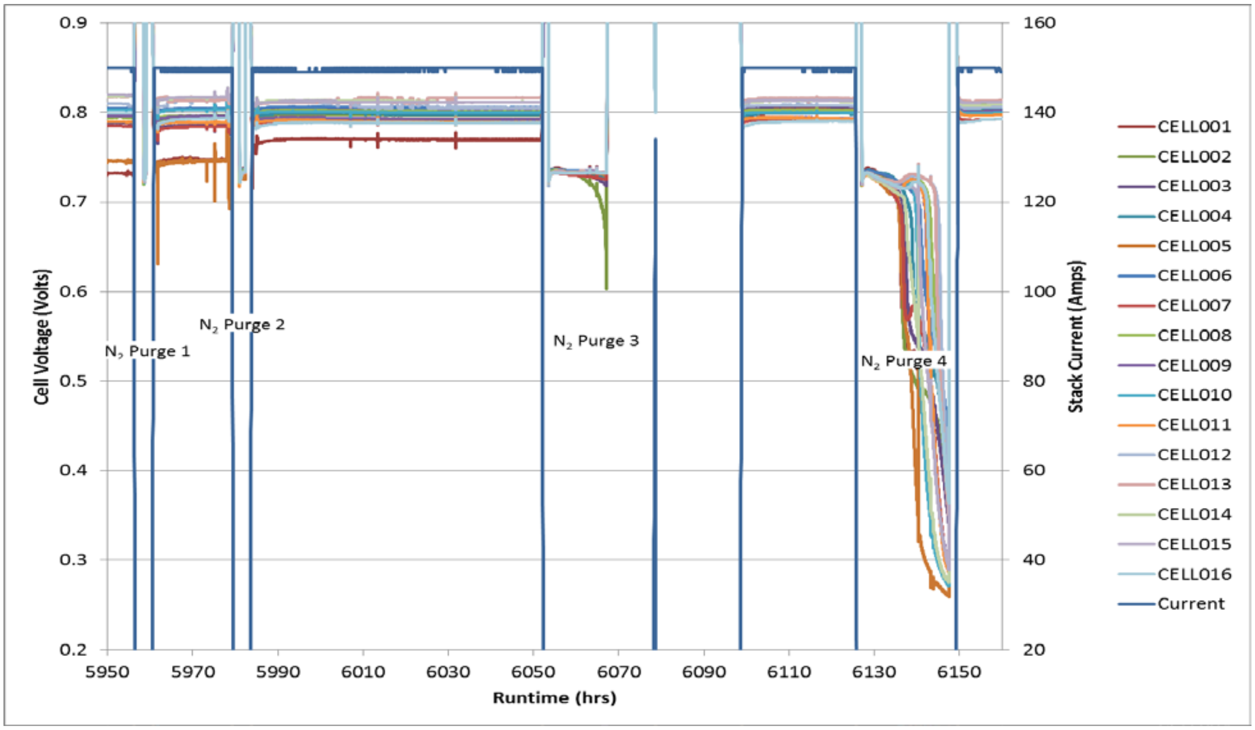

Figure 2-138. Cell Voltages and Stack Current During Load Cycle and N_2 Purge Testing

After each load cycle and nitrogen purge, the cell voltages of Cells 1 and 5, the highest degrading and lowest voltage cells, improved. After each load cycle, nearly every cell in the top half of the stack improved while nearly every cell in the bottom half of the stack experienced some minor performance loss, resulting in a net voltage improvement for the stack. This can be seen in Figure 2-139, where bars represent the individual cell voltages after various load cycles. Gain tests were performed by increasing and decreasing hydrogen flow and observing the impact on the cells. It was observed that the cells that experienced the greatest change in voltage during the gain test also experienced the greatest improvement after the load cycles.

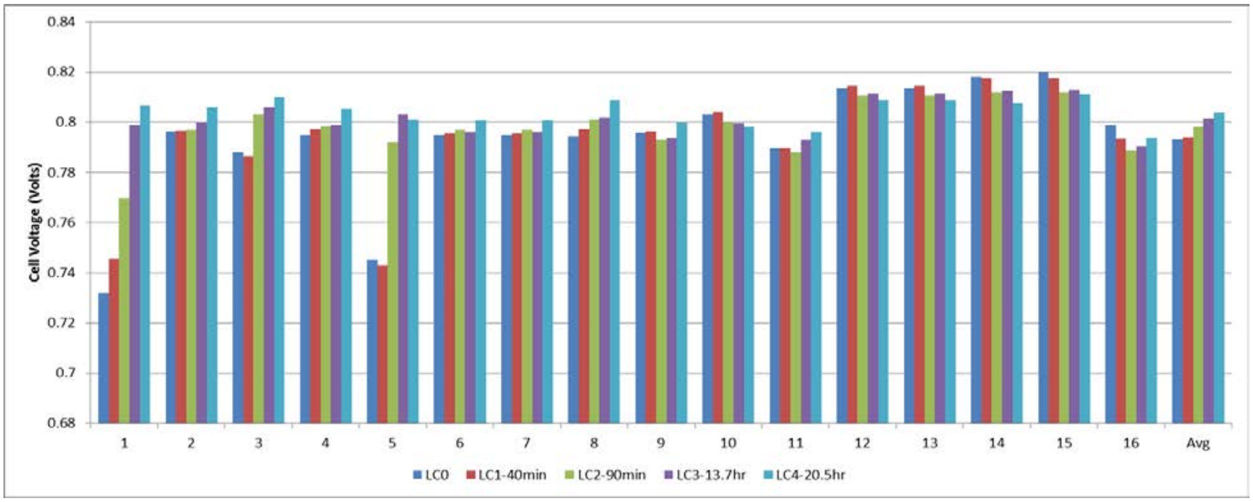

Figure 2-139. Cell Voltages after Load Cycles (of varying durations) during 16-Cell Stack Testing

After four load cycles, the stack was returned to the system conditions for another 737 hours of operation. During this time, the degradation rate had increased considerably to 7.55%/1000 hrs. At this point, two additional load cycles were performed before terminating the test.

Overall, the testing of the 16-cell stack, GT057235-0100, was very successful in demonstrating excellent performance and less than 1%/1000 hrs degradation rate while operating under system relevant conditions for several thousand hours.

2.3 Stack Fabrication for PCM System

A stack design configuration freeze for the 50 kW module stacks was implemented. The 120-cell stacks with Gen 1.0 Cr tolerant technology were built and factory tested at VPS. VPS' new 120-cell stack block design (used for PCM stack fabrication), as shown in Figure 2-140 consisted of TSC-3 cells that were 25.4 cm by 25.4 cm (0.06 cm thick) with an active area of 550 cm^2, leading to a total 66,000 cm^2 (or 6.6 m^2) of active area for each stack block. Each stack (after fabrication) was conditioned and performance tested (per Factory Acceptance Test Plan summarized below) to maximize the probability of success prior to shipping to FCE-Danbury for module installation and follow-on system testing.

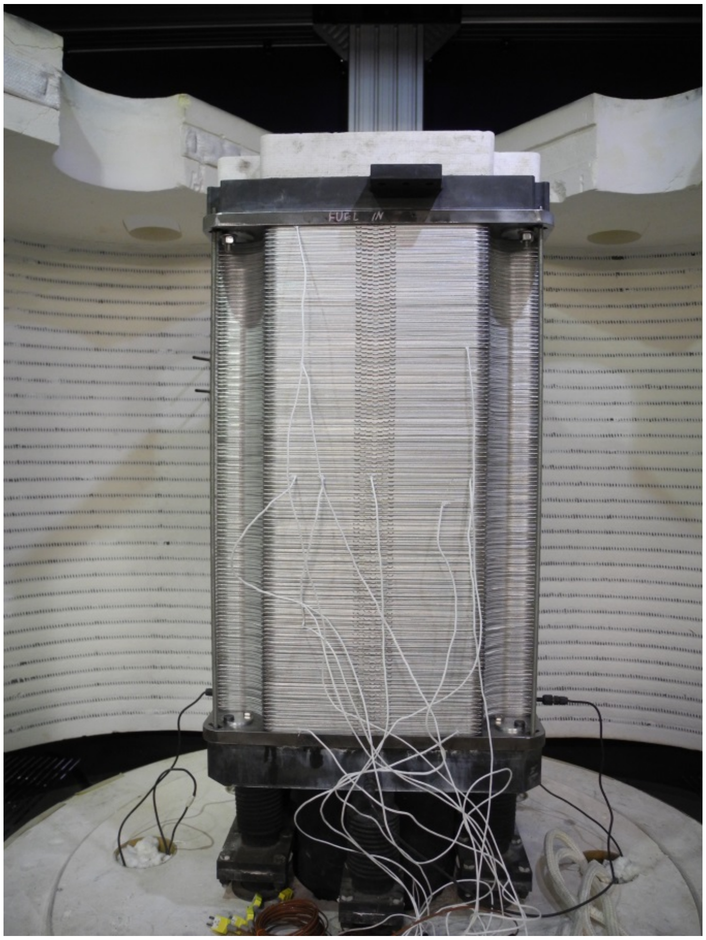

Figure 2-140. 120-cell Stack Block Deliverable

Factory Acceptance Test Plan

A factory acceptance test (FAT) plan was developed. It reduced the maximum stack test current in qualification testing from the traditional 200 A (364 mA/ cm^2) to 160A (291mA/cm^2) with a maximum fuel utilization of 75%. This change was expected to minimize thermal stresses at individual cells (ΔT_{x-y}) and for the overall stack (ΔT_{x-y-z}). The lower current density and fuel utilization also aligned with the anticipated 50 kW PCM system condition requirements. Table 2-7 lists fuel and oxidant gas flow rates (compositions) for fuel utilization testing, the historical Phase 1 system, and VPS GR system condition testing. VPS GR is a VPS gas replacement test composition aligned to targeted 50 kW PCM system compositions.

Table 2-7. Acceptance Test Gas Compositions

	Fuel Utilizations						Ph. 1	VPS GR
	50%	**55%**	**60%**	**65%**	**70%**	**75%**	**61.5%**	**68.0%**
CH_4 (slpm)	17.7	16.1	14.7	13.6	12.66	11.8	14.5	19.3
H_2 (slpm)	216.2	196.6	180.2	166.3	154.4	144.1	175.8	134.8
N_2 (slpm)	46.1	41.9	38.4	35.5	32.9	30.8	37.5	70.6
H_2O (slpm)	57.1	57.1	57.1	57.1	57.1	57.1	57.1	78.7
Total Fuel	337.1	311.7	290.4	272.5	257.1	243.8	284.9	303.4

H_2O cc/min	42.8	42.8	42.8	42.8	42.8	42.8	42.8	59.0

	13.5%	**13.5%**	**13.5%**	**13.5%**	**13.5%**	**13.5%**	**13.5%**	**15.0%**
Air	2549	2549	2549	2549	2549	2549	2549	2294

In additional to the test conditions, detailed acceptance criteria (and design specifications) were developed. These included acceptance criteria for the stack height (aligning to module design) as shown in Table 2-8.

Table 2-8. Stack Acceptance Criteria – Design and Height

Stack Criteria	**Acceptance**
Design	GT059636
Number of cells	120
Cell pedigree	GT059540 (~6 µm EL (2 layer), ~600 µm thick, TSC-3)
Stack height (4-corner average)	• 21.18” ±0.50” (inside end plates) • 22.34” ±0.54” (with end plates included)
Stack height variance (4-corner (max – min))	• 0.10” (limited experience thus far)

Table 2-9 highlights cell performance related expectations from hot test results as most of the cells in the 120-cell stack had their voltage individually measured for performance monitoring. Due to data acquisition constraints with the number of available channels, Cells 1 through 93 and 111 through 120 were individually measured, with Cells 94 through 110 monitored via 2-cell blocks.

Table 2-9. Stack Acceptance Criteria – Hot Test Results

Hot Testing	Acceptance (/cell or /double cell block)
OCV	> 1.00 V (minimum) – at hold condition prior to power curve (electrical load-up) – Steps 8 & 15
TC0 & TC 1 - 75% Uf, 13.5% Ua, 160 A, 25% DIR	> 0.84 V (average cell) > 0.80 V (minimum cell)
TC0 to TC1 change in cell performance at each utilization / hold point	< 5 mV / TC (for each cell). Individual cell failure would fail stack.
Stable cell voltages over 50 hour hold	< 10 mV decrease in individual cell voltage during hold when compared to stack cell average over same time period

Table 2-10 highlights expectations for cold (stack) test gas leakage. As the stacks must operate and function in conjunction with either three other stacks (fuel feed is in parallel for all four stacks) or one other stack (air feed is in parallel with one other stack string with each string containing two stacks in series), the cold flow results are important and must be consistent stack-to-stack.

Table 2-10. Stack Acceptance Criteria – Cold Test Results

Cold Testing	Acceptance
Stack leakage	• Stack cross leak <12 SLPM at 14±0.5 inches WC • Overboard leak on anode and cathode measured
Fuel dP variation at same cold flow on N_2	< 2% dP variation (from mean of stack set) at 600 SLPM
Air dP variation at same cold flow on air	< 2% dP variation (from mean of stack set) at 1200 SLPM

120-cell Stack Builds / FAT Results

Stack GT059636-0001 – Stack #1

The first 120-cell stack had stable voltages at 75% fuel utilization during fuel utilization testing both before thermal cycle 1 (TC0) and after thermal cycle 2 (TC2). Figure 2-141 presents the test results (TC0 and TC2). During TC1 testing, the anode current collector failed. This forced the stack to be cooled so that the current collector could be replaced.

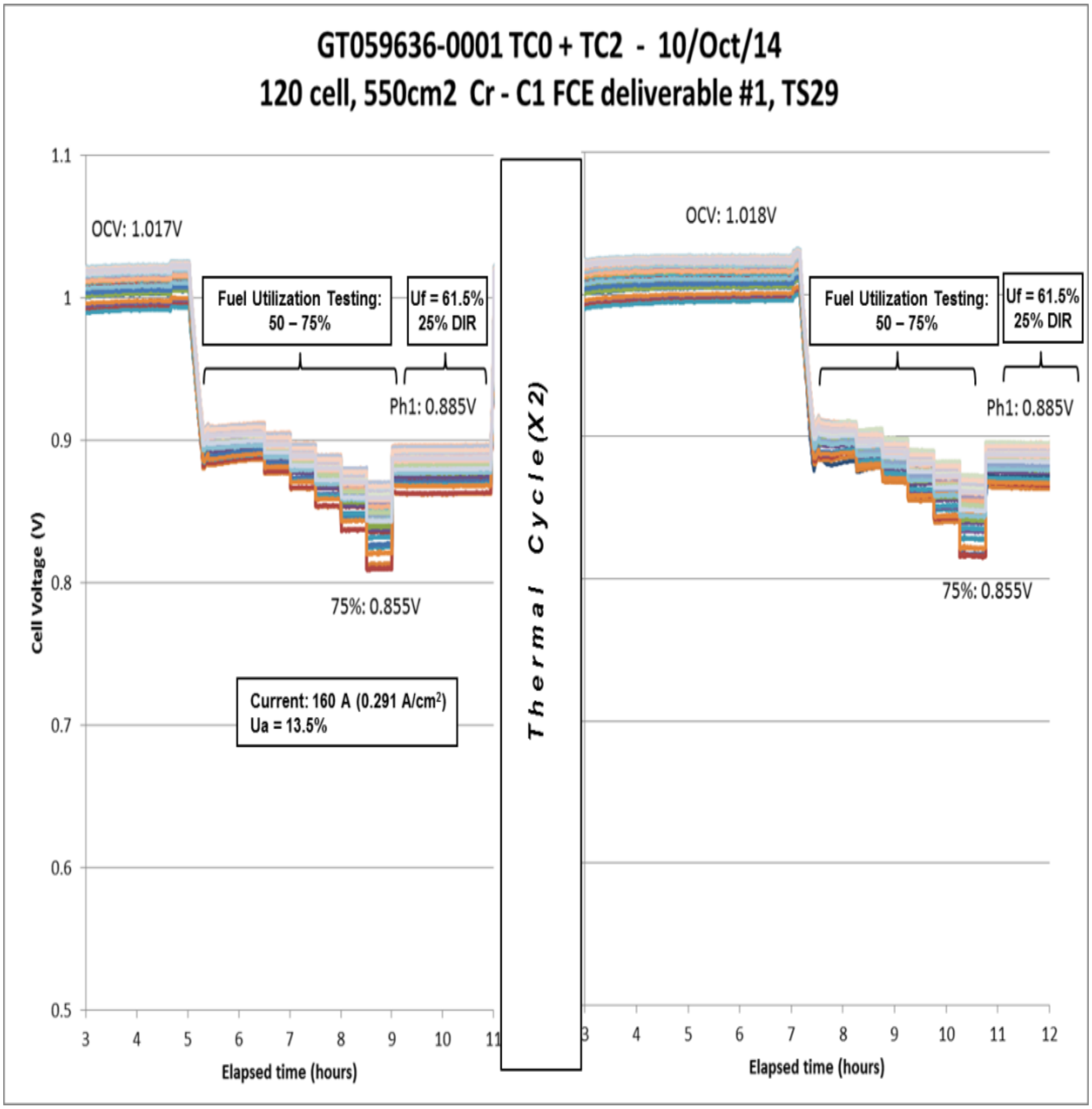

Figure 2-141. 120-Cell Stack GT059636-0001 TC0 and TC2 Performance Test Results

After a successful repair, TC2 performance characterization was carried out including a repeat of the TC0 fuel utilization test points, a short hold at Phase 1 conditions, and a 50-hour hold at VPS GR conditions (which align to the expected PCM system test conditions). The test results are shown in Figure 2-142.

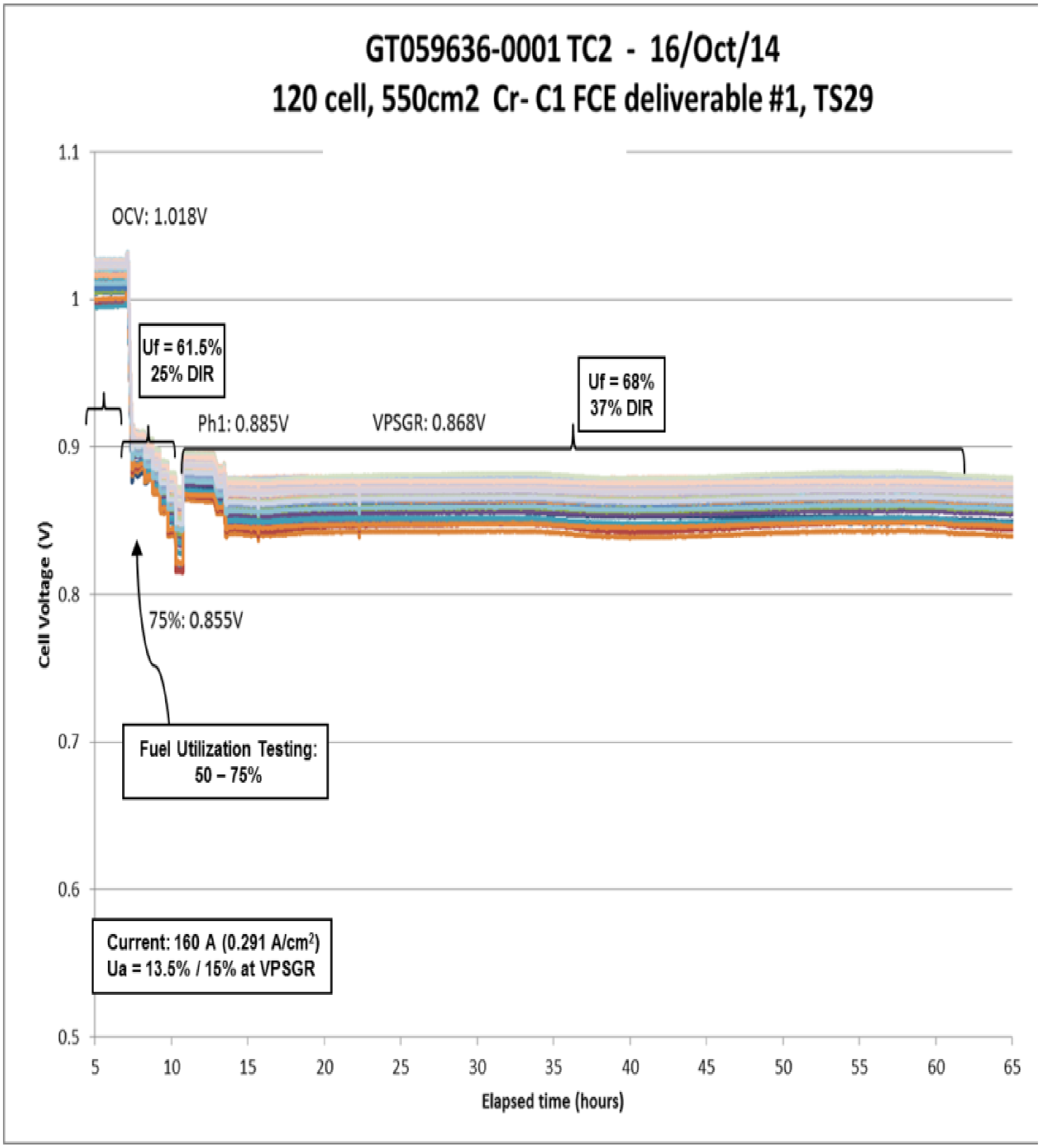

Figure 2-142. Stack GT059636-0001 Performance at VPS GR Conditions

During the 50-hour hold at VPS GR conditions, low voltages where observed from cells 35 to 42 as shown in Figure 2-143.

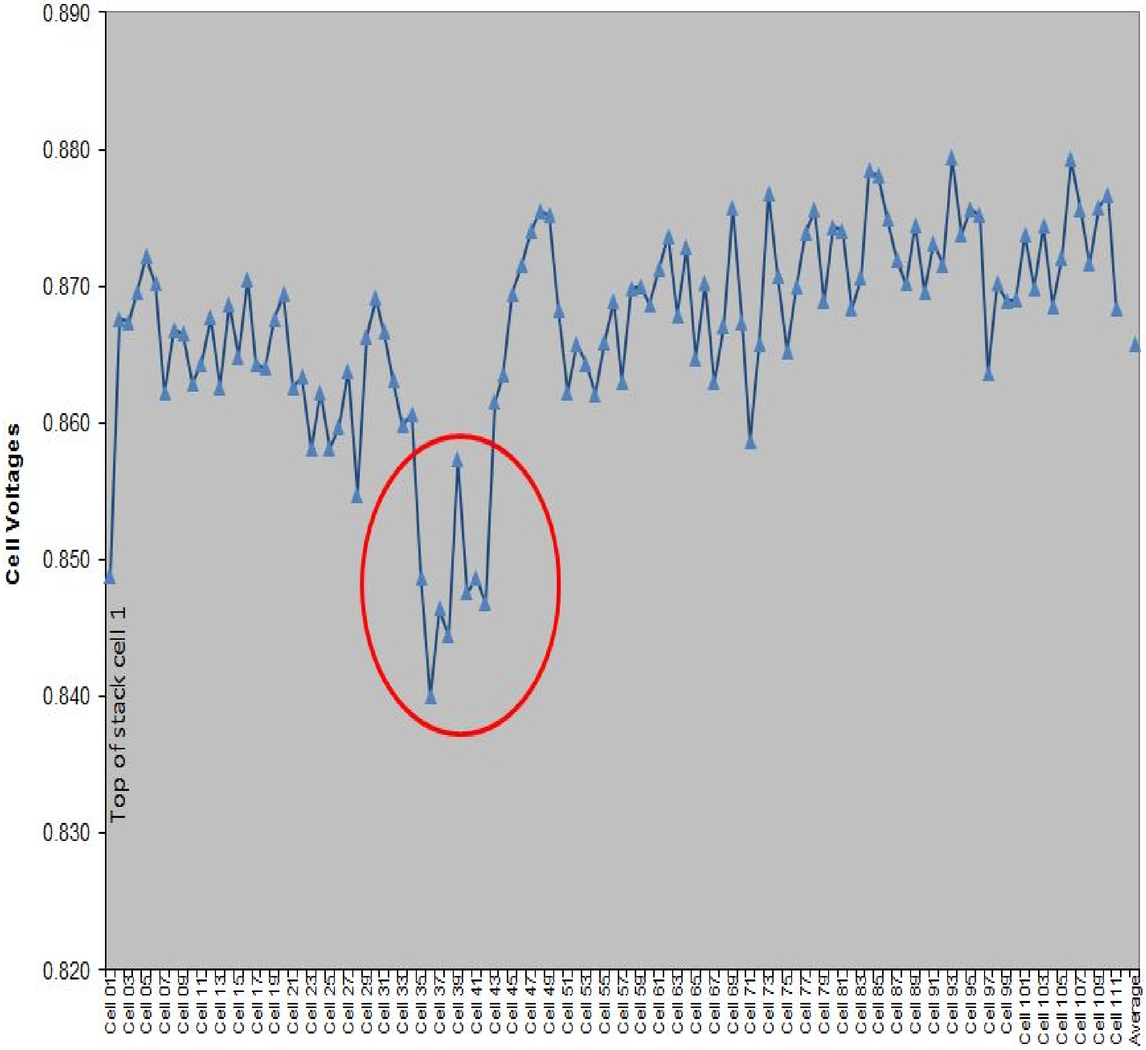

Figure 2-143. Stack GT059636-0001 Cell Voltage Distribution at VPS GR Conditions

Figure 2-144 shows the in-stack temperatures during TC2 testing. During the hold at Phase 1 system conditions of 160 A, 61.5% Uf, 25% DIR, and 13.5% Ua, a 66°C temperature delta ($\Delta T_{x\text{-}y}$) was observed in cell #80. This in addition to a stack dT of 39°C in the z- direction, results in an overall total stack $\Delta T_{x\text{-}y\text{-}z}$ of 105°C.

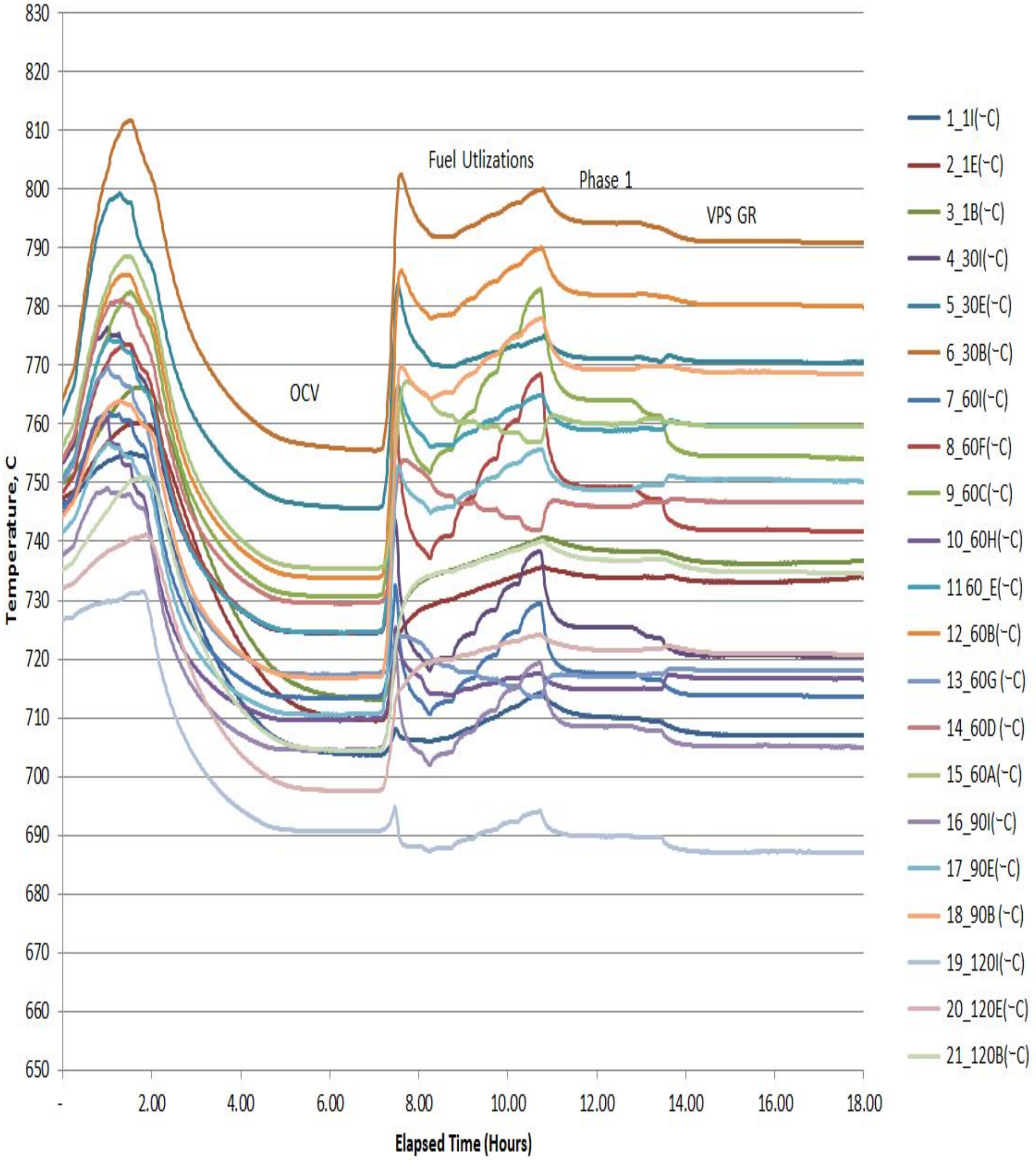

Figure 2-144. Stack GT059636-0001 In-Stack Temperatures During TC2 Testing

The on-cell stack temperatures were stable during the holds at Phase 1 system and VPS GR conditions, and dynamic during the fuel utilization test portion (as expected due to the stepping of test conditions). However, the magnitude of the high temperatures, observed during the anode reduction, for thermocouples 5 (center of cell) and 6 (oxidant out edge – mid) located on cell 30 was not expected.

During this time (nearly 90 minutes), large volumetric flow of hydrogen was passing through the anode. The explanation for high temperature is that gas leakage and combustion were occurring. During the conditioning of this stack, a number of faults occurred (as summarized below) which may have affected the stack. Alternately, a cell may have broken during the stack conditioning.

During conditioning, a high alarm on the in-stand CO gas sensor occurred during the seal burnout phase, forcing the test stand to go into emergency standby mode. When in standby mode, 4% hydrogen (balance nitrogen) is the normal anode side purge gas. This was undesirable as the stack should not be exposed to hydrogen until full reduction of the cell anodes is completed. This may result in uneven reduction of the cells. The stack was in standby mode for approximately 24 minutes and at intermediate temperatures until the errors were cleared. The direct cause of the CO alarm was from the burn out of organics from the stack. The alarm occurred due to insufficient test stand ventilation in the facility given the comparatively large amount of the organic burn out generated by the 120-cell stack. As a result of this incident, improvements were made to the test stand including:

- Addition of booster fan to each 25 kW test stand,
- Configuration change of the facility ventilation fan to improve throughput and ventilated flow rate, and
- Improved sealing and isolation of the stack furnace cabinet zone within the test stand via sealing of any air gaps.

All of these improvements were made prior to the second 120-cell stack. Hence, the second stack test was not affected by any of these issues. In addition to the improvements, a manual three-way valve on the purge line was used for the second stack. In the event of a switch to standby mode during the initial conditioning phase prior to stack reduction, nitrogen would be used instead of 4% hydrogen in nitrogen.

Due to the high temperatures observed during conditioning as well as corresponding low operating and open circuit voltages observed during FAT of the stack, the stack was not selected for PCM stack module use.

Stack GT059636-0002 – Stack #2

The second 120-cell stack also had stable voltages at 75% fuel utilization during both TC0 and TC1 performance testing (Figure 2-145). Cell voltages were slightly higher than the first stack and in-stack peak temperatures were lower. The measured cold cross leak rate was also lower.

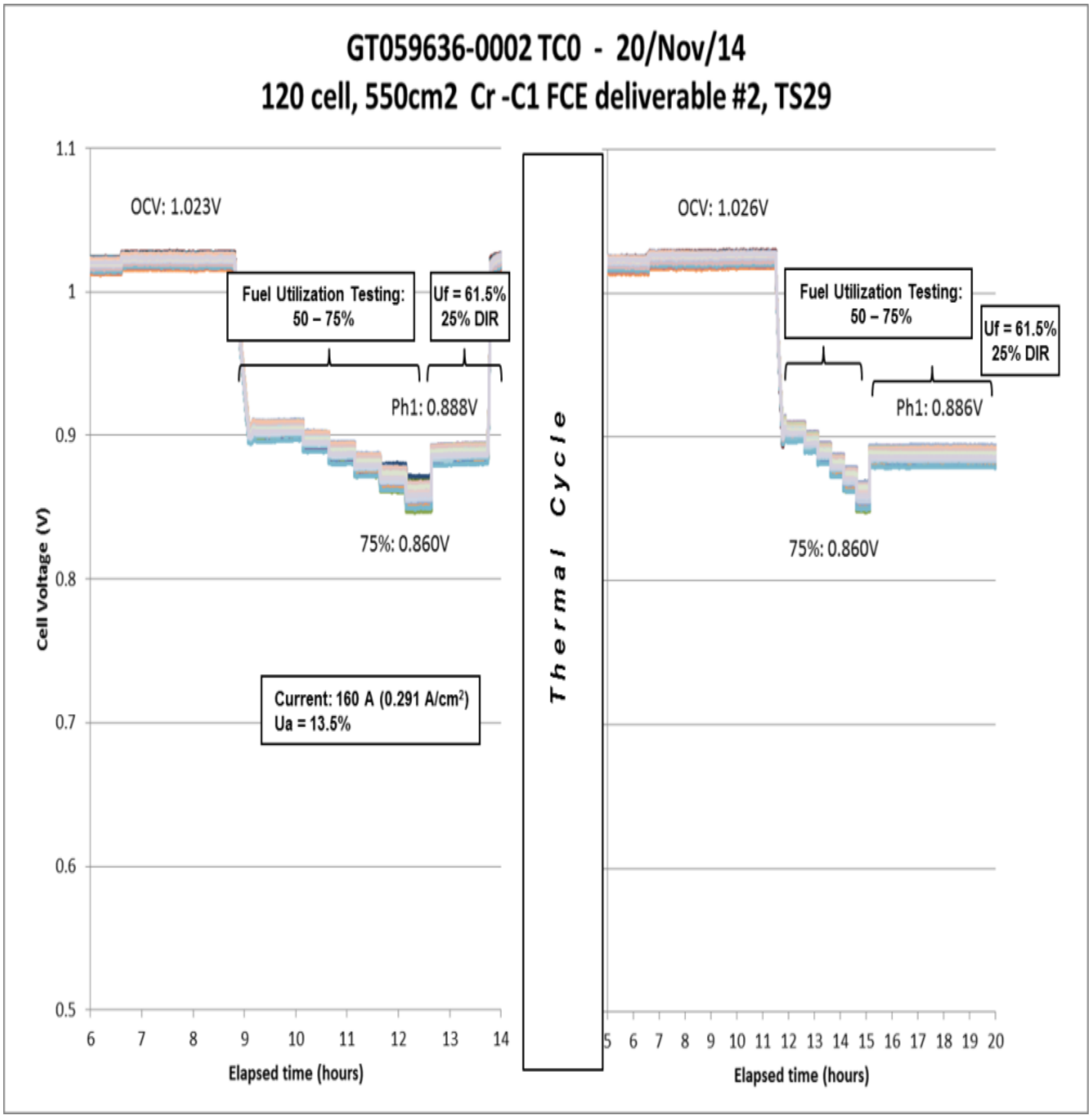

Figure 2-145. Stack GT059636-0002 TC0 & TC1 Performance Test Results

During the hold at Phase 1 system conditions (TC0), Cell #60 had a 66°C $\Delta T_{x\text{-}y}$, 39°C delta in the Z direction (104°C $\Delta T_{x\text{-}y\text{-}z}$). TC1 deltas were about the same. These temperatures were consistent between thermal cycles and within one degree of the stack GT059636-0001 results.

As shown in Figure 2-146, the on-cell stack temperatures were stable during the holds at Phase 1 system and VPS GR conditions, and changing during the fuel utilization test portion (due to the stepping of test conditions). Both were as expected. During the stack conditioning portion of the testing, the in-stack temperature rose (783°C peak), but not to the same level as stack GT059636-0001 (812°C).

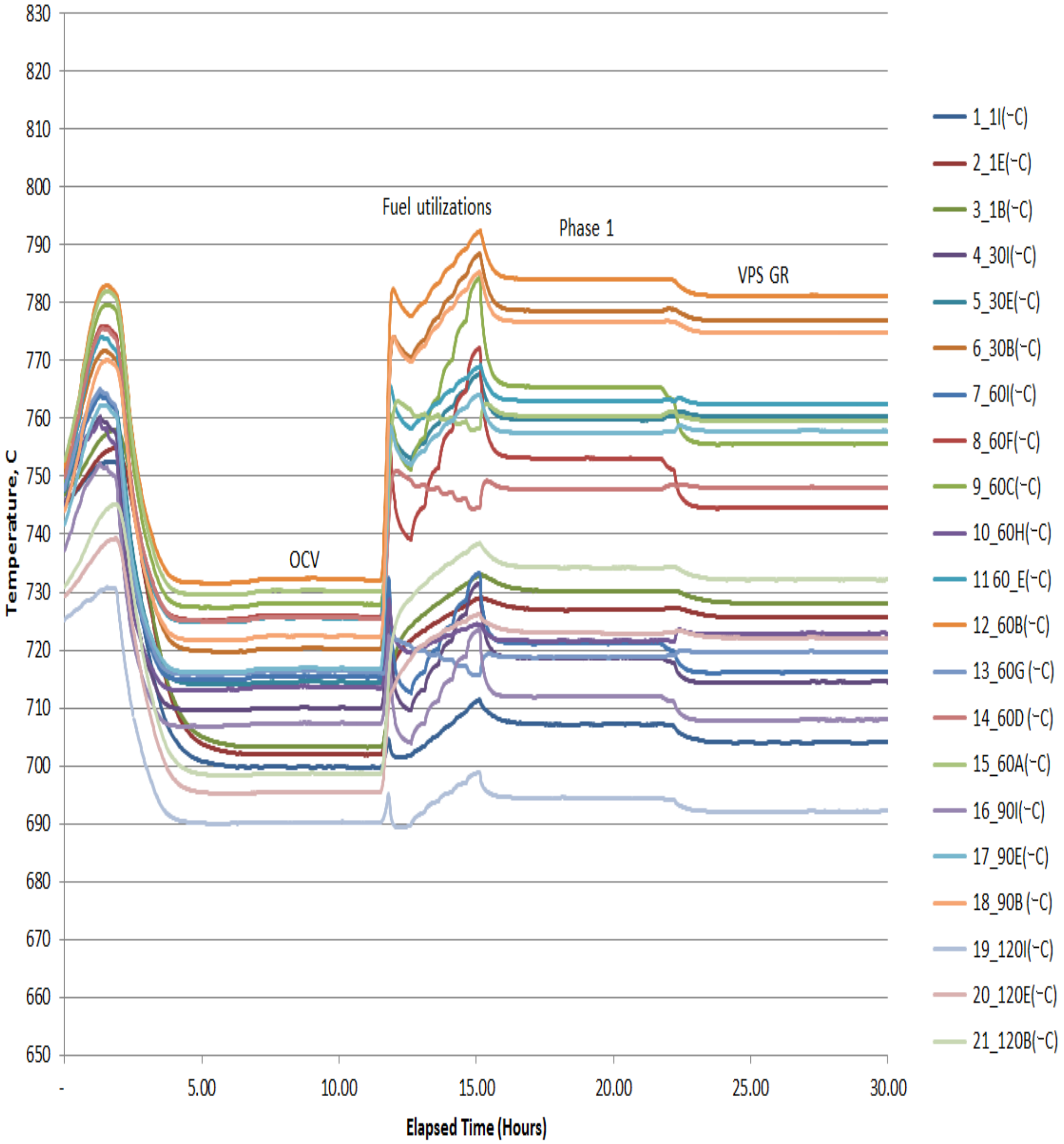

Figure 2-146. Stack GT059636-0002 In-Stack Temperatures During TC1 Testing

This stack was accepted for the 50 kW module use. Stack #2 (GT059636-0002) was bagged and stored.

Stack GT059636-0003 – Stack #3: The third 120-cell stack also had stable and repeatable voltages at 75% fuel utilization during both TC0 (before Thermal Cycle) and TC1 (after Thermal Cycle 1) performance testing, as shown in Figure 2-147.

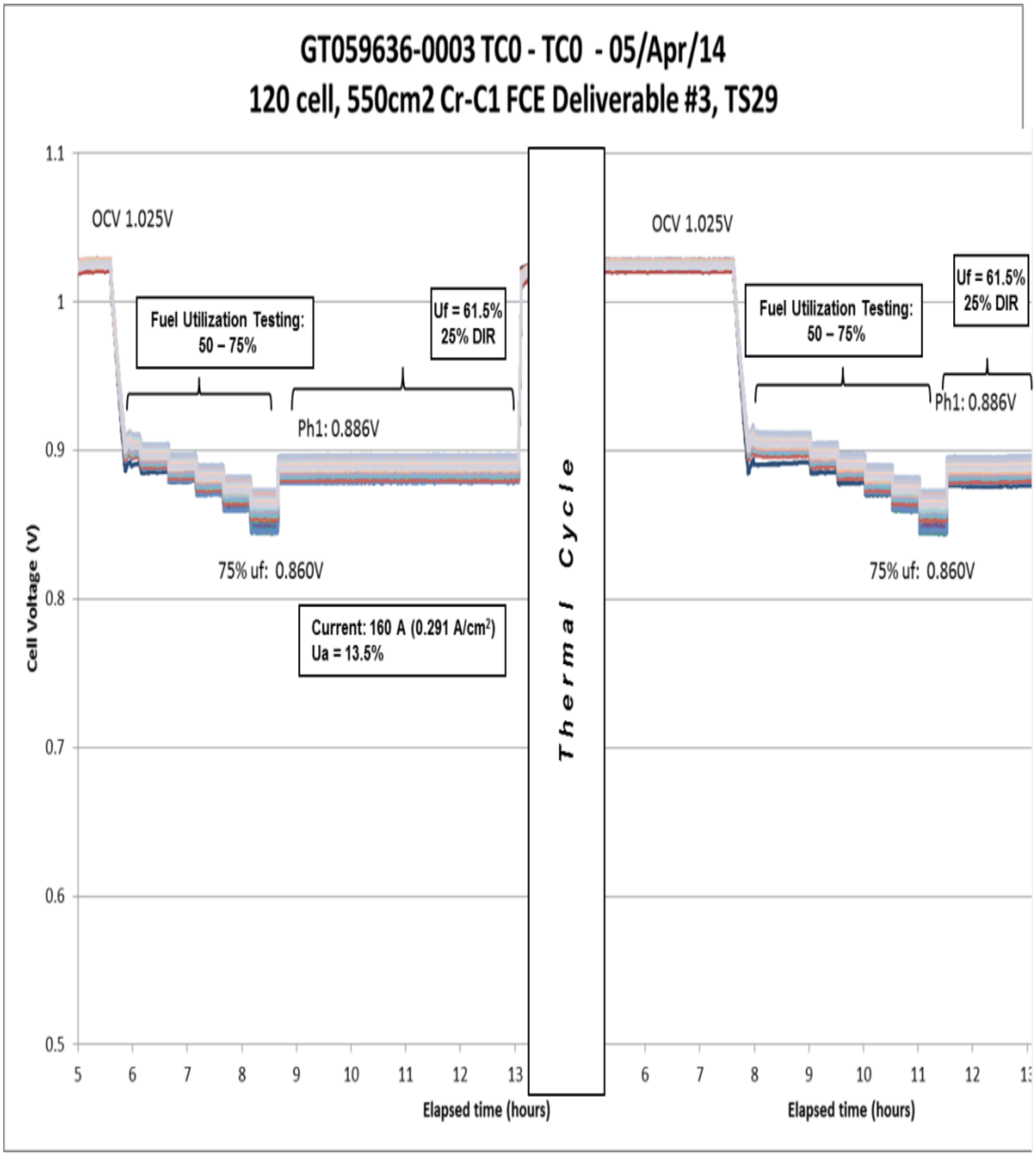

Figure 2-147. Stack GT059636-0003 TC0 & TC1 Performance Test Results

Figure 2-148 shows the TC1 portion of electrochemical testing including the hold at Phase 1 system conditions as well as the 50 hour hold at VPS GR conditions. At approximately 24 hours, the anode gas humidifier was unable to maintain acceptable steam flow rate. This lead to unloading (electrically) of the stack. At 38 hours, after several transitions and restoring the humidifier settings, the stack was successfully returned to VPS GR conditions at 160 A.

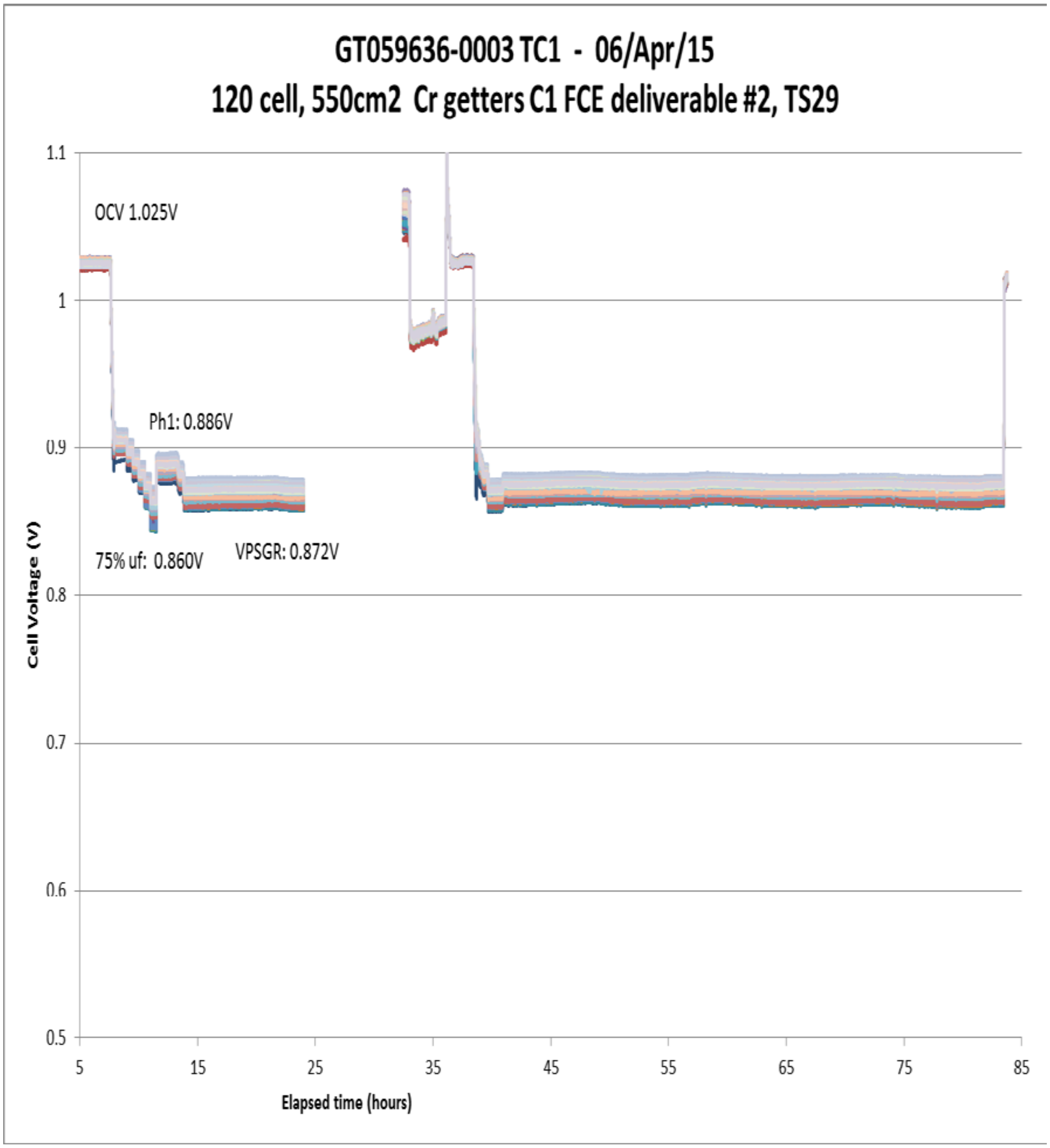

Figure 2-148. Stack GT059636-0003 Full TC1 Performance Test Results

Figure 2-149 shows in-stack temperatures during TC1 testing. A temperature differential of 63°C was observed in Cell 60 (ΔT_{x-y}). This in combination with a temperature differential of 24°C in the stacking (z) direction resulted in a stack total temperature differential of 87°C (ΔT_{x-y-z}). These numbers compare well with the temperature differentials observed during TC0 testing at Phase 1 system operating conditions: 62°C ΔT_{x-y} in Cell 60, 24°C in the Z direction and 86°C ΔT_{x-y-z}, showing consistent in-stack temperature results between thermal cycles.

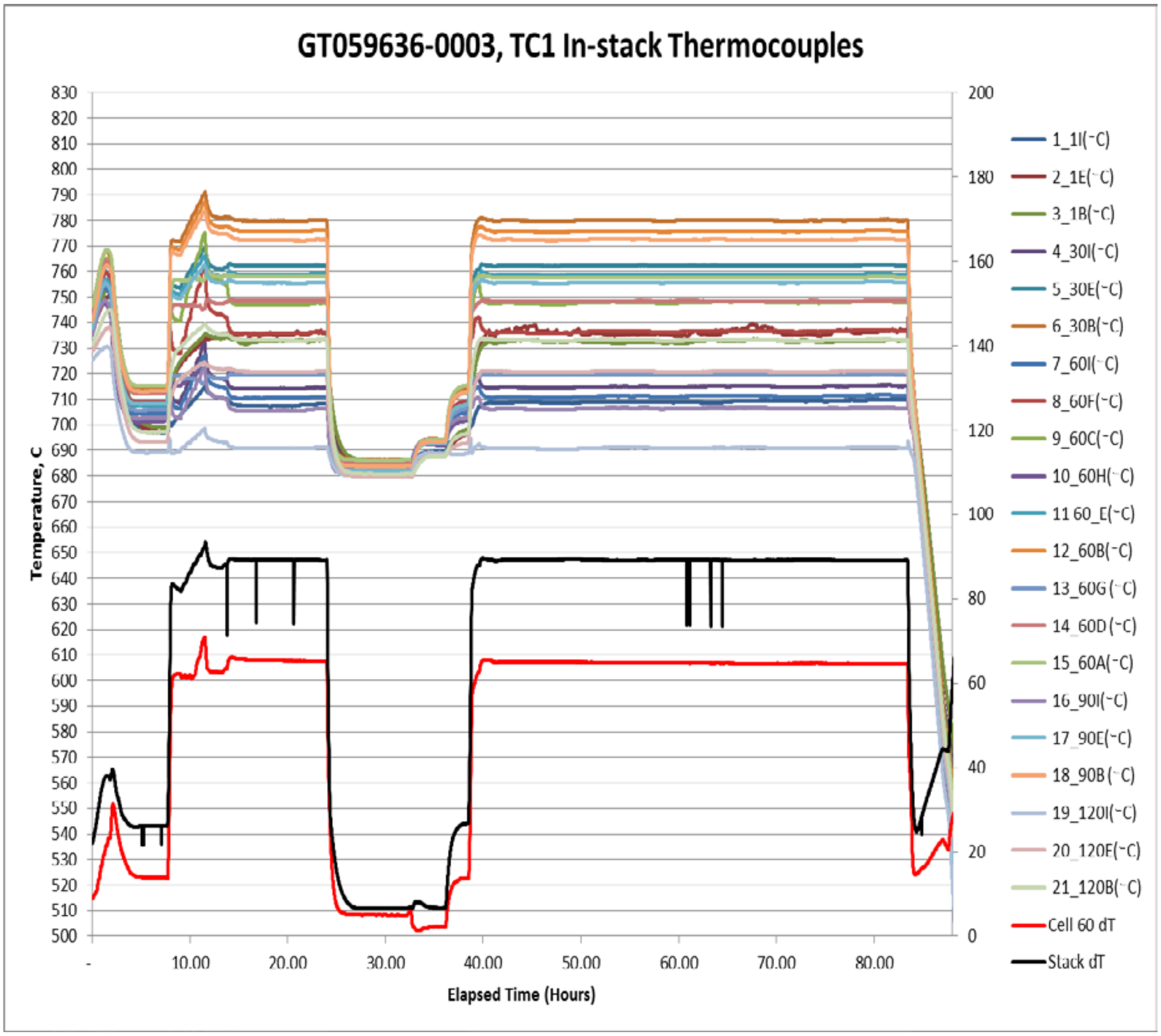

Figure 2-149. Stack GT059636-0003 TC1 In-Stack Temperatures

This stack was accepted for the 50 kW module use. Stack #3 (GT059636-0003) was bagged and stored.

Stack GT059636-0004 – Stack #4

The fourth 120-cell stack also had stable and repeatable voltages at 75% fuel utilization during both TC0 (before thermal cycle) and TC1 (after thermal cycle) performance testing, as shown in Figure 2-150.

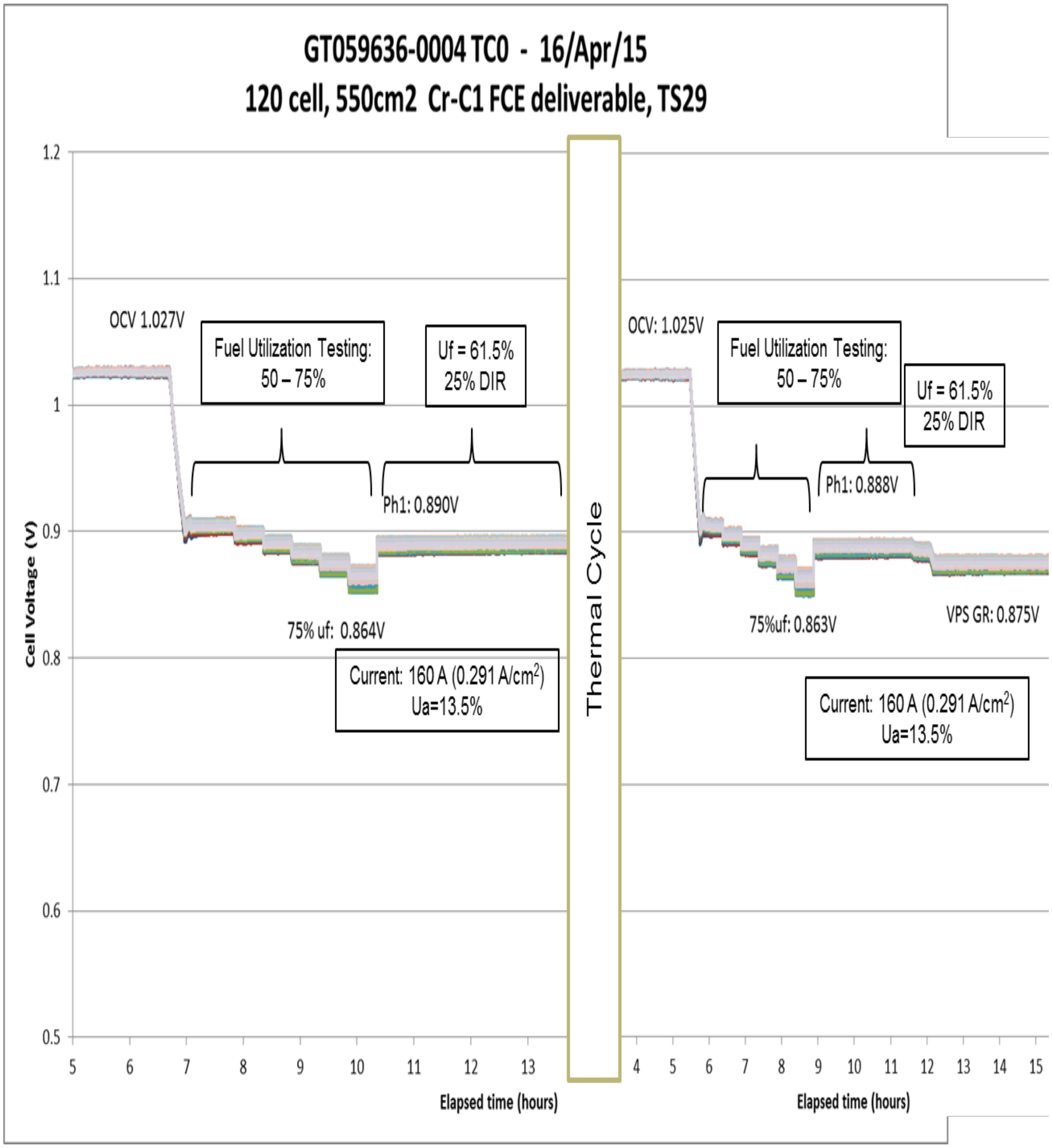

Figure 2-150. Stack GT059636-0004 TC0 & TC1 Performance Test Results

Figure 2-151 shows the TC1 portion of electrochemical testing including the hold at Phase 1 System Conditions as well as the ~50 hour hold at VPS GR conditions.

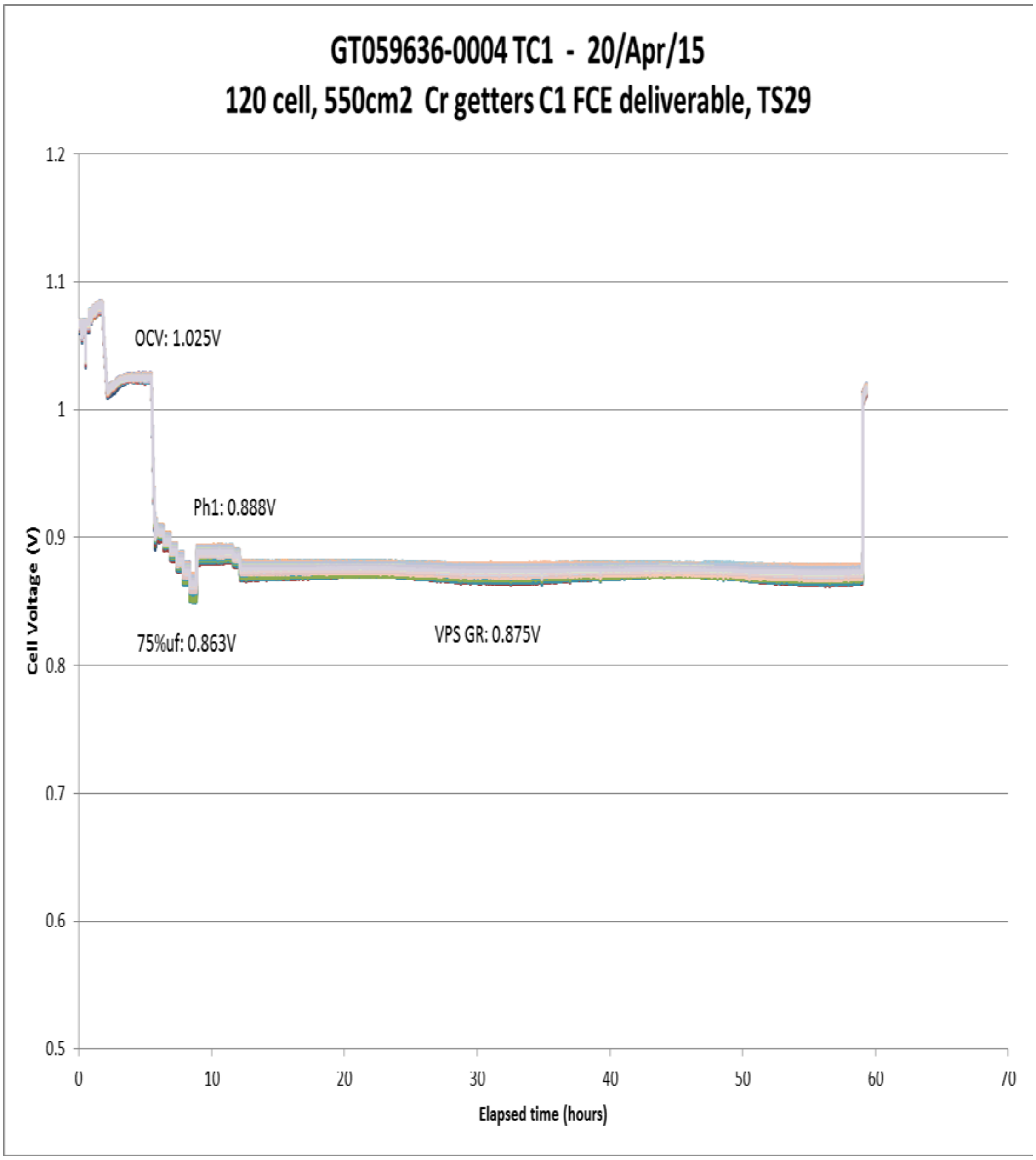

Figure 2-151. Stack GT059636-0004 Full TC1 Performance Test Results

Figure 2-152 shows in-stack temperatures during TC1 testing at Phase 1 system operating conditions. A temperature differential of 66°C was observed in cell 60 ($\Delta T_{x\text{-}y}$). This in combination with a temperature differential of 23°C in the stacking (Z) direction resulted in a stack total temperature differential of 89°C ($\Delta T_{x\text{-}y\text{-}z}$). Due to a data logging error, in-stack thermocouple data set for the entire hold duration is not available. This stack was accepted for the 50 kW module use.

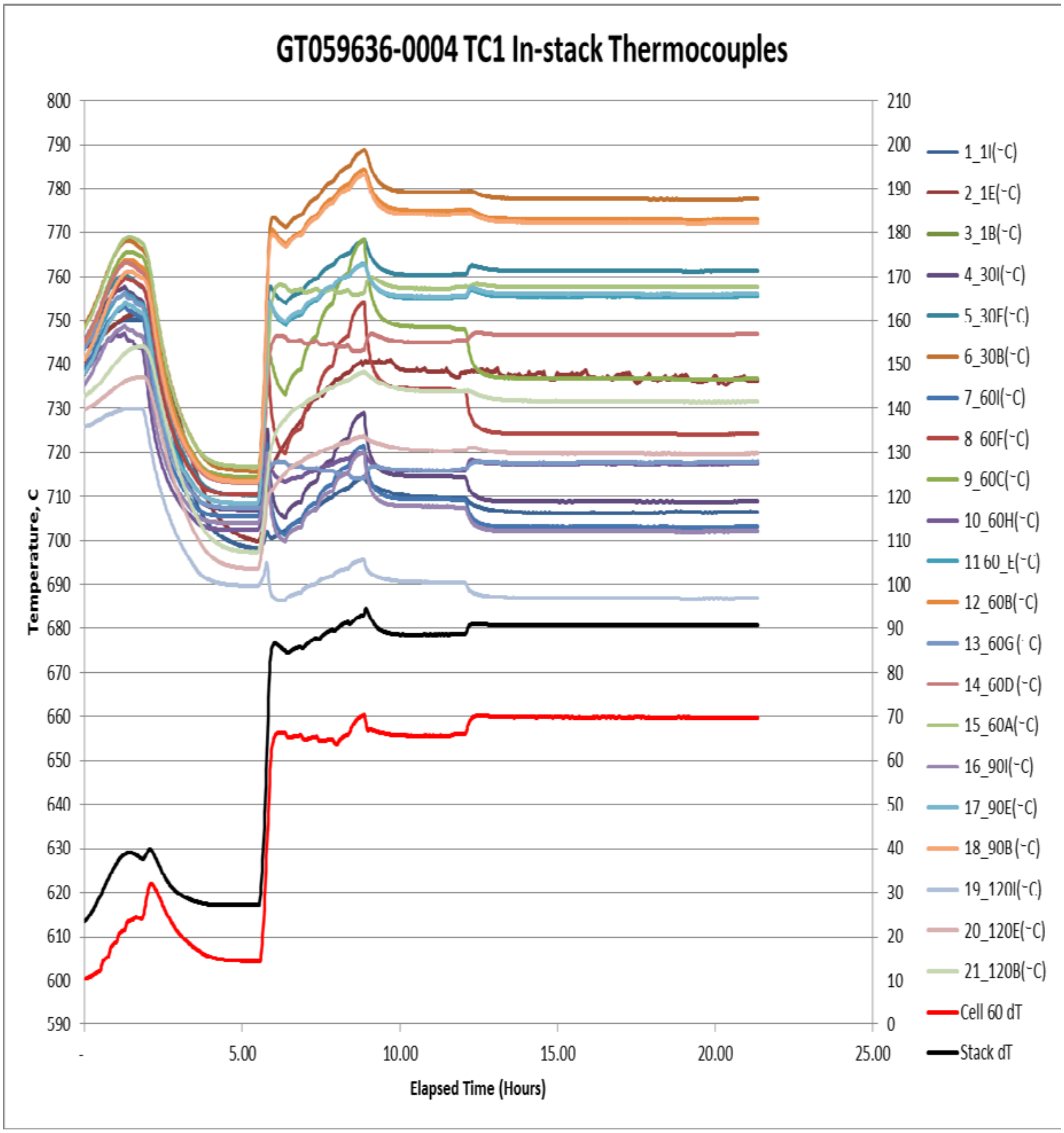

Figure 2-152. Stack GT059636-0004 TC1 In-Stack Temperatures

Stack GT059636-0005 – Stack #5

The fifth and final 120-cell stack of the 50 kW build campaign also had stable and repeatable voltages at 75% fuel utilization during both TC0 (before thermal cycle) and TC1 (after thermal cycle) performance testing, as shown in Figure 2-153.

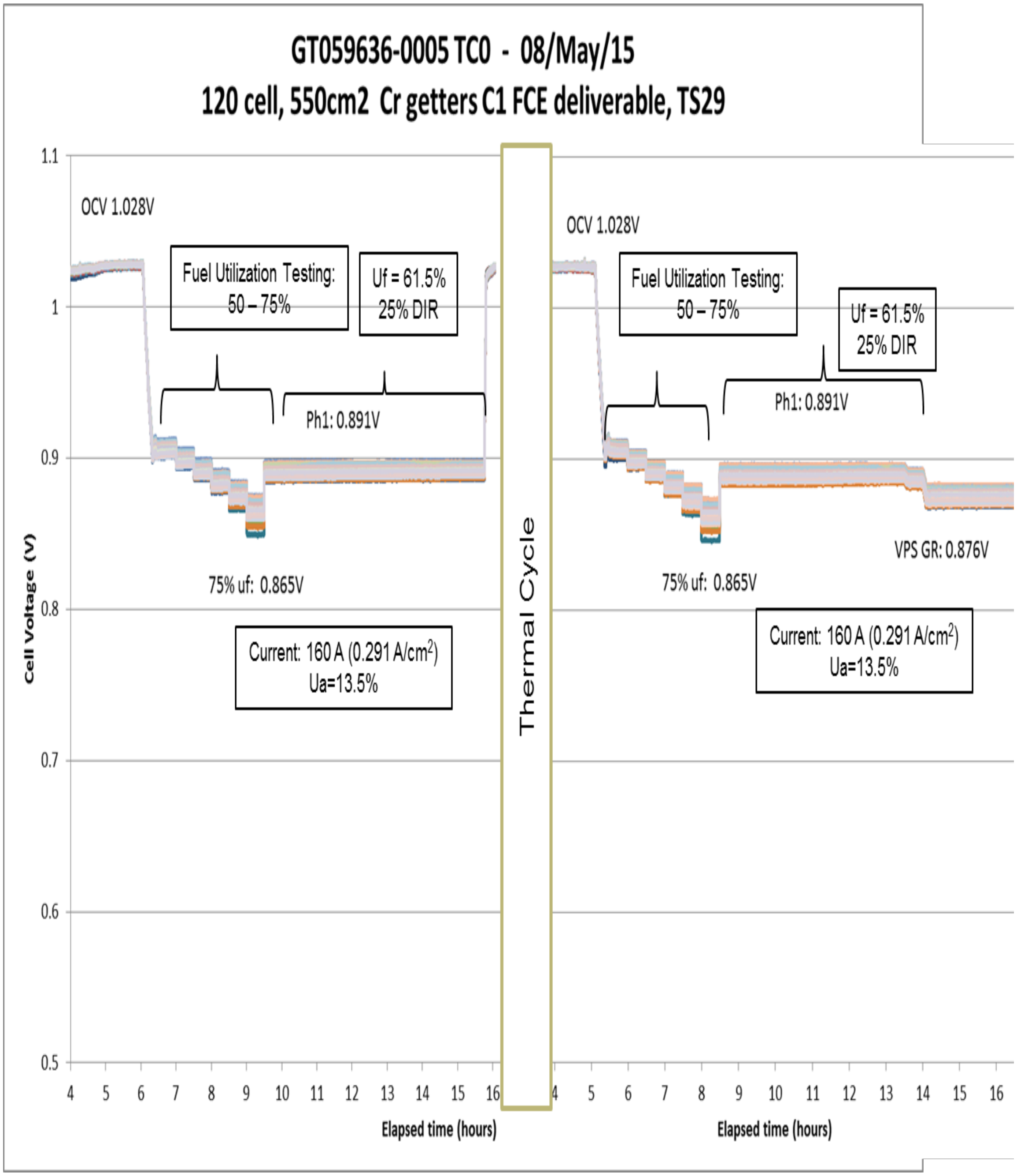

Figure 2-153. Stack GT059636-0005 TC0 & TC1 Performance Test Results

Figure 2-154 shows the TC1 portion of electrochemical testing including the hold Phase 1 system operating conditions as well as the ~50 hour hold at VPS GR conditions.

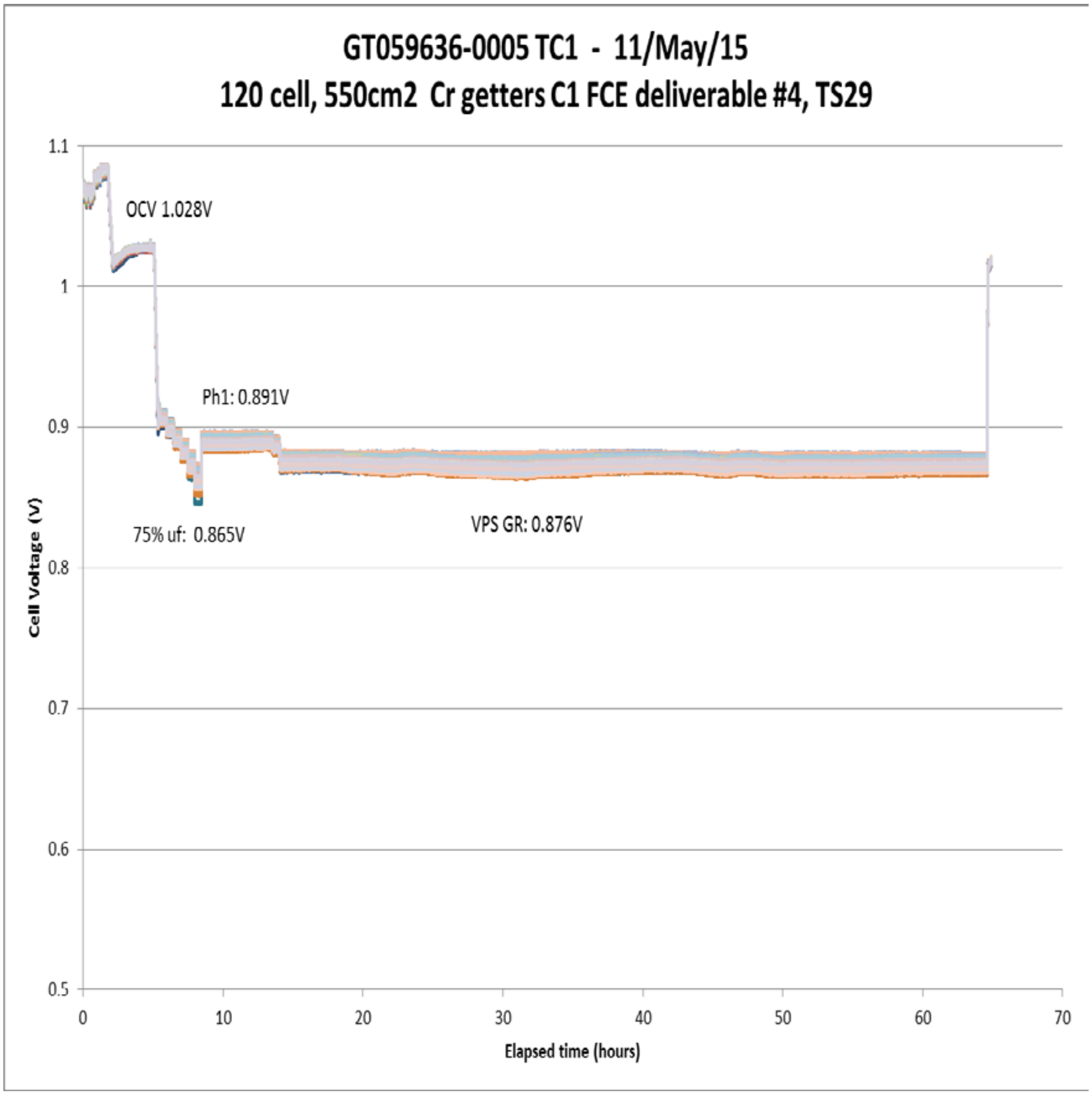

Figure 2-154. Stack GT059636-0005 Full TC1 Performance Test Results

Figure 2-155 shows in-stack temperatures during TC1 testing at Phase 1 system operating conditions. A temperature differential of 72°C was observed in cell 60 ($\Delta T_{x\text{-}y}$). This in combination with a temperature differential of 20°C in the stacking (Z) direction resulted in a stack total temperature differential of 92°C ($\Delta T_{x\text{-}y\text{-}z}$). This stack was accepted for the 50 kW module use.

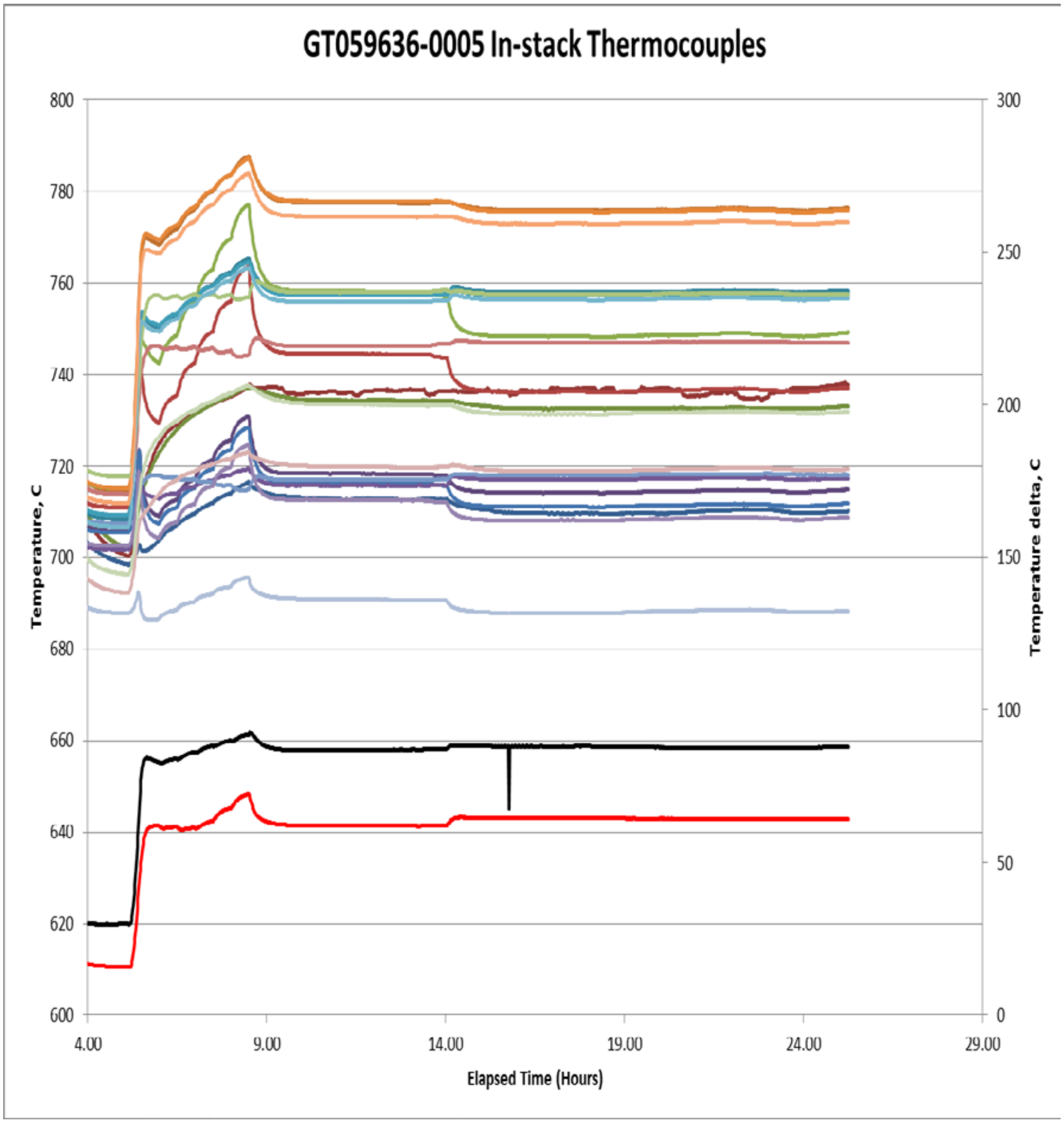

Figure 2-155. Stack GT059636-0005 TC1 In-Stack Temperatures

Accepted Stacks - Summary

The four accepted stacks were shipped to FCE Danbury. Figure 2-156 shows an overall chart of cell voltages observed during performance tests for the accepted 120-cell stacks. The stack performance varied very little amongst the four accepted stacks.

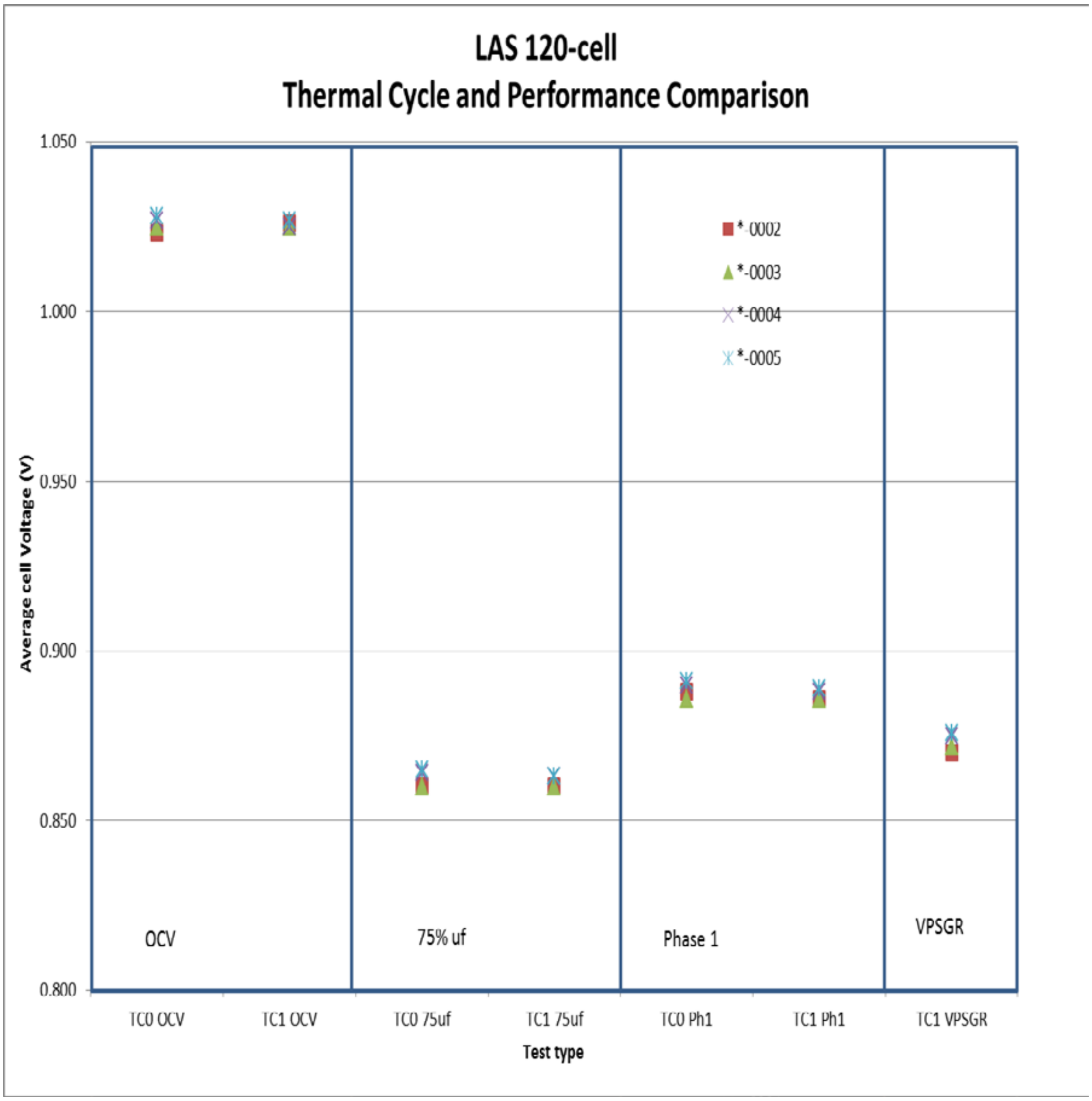

Figure 2-156. Performance During Factory Acceptance Tests of 120-Cell Stacks #2 - #5

TASK 3. STACK MODULE DEVELOPMENT

3.1. Proof-of-Concept Module Fabrication

SOFC Module Design

Accommodation (within the module) for integration of the beta-design catalytic air preheater (further described under Task 5.1) was carried out. The radiative fuel reformer (RFR) within the module (also described under Task 5.1) has been improved to provide adequate reforming, sufficient fuel gas superheating, and radiative cooling on the hot sides of the four stacks. Radiation and convection shields have been added around the quad assembly to maximize and direct radiative heat transfer from the stacks to the RFR. These will also reduce Cr vaporization into the cathode flow streams by lowering convection to exposed stainless steel non-repeat componentry. Discussion on non-repeat component related chromia vapor rate characterization and chromium evaporation mitigation is presented later in this section.

The PCM design utilizes the proven structural architecture exhibited previously on the 60 kW demonstration unit, but will be significantly more compact. The PCM dimensions are 60” wide x 77” deep x 68” tall, which represents a 54% volume reduction compared to the previous 60 kW module. This size reduction will assist with packaging in the plant system, reduce cost and lower heat losses. This accomplishment is even more impressive when considering that the PCM integrates the air pre-heater and fuel reformer internally within the module, further enabling a more compact power plant system.

Additionally, new detailed design work was performed to optimize the quad-stack architecture for use in the 50 kW PCM unit, specifically regarding series cathode flow.

Cathode Thermal Diffuser (CTD): Implementation of series cathode flow into the PCM module requires the second stack pair to be supplied with supplemental fresh (ambient temperature) air (on cathode side). Where this secondary air is injected into the system is critical to ensure adequate cathode quenching and proper mixing so that all cells in the down-stream stacks see the same temperature cathode inlet gas.

A concern with the current arrangement of stacks is the close proximity of the cathode manifold outlet of the first set of stacks to the cathode manifold inlet of the second set of stacks. This close proximity may not allow the exhaust gas from the first set of stacks to mix well with the cathode secondary air stream. This would cause hot and cold drafts within the cathode air stream going to the second pair of stacks thus imparting unwanted thermal gradients and lower stack performance. To solve this problem, a cathode thermal diffuser was developed.

A novel diffuser concept was devised, analyzed, and integrated into the current quad base architecture whereby gas is injected into the outlet manifold of the first set of stacks. Figure 3-1 shows the concept and Computational Fluid Dynamics (CFD) analysis. This design feature solves several problems: no need for a new mixing box/device located on the electrically live end of the stacks (less risk of shorting); very good mixing by utilizing the cathode-out manifold volume as a mixer (as secondary air moves up the manifold it is incrementally mixed via impingement of Cathode-Out (C/O) stream from each cell); easily packaged with no module size increase (the process gas can come in from the bottom through the cool zone and enter the stacks at the electrically grounded end).

Figure 3-1. Cathode Secondary Air Inlet Design and CFD Analysis of Effects on Manifold Wall

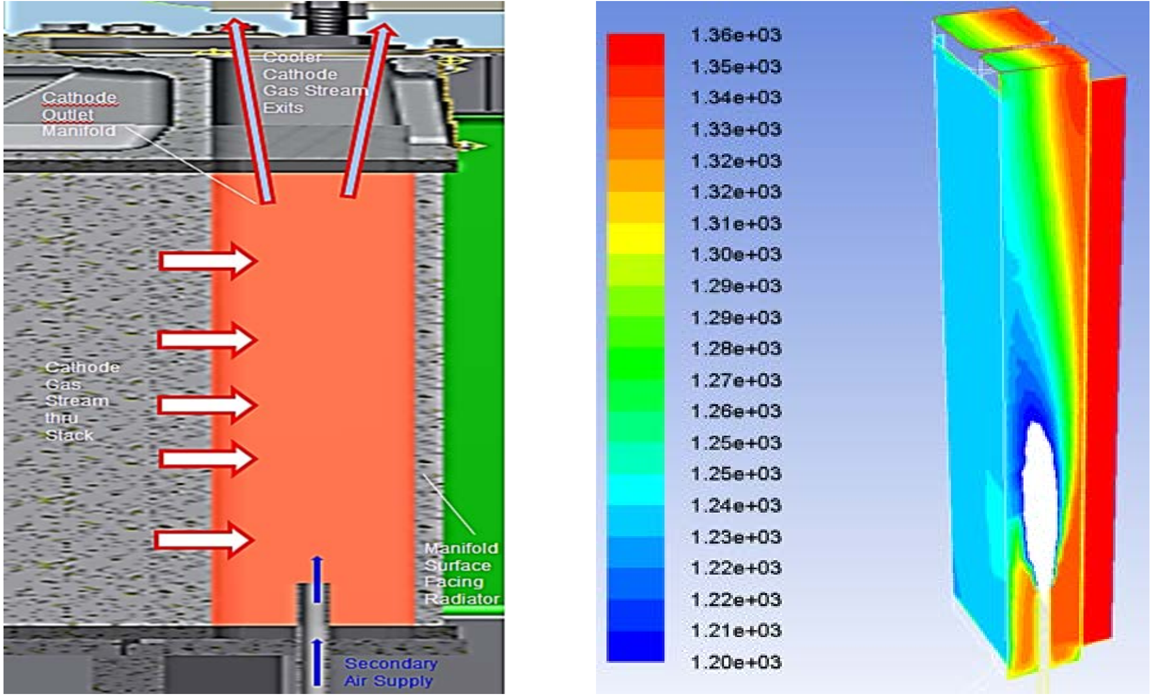

There were concerns about the effect of cooling the C/O manifold and how it would impact the heat duty of the radiator. The C/O face of the stack heats the manifold wall, which in turn heats the fuel reformer/radiator primarily via radiative heat transfer. CFD was performed to examine this effect. Design elements were introduced that kept the cool secondary air from impinging on neither the stack face nor the manifold wall (the hot surface that faces the radiator). These design features were shown in the model to effectively cool and mix the cathode gas, yet cause very small (~8°F temperature change) effect on the hot radiative surface. This is accomplished by keeping the cold gas encased by hot cathode exhaust as it gradually mixes while flowing upward in the manifold. This mixing gas stream is effectively transparent to radiation, the dominant heat transfer mechanism in this system, thus allowing the high internal manifold wall temperature to be maintained. This design ultimately results in a well-mixed cathode gas stream headed to the second stack pair, and also maintains the needed heat duty on the radiator/fuel reformer. This solution requires only moderate redesign to existing components.

Chromia Vaporization Rate Characterization: To reduce exposed chrome sources, several coatings and covering methods were investigated for use inside the module. Diffusion-bonded aluminum coatings were pursued on the cast Combined Compression Plate (CCP) which transfers compressive load and provides ducting of cathode air into and exhaust gas out of the stacks. Aluminum-coated ferritic stainless steel (Al-Alloy B) is used for insulation skins. This material has 14 times lower Cr evaporation rate than Alloy A (austenitic stainless steel). For the insulation skin, strength is not critical, and the lower thermal expansion coefficient of Alloy B can decrease the chances of buckling, making a cleaner interior design. The Ally B raw material was purchased for less than half the cost of what Alloy A material would cost for the same application.

Non-Repeat Cr Evaporation Mitigation: To minimize Cr vaporization and subsequent cathode poisoning, non-repeat module components must also be addressed. Typically, due to the high temperatures, a Cr containing alloy, such as stainless steel Alloy A, has traditionally been selected when corrosion protection is needed, strength is not critical, and super alloys are not required. This however, exasperates the Cr poisoning issue. As reported in Section 2.2.2.2, a study of different stainless steel alloys was conducted to quantify the impact alloy/coating selections will have on Cr evaporation. Surface aluminization is known to provide a tough protective layer and reduce Cr volatility, so it was also tested. In house tests have also shown that this is an effective way to limit the Cr loss.

These results directed designs toward lower cost, lower Cr containing alloys with aluminized surfaces. Al-Alloy B is commercially available and is lower cost than Alloy A, with much less Cr evaporation. For areas where corrosion protection is needed, and strength is not paramount, Alloy A was substituted. Al-Alloy B replaced Alloy A for the insulation skin, which is the largest single source of exposed SS among the non-repeat module components.

The availability of some steel alloys in commercial forms and components allows for more flexibility in design and potentially lower costs with improved fuel cell life. These specific alloys were tested for both Cr evaporation performance and manufacturability. Some examples of these components, aluminized, but prior to heat treatment are shown in Figure 3-2.

Figure 3-2. Aluminized Non-Repeat Module Components. Left- Al Coated Ducts (Prior to Heat treatment). Right- Cast Compression Plate (After Heat Treatment).

SOFC Module Fabrication Using Old (Pre-tested) Stacks

Build-to-print fabrication drawings for primary components of the module were completed. These included the module enclosure, base and internal thermal insulation, as well as instrumentation and electrical (power) penetrations/interfaces. Drawing release, quotation, and purchase order related activity was completed for all major components of the module. Some components were refurbished (from use on the previous build) for use on the 50 kW PCM unit. The module Bill of Material (BoM) included 528 individual line items.

The fabrication, procurement and qualification of the 50 kW PCM (module) non-repeat components was carried out. The activities also included refurbishing of four previously tested (60 kW module test) 96-cell SOFC stacks. Major austenitic components were coated and diffusion heat treated to mitigate Cr effects on fuel cell degradation. Assembly of the 50 kW PCM to be used for commissioning of the BoP skid was carried out. Activities for final assembly of the module and integration of the module with the BoP were carried out. The activities in different areas are summarized here.

The catalytic heat exchanger (HEX) was received and qualified. Instrumentation was added and the unit was installed into the Module. The oxidation catalyst coated Heat Exchanger (HEX) was mounted to the front wall of the Module Base. The HEX served as a target for duct and piping terminations. The position of the HEX was adjusted for stress-free piping and duct connections. Once the HEX was adjusted for optimal position, the Quad Base Assembly was hoisted and integrated.

The hot anode back pressure valve was tested and qualified for operation. The valve is opened and closed by an electrically powered actuator piston. The actuator control system was debugged to work flawlessly.

Figure 3-3 shows the quad base used for the module. Figure 3-4 shows the quad base assembly with four SOFC stacks and a radiator (uses radiated stack waste heat for fuel prereforming and preheating). To facilitate Balance-of-Plant (BOP) system operational checkout (initial phase of PCM system test), four 96-cell stacks previously used in 60 kW quad-based SOFC module test (conducted under DOE Project DE-FC26-04NT41837) were installed in the PCM. To prepare the Quad Base assembly for the Module, the 96-cell stacks were gasketed, installed and compressed. Compression springs reside below the Load Bearing Insulation. Next, the Fuel Reformer Radiator was installed. The fully assembled Quad Base Assembly resided on a transporter base until it was integrated into the Module Base.

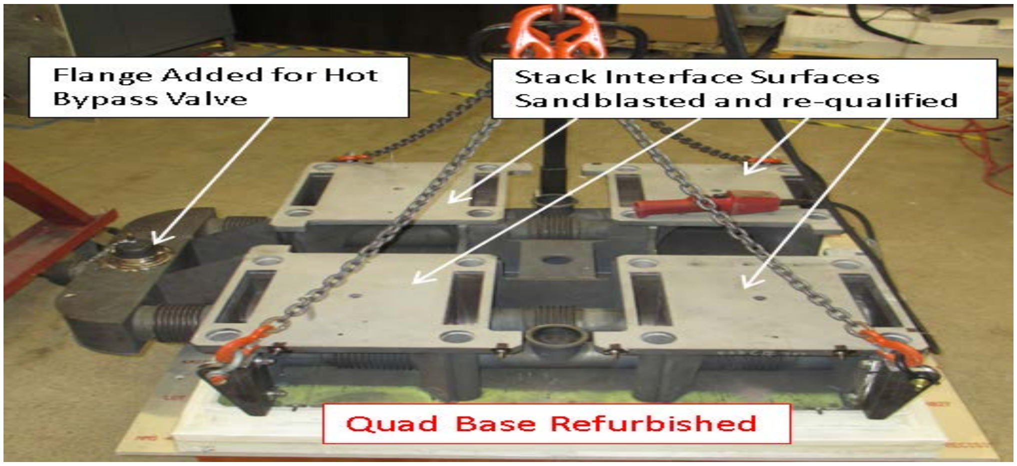

Figure 3-3. Quad Base Refurbished

Figure 3-4. Quad Base Assembly with Radiator

The hot buss bars were received and qualified. The buss bars fit perfectly. The ends were routed through the thermal boundary.

Unique cathode ducts were received and installed. Bench welds were performed to achieve sealed joints.

Key components were coated to mitigate the effects of chromium on fuel cell degradation. Because field fitting for pipes and ducts was required, it was necessary to mask selected regions on parts to facilitate welding later in the final assembly process. Additionally, all the coated parts were heat treated to diffuse the aluminum into the base metal. Figure 3-5 shows the piping components masked and aluminized.

Process piping components were procured and installed. Process piping work was done in two phases; interior piping and pass-thru piping. Bellows, elbows, pipes and custom machined flanges were welded to produce subassembly pipe strings. Interior piping was fit in position, tack welded then removed and bench welded to complete subassemblies. These subassemblies were connected inside the module and the opposite ends were routed through the enclosure pass-through nozzles. Pass-thru piping was positioned and installed with the assistance of an aluminum pipe alignment template. Pass-thru pipes were routed through the Base Wall Nozzles, insulated and sketch plates were welded to fix the pipes in position and create a seal to ambient.

Figure 3-5. (left) Piping Components Aluminized (right) Piping Components Masked and Aluminized

The hot bypass valve was installed and connected to the Fuel Exit flange on the Quad Base. The pipe assembly, which connects the Hot Valve to the Catalytic HEX, was fit, adjusted and welded in place. The Actuator was mounted in the vertical Purgatory zone and a custom linkage was installed to actuate the valve.

Instrumentation and Module Harness Wiring: Thermocouples, which were installed in the stacks at VPS/Calgary, underwent electrical checks to assure that they were functioning properly and electrically isolated. Voltage Leads were installed. Thermocouples were added to key areas within the module environment to facilitate monitoring and control of the module during hot operation.

Wiring Harnesses, consisting of mil-spec connectors and cable, were installed at the bulkhead of the Module Base Wall. The cables were routed through the purgatory zones with the ends positioned for connection to the stack wiring.

Stack instrument wires and Module harness wires were connected near each stack. These connections were made below the Base Insulation, which assures a safe operating temperature for the connectors.

All pressure tap and gas sampling (for gas chromatograph) tubings were fitted and installed.

Module Enclosure: Inspection of the fuel cell stack module base and shell was performed at the fabrication shop by FCE's commercial Quality team. A few minor quality issues identified during the inspection were rectified.

High temperature microporous Base Insulation was fitted and installed around the Quad Base. This creates a robust thermal barrier for the below-deck purgatory zone, which serves as a safe environment for the instrumentation connections and the stack compression springs.

Once all the Final Assembly work was completed, the Module Enclosure was gasketed, hoisted and installed. This milestone task signifies the completion of the module final assembly work. Figure 3-6 shows module prior to enclosure installation.

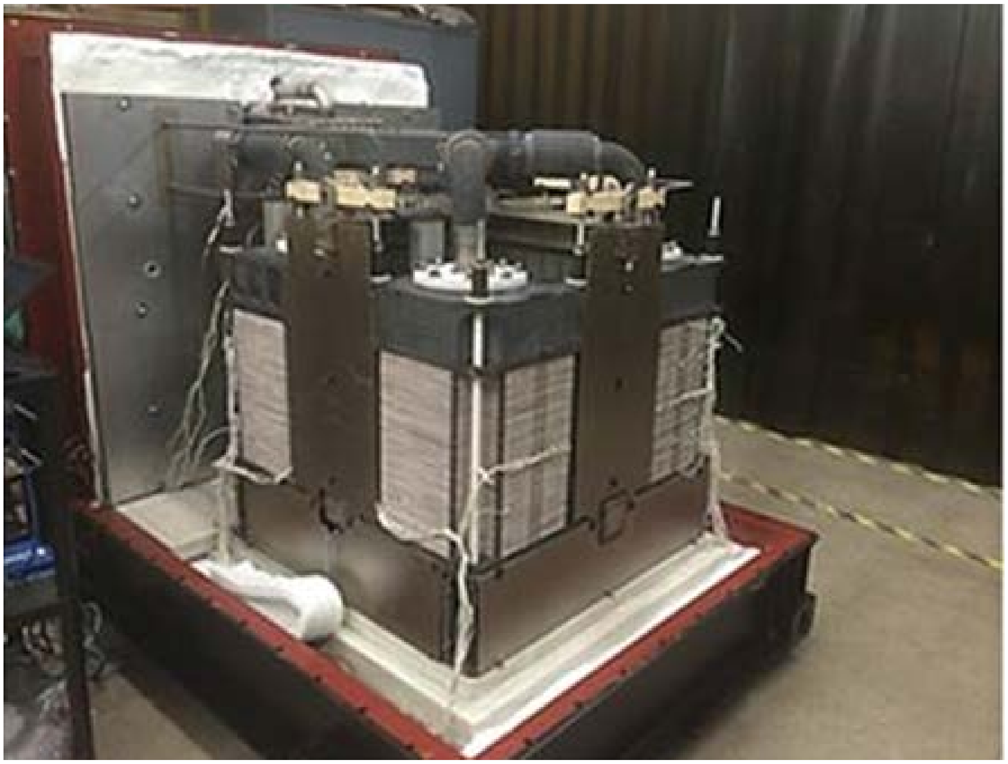

Figure 3-6. Module Awaiting Enclosure Installation

Leak Test: Module leak testing was performed to assure that all the piping penetrations, instrumentation bulkheads and gasketed joints were leak tight.

Integration with BoP: Integrating the module into the BoP was a two-phase operation. First, the module was landed in place in the BoP with the process pipe flanges loosely placed on the module pipes. Flange gaskets were temporarily installed and the Module and BoP Flanges were temporarily bolted together. This step assures proper flange alignment. The Module Flanges were tack welded and the Module was removed from the BoP. Final continuous welds were performed to connect the flanges to the Module pipes. The Module was then re-installed in the BoP and permanent flange bolted connections were established. Figure 3-7 shows the module with the BoP.

Figure 3-7. Module with Enclosure after Integration with BoP

SOFC Module Fabrication Using New Stacks

As discussed under Section 5.3, the system was tested up to 30% load level before shutting down to replace the old stacks with new 120-cell stacks. Lessons learned from commissioning and post-test examination were implemented in the module rebuild with the new unused stacks for success of PCM system demonstration test. Major activities are summarized below.

De-integration of the Module from the Plant and Post Test Inspection: The use of pipe flanges and Mil-spec pin/socket connectors on wiring harnesses facilitated efficient integration and de-integration of the module. Visual inspections were performed throughout the disassembly process. Once the Enclosure was removed, the following issues were discovered:

- Power Lead Cable Insulation Sheathing Compromised: The power lead cables, although located in the purgatory zone, exhibited signs of sheath material melting. The cable was nylon sheathed. Due to the routing of this flexible cable, which provided clearance to all adjoining components, no electrical shorting occurred. Purgatory temperatures were not high enough to melt the sheathing. Heat Conduction through the Hot Buss Bars appears to have been the root cause for the sheath melting. The hot buss bars are copper core and originate in the hot zone. To prevent sheath melting during subsequent tests, a higher temperature rated cable was used to replace the nylon-sheathed cable.

- Start-upSystem Carbon Deposition: The Start-up line (tubing) had significant amounts of carbon built up inside the tube. It was determined that cooler than expected temperatures in the CPOx line caused carbon to form and collect within the tube. Operating parameters were modified to assure tube temperature was hot enough to prevent carbon formation during subsequent tests.

- Cathode Flange Dielectric Coating Peeled: Upon removal of the Cathode Flanges, it was noted that the dielectric coating on the gasket surface was compromised. Large portions of the coating had peeled away leaving the base material with little or no dielectric coating. This peeling happened as a result of removing the flanges. It was determined that the coating thickness was the root cause of the peeling. Thicker coatings tend to peel when compression is removed. FCE collaborated with the coating supplier's engineers and Quality manager to specify an improved coating scheme. A graded thickness of coating was specified. This thickness grading is intended to provide a thinner coating in critical areas to prevent peeling. The flanges were sent back to the coating supplier for sandblasting (to remove old coating) and for re-coating.

- Insulation Gap at Base-to-Enclosure Vertical Wall Interface: Heat leak marks were noted at the interface between the Base wall and Enclosure junction. It was determined that the design of the Enclosure front wall insulation was the cause of the heat leak. When installed, the enclosure insulation and the base wall insulation did not nest intimately resulting in a small path for hot gas. A small strip of ceramic wool insulation was placed in the area where the gap existed.

- Radiative Fuel Reformer: Upon inspecting the Radiative Reformer, no issues were noted. The catalyst-coated fin (inserts) exhibited superior coating retention. This validation provides confidence for future designs, which are likely to utilize this technology.

- Catalytic HEX: Visual inspection of the Catalytic HEX revealed no issues. The core was clean and clear. No modifications or improvement were needed.

- Hot Valve: During the commissioning, the hot valve had become frozen in the closed position. Once the module enclosure was removed, testing was performed to pinpoint the root cause of the malfunction. The linkage was disconnected and an attempt was made to actuate the butterfly valve by hand. It became obvious that the valve had frozen in place proving that the problem was in the valve not the actuator. The valve was removed and sent back to the manufacturer for evaluation. The manufacturer determined that an improper material was used for the shaft bushings, which caused the shaft to seize. Repair and re-integration of the hot valve would have taken too long. In the interest of schedule, FCE decided to eliminate the hot valve from the internal module environment and replace it with an external valve installed in the MBoP. The electric actuator system was tested by cycling the actuator. The actuator worked flawlessly hereby validating actuator system design. Although the hot valve malfunctioned during the test, FCE believes that the concept of the internal hot valve has merit. Lessons learned can be implemented and future modules may benefit from this approach.

- Façade: Deintegrating the module from the BoP required removing some of the façade wall and roof panels. During the commissioning, it was necessary to gain access to certain areas within the plant. Access for servicing the MBop, EBoP and Module connections was achieved readily by quick removal of façade panels. The modular design of the façade frame and multiple panels for the walls and roof facilitated service access. The design will likely be carried forward to future plant designs.

Removal of Old Stacks: Voltage lead wires were removed from the cells on each stack while the below-deck connections remained intact. Thermocouples were disconnected below deck by unplugging the mini connectors. Cathode Flanges, Fuel Flanges and the HEX inlet/exit flanges were disconnected. This work freed the Quad Stack Assembly for removal from the Module Base. The Quad Base Assembly was rigged, hoisted and placed on the Transport Base. The Radiative Reformer and Mica Shields were removed to facilitate the removal of stacks. The temporary stack compression rods were installed and the hot tie rods were removed. After removing the 96-cell stacks, the stack mounting surfaces on the Quad Base were cleaned in preparation for the new stacks.

Installation of 120-cell Stacks and Module Integration with Plant: New unused (120-cell) stacks were installed and the module was reassembled for integration with the PCM plant for completion of the demonstration test. Figure 3-8 shows the module installation in plant. Major steps completed during module rebuild are summarized below.

Figure 3-8. Installing Stack Module in 50 kW PCM Plant

The 120-cell stacks were gasketed, installed and compressed. Next, the Fuel Reformer Radiator was installed. The fully assembled Quad Base Assembly resided on a transporter base until it was integrated into the Module Base.

Stack instrumentation wiring was less time consuming for the build with 120-cell stacks primarily because the wiring harnesses remained in place after the previous test. The below-deck voltage lead connections remained intact so only the stack end of the lead needed to be reconnected. Spot welding was performed to attach the voltage leads to the edges of the cells to complete the circuits. Thermocouples, which were installed into the stacks at VPS/Calgary, underwent an electrical check to assure that they were functioning properly and electrically isolated. Once qualified, the thermocouple mini connectors were plugged in to the wiring harness below deck. All pressure tap and gas chromatograph sampling line connections were re-established by connecting the compression fittings to their mating ports within the module environment.

The process piping work was much easier. New gaskets were installed and the connections were re-established with no fixturing or welding required. A spool piece was installed to replace the hot valve.

High temperature microporous Base Insulation was fitted and installed around the Quad Base. Once all the Final Assembly work was completed, the Module Enclosure was gasketed, hoisted and installed. Module leak testing was performed to assure that all the piping penetrations, instrumentation bulkheads and gasketed joints were leak tight.

Integrating the module into the BoP was also much less involved. The module process piping flanges remained intact so connecting to the MBoP required only installing new gaskets and re-establishing the bolted connections.

3.2. Development of MW-Class Module

One of the lessons learned from FCE's development of the MW-scale MCFC's was related to the benefit of external manifolds. Internal manifolds lend themselves to several disadvantages. They require extra unnecessary components (to manage shim seal assembly) as shown in Figure 3-9. They also require a significant amount of extra gasket and exotic metal materials to build the manifold while assembling the stack. These contribute significantly to cost.

They extend the distribution of compressive loading outside the active cell region of the stack. This leads to uncertainties of how much of the mating surfaces within the active cell region (cell, flow fields, interconnects, etc.) are in intimate contact with one another – and how much of the load is actually distributed to these mating surfaces. Uneven compression load distribution results in hot spots along the direction of stack height and decreased electrical current output.

By moving to an external manifold stack arrangement, these disadvantages would be eliminated.

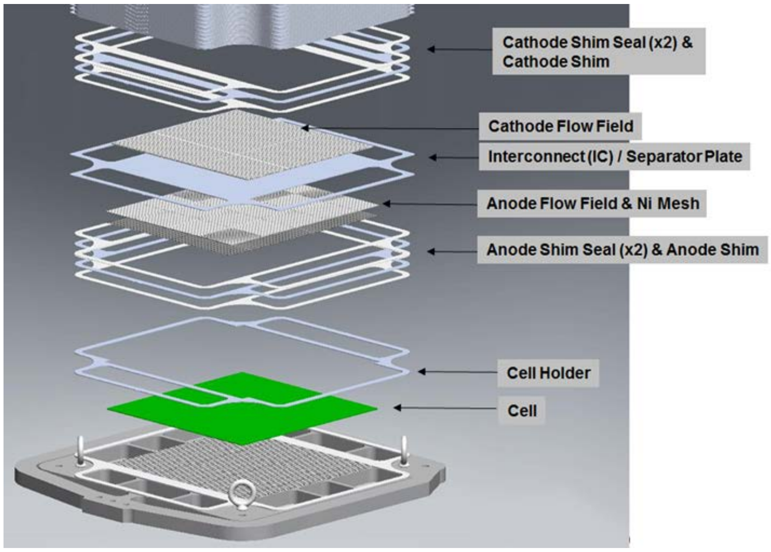

Figure 3-9. Illustration of Components and Materials Used in Internal Manifolding Design

Initial concepts using external manifolds were developed. One of the leading concept candidates is shown in Figure 3-10. In the design shown, the cathode and anode shim seals are eliminated and replaced by external manifolds which attach to the side of the cell package stack. The manifolds are made of mica to eliminate any electrical short. This design concept includes a change in footprint to scale up towards a larger cell package for MW-class module which was beneficial to the MCFC power systems. This also includes a change in flow configuration (anode and cathode flows) in order to better manage temperature distribution over the solid oxide fuel cell for these Large Area Stacks (LAS). This becomes even more important when increasing the overall footprint of the solid oxide fuel cell. There are four external manifolds in this design: two for the anode flow, one for cathode in, and one for cathode U-turn (Figure 3-10). The “cathode in” manifold directs high temperature air through only ½ of the cathode flow field area where the anode gas is hottest (the Anode-Out side). The cathode air enters the cathode U-turn manifold hotter than at the Cathode In. The Cathode U-turn manifold redirects this warmer cathode in air to where the anode gas is coldest (the Anode-In side). This helps offset localized cooling resulting from direct internal reforming (DIR). The cathode air exits into the module enclosure (vessel) area surrounding the stacks.

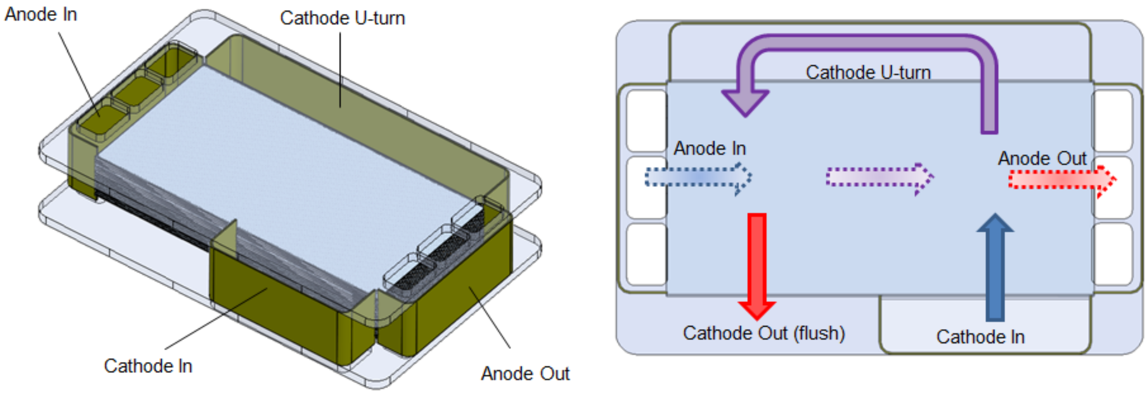

Figure 3-10. Illustration of External Manifold Concept and Flow Configuration

The external manifolds take advantage of leaf springs on notches at the sides of a sheet metal bent interconnect (See Figure 3-11). The interconnects act as shimming seal surface in place of the shim seal assemblies and divide the anode and cathode flow streams into each flow field component. When assembling the external manifold, the ends of the manifold are slid into the notches with the springs until they bottom out. The leaf springs hold the external manifold in place, which is further secured by the mica material expanding when bringing the stack up to temperature for thermal cycling checkout.

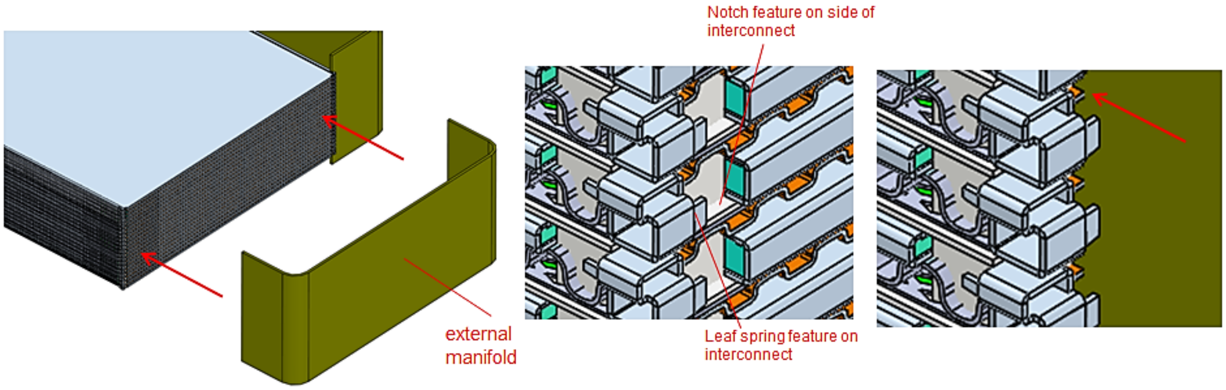

Figure 3-11 Securing External Manifold to Interconnect

Figure 3-12 illustrates a repeatable cell package which incorporates component reduction, material reduction, novel sealing strategies, and fabrication method improvements. Intumescent seals are slid into the folds of the interconnects and expand under elevated temperature to prevent anode and cathode gas from leaking out of the stack as well cross leaking into one another. The lance offset corrugations of the flow field are replaced by continuous corrugations that run the entire length of the cell package. The cathode flow field also benefits from continuous corrugations. This greatly improves repeatability of this component and allows the anode gas flow distribution in the stacking direction to be more accurately controlled. Single strip alumina seals greatly reduce material waste while providing adequate sealing of cathode and anode gases. The cell package itself is twice as long as the prior design to increase the rating of the stack.

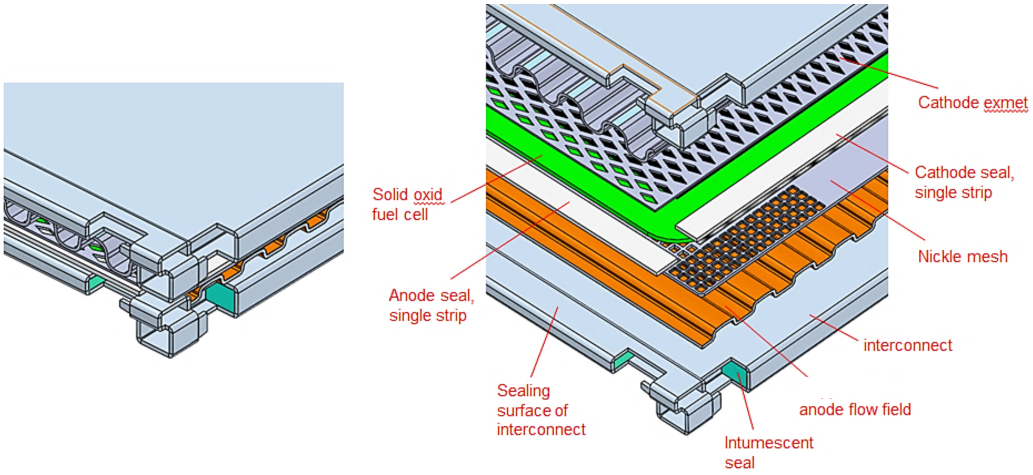

Figure 3-12 Repeatable Cell Package

TASK 4. MW-Class Process Design and Stack Costing

Process simulation activity for the 1 MW SOFC system to guide the conceptual design was carried out. A CHECAD-based simulation run at NOC condition of 250 mA/cm^2 was performed. The system configuration was kept similar to the 50 kW PCM system. The system employs SOFC stacks with cascaded cathodes for the Combined Heat and Power application. Natural gas is used as the fuel and cathode air dehumidification is accomplished using the desiccant-based subsystem. SOFC modules containing a total of 10,000 cells of 550 cm^2 cell active area are required to generate over 1 MW of net AC power output.

Stack Costing: The factory cost estimate for the SOFC stack block was updated in June 2014 as planned. The 'Baseline SOFC Power Block Factory Cost Estimate' topical report reflecting the results was prepared and issued (Rev 1) on February 12, 2015. The objective of the cost analysis was to provide an updated Factory Cost Estimate for FuelCell Energy's SOFC stack blocks which are manufactured by the company's wholly owned subsidiary, Versa Power Systems. Prior to this study, the last revision of SOFC stack Factory Cost was performed in Year 2011 under DOE contract DE-FC26-04NT41837. The current cost study, as part of the Co-operative Agreement DE-FE0011691, included bottom-up, stack production cost estimation techno-economic analyses to estimate stack production costs (\$/kW$_{\text{system net AC}}$ [2011 \$]) at volumes of >250 MW/year. The main focus of the updated estimate was to revise the cost year basis (from 2007 US\$ to 2011 US \$), to incorporate revised materials cost data, and to adjust the fuel cell stack power density basis from peak power rating to normal power rating.

The SOFC repeat unit (cell) size of 550 cm^2 (active area) and stack size of 120 cells (number of repeat units) were selected for the Factory Cost estimation, as these are technically- and economically-viable for aggregation into a ≥ 250 kW fuel cell modules, which in turn would serve as the building block for ≥100 MWe IGFC (Integrated Gasification Fuel Cell) and/or NGFC (Natural Gas Fuel Cell) systems for central power stations. The cost estimate is based on an annual production level that is sufficient for two 673 MWac IGFC plants. The previous studies under NT41837 have shown that due to incorporation of steam bottoming cycle and the anode gas expanders (toping cycle), only 529 MW of gross SOFC stacks are needed to achieve 673 MW net AC of electricity (maintaining a Net AC to Gross DC ratio of 1.272). In order to achieve 2 x 529 MWdc plants per year, a production of 53,760 stacks per year is required. At such high production volume rate, the stack assembly is projected to cost \$4,748 (Year 2011 US dollars). This cost translates to \$241 per kW gross stack dc (rated at 19.69 kW dc gross) or \$189 per kW ac at a production volume of about ~1069 MW dc. The breakdown of the stack component costs is shown in Figure 4-1. Of the total stack cost of \$4,748, \$2,700 is for procured components and \$2,048 is for in house fabrication of cells, stack assembly, and building expenses.

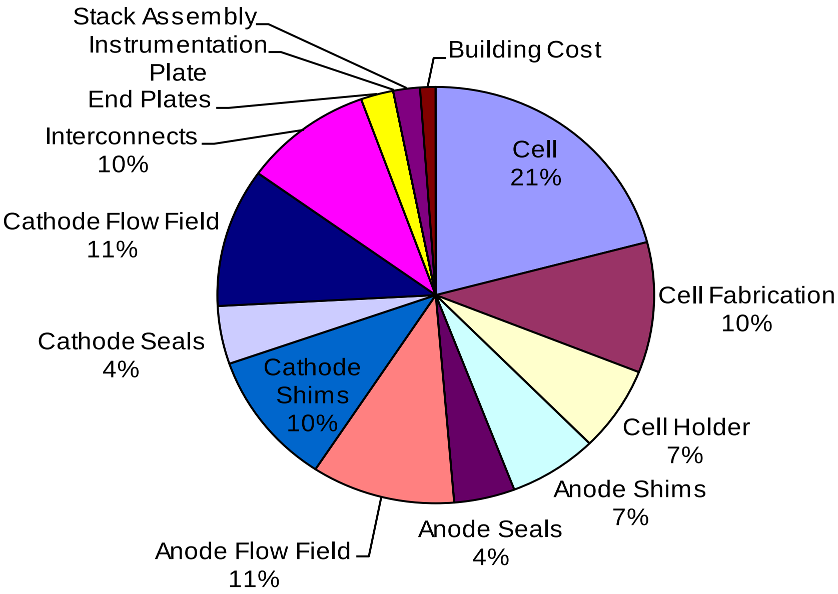

Figure 4-1 Block Cost Breakdown by Percent

Parametric studies were conducted to examine the effect of annual production rate and the power density on the stack block factory cost. The results indicated that it is feasible to meet the DOE cost target of $225/kWac (2011 US Dollar [USD]) at a volume production rate of ~ 250 MW per year. To achieve the DOE cost target, the fuel cell power density during the normal operation condition needs to be >300 mW/cm^2. The parametric studies further indicated that the Factory Cost of the stack block can approach $189/kWac (2011 USD basis) at high volume production rate of >1000 MW per year.

TASK 5. Proof-of-Concept Module (PCM) System Test

The objective of this task is fabrication, assembly, and factory testing of a ≥50 kW SOFC PCM power plant. The PCM system was based on the detailed design and fabrication package developed previously in the SECA Coal-Based Systems project (NT41837).

5.1. Balance-of-Plant (BoP) Component Fabrication

Catalytic Heat Exchanger and Catalyzed Partial Oxidation (CPOx) Reactor: The 50 kW SOFC PCM power plant system design has several innovative balance of plant (BOP) equipment enhancements. One major aspect of the PCM design is the merger of the catalytic oxidizer with the heat exchanger used to preheat the cathode inlet air. This combination is referred to as the catalytic heat exchanger. For plant start-up, the heat exchanger catalyst needs to initiate the combustion of hydrogen-rich start up gas with air from room temperature. The CPOx (catalytic partial oxidation) system is used to exothermically convert methane into a hot hydrogen-rich start up gas. The catalytic heat exchanger and CPOx system, shown in Figure 5-1, were installed and tested within the 400 kW Power Plant Facility at FuelCell Energy in Danbury, CT.

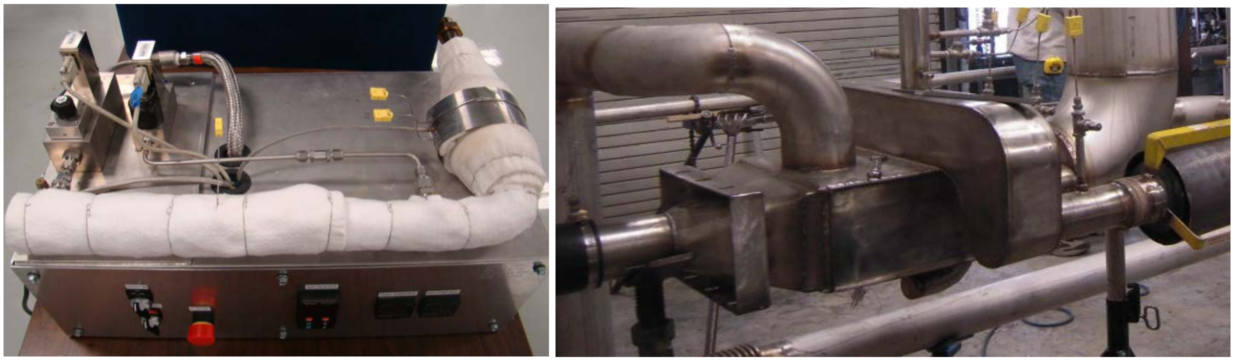

Figure 5-1. Picture of the CPOx reactor system (left) and the catalytic heat exchanger (right) installed in the 400 kW Power Plant Facility at FCE

The CPOx system was incorporated into the facility after the first round of testing. The CPOx catalyst exothermically reforms (partially oxidizes) methane into hydrogen and carbon monoxide gas. Initial testing of the CPOx system showed successful reformation, however at a lower conversion percentage than expected. The CPOx system performance can be seen in Table 5-1. Additional optimization testing is planned.

Table 5-1.Evaluation of CPOx reactor performance at two different Air to Fuel inlet flow ratios (GC measurements compared with equilibrium concentrations estimated by ChemCAD process simulations)

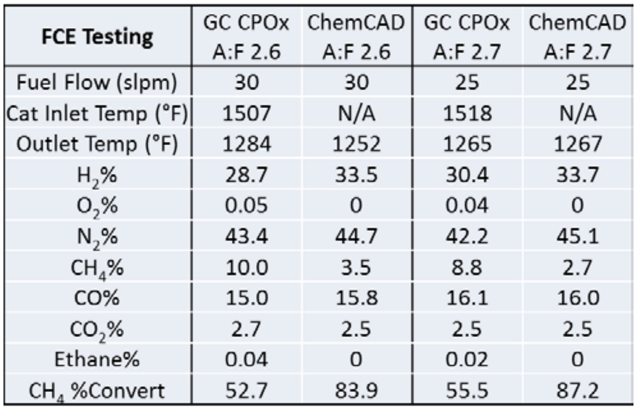

FCE Testing	GC CPOx A:F 2.6	ChemCAD A:F 2.6	GC CPOx A:F 2.7	ChemCAD A:F 2.7
Fuel Flow (slpm)	30	30	25	25
Cat Inlet Temp (°F)	1507	N/A	1518	N/A
Outlet Temp (°F)	1284	1252	1265	1267
H_2%	28.7	33.5	30.4	33.7
O_2%	0.05	0	0.04	0
N_2%	43.4	44.7	42.2	45.1
CH_4%	10.0	3.5	8.8	2.7
CO%	15.0	15.8	16.1	16.0
CO_2%	2.7	2.5	2.5	2.5
Ethane%	0.04	0	0.02	0
CH_4 %Convert	52.7	83.9	55.5	87.2

Once the CPOx system was set up, additional ambient light-off testing of catalytic heat exchanger was performed. The catalytic heat exchanger catalyst was not able to initiate the combustion reaction between the CPOx gas and fresh air at temperatures below 280°F. Both system design improvements and catalyst formulation enhancements are being evaluated to decrease the light-off temperature and increase light-off reliability.

A secondary function of the catalytic heat exchanger is to oxidize any carbon monoxide in the anode exhaust to reduce emissions to acceptable levels by the California Air Resources Board (CARB). This limit is 0.1lb/MWhr for power plants, relating to a carbon monoxide concentration exiting the catalytic heat exchanger of 10ppm. To evaluate the CO scrubbing characteristics of the catalytic heat exchanger, the CPOx system was used as a CO generator and the catalytic heat exchanger was brought up to normal operating condition. Using a CO detector, it was determined that ~75ppm of CO was exhausting from the catalytic heat exchanger, exceeding the CARB limit. It is believed that if the CO came into contact with the catalytic heat exchanger catalyst, it would have been oxidized, so design improvements are being investigated to eliminate potential slippage.

Fabrication and testing of an alpha-unit catalytic heat exchanger for the 50 kW PCM system was largely successful, with a few areas of improvement identified. Progress was made on a beta-unit design that is expected to improve upon the following areas:

1. Improved light-off characteristics – To ensure that the 50 kW PCM system can heat-up from ambient temperatures, the beta-unit of the catalytic heat exchanger includes provisions for high-temperature electrical ignition device. The purpose of the ignition device is to facilitate pre-heating of the catalyst surface prior to introduction of H_2-rich startup gas. The heated catalyst is expected to effectively "light-off" the gas from ambient temperatures, enabling continued heat-up of the plant.
2. CO scrubbing capability – To ensure that carbon monoxide present in the anode exhaust gas is effectively destroyed (to meet CARB emissions requirements), the catalytic heat exchanger internal flow baffles have been designed with tighter tolerances to seal better against the shell casing. This change will ensure that all flow is directed around the catalyst-coated tubes and prevent bypass leakage of gas to the exhaust, which would allow CO to escape before contacting the catalytic surfaces.
3. Mechanical durability – To ensure robust long-life operation of the catalytic heat exchanger throughout numerous thermal cycles, the shell-side weld joints have been modified to improve strength.
4. Flow distribution – To ensure uniform distribution of air flow to each stack, the beta-unit catalytic heat exchanger has been designed with a single air outlet (cathode inlet gas) connection, whereas the alpha-unit had dual connection points. This design change eliminates the possibility of non-uniform flow rates and gas temperatures possible with dual outlets.

The alpha-unit test article was modified to include the ignition device and was tested to ensure the design viability. The ignition device was able to heat the catalyst sufficiently and allow "light off" at low flows of the H_2-rich start up gas. Once light off was initiated, the fuel and air flows could quickly be ramped up to their required levels for system heat up. The ignition device could then be turned off once the heat exchanger temperature and flow rate were high enough to sustain the combustion reaction. This new "light off" process was found to be very successful and repeatable. The beta-unit shell design will be finalized based on these results. The beta-unit core has been fabricated and sent to the catalyst vendor for coating.

Radiative Fuel Reformer: An integrated fuel preheater (radiative) and fuel pre-reformer is being developed. Integration of a fuel radiator into the SOFC module to preheat the anode inlet gases serves to indirectly draw heat from the SOFC stack hottest faces, lowering dT. Figure 5-2 shows a schematic of the radiative fuel reformer. By integrating a reforming catalyst into the fuel radiator, the heat flux from the stack hot faces will be increased (through higher radiator/reforming heat duty) and the on-cell reforming levels will decrease. These effects are anticipated to result in lower on-cell dT and improved stack reliability and endurance. Combining input from reforming catalyst vendors, CFD analysis, and sub-scale testing will ensure that the radiative fuel reformer heat duty, pressure drop, and methane conversion targets can be achieved. The full-scale radiative fuel reformer will then be fabricated for use in the PCM power plant.

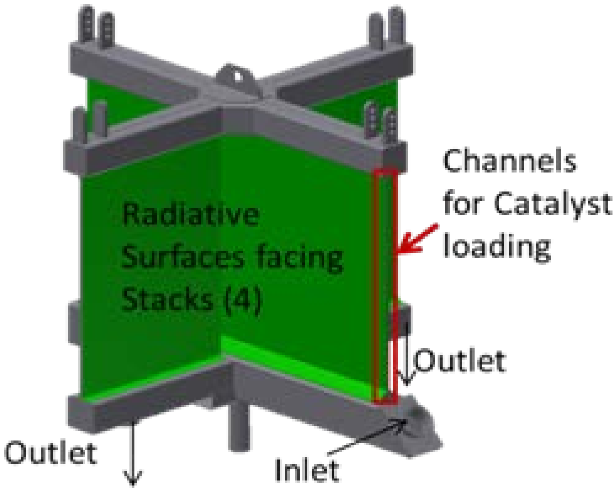

Figure 5-2 Schematic of Radiative Fuel Reformer

In previous system designs, packed bed reactors have been primarily utilized for hydrocarbon reformation. However, the PCM system employs an anode recycle blower in order to increase the system efficiency and to maintain water independence. Packed bed reactors result in a large pressure drop, which would inhibit the effectiveness of the recycle blower. In order to reduce the pressure drop effect while retaining the reforming capability, coated monolith catalysts have been evaluated from two partner companies. In-house testing at FuelCell Energy has validated the effectiveness of the catalyst coating by producing near-equilibrium outlet concentrations in a wide range of catalyst operating temperatures and space velocities. Figure 5-3, shows testing results comparing measured and expected equilibrium concentrations at the same catalyst temperatures. In addition to providing near equilibrium concentrations, pressure drop trough the catalyst was minimal and the catalyst fully reformed all higher hydrocarbons.

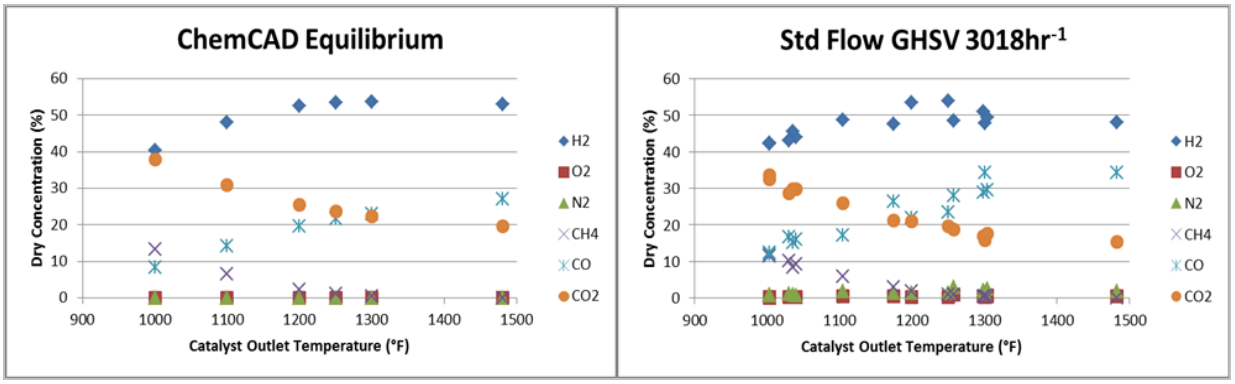

Figure 5-3. Reforming Catalyst Test Results: Measured Exit Gas Composition on Right, Compared with Expected Equilibrium Concentrations from ChemCAD Simulations on Left

After validating that the actual catalyst performance closely mirrors the simulated equilibrium concentrations from ChemCAD, additional ChemCAD simulations were performed in conjunction with CFD analyses. This analysis was used to determine potential anode inlet temperatures and compositions based on catalyst loading and expected radiative heat duty.

Progress was made on developing a suitable catalyst support structure design for the RFR. The development process included determining the shape of the corrugations by evaluating the temperature effects on the anode gas stream and pressure drop through the radiator channels.

After soliciting input from potential vendors for manufacturability, a V-shape fin was evaluated versus a straight style fin. ANSYS Fluent CFD software was utilized to model thermo-fluid effects on a partial section of one radiator channel. Endothermic effects of the catalyst coating were included as part of this analysis. Figure 5-4 shows the configuration modeled and the assumptions used for the analysis.

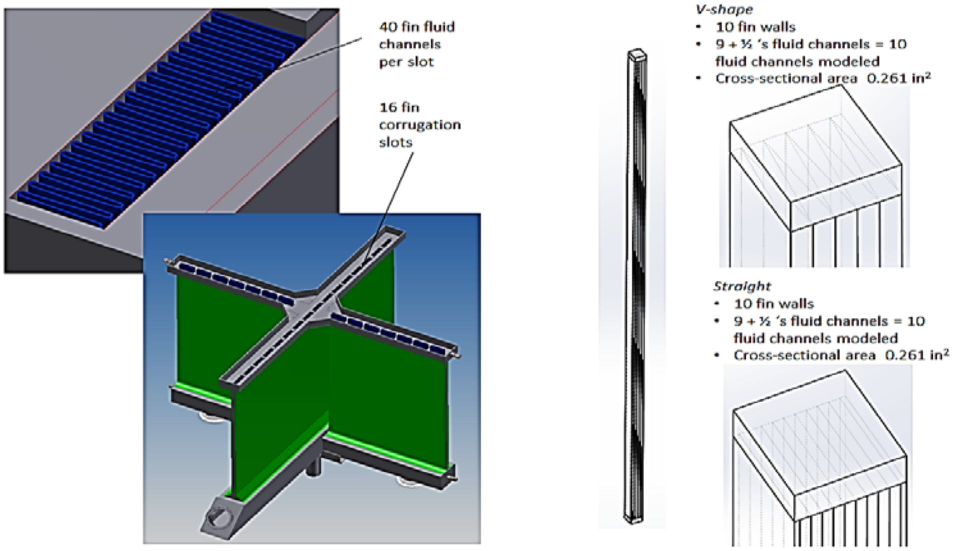

V-shape
- 10 fin walls
- 9 + ½ 's fluid channels = 10 fluid channels modeled
- Cross-sectional area 0.261 in^2

Straight
- 10 fin walls
- 9 + ½ 's fluid channels = 10 fluid channels modeled
- Cross-sectional area 0.261 in^2

Figure 5-4. Solid Models and CFD Boundary Assumptions for RFR Analysis

CFD analysis results are presented in Figure 5-5. The results showed that the V-shaped fin had better thermal performance with higher outlet temperature vs. the straight fin design. This is due primarily to the V-shaped fin having better shape factor exposure to the hot wall surfaces, thus providing more heat flux into the fin. Pressure drop along the length of the channels were similar for both designs, and significantly less than the maximum pressure drop requirement of 3 inches of water.

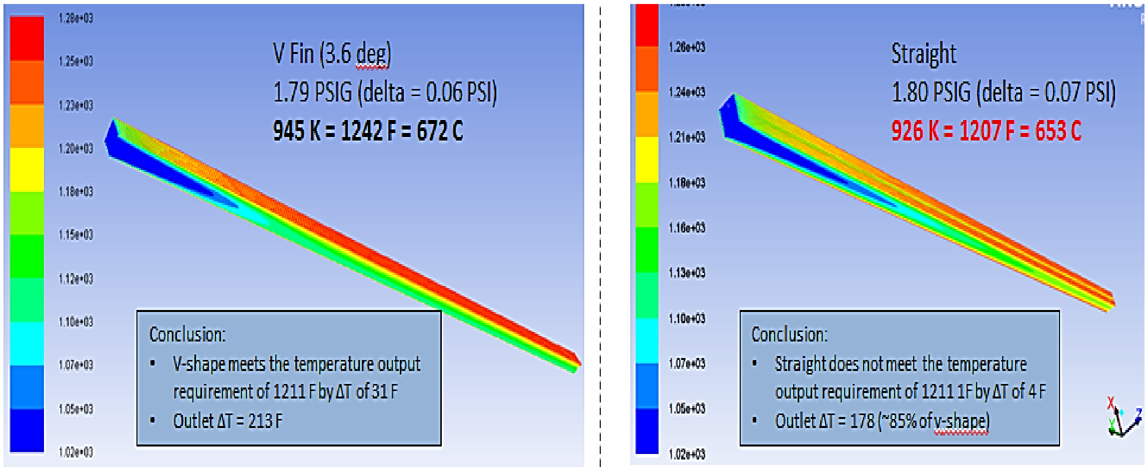

V Fin (3.6 deg)

1.79 PSIG (delta = 0.06 PSI)

945 K = 1242 F = 672 C

Conclusion:
- V-shape meets the temperature output requirement of 1211 F by ΔT of 31 F
- Outlet ΔT = 213 F

Straight

1.80 PSIG (delta = 0.07 PSI)

926 K = 1207 F = 653 C

Conclusion:
- Straight does not meet the temperature output requirement of 1211 1F by ΔT of 4 F
- Outlet ΔT = 178 (~85% of v-shape)

Figure 5-5. Comparison of CFD Analysis Results for Two Reforming Fin Insert Geometries (temperature scale shown in °F)

Manufacturing of the fin insert was examined, and several specific designs were considered. A vendor was found that could produce the fin from the required material in a form that provided added lateral stiffness (which will help maintain the shape after installation) and would closely simulate the V-fin design by exposing more of the fin to the hot wall surfaces (good shape factor). A model of the fin and the actual fin are shown in Figure 5-6. The fins will be sent to the catalyst vendor for coating, and then sent to the fabricator manufacturing the RFR for installation into the assembly.

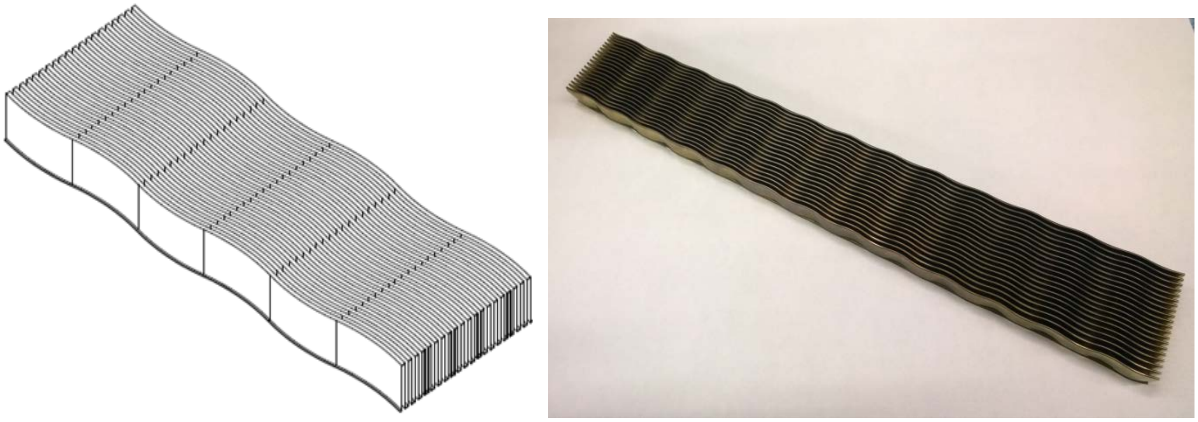

Figure 5-6. Solid Model of the Reforming Fin Insert (Left), and Actual Fin Insert (Right)

Anode Recycle Blower: A high temperature anode recycle blower was procured from a reputable vendor. Fabrication of the blower was completed. Figure 5-7 shows a photograph of the recycle blower at the vendor’s shop, prior to painting.

Figure 5-7. Photograph of Anode Recycle Blower at Vendor's Shop, Prior to Painting of the Base

The factory test for the high temperature Anode Recycle Blower was conducted and witnessed at the New York Blower test facility in LaPorte, Indiana. New York Blower is a parent company to MAS Air Systems LLC, the blower's manufacturer. The test was conducted at ambient temperatures, with results projected to operating conditions. Figure 5-8 shows the blower performance characteristics.

The specified flow and static pressure criteria were demonstrated, with a mechanical efficiency (11.8%) that was lower than predicted. The blower will satisfy all the fuel cell operating conditions, but will result in a somewhat higher parasitic power load.

Sound data collected during testing indicated 98 dbA averaged free field in a reverberant room. The data were for the bare, uninsulated blower and were corrected to exclude the sound from the motor. (The motor used for testing was supplied at the site since it needed linkage to a testing dynamometer.)

Vibration data collected at speed and during coast down exhibited no problem with harmonics or regions that would need to be avoided during variable speed operations.

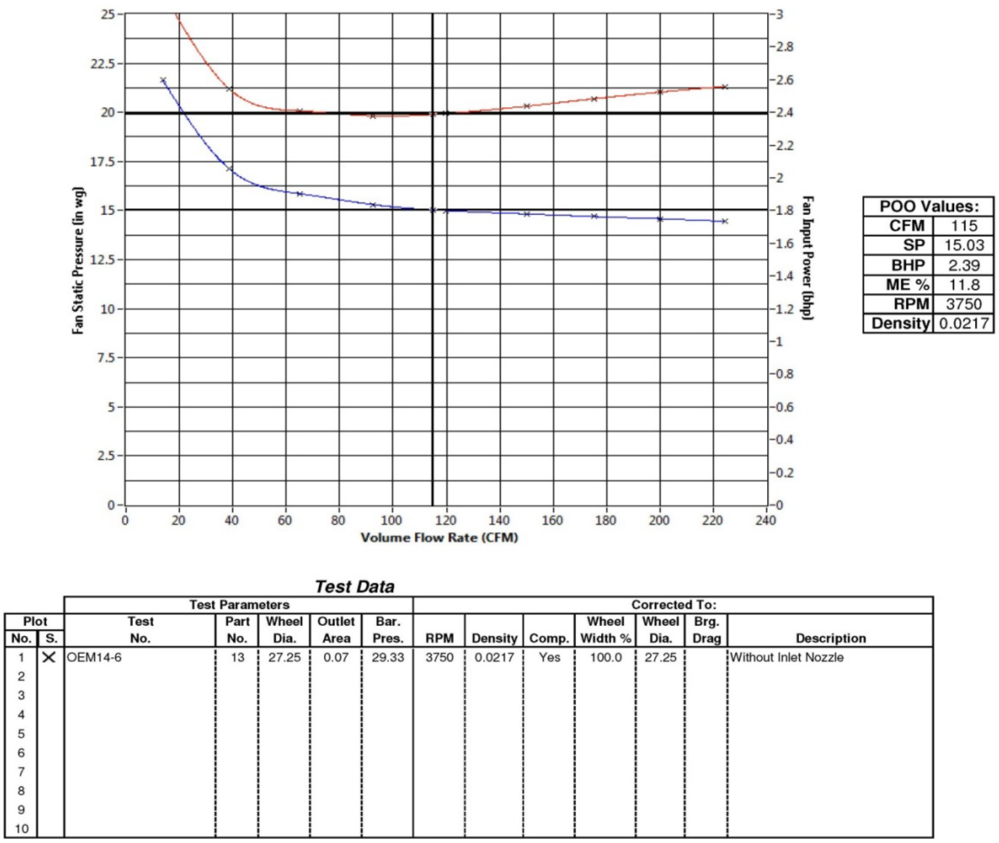

POO Values:	
CFM	115
SP	15.03
BHP	2.39
ME %	11.8
RPM	3750
Density	0.0217

Test Data

		Test Parameters					Corrected To:						
Plot No.	Plot S.	Test No.	Part No.	Wheel Dia.	Outlet Area	Bar. Pres.	RPM	Density	Comp.	Wheel Width %	Wheel Dia.	Brg. Drag	Description
1	✕	OEM14-6	13	27.25	0.07	29.33	3750	0.0217	Yes	100.0	27.25		Without Inlet Nozzle
2													
3													
4													
5													
6													
7													
8													
9													
10													

Figure 5-8. Anode Recycle Blower Performance Characteristics Observed During The Factory Acceptance Test

Anode Recycle Heater (ARH): An anode recycle heater was developed to compensate for thermal energy lost from the anode recycle blower and temperature drop from mixing with the colder water and fuel streams during start-up. By integrating an inline heater within the pipe run, the temperature of the recycled anode gas can be adjusted to satisfy required operating conditions prior to entering the fuel reformer.

The development activities focused on the heater design and ducting of the pipe spool. Critical performance measures included, pressure drop across the pipe spool, power required to heat the anode gas, and surface temperatures of pipe spool and heater.

Limiting the pressure drop across the pipe spool at the outlet of the recycle blower and heater minimizes blower power requirements and increases the overall SOFC plant efficiency. A design was chosen, with consideration for manufacturability and adaptability to recycle blower outlet. It was evaluated for pressure drop from inlet to outlet using ANSYS Fluent CFD software. Fluid material properties (density, viscosity, etc.) and boundary conditions (inlet mass flow, exit pressure, etc.) were inputs to the analysis. The pipe spool was further developed to incorporate an inline heater after CFD results showed a pressure drop below the design requirement of 0.05 PSI. Figure 5-9 shows CFD analysis for the pipe spool design**.**

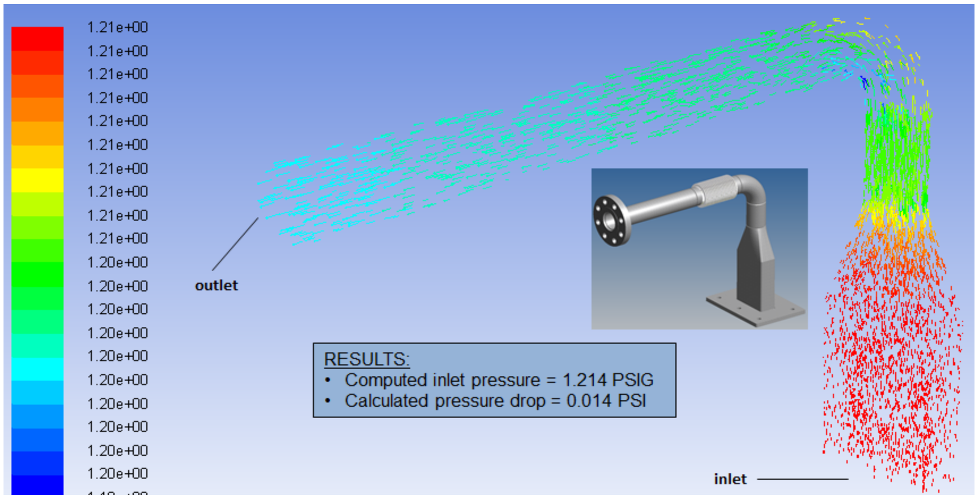

RESULTS:
- Computed inlet pressure = 1.214 PSIG
- Calculated pressure drop = 0.014 PSI

Figure 5-9. CFD Analysis of Pipe Spool Design for Exit Connection from Anode Recycle Blower

Heater development focused on utilizing a market-ready high temperature heater platform with room for some customization. A worst case temperature drop (from thermal energy losses stated above) was calculated to be 100°F. Hand calculations indicated an initial power requirement of 2 kW. The diameter and length were sized to limit the surface temperature of the heater to prevent damage. The thermal fluid effects of the inline heater were further evaluated using CFD. Appropriate fluid properties and boundary conditions (including radiation, conduction through pipe and insulation walls, natural convection, and heat flux through heater wall) were chosen as inputs. The program was run until convergence was reached for outlet temperature. Results showed that a 2 kW heater was not sufficient enough to increase the process gas temperature by 100°F. Heat flux values were then increased until this requirement was met. The resulting power requirement was determined to be 2.4 kW.

The final steps were to determine the final heater length and associated assembly configuration to prevent the inline heater from overheating as well as prevent the pipe and heater support structure from reaching unacceptable operating temperatures. The entire pipe spool assembly (heater, liner, pipe, etc.) was analyzed with the CFD software to evaluate surface temperatures. Initial results showed that the heater surface temperature was higher than maximum operating temperature of 1800ºF. The length of the heater was then increased in order to increase surface area. An increase in surface area with the same power reduced the heat flux, thus reducing the surface temperature of the heater. Iterative calculations were completed, increasing the heater length until the surface temperature of the heater was significantly below maximum operating temperature.

A support structure was required to prevent damage to the heater from drooping due to thermal effects since it was initially supported at only one end. A tripod style containment structure was chosen that would be easy enough to fabricate but provide some clearance with the heater wall within the ½" acceptable droop specification provided by the vendor. The resulting tripod structure was then analyzed in the CFD software and showed that the temperature of the inside diameter of the pipe wall was within acceptable limits (<1400°F). Figure 5-10 shows the CFD analysis results.

Detailed design work was completed, heater procured, and the final design released to fabrication. A model of the anode heater assembly is shown in Figure 5-11.

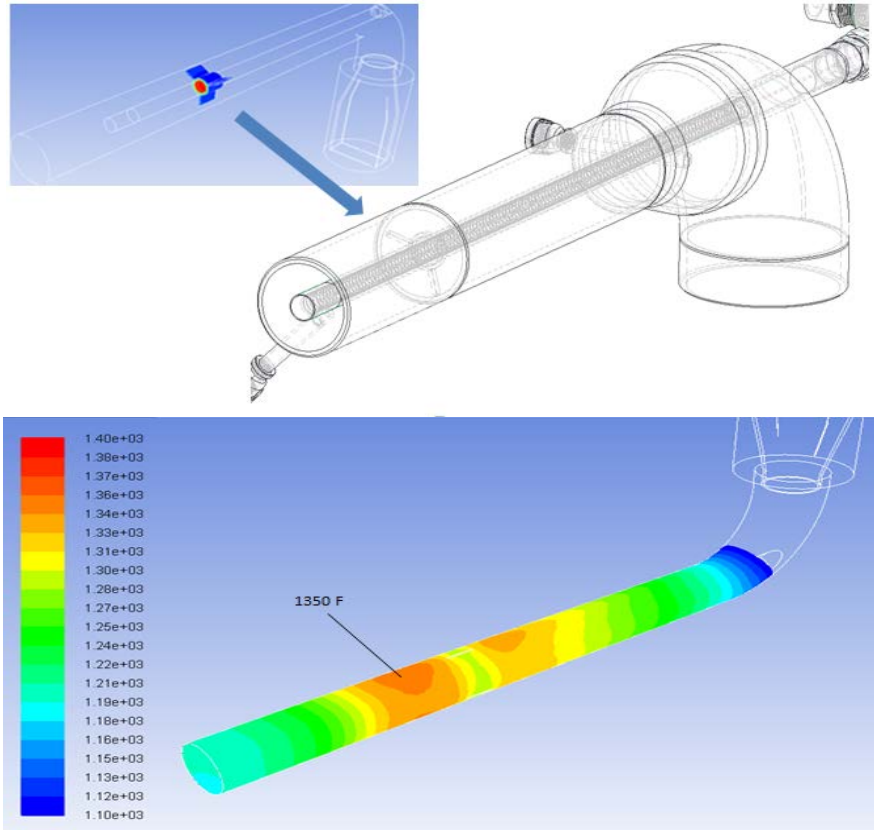

Figure 5-10. Thermal Analysis of the Heater Including Heater Support (top) and Inside Pipe Wall Temperatures (bottom, temperature scale shown in °F)

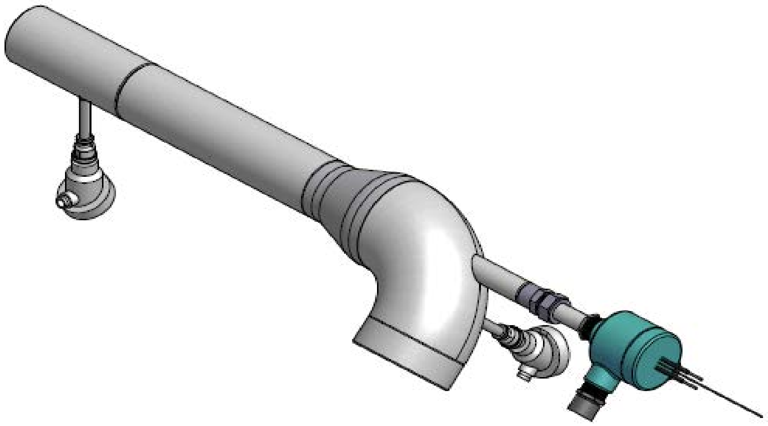

Figure 5-11. Isometric Model of the Anode Heater, Including Instrumentation

Anode Fuel Injector (AFI): An anode fuel injector was also developed. The primary function of the fuel injector is to replenish fuel that is consumed by fuel cells, in a well-mixed manner, while minimizing coking. The development activities focused on the fuel injection equipment design and location of attachment onto the pipe spool. Critical performance measures included level of mixing (qualitative), surface temperatures (to prevent coking), pressure drop across the injector and exit velocities from the injection tip.

It was found that attachment of the fuel injector to the downstream elbow of the pipe spool was ideal, allowing steam injection upstream while injecting fuel right before entering the anode recycle blower which would help with mixing. Initial concepts utilized a small diameter stainless steel tube (within a small diameter pipe) to inject cold fuel gas into the anode gas stream. CFD software was used to evaluate this initial design and evaluate critical performance factors. Initial results showed poor mixing and potential for coking prior to injecting into the anode gas stream due to high local temperatures on the nozzle, prior to mixing with the moist anode stream.

A new innovative design was developed. One feature was the utilization of an insulating material with anisotropic thermal properties to direct conductive heat transfer away from the tip of the injector. A key aspect to utilizing this material was dividing the geometry of this insulation into a thick sleeve for the bulk of the injection tube and a thick washer at the injection tip, as shown in the detail view of Figure 5-12.

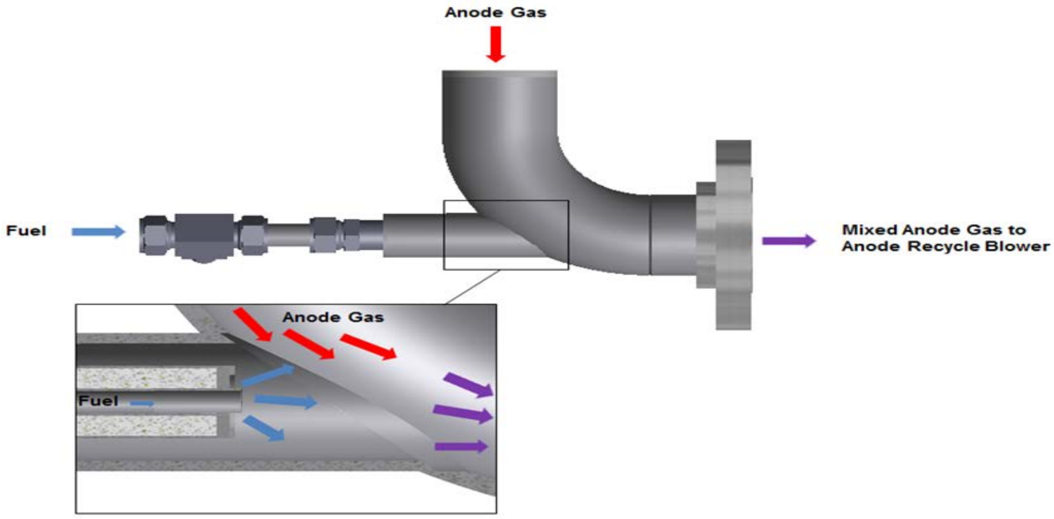

Figure 5-12. Anode Fuel Injector Model with Detailed View showing the Insulated Fuel Nozzle and Mixing of Fuel with the Anode Gas Stream

Another feature to be devised was the use of a design that both increases exit velocities at the injection tip to pull more heat out of the nozzle and also promotes mixing, thus preventing coking on surfaces around the tip of the injector body and mixing area. A triple spiral flute nozzle design was implemented as a solution. Figure 5-13 shows the design. CFD analysis results are presented in Figure 5-14. The CFD analysis showed that the reduced cross-sectional area of the fluid stream also creates a jet pump phenomena with the spiral. This combination promotes more uniform heat transfer into the cold fuel gas, thereby cooling the surrounding nozzle. It also increases the fluid mixing, allowing the fuel to exit the injector and blend with the moist anode gas stream eliminating the possibility of overheating and coking on a hot surface.

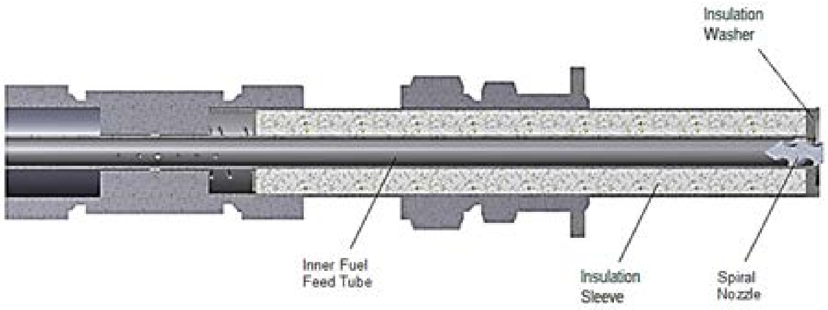

Figure 5-13. Detailed View of Fuel Injector with Triple Fluted Spiral Nozzle Tip

Detailed analysis showed an acceptable pressure drop of 0.72 psi. Temperature distribution along and within the walls of the fuel injector showed good distribution and sufficient protection of the exiting fuel gas temperature. The plume of ejected fuel gas was shown to penetrate the anode gas stream far enough from adjacent “hot” pipe surfaces to prevent coking.

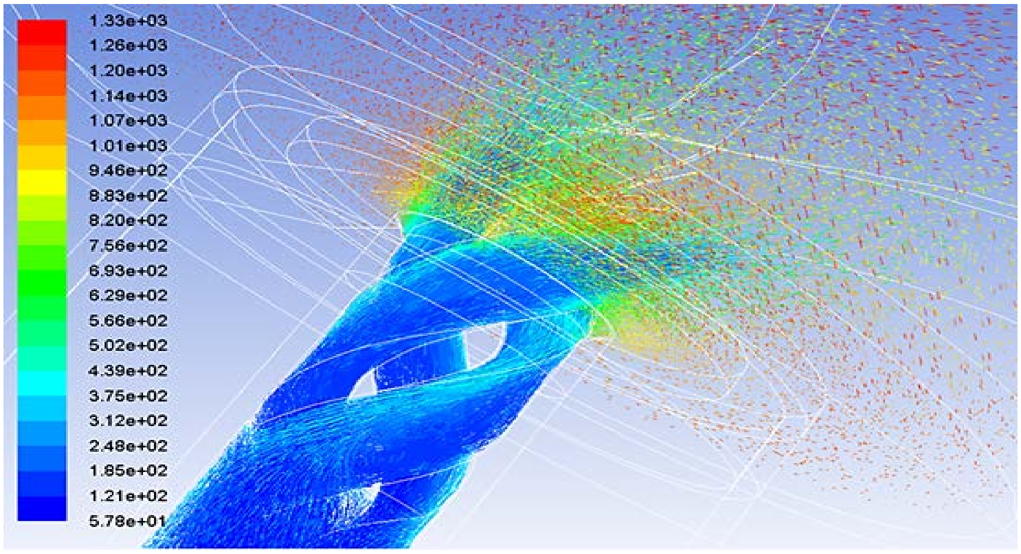

Figure 5-14. CFD Analysis showing Mixing Attributes of the Spiral Fuel Injector Design (Temperature scale shown in °F)

Anode Water Injector (AWI): An anode water (steam) injector design was developed and released for fabrication. Integration of a water injector into the anode pipe spool serves to prevent coking when fuel is injected during start-up and during operation when there is insufficient moisture in the anode recycle flow. The development activities focused on the water injection equipment design that would prevent rapid steam expansion and pulsations within the anode gas stream. Also, due to the location, the design needed to accommodate movements due to thermal expansion of the balance of plant piping. If water enters the anode gas stream not fully vaporized, there is a chance that steam explosion event can occur along the anode gas streaming path.

Due to packaging requirements, the integration of the water injector along the length of the anode pipe spool between the module and recycle blower was chosen. This design utilizes the thermal energy from the anode gas stream to vaporize water. However due to the location, it had to be in parallel with the bellows expansion joints, as shown in Figure 5-15. The design accommodates the movements by having the injector supported at both ends. The inlet water stream end is supported by a concentric pipe design that fixes the assembly axially and laterally, yet still allows slight rotation. The other end, facilitated by the installation guides, permits the steam ejection end to be free to move longitudinally and pivot, but support the vaporizer body axially. Finally, prior to injection, vaporized water passes through a diffuser to minimize pulsations and ensure only high quality steam is introduced onto the anode flow stream. Figure 5-16 shows the anode water injector detail and features.

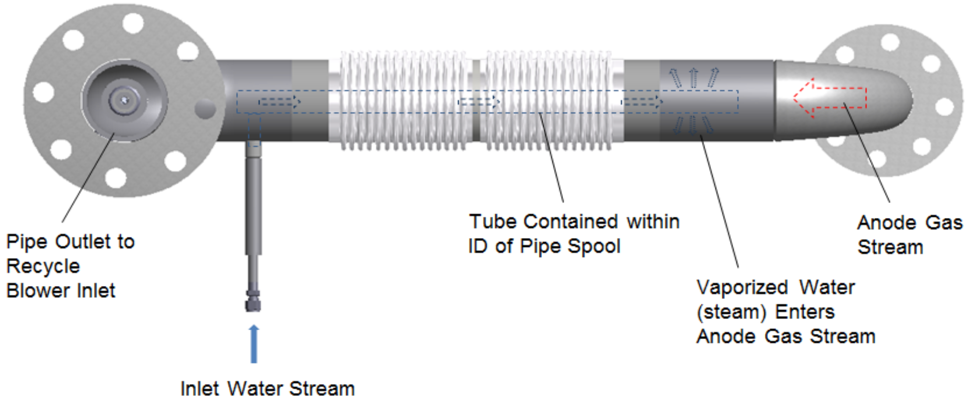

Figure 5-15. Anode Pipe Spool Assembly with Anode Water Injection

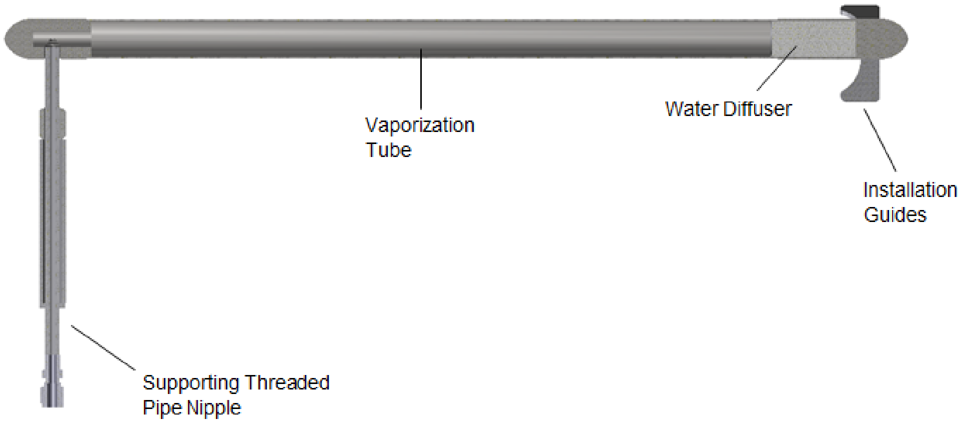

Figure 5-16. Anode Water Injector Details

Fresh Air Blower: The fresh air blower was selected and purchased. The blower is a 7.5 hp model SCL K06-MS-GOR-010 from FPZ Inc. Like the anode recycle blower, it will be controlled by a variable frequency drive.

Other Components: Fabrication drawings for custom-designed components, such as the fuel and start-up water injectors, were created and issued to vendors for quotation. All process equipment including the Desiccant Cathode Air Dehumidification Subsystem was received. All process instrumentation (including control valves, safety valves, pressure regulating valves, thermocouples, etc.) was selected and was ready for procurement by the system fabricator (Task 5.2).

Power Conditioning and Control Systems: The Power Conditioning System (PCS), consisting of resonant MOSFET-based DC-DC converters and output IGBT-based DC-AC inverter and ancillary components, was completed in terms of design and layout of components. The enclosure details including sheet metal and mounting studs were specified. Figure 5-17 shows the location of the DC-AC inverter section and the DC-DC converter section within the Electrical Balance of Plant (EBOP) enclosure. Remaining work consists of layout of custom flexible busbars. With the exception of the busbars, all items have been procured and are in-house at the vendor, ARDA Power. All components have been bench tested for conformity to specifications. The PCS occupies a little more than half of the EBOP enclosure cabinet.

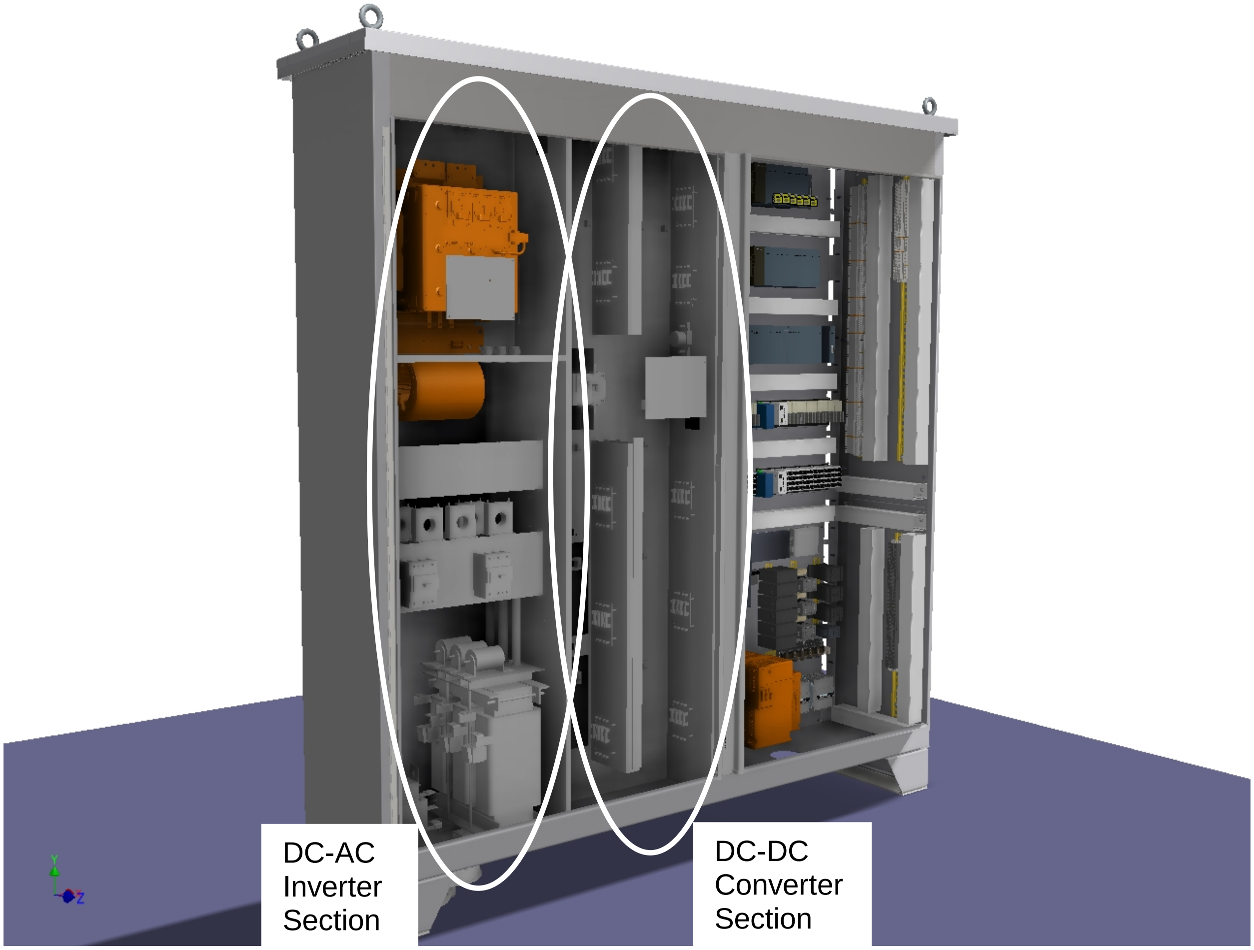

Figure 5-17. EBOP Enclosure Showing DC-AC Inverter Section and DC-DC Converter Section.

The other main section of the EBOP is occupied by the Central Control System (CCS) consisting of programmable logic controller (PLC), stack module isolation circuitry, motor drives, transformer, and protective components. Enclosure details including sheet metal and mounting studs were specified for the CCS as well. Fan cooling arrangement has been completed. The PLC racks and most modules have been procured and are in-house at FCE. The stack module isolation components have also been procured. One variable frequency drive has been received at FCE and is being configured for (fresh air blower) testing. The EBOP enclosure cabinet is currently being specified based on PCS and CCS equipment layout, for mounting details prior to submission for assembly quotation from the enclosure manufacturer. Figure 5-18 shows the enclosure with CCS section layout.

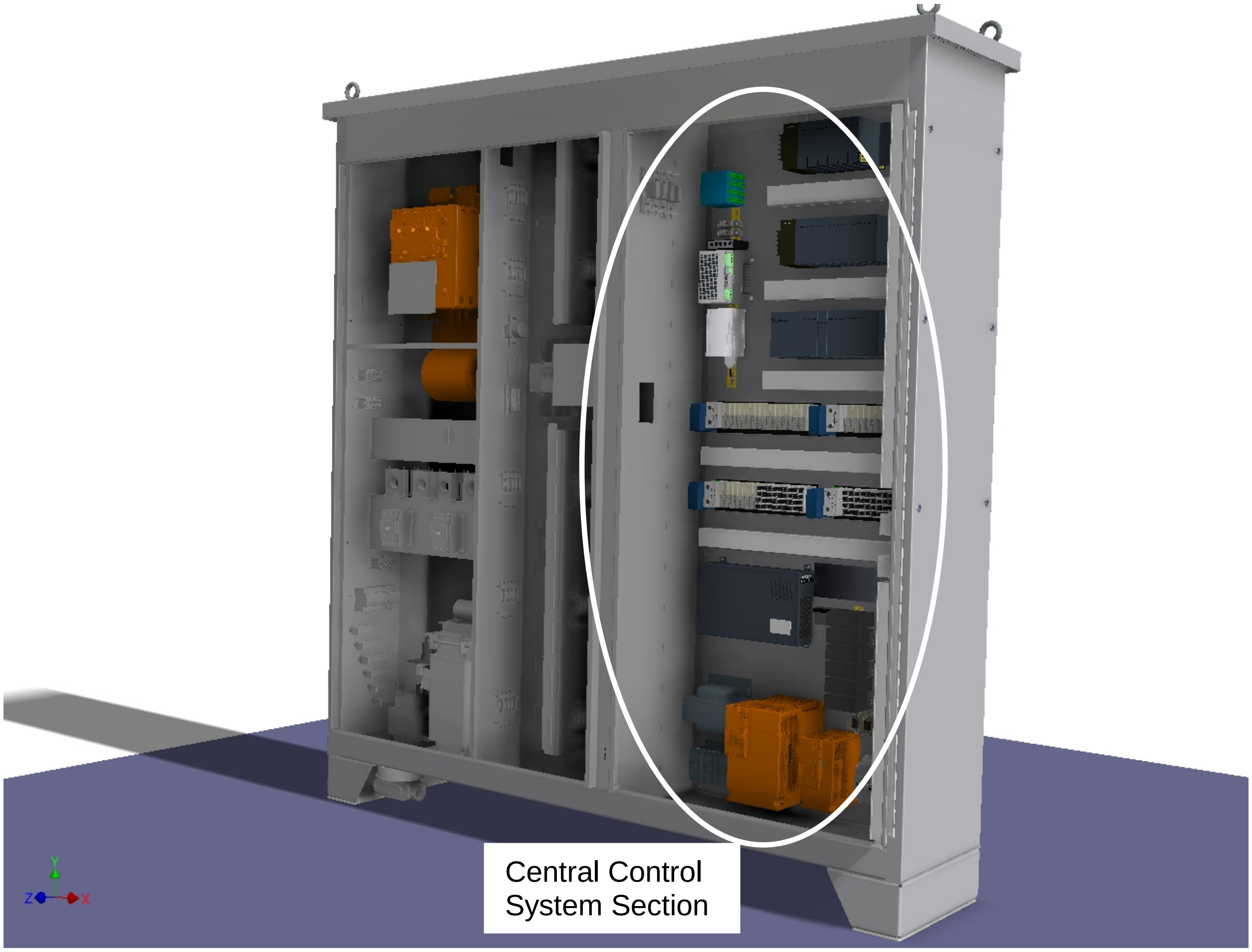

Figure 5-18. EBOP Enclosure Showing Central Control System Section.

5.2 PCM System Assembly

Assembly at Vendor Location

A Request for Quotation was issued to a fabrication shop for assembly of the PCM system and a quotation was received. A contract was awarded to a primary integrator for the plant system. The plant mechanical balance of plant sub-system was divided into seven sub-systems: anode recycle, fuel and desulfurization, air and exhaust, water, nitrogen, CPoX, and the structural skid. Detailed designs were reviewed and released for fabrication to the vendor. In addition to the mechanical plant, the other two main sub-systems included the module, and electrical balance of plant (EBoP). Construction of the system skids was carried out.

The fabrication and assembly of the system was completed. It included fabrication elements such as: structural skid; process piping of subsystems (anode recycle, air system, nitrogen, etc.), instrumentation racks, instrumentation installation (population) with checkouts, water tank with water system control box, electrical panels, cable routing and Electrical Balance of Plant. Figures 5-19 through 5-21 show pictures of major sections of the system during the assembly process.

Figure 5-19 Fabrication Photos – Structural Skid w/ Desiccant and Desulfurizer

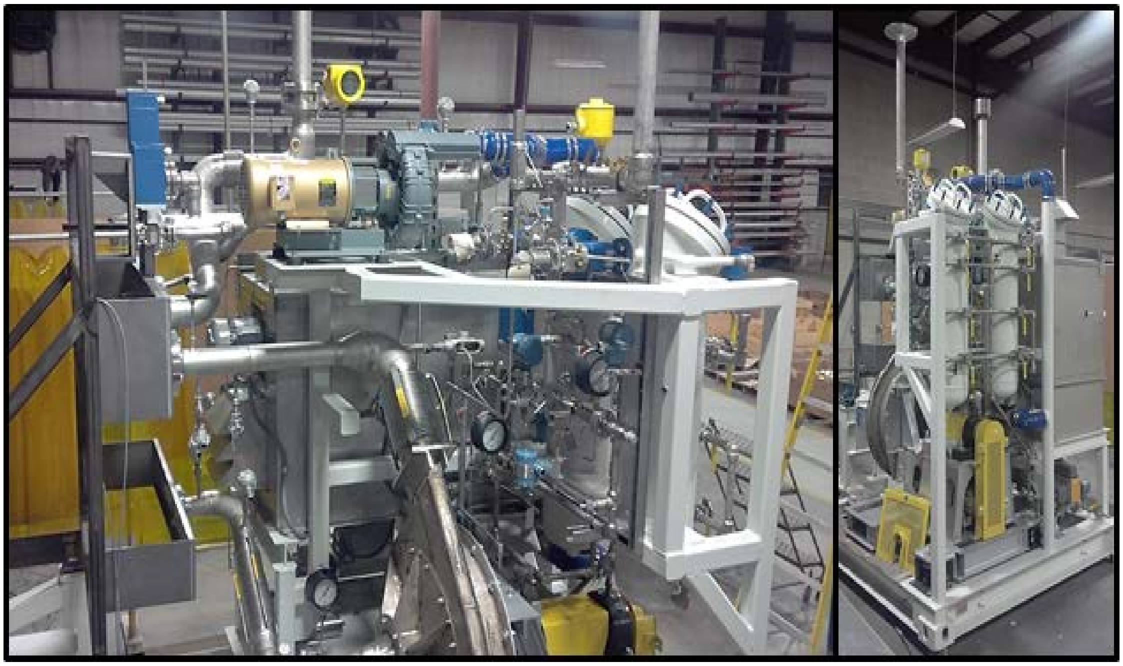

Figure 5-20 Fabrication Photos – Fresh Air, Recycle Blower, & Exhaust

Figure 5-21 Fabrication Photos – Inverter & Control Sides of EBOP Cabinet

Test Site Preparation

The 50 kW plant was planned to be installed on Pad 10 at FCE, Danbury. A layout was prepared as shown in Figure 5-22.

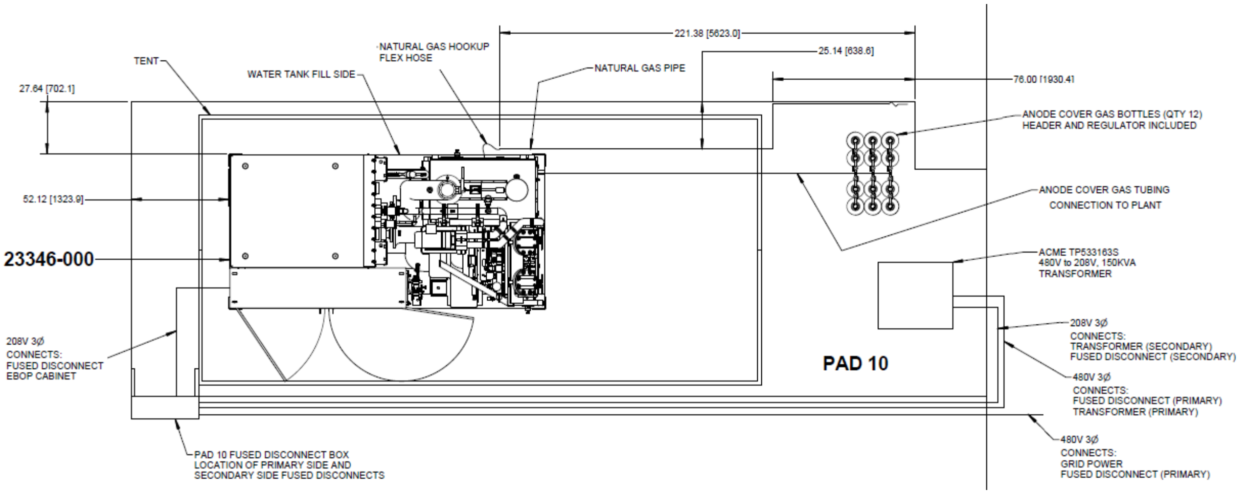

Figure 5-22 Layout of the 50 kW PCM Plant on Pad 10 at FCE, Danbury, CT

Pad 10 was previously used for a DFC300 BoP along with other smaller pieces of equipment. The equipment present on Pad 10 was relocated to make room for the 50 kW plant. Once the pad was fully vacant, electrical connections were prepared for the plant. A transformer was required to convert the 50 kW Plant's 208V output to the pad's 480V connections. Additionally, the electrical disconnects on the pad needed to be re-sized to accommodate the smaller electrical loads of the 50 kW system. New electrical disconnects and the transformer were procured.

Natural gas supply was required for the 50 kW plant. The natural gas line that served Pad 10 was in use by an adjacent facility. Final natural gas connection was made once the adjacent facility operation was completed.

A large wind and snow-rated tent-style shelter was procured for use during the plant final check-outs, to keep the weather from affecting the work.

System Installation at Test Site

The 50 kW BOP was shipped to FCE's Danbury facility by the plant fabrication vendor and put in place on pad 10 by an industrial rigging company (Figure 5-23) on April 21, 2015. A large wind and snow-rated tent-style shelter was installed Figure 5-23 shows the frame of this tent. Electrical, natural gas, and cover gas connections were made to the 50 kW BOP. A transformer was installed to convert the 50 kW Plant's 208V output to the pad's 480V connections.

Figure 5-23 50 kW BOP Installation & Frame for Protective Tent

The Module was located on BOP structural skid above the water tank (Figure 5-24). Final plumbing and electrical connections were completed. Installation of insulation on the process piping, flange connections and anode recycle blower installation were completed while equipment and instrumentation final check outs were performed. The aluminum jacketing, covering the glass wool and Microtherm insulation along the pipe, on the cathode exhaust line can be seen in Figure 5-24. A façade construction was installed around the perimeter of the plant (Figure 5-25). The purpose of this structure is to prevent inadvertent access to the plant equipment by unauthorized individuals. Several panels are framed around the perimeter of the façade structure to allow access to plant equipment by authorized qualified individuals as well as access to emergency stop switches.

Figure 5-24 Fabrication Photos – Module and BoP (left), Instrumentation Rack & Electrical Panel (right)

Figure 5-25 Façade Constructed around 50 kW PCM Plant

5.3 PCM System Factory Testing

50 kW SOFC PCM System Checkout

PLC IO (input output) Checkout: The 50 kW control system had 330 analog and digital IO points. The control system included four OPTO 22 racks for stack voltage and temperature measurements. Each rack contained a power supply and an OPTO 22 brain for communication with the main PLC via Modbus. Before communication was established, each OPTO 22 brain and each temperature channel was configured. Checkout of the IO channels was conducted to verify that all IO channels were set up properly, the wiring between the PLC and the terminal blocks was correct, and to verify the Modbus communication between the PLC and OPTO 22 devices.

Some issues were discovered during the checkout and were corrected. A defective Ethernet PLC card was found that prevented the PLC CPU from completing its boot-up sequence. This was corrected by replacing the Ethernet card. All issues were resolved with the PLC IO and focus was shifted to verification of the field components.

Component Verification, Final End-to-End Checkout and Leak Testing: After completing the IO checkout, component verification and end-to-end checkout was started. The component verification involved testing the individual components to verify that they function correctly and meet specifications. The end-to-end checkout involved a complete check from PLC to field component and verification of proper communication between these two points.

During checkout some issues were uncovered. One of the mass flow controllers, FV/FT-484 was found to be defective. The unit was repaired by the original manufacturer and installed in the system. The cathode air inlet thermal mass flow meter was giving incorrect flow and temperature reading on the PLC screen. When removed from the loop and tested with a handheld device, the correct analog signal was observed. The temperature and flow signal wires were moved to an analog card with isolated inputs to resolve this issue.

In addition to verification of the components and electrical signals, flow testing was performed on the natural gas, cPOX and purge gas sub-systems. Both the fresh air and anode recycle blower operations were verified and leak testing was completed on the natural gas system. In addition to leak testing, several of the welds were inspected by x-ray and dye penetrant, passing the inspection.

50 kW SOFC PCM System Commissioning Using Old (pretested) Stacks

First stage of the 50 kW SOFC system checkout and commissioning was conducted using pre-tested (old) 96-cell stacks. Testing was performed to identify issues with the balance of plant prior to testing with new (unused) stacks. The detailed test plan document was prepared. The primary objective of the 50 kW PCM system operation was to gain valuable experience operating large stacks in system relevant conditions while meeting operational milestones. Detailed evaluations were also planned on the many innovative features of the hot module, such as the radiative fuel reformer and catalytic heat exchanger. The 50 kW PCM system was expected to fully validate many design features to ensure the successful operation of the 100 kW system as well as other larger future systems.

Preliminary testing of the power plant was performed as part of commissioning. The power plant successfully transitioned through its start-up sequence and had sustained operation in hot standby mode. Figure 5-26 is a screenshot showing the stack voltages during hot standby and Figure 5-27 is a screenshot showing the cell temperatures. The old pre-tested stacks had several failed thermocouples.

Figure 5-26 Stack Voltages During Hot Standby

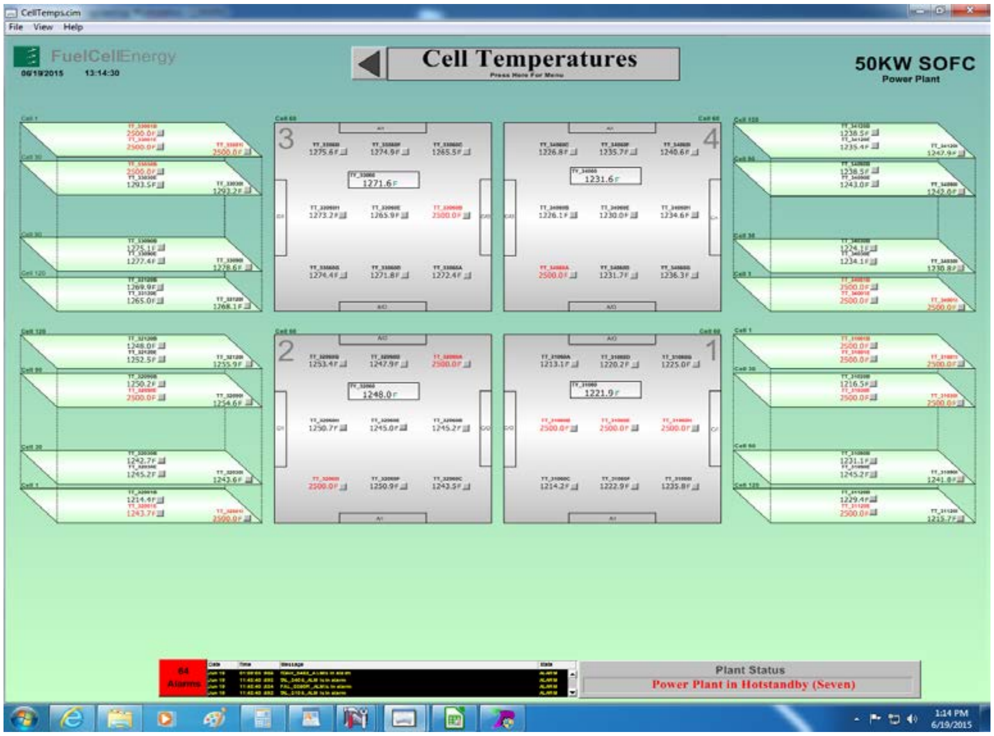

Figure 5-27 Stack Temperatures During Hot Standby

Commissioning of the 50 kW SOFC system using old stacks was completed. The power plant was successfully operated on load up to 30% load level to test performance of and tune the balance of plant. Several issues were encountered with the balance of plant during the commissioning phase and are discussed below. Corrective actions taken are also discussed.

Anode Backpressure Valve (PV360) Issue and Anode Recycle System Rework: During pressure and leak testing, leaks were found in the anode recycle blower flange seals. After an initial attempt at replacing the gasket, it was agreed upon to hermetically seal the blower volute by welding. The repair was successful and confirmed by leak testing.

During hot operation with the 96-cell stacks, the anode backpressure valve failed in closed position. During stack change-out, it was found that the valve was seized due to a material issue. It was decided to remove the valve and replace it with a pipe segment. Removal of the anode backpressure valve required a modification to the anode recycle line to prevent purge gas from short circuiting in non-recycle cooldown (NRC) and emergency shut-down (ESD) cases. A new valve was installed in the anode line between the anode recycle blower exit and the inlet to the module. The purge gas injection point was moved to just downstream of the new valve. During a NRC or ESD, the new valve would close forcing purge gas to flow through the stacks and preventing back flow through the recycle blower.

Start-up System Rework: Another issue was with the CPOx reactor igniter (cartridge heater) which failed preventing the CPOx system from heating up. The igniter was controlled using a mechanical relay and its internal thermocouple, resulting in relatively large swings in temperature during the on-off cycles. To lessen the thermal stress on the igniter, the mechanical relay was changed to a solid state relay (and controller). No additional failures were observed.

The pressure at the inlet to the Start-up reactor was observed to be higher than expected which resulted in the air and fuel mass flow controllers operating in a more open position. In addition, due to the higher pressure, the maximum achievable flow through the mass flow controllers was reduced. The mass flow controllers were recalibrated to account for the increased resistance, and a larger Start-up reactor was fabricated and installed.

During long periods in hot standby or at low power levels the Start-up reactor remains in operation causing excessive carbon deposition to occur. This results in a gradual increase in flow resistance across the Start-up system. The flow controllers eventually open to 100% and can no longer maintain the required flow resulting in decreased hydrogen to the catalytic air preheater. To mitigate this issue, a method to periodically burn off the carbon was developed and implemented in the logic.

Purge System Modifications: Enhancements were made to the purge system to ensure a complete purge during an emergency shut down (ESD). During an ESD, the system cools down at a much slower rate. The duration of the purge is therefore much longer and requires more purge gas. The changes made to the purge system included increasing the number of purge gas bottles and modifying the tubing to accommodate the new bottles. In addition, tight pressure control on the anode side is required during a purge to maintain the pressure at an acceptable level and prevent oxygen infiltration. Therefore, a separate ESD purge branch which included a low droop pressure regulator was added to the purge system.

Control System Verification: Control system verification was performed during the checkout and commissioning phase with the goal of having a properly tuned, error free system when the new cell stacks are used. The flow and temperature control loops were tuned and attention was shifted to working out any remaining issues with the control logic. Several changes to the control system were made such as correcting I/O scaling, adjusting alarm set points to prevent nuisance trips and correcting a few issues with the control logic. In addition, several enhancements were made including modification of the HMI to allow the operator to have additional control over the system, and improved data capture logic to provide an increased data capture rate during an unintended shut down. Logic changes were also implemented to allow rapid restarting of the system when the system was at high enough temperature.

Power Conversion System Issues: The initial attempts at going on load with the 96-cell stacks uncovered several issues related to the Power Conversion System (PCS). The issues included over-voltage and over-current faults, current imbalance faults and communication issues between the PCS and the power plant control system. These issues were corrected by updating PCS settings and the power plant was successfully brought to 30% load for a short period of time.

Testing with New Stacks

As reported under Section 3.1, the 96-cell stacks (old used stacks) were replaced with 120-cell stacks (new unused stacks). PCM system factory testing was completed and the test requirement of >1000 hours of hot operation was satisfied. Due to reliability issue with the power conditioning system (PCS), factory testing was completed using a DC load bank.

The system testing summary is presented here. The purpose of the factory acceptance testing was to subject the fuel cell system to field conditions and assess its performance and durability upon completion of 1000 hours of testing. The results of the factory acceptance testing will serve to gauge the progress toward meeting the stack life and degradation targets of >4 years and <0.2%/1000 hours, respectively.

Initial attempts at completing the factory testing using the PCS were unsuccessful due to numerous issues with the DC booster section of the PCS. About 120 hrs of on load testing was completed before switching to operation on the DC load bank. The change to load bank operation was made to achieve 1000 hours of continuous operation. The load bank test period was commenced on 10/14/15 (elapsed time of 1344 hrs in plots).

Operation on the load bank was successful with the exception of a trip that occurred after 540 hours of operation. The problem was found to be a faulty pressure switch along with the accumulation of leaves on the air intake of the load bank. After the load bank was repaired, the power plant was brought back on load for the completion of the 1000 hours of testing.

Upon completion of 1000 hours of testing, the power plant was placed in hot standby mode of operation. The PCS was repaired, and tested at full load supplied from a DC power source. Upon successful completion of the test, the power plant was brought back on load using the PCS. Again, a DC booster board fault occurred leaving block 2 with 9 operational boards. After operating on 19 boards for several days, another board failed on 12/24/15 causing a trip to hot standby. The power plant was then shut down due to additional issues found with the water system.

The full load testing was performed at a gross stack power (DC) of 55.8 kW. At this power level, the fuel flow was 5.02 scfm and the air flow ranged from 110 to 120 scfm. The system was run at a target fuel utilization of 85% which is shown in Figure 5-28. The air flow and air utilization during the test period are plotted in Figure 5-29. During the period of operation on the load bank, the overall air utilization decreased (increase in air flow) to maintain stack differential temperatures below 130ºF.

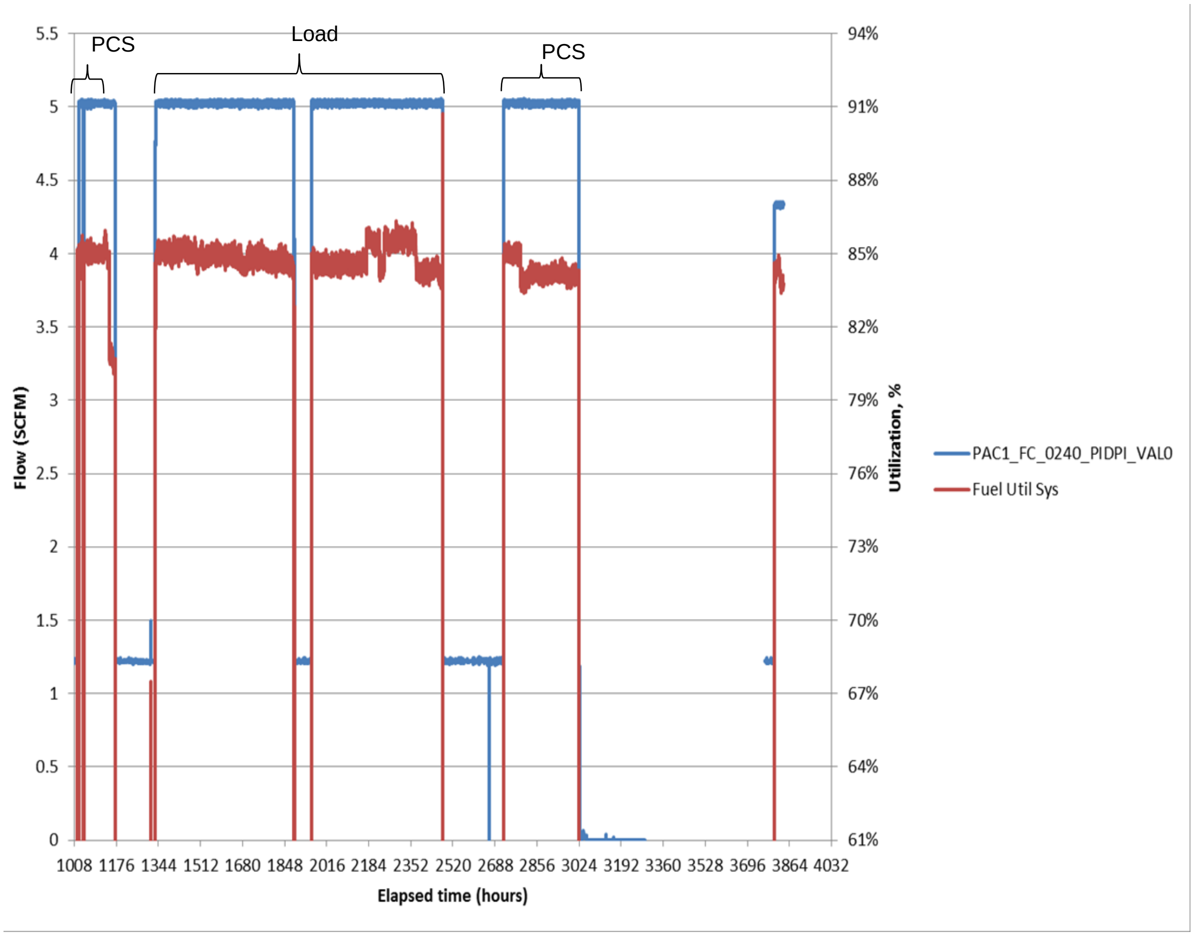

Figure 5-28 Fuel Flow Rate and Utilization During 50 kW PCM System Factory Testing

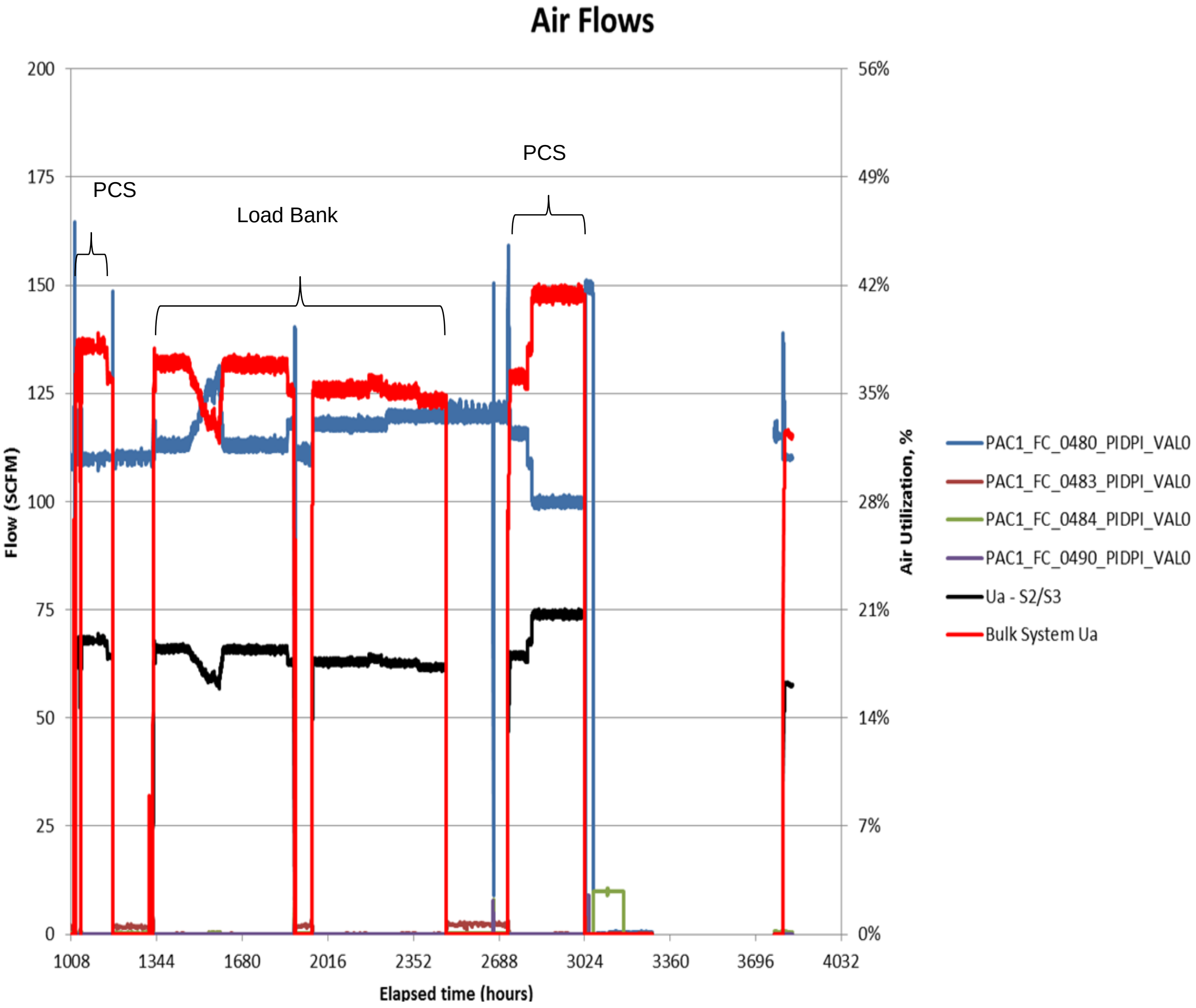

Figure 5-29. Air Flow Rate and Utilization During 50 kW PCM System Factory Testing

Figure 5-30 shows the stack currents during the test period. A limitation of operating on a single load bank was the loss of independent current control for the two power blocks. In the single load bank configuration used here, both power blocks were connected to the same point on the load bank which caused the current in each block to float. This is shown in Figure 5-30 during the load bank operation period. The connection between the stacks and load bank is shown schematically in Figure 5-31.

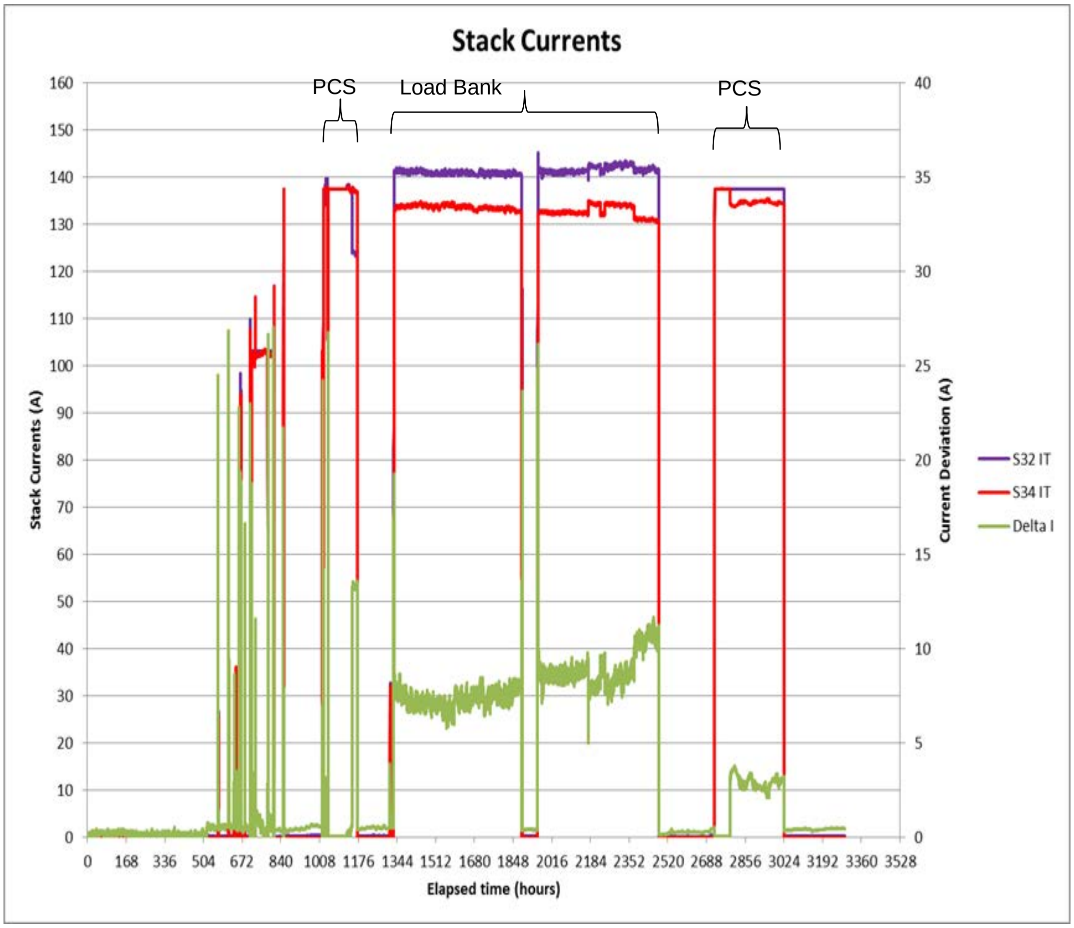

Figure 5-30. Stack Currents During 50 kW PCM System Factory Testing (PC indicates testing using power conversion system)

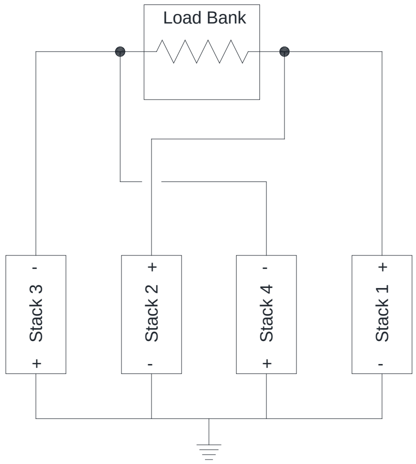

Figure 5-31. Electrical Configuration Showing Stack-Load Bank Connections

A key metric in assessing the performance of the fuel cell system is the power degradation rate. Figure 5-32 shows the fuel cell system stack power as a function of time. The voltage degradation rate was 4.5 mV/1000 h (0.5%/1000 h) during the first 539 hrs of continuous testing. The degradation rate increased to 7.8 mV/1000 h (0.9%/1000 h) during the time period from 1960 to 2480hrs. The degradation rate during both periods exceeded the target degradation rate of 0.2%/1000 h. However, the larger than expected degradation rate is likely due to the numerous trips and shutdowns that occurred from PCS failures. The plan is to continue to run the power plant to collect additional data to better assess the long term performance of the cell stacks and to gain operational experience with this type of fuel cell system.

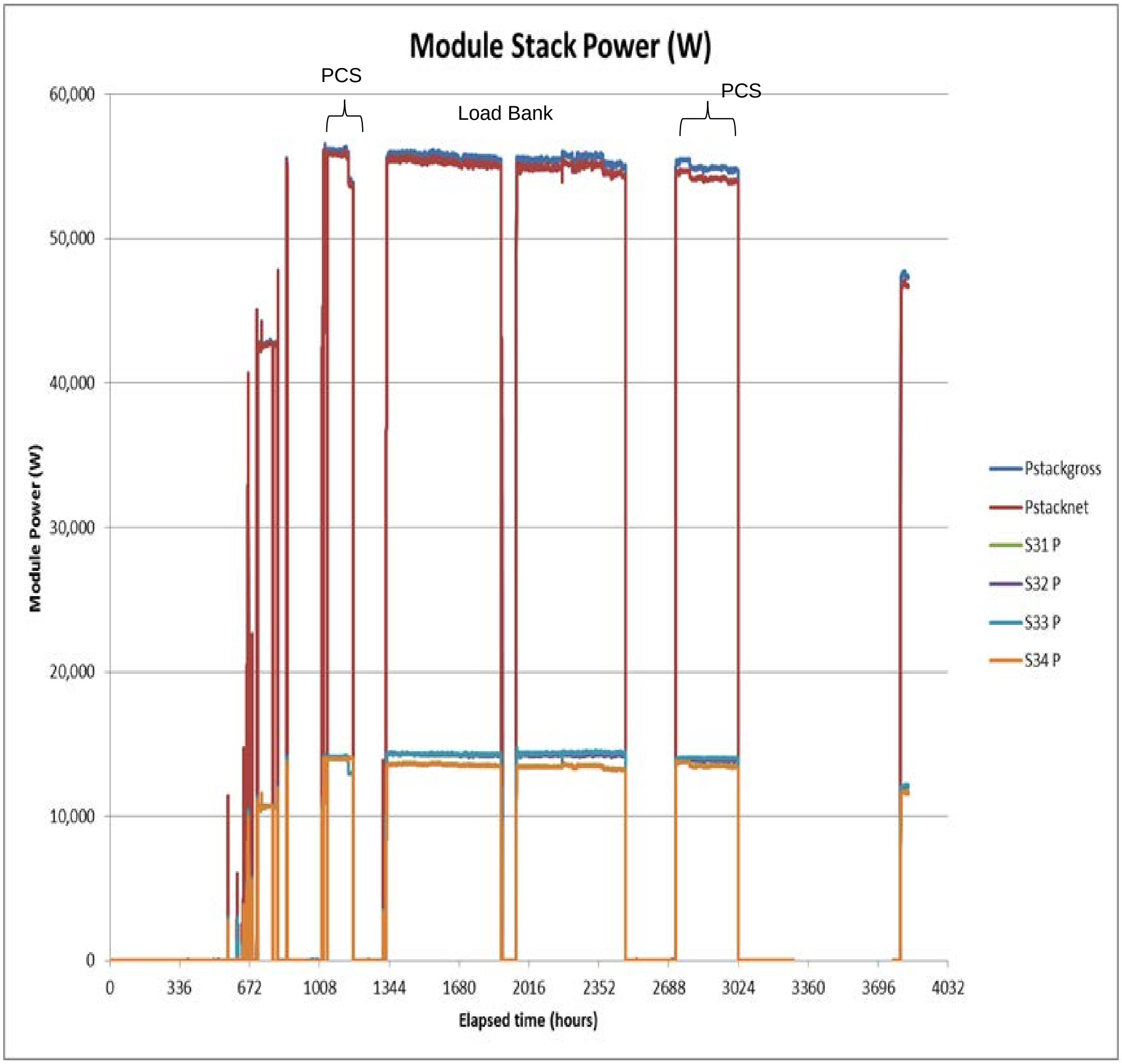

Figure 5-32. SOFC Module Power Output During 50 kW PCM System Factory Testing

The power plant efficiency was calculated using a DC/AC conversion efficiency of 97%. The gross DC and AC power produced by the power plant during the test period were 55.8 kW and 54.1 kW, respectively. The parasitic load was 4.6 kW resulting in a net AC power of 49.5 kW and an electrical efficiency of 88.8%. The overall power plant efficiency taking into account the fuel utilization was 61% which met the target efficiency of >50%.

Some of the issues observed during the testing and the corrective actions taken are discussed below.

Fresh Air Flow Meter and Blower Variable Frequency Drive: The fresh air flowmeter electronics were found to be malfunctioning causing a loss in the feedback signal. The unit was returned to the manufacturer for repair.

The blower was observed to oscillate when being controlled to certain set points. The cause of the oscillatory behavior was determined to be the VFD (Variable Frequency Drive). The VFD was returned to the vendor and replaced with a new VFD.

Cathode Air Dehumidification/Desiccant System: The humidity sensor in the dehumidification system found to be malfunctioning. The malfunctioning sensor was replaced. Achieving steady operation of the desiccant system was a challenge. The main problem was reactivation air temperature control. The reactivation air temperature was controlled by adjusting the amount of power plant exhaust fed into the hot side of the reactivation loop. The reactivation air temperature was not reaching the set point, but the temperature limit on the hot side of the loop was being exceeded. This caused unstable operation of the reactivation air valve and high temperature faults resulting in the desiccant unit to shut down. Adjustments were made to the temperature control under the guidance of the manufacturer in attempts to correct the issue. Fortunately, the desiccant system operation problems occurred during a relatively dry time of the year. Therefore, it is unlikely that any significant Cr poisoning had occurred.

Stack Voltage Maldistribution and Purge System Rework: During start up with the 120-cell stacks voltage maldistribution was observed. Excessive oxygen was observed in the anode system, as determined by GC measurements, which is an issue due to the potential for anode oxidation. Additional testing was performed to determine the amount of oxygen infiltration into the anode and to determine the amount of additional H_2 required to supplement the purge gas. A new mass flow controller was added to the system to control the addition of supplementary H_2 and the control system was updated with the required logic. In addition, the anode recycle blower shaft seal purge was changed from air to nitrogen to eliminate the potential for oxygen infiltration through the shaft seal.

Radiative Reformer: While in-cell reforming serves to provide thermal management of the stack, too much reforming can be problematic and lead to larger cell temperature gradients. The solution developed for this power plant was to shift a portion of the reforming load external to the cell stack. This was accomplished using a radiative reformer that captures the radiant energy from the stacks to drive the reforming reaction prior to fuel entering the cells. This provides lower cell temperature gradients and helps to prolong stack life.

GC samples were taken throughout the test period to determine the reforming split between the radiative reformer and the cells (stacks). Initial GC results showed approximately 45% reforming taking place in the cells with the remainder taking place in the reformer. The latest GC results show 55% reforming taking place in the cells. There are several potential causes of the performance degradation including reduction in heat transfer from scales and loss of catalyst surface area. The reformer temperatures shown in Figure 5-33 have increased over time by about 20ºC which is another indicator of reduced performance. Despite the performance loss, valuable information was gained and is being used in the radiant reformer design for the 200 kW system.

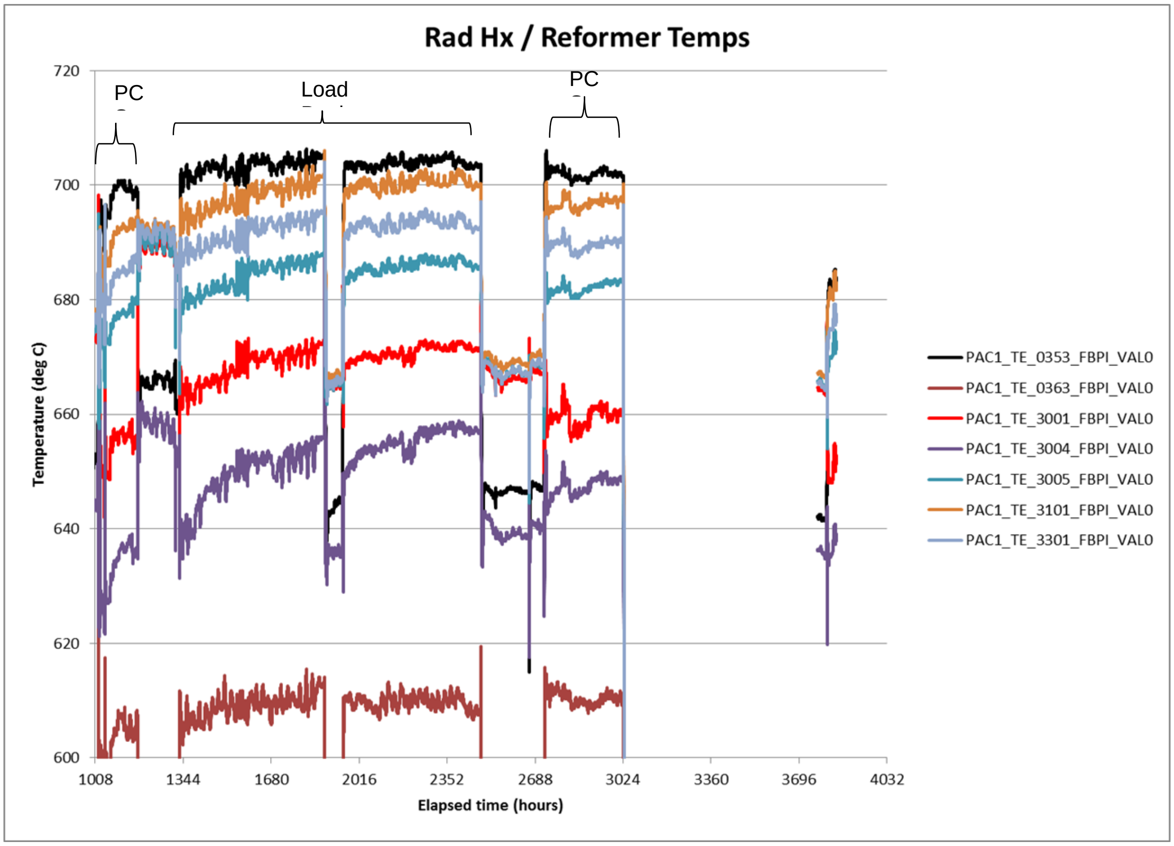

Figure 5-33. Radiative Reformer Temperatures

Power Conversion System: During stack change-out, the PCS manufacturer updated and verified PCS settings to ensure that the PCS was properly configured for running at 100% load with the new stacks. However, additional PCS issues prevented the power plant from running at 100% load. The PCS current control was giving a significant deviation from set point which caused the power plant to trip to hot standby. This was corrected by updating the DC converter settings and implementing current control loop in the power plant control system. The power plant was then able to run at 75% load continuously but tripped when brought to 85% load. This was determined to be an issue with the programmed power rating of the PCS. After updating the power rating setting, the power plant was brought to 100% load but again tripped after 45 minutes. Several DC booster boards were found to be damaged while investigating the cause of the trip. The PCS manufacturer replaced the damaged boards and the power plant was brought back on load.

Upon completion of the required 1000 hrs of testing, the power plant was shut down to perform repair work on the power conditioning system (PCS). The PCS repair involved replacing several failed DC booster boards and changing the current limit on each board to 16 amps. The repair work was performed by the PCS manufacturer ARDA Power.

The PCS successfully passed a verification test performed at full load using a DC power supply before being connected to the stacks. After connecting the PCS to the cell stacks, issues related to noise were discovered on several booster boards while attempting to go on load. Modifications were then made to the PCS in attempt to correct the observed noise issues. The modifications included the installation of capacitors on the communication lines and upgrading the firmware on the DC booster boards.

After the modifications were complete, another attempt was made to go on load. The modifications appeared to have corrected the noise problem. However, after a few days at full power, one of the block 2 booster boards tripped causing the block 2 current to drop to 134 A. The power plant was able to continue operation on 19 boards for about another 200 hours until another booster board tripped causing the power plant to trip to hot standby. An issue with the water system prevented a system restart and the system was then shut down.

CONCLUSION

Chromium-tolerant cell technology was developed. Scale-up (cell area) and stack implementation of the Cr-tolerant cell technology and longer-term performance stability evaluation for further verification were pursued. Long-term testing of a six-cell (121 cm^2 cell active area) stack containing three cells with Cr-getter material (30% Gb-70% Gc blend) and three standard TSC-3 cells was conducted. The Cr-getter cell group exhibited a lower performance degradation rate of 0.39%/1000 h than the standard cell group (0.57%/1000 h) over a 7489-h period (at 388 mA/cm^2 and 750°C). The Cr-getter configuration 1 (Design 2) evaluation was conducted in 16-cell and 64-cell stacks (550 cm^2 cell active area) at PCM system representative conditions of 68% fuel utilization, 36.4% in-stack reforming, 15% oxidant utilization, and 291 mA/cm^2. The tests showed very low performance degradation rates of 0.26%/1000 h over 6500-h period in a 16-cell stack and 0.32%/1000 h over 10000-h period in a 64-cell stack. Cr-getter Configuration 1 was selected for 120-cell stacks fabricated for the PCM system test.

To further optimize TSC-3 (thin) cell anode substrate, a parametric study was conducted using single cell (81 cm^2 active area) tests. Effect of cell build (manufacturing) variables such as cell (anode substrate) thickness and cell density (via sintering temperature) on cell performance was studied in the operating temperature range of 650 to 800°C. The four cells used in the study covered a thickness range of 0.3 to 0.6 mm and density range of 5.25 to 5.75 g/cc. Cell performance (at 750°C and 500 mA/cm^2) was also characterized in the fuel utilization range of 50 to 90%. The results indicated that for improved cell performance at high current density and/or fuel utilization, thin anode substrate and cell density of less than 5.5 g/cc are desired. Power densities approaching 700 mW/cm^2 were exhibited by a cell featuring 0.3 mm thickness and 5.45 g/cc density.

Advanced seal development activities included testing of a glass seal material (from a Japanese company) in a single cell (81 cm^2 active area). The test accumulated over 12,700 h and included 10 thermal cycles, exhibiting a low performance degradation rate of 0.5%/1000 h (at 500 mA/cm^2 and 750°C) over the test period. Post-test analysis of the cell was carried out. There was no evidence of any significant reaction or diffusion of glass components into the cell materials which was consistent with the low degradation rate observed over 12,700-hour test period. This seal material can serve as a more stable substitute for the commercially available glass coating used in Thermicullite seal.

Sub-scale module tests were conducted to guide the development of SOFC stack module. Test of a 16-cell stack (550 cm^2 cell active area) in a module (thermally self-sustaining environment) at system operating conditions (representing 50 kW PCM system) was conducted at FCE, Danbury facility, accumulating 3960 h on load. The testing included three steady state test periods at system relevant conditions (273 mA/cm^2). Overall, the stack operated at these conditions for more than 4,500 h with an average degradation rate below 1%/1000 h.

The fabrication of the PCM (SOFC module) was carried out. To facilitate Balance-of-Plant (BOP) system operational checkout (initial phase of PCM system test), four 96-cell stacks previously used in 60 kW quad-based SOFC module were installed in the (PCM) module. Fabrication of 120-cell stacks (550 cm^2 cell active area) for PCM system test was completed. The stacks were built, conditioned and factory tested at VPS. The factory acceptance testing included fuel utilization testing (up to 75% fuel utilization) before and after thermal cycle, and steady state performance characterizations at Phase I system and PCM system operating conditions. Four (factory) accepted stacks were received at FCE, Danbury, for module integration (to replace the used 96-cell stacks) and subsequent PCM system test.

The PCM system (unit) included Mechanical BOP and Electrical BOP, in addition to the SOFC module (PCM). BOP component development was carried out. The integrated fuel preheater (radiative) and fuel pre-reformer, termed Radiative Fuel Reformer, was developed combining input from reforming catalyst vendors, CFD analysis and sub-scale testing. Coated monolith catalysts, to provide the desired reforming capability with reduced pressure drop, were evaluated. Testing at FCE validated the effectiveness of the catalyst coating by producing near-equilibrium outlet concentrations in a wide range of catalyst operating temperatures and space velocities. A corrugated fin design for the catalyst support was selected in collaboration with the catalyst coating vendor. The full-scale radiative fuel reformer was fabricated for use in the PCM power plant.

PCM system drawings were developed. Specification, fabrication/ procurement, and testing of PCM system balance-of-plant components were carried out. The Power Conditioning System (part of Electrical BOP) design and layout of components were carried out. Fabrication and assembly of the mechanical and electrical balance of plant, and the site preparations at FCE, Danbury were completed. PCM system component verification, final end-to-end checkout and leak testing was also completed. Process and control tests for the 50 kW PCM system were performed. The issues identified were resolved.

First stage of the 50 kW PCM system checkout and commissioning using pre-tested SOFC stacks was carried out. Control system verification was performed and the issues identified with the control logic were resolved. Preliminary testing of the 50 kW PCM plant included successful start-up and operation in hot standby mode. Grid connected testing to verify the power control system function and load step transitioning was then carried out. The system was tested up to the 30% load level. The plant was shutdown to replace the old stacks with new (unused) factory tested 120-cell stacks. Lessons learned from commissioning and post-test examination (prior to stack replacement) were implemented in the module rebuild for success of the PCM system demonstration test. No issues were observed related to Radiative Fuel Reformer and Catalytic Heat Exchanger (cathode air preheater), imparting confidence in the BOP component design.

The reassembled stack module was integrated with the PCM plant and testing was resumed. The system operation at full load was accomplished. The PCM system factory testing was completed, meeting the test requirement of >1000 hours of hot operation. Due to reliability issue with the power conditioning system, factory testing was conducted using a DC (direct current) load bank. The full load testing was performed generating a gross DC stack power of 55.8 kW. The system was run at a target (overall) fuel utilization of 85%. The power plant efficiency was estimated using a DC/AC conversion efficiency of 97%. The overall power plant efficiency taking into account the fuel utilization was 61% which met the target efficiency of >50%. Overall, the 50 kW SOFC power plant test was successful. The testing performed during this project verified the performance of the cell stacks under field conditions. Knowledge gained will be used for developing the 200 kW SOFC system. The 50 kW test served as an important step in the development of robust process control algorithms and control strategies. In addition, valuable system design experience was gained and will result in smaller, more compact anode recycle blowers, improved fresh air desiccant system controls and improved plant heat-up strategies.

Toward MW-class module development, concepts using external stack manifolds (based on the carbonate fuel cell success) were generated. The design considered facilitated elimination of cathode and anode shim seals, significantly reducing the quantity of stack components required. To facilitate scale-up to a larger cell package (more suited for MW-class stack module), the concept employed U-flow configuration for cell cathode side. This flow configuration with the cathode gas turn manifold is expected to provide better thermal management of the MW-class SOFC stack that is required to accommodate significant in-stack reforming of natural gas fuel on anode side.

REFERENCES

[1] Sihyuk Choi, Seonyoung Yoo, Jiyoun Kim, Seonhye Park, Areum Jun, Sivaprakash Sengodan, Junyoung Kim, Jeeyoung Shin, Hu Young Jeong, YongMan Choi, Guntae Kim and Meilin Liu; *"Highly efficient and robust cathode materials for low-temperature solid oxide fuel cells*; $PrBa_{0.5}Sr_{0.5}Co_{2-x}Fe_{x}O_{5+delta}$"; Scientific Reports 2013, 3: 2426

[2] Min Yang, Edith Bucher, Werner Sitte; "*Effects of chromium poisoning on the long-term oxygen exchange kinetics of the solid oxide fuel cell cathode materials La0.6Sr0.4CoO3 and Nd2NiO4"*; Journal of Power Sources 196 (2011) 7313– 7317.

[3] Bo Huang, Xin-jian Zhu, Rui-xuan Ren, Yi-xing Hu, Xiao-yi Ding, Ye-bin Liu, Zong-yao Liu; *"Chromium poisoning and degradation at $Gd_{0.2}Ce_{.0.8}O_{2}$-impregnated $LaNi_{0.6}Fe_{0.4}O_{3-delta}$ cathode for solid oxide fuel cell";* Journal of Power Sources 216 (2012) 89-98.

[4]. Zhang, T., Fahrenholtz, W. G., Reis, S. T. and Brow, R. K., Borate Volatility from SOFC Sealing Glasses. Journal of the American Ceramic Society, 91: (2008) 2564–2569

LIST OF ACRONYMS

A	Ampere
AC	Alternative Current
AFL	Anode Functional Layer
AI	Air In
AIC	Air In Center
AO	Air Out
AOC	Air Out Center
ASR	Area Specific (cell) Resistance
ASU	Air Separation Unit
Atm	Atmosphere
BFD	Block Flow Diagram
BOL	Beginning of Life
BOP	Balance of Plant
CAD	Computer Aided Drafting
CBPP	Coal-Based Power Plant
CC	Current Collection (DC)
CDR	Component Development Requirement
CFD	Computational Fluid Dynamics
CFL	Cathode Functional Layer
CGCU	Selexol Cold Gas Cleanup
COR	Contracting Officers Representative
CT	Cooling Tower
CTE	Coefficient of Thermal Expansion
CTF	Critical-To-Function
CTP	SECA Core Technology Program
CW	Cooling Water
CWP	Cooling Water Pump
DC	Direct Current
DFC	Direct Fuel Cell (FCE Molten Carbonate Fuel Cell)
DIR	Direct Internal Reforming, meaning in-stack reforming
DOE	United States Department of Energy
DSRP	Direct Sulfur Recovery Process
EOL	End of Life

FCE	FuelCell Energy, Inc.
FEA	Finite Element Analysis
FGD	Flue Gas Desulfurization
FI	Fuel In
FIC	Fuel In Center
FO	Fuel Out
FOC	Fuel Out Center
GA	General Arrangement (Plant Layout)
GT	Gas Turbine
HAZOP	HAZard and OPerability analysis
HDS	Hydrodesulfurization
HEX	Heat Exchanger
HHCs	Heavier Hydrocarbons (C2+)
HHV	Higher Heating Value
HMI	Human Machine Interface
H&MB	Heat and Mass Balance
HP	High Pressure
HPC	High Performance Cathode
HRSG	Heat Recovery Steam Generator
HTDS	High-Temperature Desulfurization
I	Electrical Current
IC	Interconnect or separator plate
ICM	In-Cell Manifolded
IGFC	Integrated Gasification Fuel Cell
IIR	Indirect Internal Reforming, meaning in-stack, between-cell, reforming
IR	Internal Resistance, of the cell or stack, ohm-cm2.
K	degrees Kelvin
kW	Kilo-Watt
LHV	Lower Heating Value
LTS	Low Temperature Supercell
MDU	Module Demonstration Unit
MF	Mineral Fiber (thermal insulation)
MT	Microporous (thermal insulation)
MW	Mega-Watt

NETL	National Energy Technology Laboratory
Ni/YSZ	Nickel – Yttria-Stabilized Zirconia
NOC	Normal Operation Condition
OCV	Open Circuit Voltage
OTM	Oxygen Transport Membrane
PCI	Pre-commercialized Integrated
PFD	Process Flow Diagram
P&ID	Piping & Instrumentation Diagram
PNNL	Pacific Northwest National Laboratory
POC	Proof-of-Concept
PPC	Peak Power Condition
psi	Pound per square inch pressure
psid	pounds per square inch pressure differential (pressure drop)
Q	Quarter
Redox	Reduction - oxidation
S1 (2)	Stage 1 (2)
SECA	Solid State Energy Conversion Alliance
SG	Syngas
SLPM, Slpm	Standard liter per minute (at conditions of 1 atm and 70°F (21.1°C))
SOFC	Solid Oxide Fuel Cell
ST	Steam Turbine
TIPS	Thermally Integrated Power System
TSC	Tape casting Screen-printing Cofiring
UA	Total heat transfer coefficient times heat transfer surface area, a designation for heat exchanger design
Ua, U_o, UtO	Air (Oxygen) Utilization
Uf, UtF	Fuel Utilization
USA	United States of America
V	Volt
VFD	Variable Frequency Drive
VPS	Versa Power Systems Ltd.
W	Watts
WGCU	Warm Gas Cleanup